



UNIVERSITYTRANSPORTATIONCENTER
FOR UNDERGROUND TRANSPORTATION INFRASTRUCTURE

**THE CHARACTERIZATION OF DELAMINATION PROCESSES WITH
RESPECT TO WATERJET SHOTCRETE REMOVAL DURING TUNNEL
LINER REPAIR AND MAINTENANCE**

FINAL PROJECT REPORT

by
Hugh B. Miller¹
John P.H. Steele²
Brian Asbury¹
Erik Charrier³
Josef P. Bourgeois³

¹ Colorado School of Mines, Mining Engineering Department

² Colorado School of Mines, Mechanical Engineering Department

³ Colorado School of Mines Mining Engineering, Ph.D. Graduate Student

RAMAX LLC
CSM IET Waterjet Foundation
Scientific Associates Inc.

For

University Transportation Center for
Underground Transportation Infrastructure
(UTC-UTI)

October 22, 2020



COLORADOSCHOOLOFMINES
EARTH ENERGY ENVIRONMENT



CAL STATE LA
CALIFORNIA STATE UNIVERSITY, LOS ANGELES



Disclaimer

The contents of this report reflect the views of the authors, who are responsible for the facts and the accuracy of the information presented herein. This document is disseminated in the interest of information exchange. The report is funded, partially or entirely, by a grant from the U.S. Department of Transportation's University Transportation Centers Program. However, the U.S. Government assumes no liability for the contents or use thereof.

1. Report No.	2. Government Accession No.	3. Recipient's Catalog No.	
4. Title: The Characterization of Delamination Processes with Respect to Waterjet Shotcrete Removal during Tunnel Liner Repair and Maintenance.		5. Report Date October 22, 2020	
		6. Performing Organization Code	
7. Author(s): Hugh B. Miller, Ph.D., https://orcid.org/0000-0002-0146-5542 John Steele, Ph.D. Brian Asbury, CSM EMI Lab Manager Erik Charrier, Ph.D. Graduate Student Josef Bourgeois, Ph.D. Graduate Student		8. Performing Organization Report No.	
9. Performing Organization Name and Address University Transportation Center for Underground Transportation Infrastructure (UTC-UTI) Tier 1 University Transportation Center Colorado School of Mines Coolbaugh 308, 1012 14th St., Golden, CO 80401		10. Work Unit No. (TRAIS)	
		11. Contract or Grant No.	
12. Sponsoring Agency Name and Address United States of America Department of Transportation Research and Innovative Technology Administration		13. Type of Report and Period Covered	
		14. Sponsoring Agency Code	
15. Supplementary Notes Report also available at: https://zenodo.org/communities/utc-uti			
16. Abstract: This research seeks to develop an advanced excavation system for the removal of damaged and compromised shotcrete structural liners used in underground workings and tunnels. Waterjet technology has the potential to circumvent many of the technical and operating challenges commonly associated with conventional shotcrete removal methods utilized in liner repair and maintenance. Empiric evidence suggests that waterjets are capable of selectively removing damaged areas of support liners without structurally compromising the material adjacent to the area being repaired. The primary objective of this research is to compare and contrast the unintended damage caused to the surrounding liner and substrate by both conventional impact hammers and waterjet excavation methods during empiric testing. This analysis utilized simulated shotcrete panels that were instrumented to quantify vibration during excavation, substrate damage, and delamination. Vibration data, ground penetrating radar, and visual inspection strongly supports the hypothesis that waterjet cutting generates less collateral damage to surrounding shotcrete and liner substrate, as well as detrimental impact to the steel reinforcement within the liner. The results of this research will be used as the fundamental basis for future work in this area.			
17. Key Words: Shotcrete Excavation and Repair, Waterjet Excavation, Tunnel Rehabilitation		18. Distribution Statement No restrictions.	
19. Security Classification (of this report) Unclassified	20. Security Classification (of this page) Unclassified	21. No of Pages: 300	22. Price NA

Table of Contents

CHAPTER 1 - INTRODUCTION	16
1.1 Research Objectives	17
1.2 Research Limitations	18
1.3 Research Originality	19
1.4 Methodology	20
CHAPTER 2 – LITERATURE SEARCH	23
2.1 Introduction	23
2.2 Underground Structural Liners	23
2.3 Fracture Mechanisms of Impact Bits	34
2.4 High-pressure Waterjet Scaling	44
2.5 High-pressure Waterjet Excavation of Shotcrete/Concrete Liners	45
2.6 Instrumentation of High-Pressure Waterjet Systems	46
2.7 Hydraulic Fracturing Excavation Systems and Fracture Mode	50
2.8 Visual and Non-Destructive Analysis	59
2.9 Summary	67
CHAPTER 3 - RESEARCH METHODOLOGY	69
3.1 Introduction	69
3.2 Experimental Setup	70
3.2.1 Test Panel	70
3.2.2 Mechanical Excavation	72
3.2.3 Waterjet Excavation	73
3.2.4 Vibration Data Acquisition	78
3.2.5 Visual Inspection and Examination of Cuttings	80
3.2.6 Ground Penetrating Radar	82
3.2.7 Coring and Microcomputed Tomography	87
CHAPTER 4 - TESTING RESULTS WITH RAW AND PROCESSED DATA	94
4.1 Introduction	94
4.2 Investigation of Waterjet System Operating Parameters Necessary to Cut Shotcrete Layer	94
4.2.1 Changes in Waterjet System Operating Parameters During Testing	94
4.2.2 Comparing Waterjet Excavation Process to Impact Hammer Excavation Process	96
4.3 Investigation of Fracture Mechanisms Imposed by Waterjet Shotcrete Cutting	97
4.3.1 Material Removal Geometry for Both Excavation Methods	98
4.3.2 Examination of Cuttings Generated by Both Excavation Methods	100
4.4 Verification of Waterjet Effectiveness as an Alternative Shotcrete Removal Tool	102
4.4.1 Post-Excavation Physical Inspection of Test Panels	102

4.5 Validation of Hypothesis that Waterjet Removal of Concrete/Shotcrete Liners will Result in Less Collateral Damage than Conventional Methods.....	102
4.5.1 Visual Inspection Comparison of Kerf and Damage of Steel Infrastructure.....	103
4.5.2 Vibration Comparison from DAQ Results.....	107
4.5.3 Non-Destructive Analysis from Processed GPR Scan Comparison.....	119
4.5.4 Non-Destructive Analysis from microCT Scans of Cores from Panel 4 and Panel 7.....	137
CHAPTER 5 - DISCUSSION OF RESEARCH RESULTS	142
5.1 Introduction	142
5.2 Investigation of Waterjet System Operating Parameters Needed to Cut Shotcrete Layer.....	142
5.3 Investigation of Fracture Mechanisms Associated with Waterjet Cutting of the Shotcrete Layer.....	143
5.4 Verification that Waterjets can Successfully be Used as an Alternative Shotcrete Removal Tool	145
5.5 Validation of the Hypothesis that Waterjet Liner Excavation will likely result in Less Collateral Damage than that Produced by Conventional Methods.....	145
CHAPTER 6 – SUMMARY AND CONCLUSIONS	153
6.1 Introduction	153
6.2 Summary and Conclusions.....	153
6.2.1 Characterizing the Excavation Process Associated with Removal of Deteriorated Shotcrete Using Waterjet Technology.....	153
6.2.2 Validating the Hypothesis that Waterjet Excavation of Deteriorated Liners Will Result in Less Collateral Damage than Conventional Methods	154
6.3 Recommendations for Additional Work	155
 REFERENCES	
 APPENDIX A – TECHNOLOGY TRANSFER ACTIVITIES	
1 Accomplishments	
1.1 What was done? What was learned?	
1.2 How have the results been disseminated?	
2 Participants and Collaborating Organizations	
3 Outputs	
4 Outcomes	
5 Impacts	
 Appendix B: PROJECT DATA AND CALCULATIONS	
Section B-1: Concrete and Quikrete Specification	
Section B-2: Fluid and System Parameters	
Section B-3: Visual Inspection of Panels After Excavation	
Section B-4: Accelerometer Data	
Section B-5: Ground Penetrating Radar Data	
Section B-6: 1600 MHz Radargram Interpretation Notes	

List of Figures

Figure 1-1: Conventional mechanized scaler for operating heights below 20 meters (left) and a manlift with operators and manually held impact hammer for operating heights above 20 meters (right) [6].

Figure 1-2: Hydroexcavation robot removing damaged concrete in Channel Tunnel liner [7].

Figure 2-1: Illustration showing three phases of concrete structure including aggregate, transition zone, and bulk cement paste [11].

Figure 2-2: Early strength partial beam test results for dry mix shotcrete and concrete conducted by NIOSH, n=54 samples [15].

Figure 2-3: Completed shotcrete ground control system for underground mining operation in weak rock [12].

Figure 2-4: Permanent lining design types [8].

Figure 2-5: Maximum shear stress data under varying drilling conditions including (1) axial percussion plus torsional percussion plus rotary action, (2) axial percussion plus rotary action, and (3) axial percussion [20].

Figure 2-6: According to Karanam and Misra (a) forces acting on system during percussive drilling (b) how wedge angle effects geometry of forces during percussive drilling [19].

Figure 2-7: Mathematical models of chip formation from wedge [19].

Figure 2-8: Morphology of fractures induced by a single indenter [26].

Figure 2-9: Hydroexcavation robot removing damaged concrete in tunnel liner [7].

Figure 2-10: Components typically found in waterjet systems [32].

Figure 2-11: Discharge coefficients (C) associated with generic nozzle shapes [33].

Figure 2-12: Common flow straighteners for nozzle performance testing [34].

Figure 2-13: High speed waterjet showing sections of continuous flow jet, droplet layer, and final zone consisting of droplets and air [32].

Figure 2-14: Fracture zone produced in tension-softening material [10].

Figure 2-15: Incubation period and erosion period of concrete according to (a) flow velocity and (b) exposure time [37].

Figure 2-16: Relationship between threshold jet velocity and fracture toughness in varying rock types and concrete [37].

Figure 2-17: Summary of non-destructive testing techniques [40].

Figure 2-18: Schematic illustrating GPR data collection process [43].

Figure 2-19: Alani et al GPR scan with rebar locations and deteriorated area of bridge deck [45].

Figure 2-20: Plan-view GPR sections at increasing depths below surface [45].

Figure 2-21: GPR scan showing concrete deterioration on bridge deck [46].

Figure 3-1: Composite panel dimensions (shown in inches) used for experimentation.

Figure 3-2: Process of mechanical excavation using Bauer impact hammer.

Figure 3-3: Waterjet instrumentation and cutting setup at SAI/RAMAX waterjet laboratory.

Figure 3-4: Target parameters associated with a twin orifice nozzle rotary head jet system [10].

Figure 3-5: Waterjet excavation – SAI/RAMAX Laboratory set-up (upper left) start of slot in panel (upper right) kerf in panel (bottom left) close-up of kerf in panel (bottom right).

Figure 3-6: Accelerometer mount (left) and ADXL337 (right).

Figure 3-7: Accelerometer locations (left) accelerometers on actual panel (right).

Figure 3-8: Data acquisition setup.

Figure 3-9: Example of visual inspection scenario for left face of panel 2.

Figure 3-10: Model RX-29 Tyler sieve shaker used for sieve analysis of impact hammer cuttings.

Figure 3-11: 2600 MHz radar antenna connected to SIR 3000 radar system control unit (left) 1600 MHz radar antenna coupled with SIR 4000 radar system control unit.

Figure 3-12: Top shotcrete face with GPR gridlines (top left) back timber form face to receive one GPR scan (top right) front timber form face to receive one GPR scan (bottom left) bottom plywood/concrete face with GPR gridlines (bottom right).

Figure 3-13: GPR scan sequencing for top shotcrete face along with directions of single scan for sample's front, right, left, and back-timber form face.

Figure 3-14: GPR scan sequencing for bottom plywood/concrete plan face.

Figure 3-15: Coring process showing (1) proposed locations of cores and (2) actual locations of cores.

Figure 3-16: Core drill and bit set-up with forklift at EMI.

Figure 3-17: Cores and their respective lengths. Lettering "T" indicates the top of the core while "B" indicates the bottom of the core.

Figure 3-18: MicroXCT-400 equipment used for microCT analysis of core segments.

Figure 3-19: Process of acquiring a microCT scan.

Figure 3-20: Location of focus areas for microCT scans of each core sample.

Figure 4-1: Photos taken at panel face showing cutting geometry and bond surface left after impact hammer testing (left) and waterjet testing (right).

Figure 4-2: Example of inconsistent kerf and damage to steel infrastructure during impact hammer testing.

Figure 4-3 Comparison of shotcrete cutting with twin orifice rotating waterjet to Momber's diagram [10]

Figure 4-4: Ribs of shotcrete left on edges of panel TEST due to traverse limitations in reversing direction.

Figure 4-5: Semi-logarithmic plot of impact hammer sieve analysis tests.

Figure 4-6: Impact hammer excavation upper wall profile visual inspection on panel 3.

Figure 4-7: Waterjet excavation upper wall profile visual inspection on panel 7.

Figure 4-8: Impact hammer testing, Panel 2, Run 1 of 7.

Figure 4-9 Waterjet testing, Panel 7, Run 1 of 6.

Figure 4-10: Vibration data acquired from accelerometers during impact hammer testing on panel 2.

Figure 4-11: Vibration data acquired from accelerometers during impact hammer testing on panel 3.

Figure 4-12: Vibration data acquired from accelerometers during impact hammer testing on panel 4.

Figure 4-13: Vibration data acquired from accelerometers during waterjet testing on panel 1.

Figure 4-14: Vibration data acquired from accelerometers during waterjet testing on panel 7.

Figure 4-15: Vibration data acquired from accelerometers during waterjet testing on panel TEST.

Figure 4-16: GPR scan processing flow.

Figure 4-17: Sample scan that goes through time zero correction (1) DeWow (2) Fourier filtering (3) time gain (4) and background subtraction (5).

Figure 4-18: Schematic showing path of EM wave at interface of two materials.

Figure 4-19: Microwave reflection profile for concrete pavement without a void and with a void [53].

Figure 4-20: Example of processed GPR scan before and after returning the upper envelope in MATLAB.

Figure 4-21: 1600 MHz post excavation south to north scans on panel 2 showing the lowest recorded amplitude increase within the substrate for a panel cut by the impact hammer.

Figure 4-22: 1600 MHz post excavation east to west scans on panel 2 showing the lowest recorded amplitude increase within the substrate for a panel cut by the impact hammer.

Figure 4-23: 1600 MHz post excavation south to north scans on panel 3 showing the second highest recorded amplitude increase within the substrate for a panel cut by the impact hammer.

Figure 4-24: 1600 MHz post excavation east to west scans on panel 3 showing the second highest recorded amplitude increase within the substrate for a panel cut by the impact hammer.

Figure 4-25: 1600 MHz post excavation south to north scans on panel 4 showing the highest recorded amplitude increase within the substrate for a panel cut by the impact hammer.

Figure 4-26: 1600 MHz post excavation east to west scans on panel 4 showing the highest recorded amplitude increase within the substrate for a panel cut by the impact hammer.

Figure 4-27: 1600 MHz post excavation south to north scans on panel 7 showing the highest recorded amplitude increase within the substrate for a panel cut by the waterjet system with notably lower amplitude increase than any of the impact hammer panels.

Figure 4-28: 1600 MHz post excavation east to west scans on panel 7 showing the highest recorded amplitude increase within the substrate for a panel cut by the waterjet system with notably lower amplitude increase than any of the impact hammer panels.

Figure 4-29: 1600 MHz post excavation south to north scans on panel TEST showing the lowest recorded amplitude increase within the substrate for a panel cut by the waterjet system with notably lower amplitude increase than any of the impact hammer panels.

Figure 4-30: 1600 MHz post excavation east to west scans on panel TEST showing the lowest recorded amplitude increase within the substrate for a panel cut by the waterjet system with notably lower amplitude increase than any of the impact hammer panels.

Figure 4-31: Core 1, panel 7 top half microCT scan sections with reference on core sample.

Figure 4-32: Core 1, panel 7 bottom half microCT scan sections with reference on core sample.

Figure 4-33: Core 1, panel 4 top half microCT scan sections with reference on core sample.

Figure 4-34: Core 1, panel 4 bottom half microCT scan sections with reference on core sample.

Figure 5-1: Example of edge effect caused by wire mesh, blocking erosion by waterjet, leaving shadow of shotcrete behind steel reinforcement.

Figure 5-2: Range of measured acceleration during testing of each developed panel.

List of Tables

Table 1-1: Summary of research methodology steps taken to achieve research objectives.

Table 2-1: Typical shotcrete mix designs [12].

Table 2-2: Typical sprayed/cast concrete design [8].

Table 2-3: Typical sprayed/cast concrete properties [8].

Table 2-4: Ground categories in which liners are constructed [8].

Table 2-5: Advantages and disadvantages of using a hydraulic drill in place of a pneumatic drill in underground working environments [21].

Table 2-6: Pressures used for range of material removal processes [36].

Table 2-7(a): Dielectric properties of common geomaterials [44].

Table 2-7 (b): Dielectric properties of common geomaterials [42].

Table 3-1: Composite panel properties used for experimentation.

Table 3-2: Variance in nozzle flow rate due to slippage and leakage through the system's flow controls.

Table 3-3: Continuous waterjet testing parameters.

Table 3-4: SIR 3000 control unit input parameters.

Table 3-5: SIR 4000 control unit input parameters.

Table 3-6: Proposed and actual core locations on panel 4 and panel 7.

Table 3-7: Measurements for designated scan area for each core sample.

Table 4-1: Panel number and associated testing method.

Table 4-2: Notes taken regarding operating parameters during waterjet excavation.

Table 4-3: Observations made during each testing method that consider mode of operation and health and safety hazards.

Table 4-4: Results of impact hammer cuttings sieve tests.

Table 4-4: Results of impact hammer cuttings sieve tests (continued).

Table 4-5: Results of fracture/failure count and measured distance, measured delamination, and percent split aggregate (exposed).

Table 4-6: Positive and negative peak acceleration values (g) reached during impact hammer and waterjet excavation according to each accelerometer.

Table 4-7: Distance in nanoseconds to panel components from plywood bottom.

Table 4-8: EM properties and reflection coefficients of materials in GPR scans.

Table 5-1: Peak amplitude measured by upper envelope scans of each panel.

Table 5-2: Post excavation rebar amplitude measurements.

Table 5-2: Post excavation rebar amplitude measurements (cont.).

Table of Abbreviations

AWJ:	Abrasive Waterjet
C:	Coefficient of Flow
cm:	Centimeters
CSL:	Composite Shell Lining
CSM:	Colorado School of Mines
DAQ:	Data Acquisition System
Degree F:	Degree Fahrenheit
DSL:	Double Shell Lining
EMI:	Earth Mechanics Institute
EM:	Electromagnetic Waves
Ft:	Foot/Feet
G:	Force per unit mass due to gravity
GPa:	Gigapascal
GPM:	Gallons per minute
GPR:	Ground Penetrating Radar
HP:	Horsepower
Hz:	Hertz
In:	Inch
Kg:	Kilogram
KSI:	Thousands of pounds per square inch
KW:	Kilowatt
L:	Liters
lb:	Pound
LPM:	Liters per minute
m:	Meter
microCT:	Microcomputed Tomography
MINARCO:	Mining Innovation, Rehabilitation, and Applied Research Corp.
mm:	Millimeter
MPa:	Megapascal
MSHA:	Mine Safety and Health Administration
N:	Newton
NATM:	New Australian Tunneling Method
NDT:	Nondestructive Testing
NIOSH:	National Institute for Occupational Safety and Health
PSI:	Pounds per square inch
PSL:	Partial Shell Lining
PSPA:	Portable Seismic Property Analyzer
RPM:	Rotations per Minute
RX:	Receiving Antenna
SAI:	Scientific Associates Incorporated
Sec./S:	Second

SME:	Society for Mining, Metallurgy, and Exploration
SSL:	Single Shell Lining
TX:	Transmitting Antenna
USW:	Ultrasonic Wave
V:	Volts
Wgt:	Weight
WJTA:	Waterjet Technology Association
yd:	Yard

EXECUTIVE SUMMARY

To circumvent the technical and operating challenges associated with conventional shotcrete removal methods used in the repair and rehabilitation of underground support liners, this research sought to develop and evaluate a unique system that utilizes waterjet technology as the primary excavation tool. Building upon the success of previous research activities at the Colorado School of Mines (CSM) in underground rock scaling and scarification, empiric evidence suggests that waterjets are capable of selectively removing damaged areas of these liners without structurally compromising the intact material adjacent to the area being repaired. The primary research objective was to compare and contrast the unintended damage caused to the surrounding shotcrete liner and concrete substrate by both conventional impact hammers and waterjet excavation methods during empiric cutting tests. This analysis involved physical testing on instrumented shotcrete panels designed to quantify fracture propagation, the mode of failure, and the delamination of the substrate and steel reinforcement from the shotcrete simulant. The motivation for this research was to mitigate the collateral damage caused to surrounding liners during excavation, as well as improve the adhesion between shotcrete and the substrate for longer lasting ground support and ultimately, to improve overall safety for workers in underground environments. It is hoped that facilitating a better understanding of the dynamic excavation processes associated with liner repair will translate to developing a future prototype system applicable for field testing.

The results of this research illustrate a stark contrast between the excavation processes associated with conventional mechanical impact hammers and waterjet methods. An analysis on the fracture mechanisms and operating parameters of each method was completed. Within this analysis, instrumented shotcrete panels were physically tested to quantify vibration during excavation, and examined through visual and analytic processes, including ground penetrating radar and microcomputed tomography, to determine substrate damage and delamination. Based upon empiric testing and analysis, the data strongly indicates that waterjet cutting creates less collateral damage to the surrounding intact liner and substrate when compared to that of conventional impact hammers. In addition, the research provided invaluable insights related to nondestructive testing of the test panels, as well as the instrumentation required for quantifying induced vibrations within the structural elements. This research is intended to provide a scientific basis for additional applied investigations into the rapid excavation and rehabilitation of shotcrete/concrete support systems.

CHAPTER 1 - INTRODUCTION

The repair of concrete and shotcrete liners that have been structurally compromised or damaged is a common maintenance and rehabilitation activity in tunnels and other types of underground workings. Age, in-situ stresses, geology, chemical and physical decomposition, accidental impacts, and water flow/seepage are but just a few of the many factors that necessitate the repair of these structural systems over time. In many cases, it is prudent to limit the repair to the isolated removal of the structural liner around the damaged area rather than the complete excavation of large sections of the support system. In specific types of geology and in high stress environments, the large-scale removal of the liner represents an inherent hazard associated with rock falls and failure. In these applications, traditional methods of liner removal include the use of hydraulic or pneumatic hammers that break and excavate the liner material through repetitive percussive impacts using spade or chisel bits. In operating environments where working heights are less than 20 m, these hammers are usually mounted to articulated booms attached to mobile rubber-tired or track equipment, such as a mechanical scaler. In applications that extend beyond the reach of conventional scalers, the height of the operating envelope usually necessitates the use of man-lifts, where workers manually remove the damaged areas from these elevated platforms using hand-held equipment. Each of these rehabilitation scenarios are shown in Figure 1-1.

In both applications, there are significant drawbacks to the use of these traditional methods. It is a long-held belief that the percussive impacts generated by hydraulic/pneumatic hammers while removing the compromised area of the liner also causes unintentional damage to the surrounding intact shotcrete and/or concrete because of the propagation of fractures and the delamination of the liner from the rock substrate, as well as any contained rebar or wire mesh/screen backing [1, 2, 3]. In addition, there is a host of potential safety hazards commonly associated with the use of these traditional technologies. This is particularly true for work performed from elevated platforms, including the close proximity of workers to unstable roof/back and the potential of falling from these platforms, the man-lift tipping or overturning, and the limited ability for rapid egress.

Another important motivation driving this research is the potential for significant growth in work associated with the rehabilitation of underground workings and tunnels due to aging urban infrastructure and the need to expand the capacity of these workings [4]. The size and complexity of many of these underground construction projects, coupled with challenging social and ground conditions, necessitate a different technical approach than traditionally used in the past. Greater emphasis on safety, project costs, dependency on skilled labor, time of completion, social impacts, and risk are driving companies to investigate innovative technologies and systems in order to remain competitive. Nowhere is this more pronounced than the rehabilitation and repair of underground urban infrastructure related to transportation, sewers and water storage, and utilities. In many cities, much of this infrastructure has exceeded its designed operating life and is in critical need of maintenance, repair, and partial or complete replacement. Given the historic reliance of shotcrete and concrete in underground support systems, the cumulative

impact of this situation is the catalyst for developing safe, economic, and reliable rehabilitation practices and technologies that can be remotely operated in a wide range of operating environments [5].

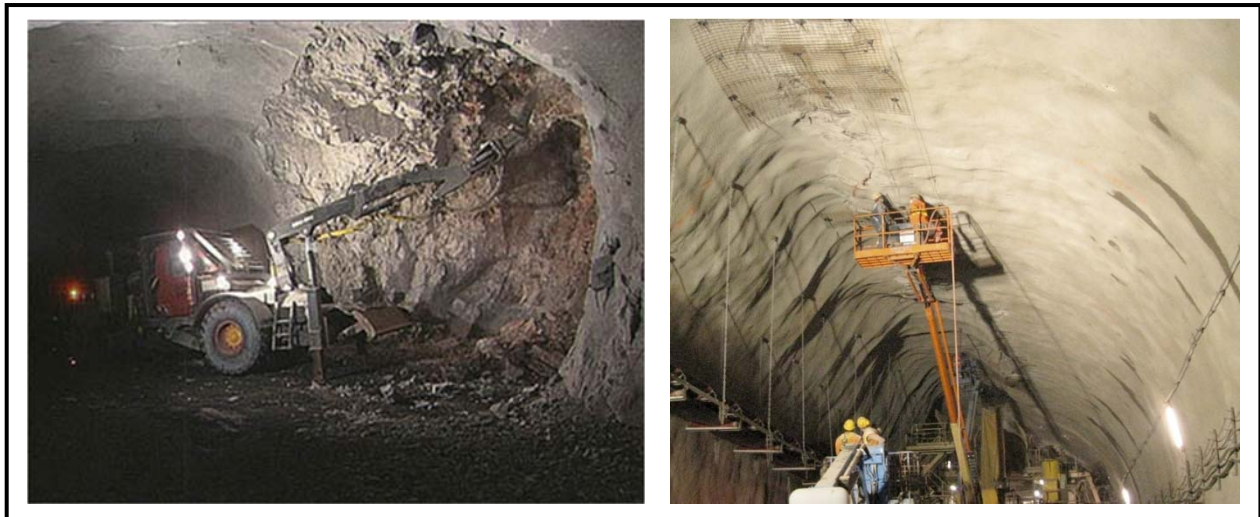


Figure 1-1: Conventional mechanized scaler for operating heights below 20 meters (left) and a manlift with operators and manually held impact hammer for operating heights above 20 meters (right) [6].

To circumvent these technical and operating challenges, this research seeks to develop a unique system that utilizes waterjet technology as the primary excavation tool for use in liner repair and maintenance. Building upon the success of previous Colorado School of Mines (CSM) research activities in hydraulic underground rock scaling and scarification, empiric evidence indicates that waterjets are capable of selectively removing damaged areas of support liners without structurally compromising or harming intact material around the area being repaired, as well as the underlying substrate and steel reinforcement. The intent of this research is to facilitate a better understanding of the dynamic excavation processes associated with liner repair in hopes of developing a future prototype system applicable for field testing.

1.1 Research Objectives

The primary objective of this research is to conduct a comparative analysis of the collateral damage created by both conventional mechanical and waterjet excavation systems on a standardized section of an engineered, simulated shotcrete panel. Data from empirical testing obtained during shotcrete removal will be used to compare unintended damage caused to the surrounding structural liner and substrate by these excavation methods. The testing program will rely extensively on a quantitative comparison of vibration data obtained from accelerometers attached to the panels during testing, as well as a qualitative assessment based on visual inspection of the kerfs and interpretation of ground penetrating radar data. The intent was to demonstrate whether the hypothesis that waterjet excavation would create significantly less collateral damage than conventional mechanical tools was correct. If true, this research would

create the foundation for further work in this area with hopes of eventually developing a prototype system amenable for field testing.

The secondary objective of the research was to provide graduate students with the necessary professional training, education, and skill-sets to become productive scientists and engineers upon the completion of their degree programs. This research will form the basis of a Ph.D. dissertation that is scheduled for competition in December 2020.

1.2 Research Limitations

The research associated with this project possessed the following limitations and conditions:

- This research did not attempt to optimize the operating parameters of the waterjet excavation process as it would require significantly more empiric testing than what was needed to achieve the project objectives;
- The physical dimensions of the instrumented shotcrete panels were intentionally designed to make them representative of discrete sections of a shotcrete liner indicative of what might be found in a conventional tunnel or underground working. A secondary consideration was to construct the test panels in a manner that would ensure their rigidity during cutting tests but also would allow them to be readily transported between different laboratory facilities by truck and trailer and manipulated within the laboratory by forklift. Given the dimensions of the resulting test panels, they proved to be too small for consistent placement of shotcrete using either a wet or dry sprayer. The edge effects of the test panels would result in variable depths and density of the shotcrete layer. Using recommendations found in the literature, a sand/topping cement mixture was used as a shotcrete simulant in order to generate uniform thickness in the test samples. A Quikrete sand/topping mix was deemed appropriate for use as a shotcrete simulant due to its similar physical and chemical properties, fast setting time, and 28-day compressive strength of 34.5 MPa (5000 PSI);
- A type I/II 31 MPa (4,500 PSI (min)) commercial ready mix with 19-mm ($\frac{3}{4}$ inch) aggregate and 28-day compressive strength of 45.4 MPa (6,590 PSI) was used for the concrete substrate within the instrumented shotcrete panels; and
- Based on waterjet applications in rock cutting, it would have been the preference of the research team to use a high-pressure pump with a nominal operating pressure of 172 MPa (25,000 psi) and a flow rate of 76-95 lpm (20-25 GPM) for the empiric testing. However, the pump available at the RAMAX/SAI Laboratory was a 119 kw (150 HP), 193 MPa (28,000 psi) high pressure pump with a flow rate of 21.2 lpm (5.6 GPM). This pump was deemed suitable because the system far exceeded the threshold pressure needed to effectively cut the target material and achieve the research objectives.

As stated previously, the primary objective of this research was to compare and contrast the characteristics of the excavation process associated with the removal of shotcrete within a steel reinforced structural liner using both mechanical and waterjet methods. The empiric testing was designed to isolate relationships associated with material failure and to validate the hypothesis that waterjet removal of these liners will result in less unintended damage as compared to conventional techniques. As such, these research objectives made it less crucial to conduct the necessary number of tests required to optimize the parameters of the cutting process for either system. Further research will be conducted utilizing this project's findings in order to quantify key operating variables necessary to determine productivity and the cost of liner excavation at a later time.

1.3 Research Originality

A literature search was conducted to identify research papers that correlate with hydroexcavation of structural liners in underground workings. At the conclusion of the search, only one research paper was discovered for this particular field of work. In 2009, SME Mining Engineering published a journal article discussing how a conventional twin orifice rotating waterjet system selectively removed concrete damaged by a major fire that occurred in the Channel Tunnel linking Britain and France [7]. The tunnel fire burned for approximately 16 hours, with extreme temperatures rising up to 1,000 degrees Celsius, causing extensive damage to the concrete lining. Four conventional twin orifice rotating waterjet nozzle assemblies were utilized to remove the damaged concrete by cutting at a depth of 30 mm (1 inch) into 9,500 square meters (102,257 square feet) of the tunnel. Figure 1-2 shows the rehabilitation scenario.

Comprising the excavation system, jet motion was controlled using robots that were equipped with modified arching feedbeams, which carry the jet nozzle, to match the curvature of the tunnel wall. This specific equipment configuration was also equipped with a vacuum attachment to collect all of the water and excavated material during operation. The repair contract was deemed a success and a new concrete lining was sprayed for reinforcement before reopening the tunnel for shuttle train service.

While this article demonstrates that rehabilitation of tunnel liners using high-pressure waterjets as an excavation tool is possible, it did not disclose why the method was chosen or provide detailed information about the system, operating parameters, and material characteristics. No disclosure of operating efficiency, fragmentation dynamics, and other important information was provided through which a quantitative analysis could be made. Therefore, the following research offers original quantitative and qualitative results that will benefit the heavy underground construction industry and provides the basis for future research.



Figure 1-2: Hydroexcavation robot removing damaged concrete in Channel Tunnel liner [7].

1.4 Methodology

A central element of the research methodology involves empiric cutting tests performed on engineered, instrumented shotcrete panels designed to quantify vibration and facilitate qualitative comparison of substrate delamination and collateral damage associated with the two primary excavation processes. To accomplish this, the first phase of the project was devoted to conducting a detailed literature review, the development of the testing methodology and the engineering design of the panels. Design parameters of the panels were selected based on a technical review of common liner design criteria, as well as the physical characteristics of the shotcrete and substrate. In addition, this also included the selection of testing parameters related to both the mechanical and waterjet systems. The next phase focused on the laboratory setup, including the assembly of the high-pressure pump and fluid handling system, the design and fabrication of the nozzle assembly and motion system, and construction of the panel test stand. The third phase involved the construction, instrumentation, and characterization of the target panels. The fourth phase of the research methodology focused on experimental testing, where six (6) individual composite panels comprised of a steel reinforced concrete substrate with a 10 cm shotcrete layer were cut using the two selected modes of excavation. A seventh (7th) instrumented panel was constructed and held in reserve for contingency in the event one of the other panels were damaged. In this testing scenario, three (3) of the test panels were cut by a rotating twin-orifice, high-pressure continuous waterjet at the SAI/RAMAX laboratory in Lancaster, CA and three (3) panels were mechanically excavated by an electric percussive demolition hammer at CSM's Earth Mechanics Institute (EMI). Instrumentation of these panels was performed using accelerometers attached to the rebar and cement, where pre and post testing of the panels were performed using ground penetrating radar (GPR). The fifth phase of the research was directed on the analysis of data derived from the accelerometers, visual inspection of the kerfs, and ground penetrating radar. The final research phase focused on the

writing of the report. It is important to note that a Ph.D. dissertation was conducted from the data generated from this research and is scheduled for competition in December 2020. Lastly, it is anticipated that two additional journal submissions stemming from this research will occur in 2021.

A summary of the research methodology has been broken into the following steps:

1. Comprehensive literature review;
2. Established research methodology;
3. Established testing methodology and operating parameters;
4. Laboratory and equipment set-up at EMI and SAI/RAMAX Waterjet Lab;
5. Construction of engineered and instrumented test panels;
6. Development of data acquisition system;
7. Design and assembly of the motion control system;
8. Pre-testing Ground Penetrating Radar (GPR) scanning of test panels;
9. Preliminary testing trials and system modifications;
10. Mechanical impact hammer testing at EMI;
11. Waterjet excavation testing at SAI/RAMAX Waterjet Lab;
12. Post-testing physical inspection of test panels;
13. Post-testing GPR scanning of test panels;
14. Data analysis through visual inspection and sieve analysis of cuttings;
15. Data analysis of vibration during testing for both excavation processes;
16. Data analysis of pre and post testing GPR scans for both excavation processes; and
17. Writing of Final Report, including recommendations for future work.

Under the testing methodology, non-destructive structural analysis of the panels was performed before and after testing using GPR and through visual examination. GPR data helped visualize differences in substrate damage and delamination. In an effort to obtain additional information on the propagation of fractures generated by each excavation method, core samples were taken from two panels, one excavated by the impact hammer and the other by the waterjet, and examined using microCT. Data from empirical testing of simulated shotcrete removal was used to compare unintended damage caused to the surrounding structural liner and substrate by impact hammer and waterjet excavation methods. Quantitative comparison uses vibration data, visual fracture/failure and split aggregate measurements, and microcomputed tomography data while qualitative comparison is based on physical inspection of the kerfs, and interpretation of GPR data before and after testing to analyze any potential occurrences of substrate damage and delamination from each panel as a consequence of testing. Table 1-1 show completion of the research methodology helped achieve the objectives outlined within the scope of this project. It is anticipated that the resulting data will service as the foundation for subsequent research activities.

Table 1-1: Summary of research methodology steps taken to achieve research objectives.

Research Objective	Research Methodology Step
Investigate waterjet system operating parameters necessary to cut the shotcrete layer	Documentation of parameters used for waterjet system as well as how adjustments in parameters led to changes in cutting behavior within shotcrete layer
	Compare the waterjet excavation process to the impact hammer excavation process
Investigate the fracture mechanisms imposed by the waterjet system to cut shotcrete layer	Documentation of material removal geometry created by both waterjet and impact hammer impingement
	Analysis of cuttings from waterjet and impact hammer impingement
Verify that waterjets can successfully be used as an alternative shotcrete removal tool	Post-excavation physical inspection of test panels
	Documentation showing that the waterjet system can complete the same material removal task as an impact hammer
Validate the hypothesis that waterjet removal of these liners will result in less collateral damage than conventional methods	Visual inspection comparison of kerf and damage of steel infrastructure caused by both excavation methods
	Vibration comparison between both excavation methods during removal of shotcrete layer
	GPR scan comparison of substrate damage and delamination caused by both excavation methods
	Microcomputed tomography comparison of substrate damage caused by both excavation methods

CHAPTER 2 – LITERATURE SEARCH

2.1 Introduction

This chapter covers background information on underground structural liner composition, use, and repair, followed by background literature on fracture mechanisms of impact hammer bits in order to create an understanding of current rehabilitation practices as well as conventional equipment used in these applications.

This chapter also reviews the literature associated with the use of high-pressure waterjet systems to perform scaling procedures in underground operations, followed by an analysis of the available literature associated with shotcrete/concrete liner hydroexcavation. It is important to note that these two processes are fundamentally different. Waterjet scaling applications involve the removal of loose, structurally compromised rock along the ribs, face, and back of a tunnel or underground working, typically due to the fracture envelope caused by blasting or weaknesses in the rock mass. Scaling is a necessary unit activity to maintain safe work areas in underground environments. Conversely, shotcrete/concrete liner excavation involves the systematic removal of structurally compromised or deteriorating shotcrete/concrete within a specific area that requires repair and maintenance, while avoiding removal of the underlying host rock and steel reinforcement. Both scenarios require different waterjet system operating parameters, but are similar in the types of equipment and motion systems employed.

The literature search concludes with a summary of instrumentation commonly associated with high-pressure waterjet systems, the fracture mechanics of hydraulic excavation systems related to shotcrete/concrete removal, and, finally, concrete structure integrity analysis through visual and non-destructive testing methods.

2.2 Underground Structural Liners

A wealth of information regarding the design of underground structural liners can be gained from the text, “Sprayed Concrete Lined Tunnels” [8]. Within this publication, Thomas outlines fundamental tunneling principles based on input from professionals and consultants within the industry. In principle, the load supported by the structural liner is a combination of in-situ stresses and groundwater pressure. In many rock types, ground deformation after excavation often occurs and must be controlled in order to create a new state of equilibrium. Overall, deformation of the ground is an indicator of its strength. Therefore, the load on the structural liner will ultimately depend on how much ground deformation is permitted, as well as how much stress redistribution within the ground is possible.

Early researchers, such as Rabcewicz, developer of the New Austrian Tunneling Method (NATM), recognized that sprayed concrete was well suited for tunneling due to it being a structural material that could be used for permanent lining [8]. Behaviorally, when shotcrete is

applied, it is initially soft and creeps under load while being able to withstand large strains at an early age. It increases in stiffness and strength over time and is attuned to controlling deformation through stress redistribution in the ground so that strain softening does not lead to unstable failure. According to Poeck [9], unstable failure, which is classified as a collapse of material that occurs when a volume of rock has been suddenly loaded beyond its strength, requires the combination of brittle material behavior and a soft loading system. Brittle material behavior is characteristic of most rock types and refers to the loss of structural integrity and strength that occurs when a volume of material is compressed beyond its point of failure. A soft loading system is defined as a system that is capable of sudden displacements when opposing forces are removed. The loading conditions for underground workings vary with local geology and groundwater pressure, and can exhibit characteristics of a soft loading system.

Concrete consists of cement paste, pore water, and inserts, such as aggregate particles and reinforcements. According to Momber, the interfaces between these components significantly affects the mechanical properties and behavior of the concrete under load. More specifically, the interface between the cement and the aggregate is the weak link in concrete which must be considered when analyzing structural integrity [10]. This weak link is shown in Figure 2-1 as the transition zone between the aggregate and bulk cement paste. According to Luna et al, the transition zone controls multiple characteristics of concrete including the elasticity and strength, its power of retraction, and its fluency [11]. Proper development of the transition zone is a vital factor in reaching optimal mechanical strength of a concrete structure.

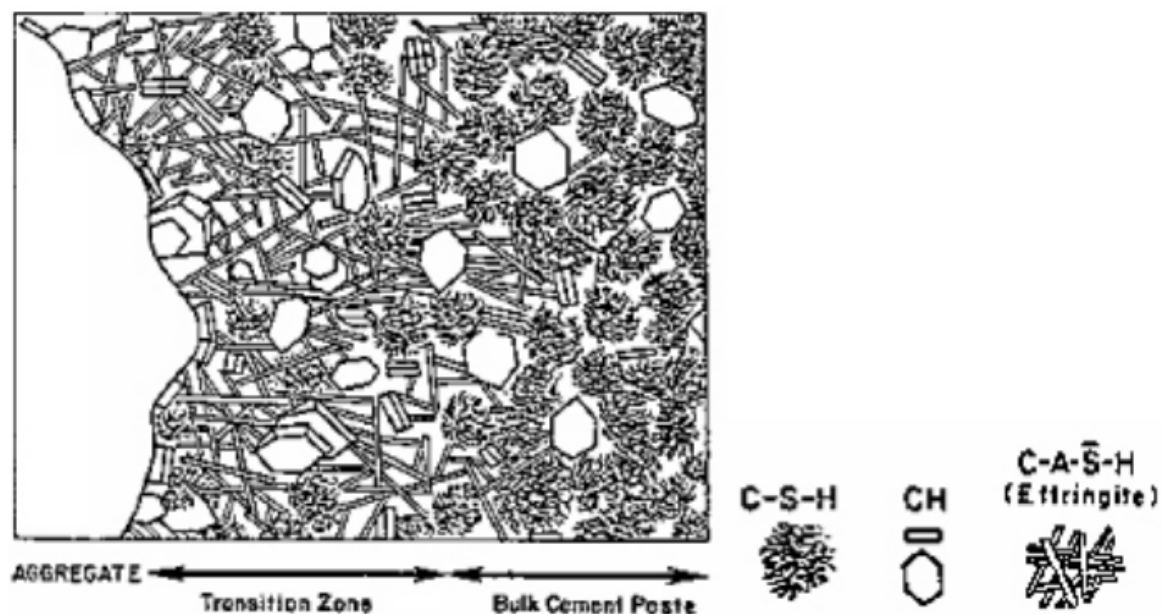


Figure 2-3: Illustration showing three phases of concrete structure including aggregate, transition zone, and bulk cement paste [11].

Shotcrete is applied to a substrate by pneumatically spraying concrete, with a mix of constituents, at high velocities, and therefore, does not require forming or compaction [1]. This placement method of utilizing shotcrete can provide operators more flexibility in concrete applications for ground support. Compared to cast in-situ concrete, shotcrete uses a smaller size aggregate which, combined with the added mix component of sand, creates a different texture optimal for spraying. Luna et al state that grain size used for shotcrete typically reaches a maximum size between 10-12 millimeters (0.4-0.5 inches). Additionally, sand content less than 8 millimeters (0.3 inches) in size will not exceed 10% of the total cement mixture [11]. Using smaller aggregate and sand in the mix composition aids the pumping process by avoiding obstruction of the nozzle and reducing material rebound.

The process of shotcrete application can be divided into dry-mix and wet-mix. With the dry-mix shotcrete process, the concrete materials are pre-mixed, oven-dried, and pneumatically propelled to the nozzle, where water is then added and sprayed towards the substrate. With regards to the wet-mix shotcrete process, the concrete materials and the water are all mixed prior to being accelerated and pumped to the nozzle. Both dry-mix and wet-mix techniques have their advantages and disadvantages. Decision on a technique depends upon the needs of the project and type of shotcrete application. Dry-mix shotcrete spraying offers advantages through its use of smaller machines and batch processes which is especially useful in confined spaces and remote underground locations, making it a more accessible method as timing and transportation of materials is not as much of an issue. Wet-mix shotcrete can be difficult to transport over large distances by hose or slick line due to the need for constant mixing before spraying. A delay in the transportation of the wet-mix shotcrete can result in wasting entire batches, forcing the remix truck operator to dump the unusable concrete. In tunneling applications, wet-mix shotcrete spraying is used more frequently as it offers advantages through lower dust production and higher throughput. Additionally, the wet-mix process shows advantage by reducing the amount of rebound material during the spray process. Martin et al discuss typical shotcrete mix designs in both dry and wet forms that can be used as a starting point reference. Both mix designs are shown in Table 2-1 [12].

Martin et al, note that most shotcrete mixes are pre-blended by suppliers who have a specific number of mix variations according to application and cost. Otherwise, many large underground construction projects will contain a batch plant on site that delivers wet mix shotcrete from the surface to remix trucks via slick line. For additional reference, Table 2-2 shows a typical mix design of a high-quality sprayed concrete in comparison to an equivalent strength cast in-situ concrete according to Thomas.

Table 2-1: Typical shotcrete mix designs [12].

Dry Mix

Mix Constituent	Amount, kg/m ³ (lb/yd ³)	Percentage of Dry Materials, %
Cement	420 (708)	19
Silica Fume Additive	50 (84)	2.2
Blended Aggregate	1,670 (2,815)	75.5
Steel Fiber	60 (101)	2.7
Accelerator	13 (22)	0.6
Water	Controlled at Nozzle	Controlled at Nozzle
Sum	2,213 (3,730)	100

Wet Mix

Mix Constituent	Amount, kg/m ³ (lb/yd ³)*	Percentage of Dry Materials, %
Cement	420 (708)	18.1
Silica Fume Additive	40 (67)	1.7
Blended Aggregate	1,600 (2,697)	68.9
Steel Fiber	60 (101)	2.6
Accelerator	13 (22)	0.6
Superplasticizer	6 L (6.3 qt)	0.3
Water Reducer	2 L (2.1 qt)	0.1
Air Entraining Admixture	If Required	If Required
Water	180 (303)	7.7
Sum	2,321 (3,912)	100

*Unless listed otherwise as liters and quarts

Martin et al, note that most shotcrete mixes are pre-blended by suppliers who have a specific number of mix variations according to application and cost. Otherwise, many large underground construction projects will contain a batch plant on site that delivers wet mix shotcrete from the surface to remix trucks via slick line. For additional reference, Table 2-2 shows a typical mix design of a high-quality sprayed concrete in comparison to an equivalent strength cast in-situ concrete according to Thomas.

Table 2-1: Typical shotcrete mix designs [12].

Dry Mix

Mix Constituent	Amount, kg/m ³ (lb/yd ³)	Percentage of Dry Materials, %
Cement	420 (708)	19
Silica Fume Additive	50 (84)	2.2

Blended Aggregate	1,670 (2,815)	75.5
Steel Fiber	60 (101)	2.7
Accelerator	13 (22)	0.6
Water	Controlled at Nozzle	Controlled at Nozzle
Sum	2,213 (3,730)	100

Wet Mix

Mix Constituent	Amount, kg/m ³ (lb/yd ³)*	Percentage of Dry Materials, %
Cement	420 (708)	18.1
Silica Fume Additive	40 (67)	1.7
Blended Aggregate	1,600 (2,697)	68.9
Steel Fiber	60 (101)	2.6
Accelerator	13 (22)	0.6
Superplasticizer	6 L (6.3 qt)	0.3
Water Reducer	2 L (2.1 qt)	0.1
Air Entraining Admixture	If Required	If Required
Water	180 (303)	7.7
Sum	2,321 (3,912)	100

*Unless listed otherwise as liters and quarts

Table 2-2: Typical sprayed/cast concrete design [8].

	High-Quality Wet Mix Sprayed Concrete [13]	Cast In-Situ Concrete [14]
Grade	C40	C40
Water-Cement Ratio	0.43	0.40
Portland Cement, PFA, Special Cements, etc.	430 kg/m ³ (725 lb/yd ³)	375 kg/m ³ (632 lb/yd ³)
Accelerator	4-8%	-
Plasticizer	1.6% bwc	1.5% bwc
Stabilizer	0.7% bwc	-
Micro Silica	60 kg/m ³ (101 lb/yd ³)	-
Max. Aggregate Size	10 mm (0.4 in)	30 mm (1.2 in)
Aggregate < 0.6 mm	30-55%	32%

Note: bwc means "by weight of cement"

As shown in Table 2-2, there are differences between mix compositions because sprayed concrete has to possess sufficient adhesion capabilities in order to support the target area under load and keep structural integrity against damaging factors, such as blasting and impact during construction activities. For example, the water-cement ratio is higher and the maximum aggregate size is smaller for shotcrete in order to easily pump and spray the mixed material. Accelerators are used to generate a faster hydration reaction in order to set at a rapid rate and achieve early age strength. Admixtures, such as plasticizers and stabilizers, are added to improve

concrete structure. Micro silica is added to improve immediate adhesion and long-term density [8]. Table 2-3 shows the properties of the typical sprayed/cast concrete design shown in Table 2-2.

Table 2-3: Typical sprayed/cast concrete properties [8].

	High-Quality Wet Mix Sprayed Concrete [13]	Cast In-Situ Concrete [14]
Compressive Strength at 1 Day, MPa (PSI)	20 (2,901)	6 (870) (est.)
Compressive Strength at 28 Days, MPa (PSI)	59 (8,557)	44 (6,382)
Elastic Modulus at 28 Days, GPa (KSI)	34 (4,931)	31 (4,496) (est.)
Poisson's Ratio at 28 Days	0.48-0.18	0.15-0.22
Tensile Strength at 28 Days, MPa (PSI)	> 2 (290) (est.)	3.8 (551) (est.)
Initial Setting Time, Min	3-5	45-145
Shrinkage after 100 days, %	0.1-0.12	0.03-0.08
Specific Creep after 160 Days, %/MPa	0.01-0.12	0.0008
Density, kg/m ³ (lb/yd ³)	2,140-2,235 (3607-3767)	2,200-2,600 (3708-4382)
Slump, mm (in)	180-220 (7.1-8.7)	50 (2.0)

The compressive strength of the concrete, whether sprayed or cast, at an early age is critical to the safety and capacity of the support system. Many numeric models exist to predict the increase in concrete compressive strength and elastic modulus over time. These models differ depending on specific factors, such as concrete mix composition, time limit, and specific design of the structure (prisms, cylinders, beams, etc.). Authors who have developed these predictive equations include; Weber in 1979, Pöttler in 1990, Aldrian in 1991, Chang in 1994, Alkhiami in 1995, Yin in 1996, and Meschke in 1996 [8]. Strength increases with age due to hydration of the cement paste which decreases the quantity of pores within the material. Research conducted by Martin determined early-strength values from cast and sprayed concrete samples, using the partial beam test system developed by the National Institute for Occupational Safety and Health (NIOSH), as shown in Figure 2-2 [15]. The partial beam test is a process where, every hour, a driven press applies a fixed-rate load to a molded concrete/shotcrete sample until the operator observes a well-defined peak in the load profile curve, indicating failure of the sample and completion of the test. The testing unit is a self-contained, servo-controlled, stiff-frame press and samples are cast/sprayed into a 102 x 102 x 152 mm (4 x 4 x 6 inch) mold box.

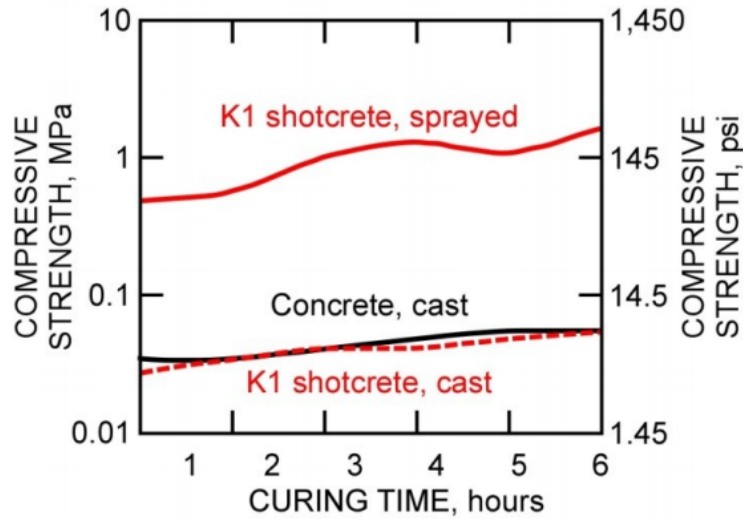


Figure 2-2: Early strength partial beam test results for dry mix shotcrete and concrete conducted by NIOSH, n=54 samples [15].

The partial beam test was conducted on 54 samples to acquire the results in Figure 2-2. Martin noted that the cast shotcrete samples have a strength gain profile similar to that of the cast concrete samples. Thomas states that concrete failure in compression is dictated by how the material cracks under uniaxial compression testing. Micro-cracks can exist within the concrete sample due to hydration and shrinkage as the material dries, and are typically located at the interface between the aggregate and the hardened cement paste. These micro-cracks can start to grow when the loading on the concrete exceeds approximately 30% of its maximum compressive strength [8]. As this occurs, the effective area that resists the load decreases which leads to strain hardening. Once 70% of the concrete's maximum compressive strength is reached, cracking can occur within the hardened paste and micro-cracks start to coalesce, leading to the formation of a major plane of failure [8].

The tensile strength of concrete is typically estimated to be one tenth of its compressive strength and results in brittle failure when it reaches maximum capacity [8]. It is generally assumed that the tensile strength of concrete increases according to time at the same rate as compressive strength. From a design standpoint, tensile reinforcement is added to the shotcrete support system in the form of steel wire mesh or steel fibers within the mix composition. The bond between the intact concrete/shotcrete and steel reinforcement allows a gradual transfer of the tensile load from the cracking concrete to the steel as the load increases, which is known as tension stiffening [8]. Therefore, the composite support system has a stiffer response to loading than shotcrete alone. Martin states that, without wire mesh reinforcement, shotcrete has the ability to bond directly with the rock/substrate, generating stability through interface shear strength and filling of rock fractures. However, if there is no wire mesh or steel fibers present, the support system loses its load-bearing capacity after a few millimeters of flexural displacement and demonstrates a completely brittle failure mode [16]. Therefore, use of steel

reinforcement is critical in underground operations that have a long life, weak rock, and experience significant ground movement.

Use of short steel or polypropylene fibers within the mix composition, instead of steel wire mesh, can also increase post-crack ductility of concrete when subjected to tensile stress. Martin et al state that the benefits of using steel fibers include a reduction in cost and workload due to the elimination of equipment and personnel that would be necessary for handling and installing the wire mesh panels. Additionally, if fibers are included in the mix composition, a uniform thickness can be applied over irregular surfaces, whereas wire mesh panels cannot always follow the exact contour of the rock surface, leading to the creation of bridged voids. Disadvantages of using steel fibers include the potential of clogging sump pumps and injury from abrasive contact when handling the material [12].

Creep is the increase in strain with time while under a sustained stress [8]. With regards to concrete, creep increases under the following conditions:

- Relative humidity decreases;
- Cement content increases;
- Stress on concrete increases; and
- Strength of concrete decreases.

In accordance with the conditions above, creep and creep rates are significantly higher for concrete at an early age of loading. Comparatively, an early age sprayed concrete, with the use of accelerator, typically does not experience a high creep rate due to the faster setting time and higher early age strength achieved through its chemical composition. Slump is an indicator of whether the concrete is too stiff or too fluid. Slump values for sprayed concrete are higher than that of cast in-situ concrete because they have to be pumped through a nozzle system. The value shown in Table 2-3 for high quality wet mix sprayed concrete is typical for liner support. It's important to note that if the water content is too high, the concrete may not adhere to the target surface when applied.

Design of a temporary or permanent underground structural liner can widely vary depending on the site-specific geology and environmental conditions at the depth of excavation. The goal of the structure is to help maintain the inherent strength of the ground so that the load carried by the structure is minimized. Additionally, the design should be easy and safe to construct. According to Thomas, the ground in which liners are constructed can be divided into three categories: soft ground, blocky rock, and hard rock. Details of these three categories are outlined in Table 2-4.

With regards to soft ground applications, it typically requires full support immediately after excavation and deformation control is critical due to occurrence of plastic yielding [8]. The lining could consist of 150 to 300 mm (6 to 12 inches) of sprayed concrete with layers of steel wire mesh and/or rebar reinforcement, or fiber reinforcement. Additionally, lattice girders

Table 2-4: Ground categories in which liners are constructed [8].

Variable	Soft Ground	Blocky Rock	Hard Rock
Classification	Soils and weak rocks	Weak to moderately strong rocks	Massive strong rocks
Mode of Behavior	Continuum	Discontinuum	Continuum
Strength (MPa)	Less than 1	Between 1 and 50	More than 50
Examples	Sands, clays, chalk	Limestone, sandstone	Basalt, granite

can be used to control the shape of the tunnel and support the steel wire mesh during spraying. Blocky rock is said to behave as a discontinuum due to the rock mass being a collection of discrete blocks rather than one continuous structure [8]. Blocky rock does not need full support immediately like soft ground; however, it typically has a stand up that ranges from a few hours to a few days. The lining could consist of 50 to 150 mm (2 to 6 inches) of sprayed concrete reinforced with steel or fibers, as well as a rock bolt pattern designed in accordance to the jointing on the rock mass. Rock bolts are especially important to use in liners within blocky rock as they provide a wedge within the discrete blocks keeping them from failure. With regards to hard rock, stand up time after excavation for the whole system can range from days to years, while certain sections of the excavated profile might require immediate support. In these cases, the role of sprayed concrete is to support these isolated areas that require immediate support. In some hard rock applications, the entire system could be potentially stronger than the sprayed concrete liner which makes its use unnecessary, unless there are areas that are highly jointed, thus requiring a liner design similar to that of blocky rock. Not all underground excavation projects will specifically fit into one ground category outlined in Table 2-4. For example, at certain underground mining operations in Nevada, one may encounter carbonate host rock with associated granodiorite and quartz diorite sills, requiring a structural liner that provides a safe working environment within highly altered rock that encompasses soft, blocky, and hard ground. It is also important to consider the possibility of air slacking within an underground development area. Air slacking occurs when there is a change in atmospheric conditions, typically linked to humidity changes, causing deterioration of the roof/back of a tunnel. Researchers, such as Cummings, found that air slacking can affect rocks of differing mineralization and the behavior seems to connect with the dilation of the strata that typically uptakes moisture [17]. Certain rock types can be chemically altered when exposed to water. For example, feldspar, a large group of rock-forming silicate minerals that makes up approximately 50% of the Earth's crust, can be chemically weathered through hydrolysis, causing it to turn into Kaolinite, which is a clay mineral. To avoid instances of both air slacking and chemical alteration, coatings such as shotcrete can be utilized to provide a skin support that protects the rock, keeping it shielded from air and water present within the underground environment.

Martin et al discuss shotcrete liners utilized in the mining industry, particularly in underground mining operations with weak rock conditions, such as those in Nevada [12]. When

squeezing and raveling rock is encountered within rock mass with a low Rock Mass Rating (RMR), the support system must be installed as a part of the active mining cycle. To start, a thin layer of shotcrete, typically 25 mm (1 inch) thick, is applied as surface control to stabilize the newly exposed surface, prevent small rock from falling, as well as prevent air slacking and dehydration of the rock exposed to voids. After this initial layer is applied, a 102 x 102 mm (4 x 4 inch) six-gauge welded wire mesh is prepositioned and installed with friction bolts to hold the mesh reinforcement in place. This wire mesh prevents unraveling of the rock mass and stabilizes the ground between the rock bolts. A second layer of shotcrete, typically 76 to 102 mm (3 to 4 inches), is then applied to cover the first layer of shotcrete, wire mesh and split set bolts to create a composite support system. From there, depending on the Rock Mass Rating (RMR) of the host rock, additional reinforcement in the form of long swellex or split-set bolts can be installed in the back and in the ribs. An example of a completed shotcrete support system is shown in Figure 2-3. The red cones in Figure 2-3 show the local support provided by the shotcrete mesh and short bolts. The primary bolts (longer friction bolts) provides global support as shown by the diamond shaped dotted lines and forms a compression arch which, according to Martin et al, has the greatest influence on stabilizing the underground opening and preventing failure [12].

With regards to the underground construction industry, there are numerous types of permanent tunnel liner designs and they vary depending on the durability of the sprayed concrete and the specific method of waterproofing. Options for permanent tunnel linings include double shell lining (DSL), composite shell lining (CSL), partial composite lining (PCL), and single shell lining (SSL). Typical design of these permanent linings is shown in Figure 2-4.

The finishing layer can be optional for all the lining designs shown in Figure 2-4. Secondary linings are typically cast in-situ concrete; however, it could also be another layer of sprayed concrete depending on the operating scenario. The spray applied membrane is bonded on both sides to the substrate allowing the potential for load sharing between both the primary and secondary linings. With regards to the single shell lining, the single shell itself can consist of several layers of sprayed concrete placed at different times to act as a composite structure that carries load over the life of the tunnel.

When considering a permanent sprayed concrete structural liner, the design life can range from 50 to 100 years or more depending on its purpose for the developed area. This makes it crucial to consider the structural liner's durability and external conditions that could cause the need for rehabilitation and maintenance. Durability of the liner is directly related to the mix composition and spraying technique used by the equipment operator, as well as the preparation of the substrate and underlying layers. Poor spraying technique could lead to defects in the concrete lining in the form of shadowing, sloughing, laminations, rebound, and overuse of accelerator. With specific regards to steel reinforcement, defects, such as voids left in the concrete lining, reduce the bonded length of the rebar or wire mesh and can lead to corrosion of the steel if water permeates through the structure. As previously stated, steel fibers can be used

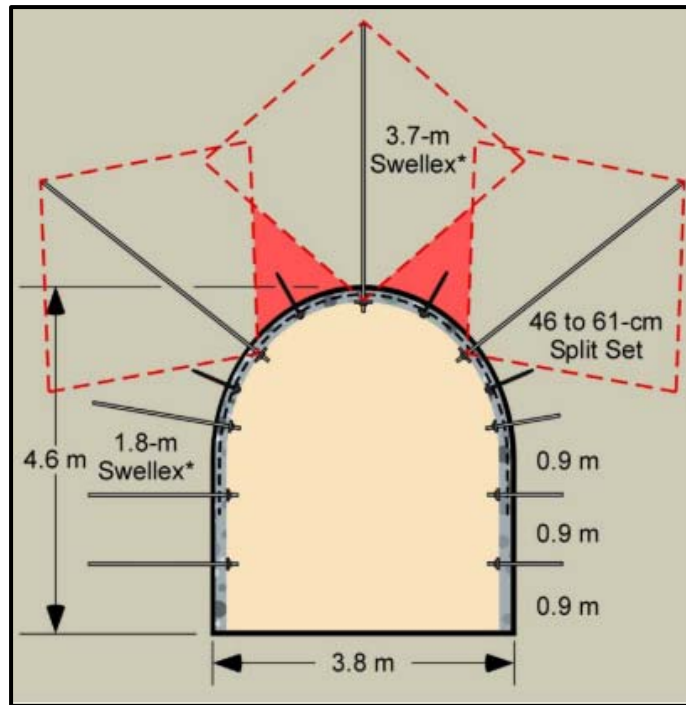


Figure 2-3: Completed shotcrete ground control system for underground mining operation in weak rock [12].

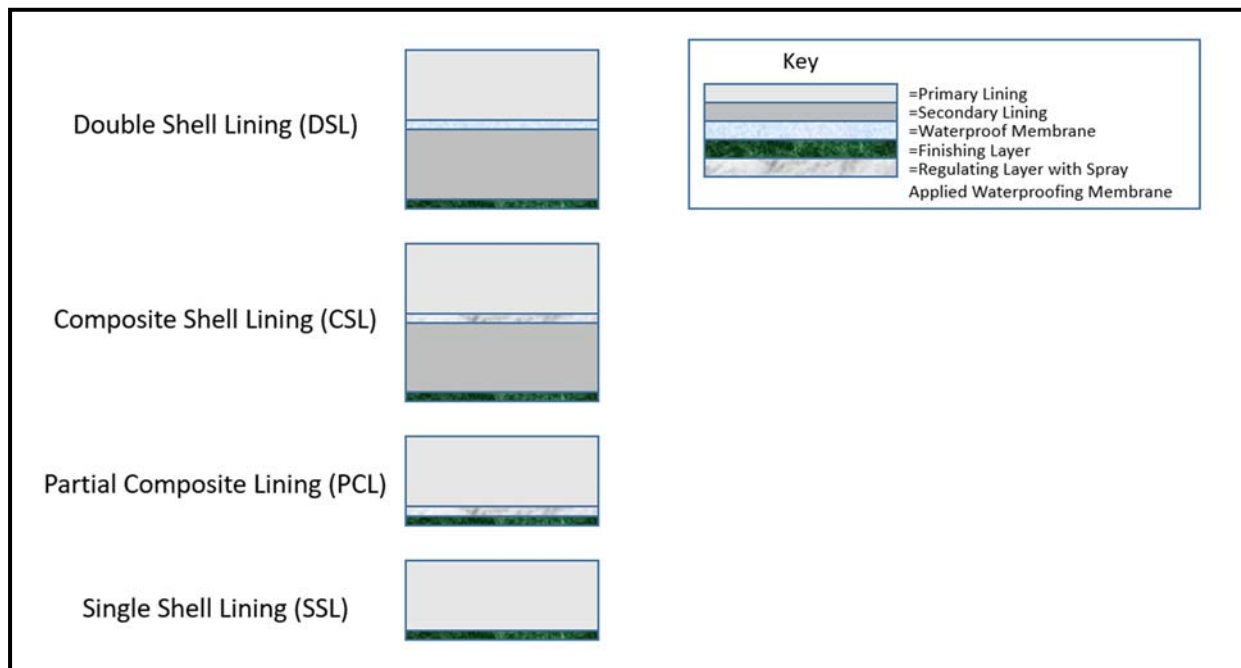


Figure 2-4: Permanent lining design types [8].

in the concrete mix composition to avoid common spray defects commonly associated with wire mesh reinforcement and produce a uniform shotcrete thickness that can be applied over irregular surfaces. However, there is still potential for the steel fibers to be exposed to corrosion if the local geology of the operating environment allows for sulphate attack. Additional sources of shotcrete failure include age, in-situ stresses, geology, inadequate mix composition, poor water quality in the mix composition, accidental impacts, shrinkage, excessive groundwater, freeze-thaw conditions, electrochemical corrosion, and sintering [1].

According to Thomas, when maintenance and rehabilitation work needs to be performed on particular sections of liners, larger areas of defective concrete can be removed either through mechanical impact or by high-pressure water before prepping the surface for a new layer of sprayed concrete [8]. Each excavation method has differing operating parameters and fragmentation mechanisms which are investigated within the remainder the literature search. Background knowledge in both rehabilitation methods is crucial in understanding how waterjet systems may solve issues related to health, safety, and structural integrity commonly associated with the use of impact hammers.

2.3 Fracture Mechanisms of Impact Bits

While the mechanical excavation elements of this research focus on data generated by percussive mechanical impact hammers, it's important to note how they differ from combined rotary percussion drilling. The process of excavation through the use of impact bits involves disintegration of the concrete mass at the bit-concrete interface. Penetration is achieved when the applied stress through the impact hammer exceeds the compressive strength of the concrete and the rate of penetration is dependent on the mode of energy transfer at the bit-concrete interface. Combined rotary-percussion drilling uses both axial and torsional energy to penetrate into target material. Rock damage and failure through this method of drilling can be described through the following processes [18]:

- Rock crushing through repetitive compressive bit load;
- Rock fracturing through shearing and tensile forces; and
- Rock weakening through repetitive compression-tension loading.

The axial percussion penetrates the rock, similarly to impact hammers, while the additional torsional component forces the cutter to chip out the rock. Rao Karanam and Misra state that there is no single physical or mechanical property of a rock that is directly relatable to drillability and the best method for determining that factor is to simply drill it and observe the results [19].

Differences in maximum shear stress generated by varying drilling techniques were discovered by Zha et al while collecting drill data in Tuha Oilfield, China. These results are shown in Figure 2-5 [20]. Within Figure 2-5, the maximum shear stress is plotted for axial percussion plus torsional percussion plus rotary action (line 1), axial percussion plus rotary action (line 2),

and axial percussion (line 3). These differences in achieved maximum shear stress lie in the operation of the drill. For example, with line 1, the rotary shaft is coupled with the forward shaft of the percussion drive, causing the axial percussion and the torsional percussion to combine. With line 2, the axial percussion and rotary action operate independently from each other with the rotation occurring between bit impact. Overall, their data shows that, compared to using axial percussion alone, the application of combined rotary-percussion drilling can increase the maximum shear stress by 87.4%. This shows that there is a significant difference in operational dynamics between percussive impact hammering and rotary-percussion drilling.

Within Karanam and Misra's book, "Principles of Rock Drilling", the authors state that percussive hammering is generated when compressed air or hydraulic fluid accelerates a piston along a cylinder and comes in contact with a drill steel. When making contact, the momentum and energy in the piston is transferred to the steel as a stress wave, or compressive strain pulses, which then transmits along the steel to the interface of the bit and the target material. The type of drill used depends on the application and infrastructure set within the working environment. According to Marshall, there are advantages and disadvantages to the use of a hydraulic drill in place of pneumatic [21]. These are listed in Table 2-5. It is important to note that, while hydraulic drills pose significant advantages over the use pneumatic, there are situations where pneumatic operation is the favorable option, such as when the necessary compressor capacity is already in place. Additionally, depending on the operating environment, pneumatic drills may be favorable due to the cooling effect provided by the exhaust air.

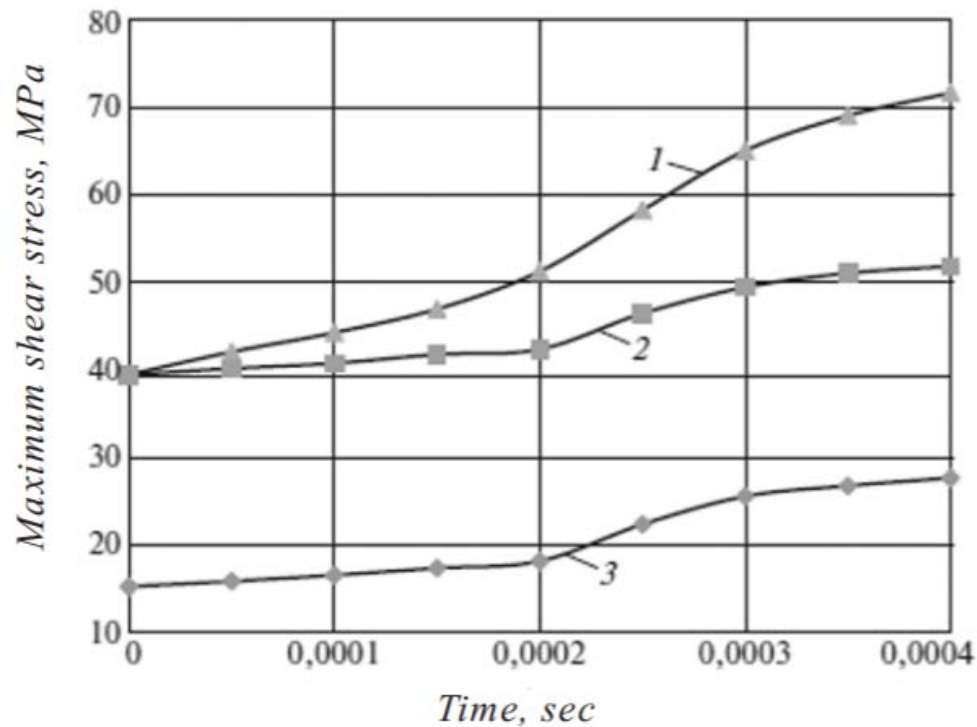


Figure 2-5: Maximum shear stress data under varying drilling conditions including (1) axial percussion plus torsional percussion plus rotary action, (2) axial percussion plus rotary action, and (3) axial percussion [20].

Table 2-5: Advantages and disadvantages of using a hydraulic drill in place of a pneumatic drill in underground working environments [21].

<i>Advantages</i>	<i>Disadvantages</i>
Overall efficiency is higher, therefore can cost less to use	These drills can be less reliable as the power source typically comes from the drill rig rather than a compressor
It is easier to vary the working parameters such as volume flow, pressure, and blow frequency	Equipment requires a fine degree of cleanliness to operate successfully
They can be operated at higher pressures, making it possible to use a piston shape that will provide a more effective stress wave shape	The control systems are more complex, and the working fluid needs to be clean for longer operating life, requiring knowledgeable operators and maintenance workers
There is no exhaust air which results in less noise. Lack of exhaust air also eliminates the release of mist and oil into the working environment	All electric energy provided to the drill is liberated into working environment as heat whereas pneumatic drills produce a cooling effect from the exhaust air

Different types of drill bits, such as cross, button, or wedge, can be used depending on the application and target material being drilled upon. With regards to the use of an impact

hammer, wedge bits are typically used and their shape can have an effect on rate of penetration. As the bit comes in contact with the target surface, part of the generated stress wave goes into breaking the target material while another part is reflected. Equation 2.1 and Equation 2.2 give the instantaneous force and particle velocity which is developed through the interaction of longitudinal waves at the cross-section in drill steel [19].

$$F = (\sigma_i + \sigma_r)A + F_0 \quad (2.1)$$

Where:

F = Total force between bit and rock;
 F_0 = Force between the bit and rock before stress wave arrival;
 σ_i = Incident stress;
 σ_r = Reflected stress; and
 A = Cross sectional area.

$$\frac{du}{dt} = \frac{C}{E} (\sigma_i + \sigma_r) + V_0 \quad (2.2)$$

Where:

$\frac{du}{dt}$ = Particle velocity;
 C = Wave velocity in the drill steel;
 E = Young's modulus of the drill steel; and
 V_0 = Bit velocity before stress wave arrival.

These equations assume that the bit and target material, such as concrete, are in contact at the same time the first incident wave arrives at the bit-concrete interface. In order for this to occur, an axial thrust force must be applied to the drill, which is directed toward the rock, and is shown in Equation 2.3 [19]. This required thrust must be continually applied so that the bit is in contact with the target material during subsequent impacts.

$$F_t = 2(1 + \alpha_t)NW_pV_p \quad (2.3)$$

Where:

F_t = Minimum thrust required;
 α_t = Constant dependent on piston geometry and shape of wave reflected at the bit-target material interface;
 N = Number of impacts per minute;
 W_p = Weight of the piston; and
 V_p = Piston impact velocity.

If the thrust force is below the minimum, a significant amount of the energy dissipates in the form of heat and noise. This dissipated energy transmits into the drilling equipment and the drill steel/bit which reduces the life of the steel. If thrust force is above the designed range, penetration will be reduced due to problems with indexing and bit flushing. With regards to the drill system, if air/hydraulic pressure supply is increased, the optimum thrust force will also increase. Marshall states that, due to limited compressed-air pressures, an increase in output from the drill requires an increase in the size of the hammer piston [21]. Eventually, the increase in physical size of the equipment is not ideal for the operating condition. An increase in air pressure is possible, however, this could facilitate issues associated with worker safety as well as an increase in transmission losses, leading to the use of a hydraulic hammer which can operate at a higher pressure instead of increasing the piston size. The shape of the impact bit, specifically the angle of the wedge, also has an influence on depth of penetration and contact stress. These differences are illustrated according to Karanam and Misra in Figure 2-6.

Figure 2-6 shows that if the bit shape has a more obtuse angle, there will be a small depth of penetration and a large area of contact, whereas a sharp bit with a more acute angle will lead to higher contact stresses. While there is not a scale provided in Figure 2-6, it is important to note that the depth of the zone of pulverized rock would be larger for an acute wedge angle compared to that of an obtuse angle. With an acute angle, the maximum compressional stress component will be at a smaller angle to the surface of the rock, making it easier to chip the target material to the free surface. However, sharper bits can wear faster than bits with an obtuse shape, making it necessary to find an optimal wedge angle for the specific material being excavated. During operation, attack angle, or angle of the bit relative to the target material's surface, should also be considered as it can reduce vibrations to the equipment, therefore leading to less wear of cutting components.

Karanam and Misra state that numerous studies on bit penetration into brittle materials have been published based on a wedge penetration model created by Paul and Sikarskie [22]. Within their model, it is assumed that the brittle material fails according to the Coulomb-Mohr failure criterion. It predicts the orientation of the failure plane, as well as the load associated with shear failure through a two-dimensional analysis of the load associated with the indent formed by the wedge. Dutta formed a theory in 1972 stating that initial fracturing takes place when a rigid bit makes first contact with the brittle target material [23]. When there is an increase in load and penetration, crushing takes place followed by instances of chipping when there is a sudden release of strain energy. When the initial crushing phase is taking place, the wedge of the crushed rock is formed. This brittle mass of material within the wedge becomes subjected to a high triaxial stress condition as it is confined within two shear planes on each side of the wedge. When the load has increased and no more deformation can take place, the crushed mass of material acts as a rigid body and transmits the load to the surrounding rock and the chipping process occurs. This chipping process is shown in Figure 2-7 where variable, h , represents depth of initial penetration when chipping commences, variable, d , represents depth to the end of the zone of pulverized brittle material due to penetration, variable, ψ , represents angle of fracture plane to

the brittle material surface, and variable, θ , represents half-wedge angle of the crushed rock mass.

Bilgin, Copur, and Balci's book, "Mechanical Excavation in Mining and Civil Industries" outlines the working principles and operational features of impact hammers [24]. Impact hammers offer the advantage that they can selectively remove material at high levels of impact energy compared to other continuous methods of mechanical excavation. The authors state that the specific energy, or the energy required to break a unit volume of rock, is inversely proportional to the blow energy and is shown in Equations 2.4 and 2.5 [24].

$$SE = \frac{k}{\sqrt{E_i}} \quad (2.4)$$

$$E_i = \frac{MV^2}{2} \quad (2.5)$$

Where:

SE = Specific energy;

E_i = Impact or blow energy;

M = Weight of the piston;

V = Piston velocity; and

k = Constant.

Bilgin et al state that theoretical performance prediction of hydraulic hammers was studied by Evans in 1974 [23]. Evans found that the susceptibility of rock to fail due to impact breakage was a function of both compressive and tensile strength. Underlying tensile failure through use of an impact hammer can lead to future structural issues depending on the excavation application. For example, pertinent information on this issue can be found in the analysis of bridge deck concrete removal. When concrete on bridge decks deteriorates, it needs to be removed before new overlay concrete is applied. Traditionally, this concrete is removed using jack hammers or some type of impact hammer excavation method.

Researchers and industry professionals in the field of civil construction have found that impact hammer excavation methods cause micro-fracturing of the concrete left in place. In 2002, J.D. Wenzlick of the Missouri Department of Transportation found that the micro-fracturing caused premature loss of bond in the overlaid concrete surface leading to extensive cracking and de-bonding that caused premature deterioration well before the end of their design life [25]. This premature deterioration costs a significant amount of time and resources to companies performing the rehabilitation due to additional work required to fix the bridge deck. In 2018, a study by Izumi et al was conducted to quantitatively evaluate the severity of impact hammer

induced collateral damage in concrete substrates [26]. In this experiment, a pneumatic breaker was used to remove a concrete substrate layer. After testing was completed, an X-ray computed tomography method was used to investigate the porosity, crack width, and connectivity in the concrete substrates. After analysis of the results, Izumi et al were able to develop a figure showing morphology of fractures induced by the pneumatic hammer as shown in Figure 2-8.

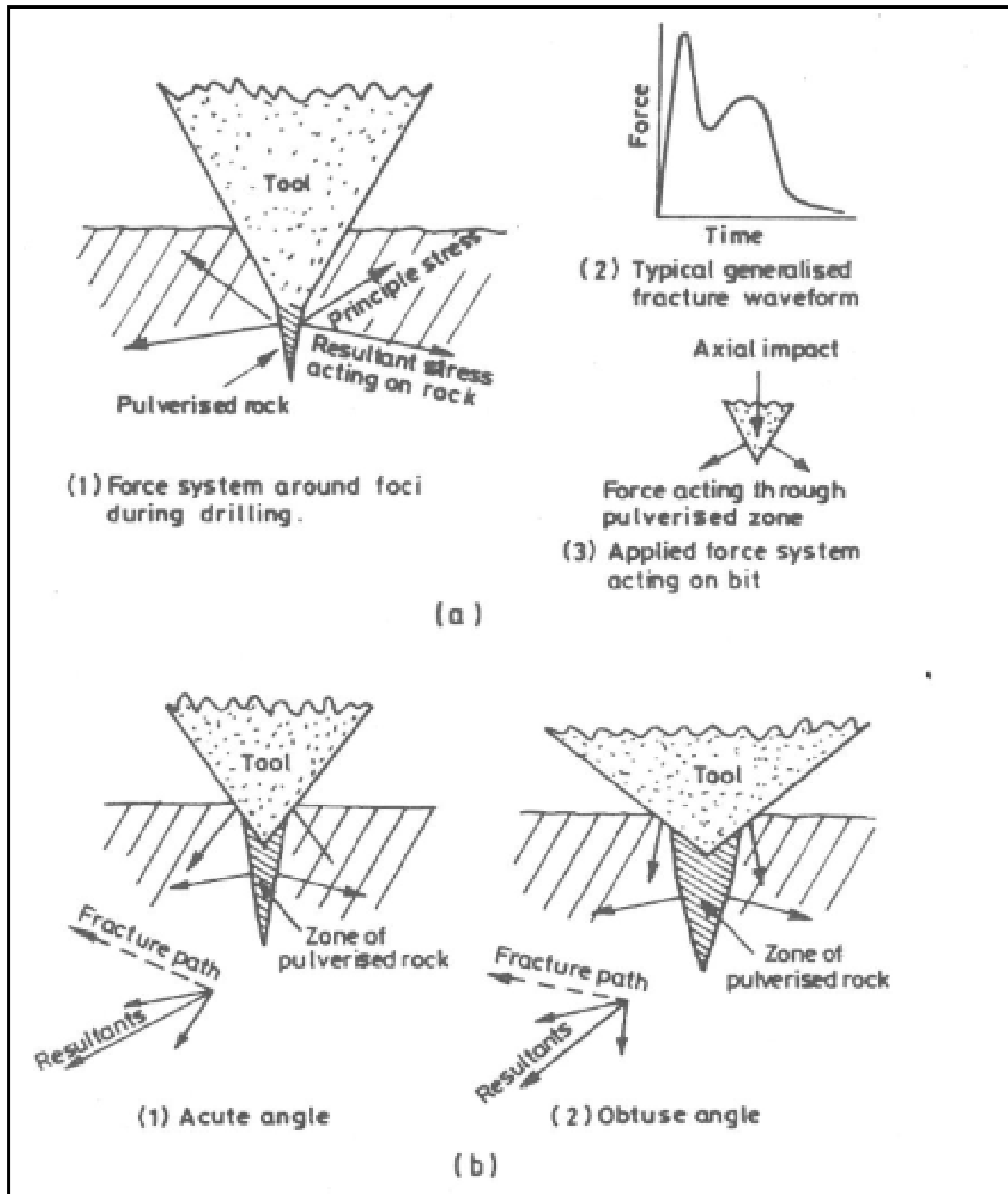


Figure 2-6: According to Karanam and Misra (a) forces acting on system during percussive drilling (b) how wedge angle effects geometry of forces during percussive drilling [19].

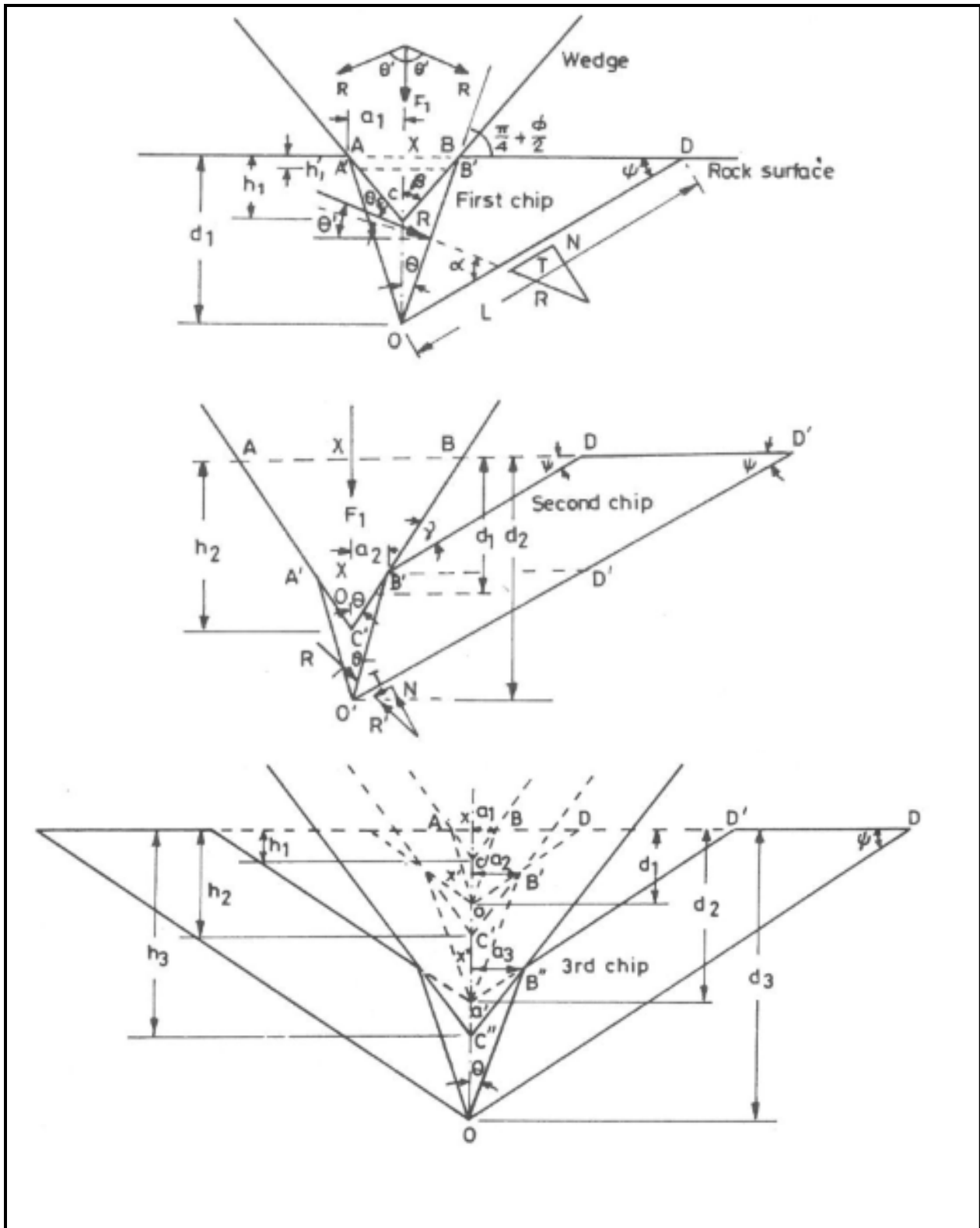


Figure 2-7: Mathematical models of chip formation from wedge [19].

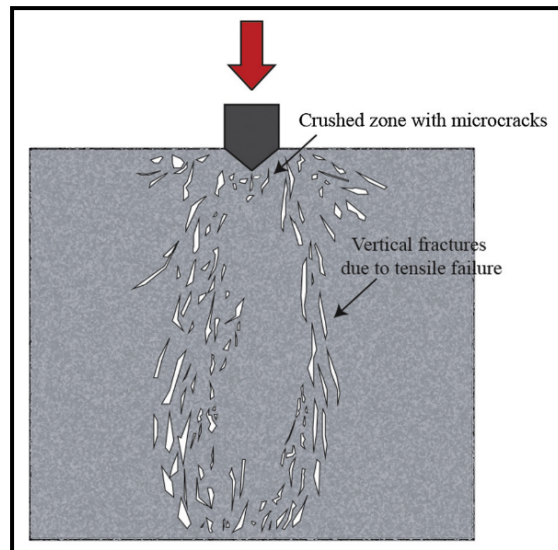


Figure 2-8: Morphology of fractures induced by a single indenter [26].

Izumi et al found that, with regards to the single indenter, cracks are initiated around the corner of the indenter followed by the formation of a crushed zone with micro-cracks. From a quantitative analysis, it was discovered that surface chipping with an impact hammer can induce many micro-cracks with a width of approximately 0.1 mm (0.004 inches) in the region emanating from the impact surface to a depth of 4 cm (1.6 inches). This supports Wenzlick's research regarding the issue of premature loss in bonding between the substrate and new concrete overlay. If a deteriorated concrete surface is excavated to the concrete/substrate interface, there is potential for the impact hammer to induce micro-cracks into the substrate. If the operator is unaware of this, there is potential for unanticipated structural integrity issues that could jeopardize the safety of not only the workers associated with the rehabilitation work but also the civilians who use the structure on a day to day basis.

Impact hammers have been an effective tool traditionally used for rehabilitation work in concrete structural liners. Overall, the shape of the impact bit, specifically the angle of the wedge, has an influence on depth of penetration and contact stress and it is important to find an optimal wedge angle for the specific material being excavated. With issues related to micro-fracturing and loss of structural integrity due to the use of this tool coming to the forefront, it is important to investigate alternative methods of shotcrete/concrete removal. More specifically, a new tool should be evaluated to eliminate the aforementioned issues generated by impact hammers. High-pressure waterjets have the potential to do so and are further outlined in Sections 2.5, 2.6, and 2.7 of this literature search.

2.4 High-pressure Waterjet Scaling

In 2008, Poeck published a thesis evaluating the performance of various nozzle designs for waterjet scaling in underground excavations. Within this thesis, Poeck discussed the use of this technology for scaling procedures through recent history [27]. For example, The Centre for Mining Technology, a division of the Mining Innovation, Rehabilitation, and Applied Research Corporation (MINARCO) located in Sudbury, Ontario, conducted tests investigating the applicability of high-pressure waterjet scaling for underground hard rock drift operations, where the ultimate goal was to increase mine development rate. The research utilized a 10.3 MPa (1,500 PSI) waterjet operating at 228 lpm (60 gpm) with an average standoff distance of 2 to 3 meters (6.5 to 10 feet) scaling the ribs and back of a heading that was under development. The testing concluded that there was a reduction in shotcrete spraying time due to a reduction in shotcrete re-work, reduction in rock fall during operation, and increased adhesion of the shotcrete to the rock surface.

Poeck also discussed past research conducted in Idaho Springs, Colorado by Colorado School of Mines (CSM) investigating the change in adhesion strength of sprayed concrete as a function of water pressure used to treat the underlying surface with pressures ranging from 0.7 to 41.4 MPa (100 to 6,000 PSI). It was discovered that 20.7 MPa (3,000 PSI) was the optimal working pressure for scarifying the rock surface, which was used for further research in waterjet scaling to quantify the performance of waterjet versus manual scaling in an underground mine drift 3 x 3 meters in size (10 x 10 feet). After a 1.8-meter (6 foot) round was blasted and mucked, the previously blasted area was scaled using both a waterjet system and a manual scaling bar. At the conclusion of this experiment, it was discovered that it is difficult to quantify the effectiveness of the scaling operation due to the fact that the longer an area is scaled, the more material can be brought down. However, the research team did find that the overall effectiveness of the scaling operation could be improved by rapidly moving the jet across the rock face which is achieved by using a rotating nozzle or by using a oscillating hydraulic head cylinder mounted at the end of the boom [27].

In 2009, Naggar and Sabouni published an article that reviewed Lundmark and Milsson's research in using waterjets for surface preparation in a tunnel in Hallandsas, Sweden [28]. Lundmark and Milsson's research analyzed how waterjet scaling provided higher adhesion strength for the application of new shotcrete compared to mechanical scaling and cleaning. However, Naggar and Saboudi stated that the scatter of adhesion strength resulting from waterjet surface preparation was so large that it was not possible to draw conclusions from the statistical data on whether it was significantly higher than that of mechanical methods. While no statistical conclusions could be drawn, the authors believed that waterjet scaling appears to be an acceptable technique for preparing the surface of concrete lining before applying a new shotcrete layer.

2.5 High-pressure Waterjet Excavation of Shotcrete/Concrete Liners

Society for Mining, Metallurgy & Exploration (SME) Mining Engineering published a journal article in 2009 discussing how a conventional twin orifice rotating, continuous waterjet selectively removed concrete damaged by a major fire that occurred in the Channel Tunnel linking Britain and France [7]. The tunnel fire lasted for approximately 16 hours, with extreme temperatures rising up to approximately 1,000 degrees Celsius (1,832 deg. F), causing extensive damage to the concrete lining. Four conventional twin orifice rotating waterjet systems were utilized to remove the damaged concrete by cutting at a depth of 30 mm (1 inch) over 9,500 square meters (102,257 square feet) of the tunnel. Figure 2-9 shows the rehabilitation scenario.

The robots were equipped with modified arching feedbeams, which carried the jet nozzle, to match the curvature of the tunnel wall and maintain a consistent standoff distance between the nozzle and the rock surface. This specific system was also equipped with a vacuum attachment to collect the water and excavated debris during operation. The repair contract was deemed a success and a new concrete lining was sprayed for reinforcement before reopening the tunnel for shuttle train service.



Figure 2-9: Hydroexcavation robot removing damaged concrete in tunnel liner [7].

While this article demonstrates that rehabilitation of damaged tunnel liners using high-pressure waterjets as an excavation tool is possible, there is no disclosure of any substantive information on the operating parameters, system performance, cutting mechanism, and how it compared to alternative technologies, such as traditional mechanical excavation. Furthermore,

the paper provided no disclosure of operating efficiency, fragmentation dynamics, and other important data through which a quantitative analysis could be made. Therefore, there is a lack of relevant information within the current literature associated with shotcrete/concrete liner excavation from which to draw quantitative relationships or conclusions. In response, this research offers original quantitative and qualitative results that will benefit the tunneling and underground heavy construction industry, as well as provide the basis for future research.

2.6 Instrumentation of High-Pressure Waterjet Systems

Over the last three decades, significant strides have been made in the development of reliable high-pressure pumps, accessories, and system components, as well as an understanding of the complex relationships that exist between jet productivity and numerous operating variables. These improvements have been fueled by the rapid growth of waterjet systems in a wide variety of industrial and manufacturing applications, including petrochemical plant cleaning, the removal of corrosion, contaminants, and coatings from a variety of substrates, hydro-fracking, the cleaning of piping networks, sewers, and tanks, and ultra-high-pressure and abrasive jet cutting. As a consequence of growth in these economic applications, high-pressure equipment is now widely commercially available from numerous North American manufacturers.

Researchers, such as Miller and Wang, state that the term “waterjet technology” comprises a wide spectrum of differing techniques and equipment designs, all of which possess their own individual hydrodynamic and impingement characteristics [29]. Wright and Hardy of StoneAge, Inc. state that planning a job using a waterjet system starts with understanding the pressure, flow, and tooling required to remove the target material [30]. All materials have a minimum energy impact, or threshold pressure, at which a specific material can be cut or fractured by a waterjet. When constructing a waterjet system, it is crucial to first determine what pressure and flow rate are needed to achieve a prescribed objective. The pressure desired can vary depending on the application for the waterjet. For example, the pressure, flow, and standoff distance, or the distance between the nozzle orifice and target material that the waterjet must travel, needed for cleaning are significantly different from those needed for precision cutting. Quantifying a threshold pressure for an isotropic material, such as metal, is possible due to their uniform composition in all orientations. However, it is difficult to determine a threshold pressure that applies to a specific rock type or concrete. According to Summers [31], relative crack length is a function of grain size which is also inversely proportional to the pressure required to generate crack extension. Differential compression of dissimilar materials under jet impingement contributes to increased dilation of surface flaws. Failure occurs at the weakest point to which the jet has access whether it be a mineral constituent or a plane of weakness. Therefore, jet performance will vary between samples of the same type of rock or mix of concrete, making it difficult to identify a single threshold pressure.

There are several different types of fluid jet systems used for specific cleaning or cutting applications, such as the following:

- Continuous waterjets;
- Abrasive waterjets (AWJ) or abrasive suspension waterjets (ASJ);
- Cavitating waterjets;
- Low and high frequency pulsed or segmented waterjets; and
- Cryogenic fluid jets.

These systems can vary from ultrahigh-pressure systems greater than 690 MPa (100,000 PSI) and flow rates less than 3.8 lpm (1 gpm) to low-pressure systems of 7 MPa (1,000 PSI) at extremely large volumes of more than 7,010 lpm (1,850 gpm). Researchers, such as Vijay, found that precision cutting of most materials can only be obtained with a continuous waterjet at high-pressures or with entrained abrasives in the stream [32]. AWJ is not used within the scope of this research due to system complexity, cost, and material response. The focus of the literature search is directed primarily on conventional continuous waterjet systems. Figure 2-10 shows a schematic of a waterjet system's general components according to Vijay.

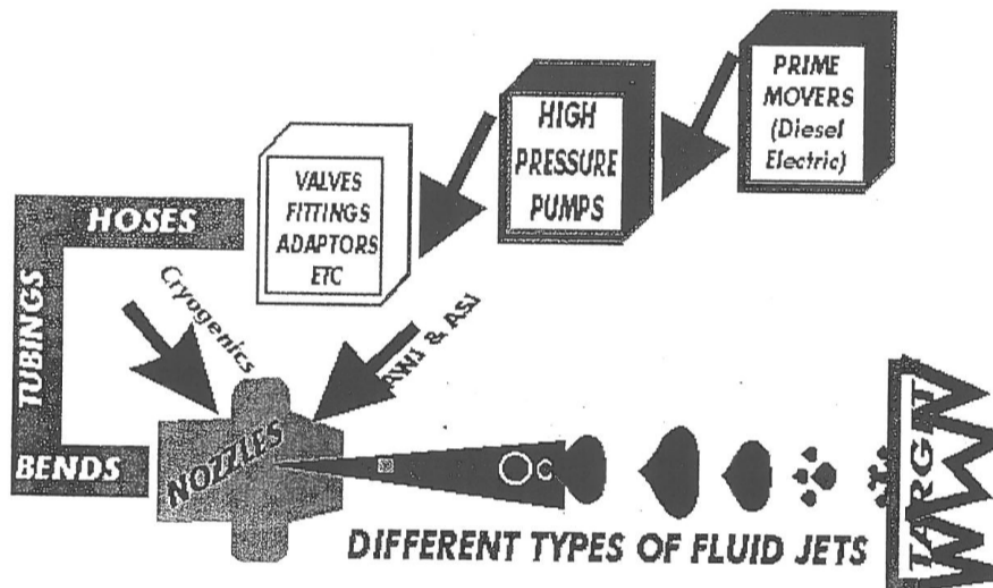


Figure 2-10: Components typically found in waterjet systems [32].

All components shown in Figure 2-10 have a significant influence on the jet and its performance when it impinges upon the target material. It is important to understand that there will be pressure losses throughout the waterjet system, meaning that the pressure measured at the pump does not equal the pressure at the nozzle. Pressure loss can occur in the hoses, fittings, and the tooling used due to friction and flow instability as the water moves through the system. If there is a significant distance between the nozzle and the pump, the system is improperly designed, or possesses a large number of flow controls, pressure loss should be taken into consideration. For example, pressure loss through the length of the hose can be calculated using Equation 2.6 [30].

$$PL = \left(\frac{F}{53 \left(\frac{I.D.^{2.5}}{L^5} \right)} \right)^2 \quad (2.6)$$

Where:

PL = Pressure loss in PSI;

F = Flow in GPM;

$I.D.$ = Inner diameter of the hose in inches; and

L = Length of hose in feet.

Upstream flow conditions from the nozzle are important to consider when configuring a waterjet system. Proper upstream conditions are generated when there is stable flow which is affected by certain waterjet system components, such as bends near the entry to the nozzle, surface finish of the orifice, non-symmetric flow passage geometry, and the geometry and transitional diameters leading into the nozzle. The upstream conditions should be as close to laminar flow as possible [32]. Summers discusses research from Labus which states that a coefficient of discharge should be incorporated when calculating the flow rate through a system. The nozzle shape determines the discharge coefficient which is a value that correlates the volume of water that passes through the orifice as a portion of the flow where the jet would fill its entirety [33]. Examples of discharge coefficients (C) associated with generic nozzle shapes, according to Labus, are found in Figure 2-11.

Testing from Wright et al. on cement/sand aggregate samples demonstrated that poor upstream conditions can reduce a jet's performance by 25 to 55 percent [34]. If poor upstream conditions exist, flow straighteners can be used, such as vanes, to mitigate reduction of jet performance due to flow turbulence. Examples of flow straighteners are shown in Figure 2-12. It is important to note that flow straighteners are typically less effective than nozzles with good upstream conditions [34].

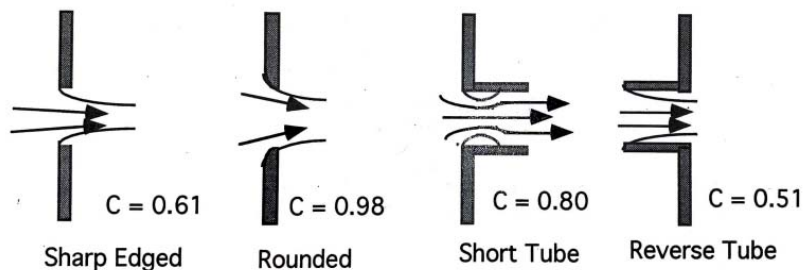


Figure 2-11: Discharge coefficients (C) associated with generic nozzle shapes [33].

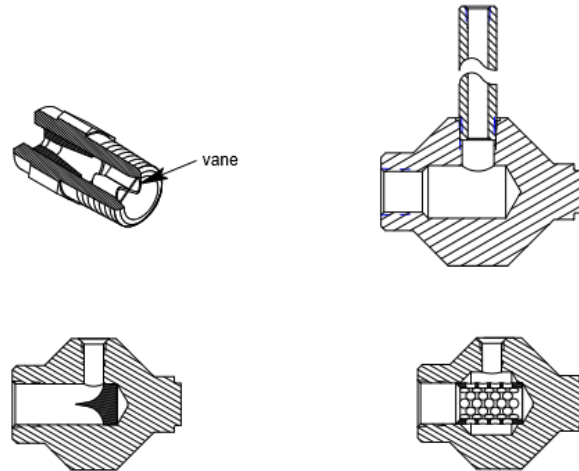


Figure 2-12: Common flow straighteners for nozzle performance testing [34].

The type of material from which the nozzle is constructed has a significant impact on the overall functionality of the jet operation. As the nozzle wears out, jet quality deteriorates, and therefore, decreases the jet productivity, making it crucial to use the material that best suits the operating conditions (pressure, flow, and water quality). There are varying nozzle material types commonly used in commercial applications, including different grades/alloys of steel, carbide, and sapphire. If unfiltered water is used, carbide is the material of choice for most medium pressure applications and there are different variations with regards to binder type and percentage of binder. If the water is filtered to 25 micron or better, and the operating pressure is below 137.9 MPa (20,000 PSI), steel nozzles can be used as they will often outlast carbide. If the water is filtered to 10 micron or better, the flow is greater than 19 lpm (5 gpm), and the operating pressure is above 137.9 MPa (20,000 PSI), sapphire can be a suitable nozzle material option [35]. It is important to note that nozzle wear is non-symmetrical and, depending on the material type, once the nozzle begins to deteriorate, it can rapidly fail. In the end, nozzle selection relies on cost, the expected life, and acceptable performance. Depending on the application, the stream quality may or may not be an important operating factor. Buying the most expensive nozzle does not necessarily make it the best option, especially during a trial and error process, as manufacturing quality, materials, and design of the same size/type can vary between suppliers.

At the 2019 Waterjet Technology Association, Basics and Beyond Short Course in New Orleans, Louisiana, Dr. Summers discussed a historical perspective on waterjet development. He outlined pressures used to excavate a range of materials as shown in Table 2-6 [36]. These pressures were collected by Swan through empiric testing and should be used for reference rather than as a definitive value for future applications. As stated earlier, jet performance will vary between samples of the same type of rock or mix of concrete because the material removal process is controlled by the initial flaws/cracks present within the sample, meaning there is no definitive threshold pressure for rock or concrete. Table 2-6 shows that the pressure range, which varies as a function of flow rate, for cutting and removing concrete is 69 to 103 MPa (10,000 to

15,000 PSI). These pressures, combined with the system's flow rate, will result in pump horsepower which can be calculated from Equation 2.7 [36].

Table 2-6: Pressures used for range of material removal processes [36].

Material Removed	Pressure, MPa (PSI)
Silt, loose debris	10.3 (1,500)
Light marine fouling, light scale, fuel oil residue, aluminum cores and shells	20.7 (3,000)
Weak concrete, medium marine growth, sandstone and mudstone, light mill scale, limited core removal, loose paint and rust	31.0 (4,500)
Concrete in pipes, severe marine fouling, ferrous casting molds, runway rubber, soft limestone, lime scale, burnt oil deposits, medium mill scale, petrochemicals	41.4-68.9 (6,000-10,000)
Concrete cutting and removal, most paints, medium limestone, most mill scale, silica cores, burnt carbon deposits, heavy clinkers	68.9-103.4 (10,000-15,000)
Granites, marble, limestone, marine epoxies, aluminum, lead, rubber, frozen food	103.4-206.8 (15,000-30,000)

$$HP = \frac{FP}{1714 \eta} \quad (2.7)$$

Where:

HP = Pump horsepower;

F = Flow in GPM;

P = Pump pressure in PSI; and

η = System efficiency.

Overall, when considering instrumentation of high-pressure waterjet systems for the cutting of rock and other nonhomogeneous materials, the important design considerations should include not only flow rate, standoff distance, and the dynamics of the jet stream, but also the rock structure, the orientation of impingement, and jet motion. It can be difficult to identify the pressure and flow required to excavate a particular type of rock or concrete, however, with regards to shotcrete/concrete, historic empiric testing has provided a sufficient baseline for future testing applications, specifically the research conducted for this project. Based on this knowledge and equipment availability, the pressure and nominal flow used for this research are approximately 179 MPa (26,000 PSI) and 21.3 lpm (5.6 gpm) respectively.

2.7 Hydraulic Fracturing Excavation Systems and Fracture Mode

Miller states that waterjets differ from conventional excavation methods in their mode of fragmentation and, in many applications, they possess inherent advantages over blasting methods and mechanical tools [29]. According to Summers, high-pressure waterjets solve many

of the drawbacks associated with using mechanical tools for cutting processes, such as being limited in speed of operation, variability in bit wear, generating dust and gas, and heating the edges of the material being cut [36]. For example, with regards to waterjet technology used in rock/concrete cutting applications, there is no mechanical contact between the tool and the target material, where the absence of significant reactive forces allows the system to be lightweight and highly flexible. In addition, forces can be applied to surfaces at any angle from the primary axis of the production face without appreciable losses in energy. The waterjet system generates no dust or toxic gases, is highly amenable to remote and robotic operation, and the excavation process is continuous. One of the most enduring features of conventional high-pressure, continuous waterjets is the selective nature by which they cut rock and other nonhomogeneous materials. In these applications, material failure is facilitated by a combination of the erosion of the rock matrix or vulnerable mineral components comprising the rock, the exploitation of impurities within the rock mass, like cracks, internal structure, and foliation, and/or the dilation of flaws between individual grains/crystalline constituencies within the rock due to differential compression. The ability to control the jet's operating parameters often in real-time, provides a unique capability to rapidly adjust the system relative to changes in the rock or cutting orientation.

Chapter 2 of Miller's dissertation, "The Characterization of Crack Propagation and Brittle Failure Induced by Discrete, High Velocity Waterjet Impacts In Crystalline Rocks", presented a summary of continuous fluid impingement fragmentation models developed by researchers up until 1996 [31]. He states that waterjet researchers have been in pursuit of a holistic theory that accurately describes the dynamic processes of hydraulically induced rock failure since the technology first existed. While a comprehensive understanding is possible, the processes that facilitate failure are directed by a vast accumulation of rock and jet properties that prevent the existence of an all-encompassing theoretical model. This led to the development of incremental relationships between critical system variables within finite applications. According to Miller, most theoretical investigations consist of derivations that attempt to predict the depth of penetration or the geometry of failure while empirical studies validate or instigate reexamination of these models.

Vijay outlines the structure of a high speed waterjet as it exits the nozzle, showing various sections of a continuous jet, droplet layer around the core, and final droplet and air zone as shown in Figure 2-13 [32]. As the jet travels in free-stream through the initial, transitional, and main regions, its structure changes from a coherent core to air-entrained and droplet zones. Following Bernoulli's equation, pressure within the waterjet system transitions into velocity as it exits the nozzle orifice, leaving the confined space and entering open air, exemplifying a change from potential to kinetic energy.

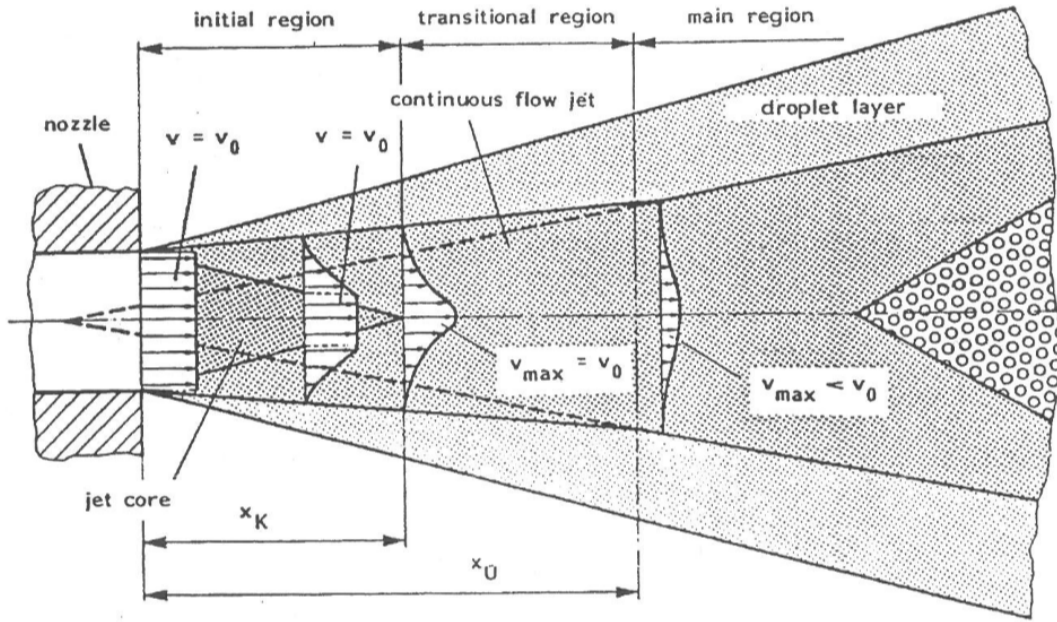


Figure 2-13: High speed waterjet showing sections of continuous flow jet, droplet layer, and final zone consisting of droplets and air [32].

The water that travels at the velocities discussed with respect to these high-pressure waterjet systems behaves as a non-Newtonian fluid. Under normal conditions, water is usually treated as an incompressible liquid, however when subjected to high-pressures and directed through a nozzle with a relatively small diameter, it exhibits compressible behavior where individual flow elements comprising the jet's free-stream have specific spatial and dynamic properties. The velocity profile changes according to distance due to aerodynamic drag acting on the jet boundary. For cutting purposes, a short standoff distance is generally preferred whereas cleaning purposes require a higher standoff distance due to the droplets acting as natural pulsed jets resulting in a higher area of erosion. The core continuous jet region, with a specific length, will vary depending on the nozzle design, surface finish of the nozzle, and upstream/entrance flow conditions into the nozzle. Momber's book, "Hydrodemolition of Concrete Surfaces and Reinforced Concrete Structures" discusses research from Nokonov that defines how the length of the core zone can be calculated, if the Reynolds number (Re) is less than 4×10^5 , using Equation 2.8 [10].

$$\frac{x_C}{d_N} = (A^* - B^*)Re \quad (2.8)$$

Where:

x_C = Length of core jet zone;
 d_N = Nozzle diameter; and

A^* and B^* = Parameter constants dependent on Reynolds number of the jet flow and nozzle geometry/quality.

It should be noted that calculating the length of the core zone using Equation 2.8 requires numerous assumptions regarding jet flow, the coefficient of flow, and nozzle geometry/quality. If the nozzle is well designed and there are ideal upstream conditions, the specific length of the continuous jet could potentially reach 1,000 times the orifice diameter while poor nozzle design and upstream conditions could result in no effective length at all.

According to Summers, waterjet impact can be defined by both jet stagnation pressure and water hammer pressure [33]. Jet stagnation pressure is a simplistic measure of the energy per unit volume transmitted to a target surface which is represented by the equation for kinetic energy.

$$p_s = \frac{1}{2} \rho V_o^2 \quad (2.9)$$

Where:

p_s = Stagnation pressure in PSI;
 ρ = Mass density of jet fluid in slugs/ft³; and
 V_o = Jet velocity at the nozzle exit in ft/sec.

Water hammer pressure is an increased pressure created, on occasion, at the instant of initial impact where a shock wave is induced into the target material. This pressure is calculated using Equation 2.10. Shock wave velocity in water is 1,470 m/sec (4,823 ft/sec). This shows that there is potential for augmentation in jet pressure at the instant of droplet impact. However, this phenomenon rarely occurs as the surface in which the water impinges upon needs to be flat, hard and completely dry or contain a stationary layer of water on a flat surface. Additionally, the jet needs to traverse across the material in order to continually impinge dry surfaces in search of material flaws such as a mineral constituent or a plane of weakness.

$$p_{WH} = \rho C V_o \quad (2.10)$$

Where:

p_{WH} = Water hammer pressure in PSI; and
 C = Shock wave velocity in ft/sec.

In order to determine the jet velocity at the nozzle exit, Bernoulli's equation is applied between two points in the flow across the nozzle. Additionally, the continuity equation must be

applied to provide a second relationship between velocities at the two points in the flow. Using the pressure at the two points across the nozzle yields Equation 2.11 [32].

$$V_J = 12.19 \sqrt{\frac{2(p_1 - p_2)}{1 - \frac{d(in)_2^4}{d(in)_1^4}}} \quad (2.11)$$

Where:

V_J = Jet velocity at the nozzle exit in ft/sec;

p = Static pressure at specific point in the nozzle in PSI; and

d = Diameter at specific point in the nozzle in inches.

This equation assumes that the flow areas are circular, there is laminar flow, the mass flux of the jet fluid is the same at both points, and that the weight density of the fluid is that of water (62.4 lb/ft³). As stated earlier, the assumption that the density of the jet fluid is the same at both points is not entirely correct due to the compressibility of water at high-pressure/temperature. According to Momber, as the waterjet exits the nozzle, its kinetic energy can be calculated using Equation 2.12, Equation 2.13, and Equation 2.14 [10].

$$E_J = \frac{1}{2} m_W V_J^2 t_E \quad (2.12)$$

$$m_W = \alpha_m \left(\frac{\pi}{4} \right) d_N^2 V_J \rho \quad (2.13)$$

$$t_E = \frac{d_N}{v_T} \quad (2.14)$$

Where:

E_J = Kinetic energy of waterjet;

\dot{m}_W = Flow rate of water mass;

t_E = Exposure time;

α_m = Nozzle discharge parameter; and

v_T = Traverse speed of the nozzle.

To account for the compressibility of water at high-pressure, the nozzle discharge parameter considers alteration in water mass flux due to sudden changes in fluid conditions for a nozzle with a sharp orifice. This particular parameter is dependent of nozzle diameter and geometry. Momber then uses the calculated kinetic energy calculated from Equation 2.12 to determine the specific energy of a stationary waterjet eroding a volume of material as shown in

Equation 2.15 and Equation 2.16 [10]. These equations can be applied within specific limits of hydraulic parameters, such as operating pressure, volumetric flow rate, and nozzle diameter, as well as performance parameters including standoff distance, traverse rate, and impact angle.

$$V_M = \frac{\pi w_M^2 h_M}{4} \quad (2.15)$$

$$E_S = \frac{E_J}{V_M} \quad (2.16)$$

Where:

V_M = Volume removal in m³;

w_M = Volume removal width;

h_M = Depth of cut; and

E_S = Specific energy in kJ/m³.

Through empiric testing, Wright developed a jet surface impact calculation in 1999 which incorporates flow in terms of the ratio of standoff distance to nozzle diameters since nozzle diameter and pressure determine flow rate [34]. This equation is shown below.

$$I_S = 0.81022e^{(-.00177072 \cdot \frac{d_s}{d_N})} P_N \quad (2.17)$$

Where:

I_S = Impact at surface in PSI;

d_s = Standoff distance in inches;

d_N = Nozzle orifice diameter in inches; and

P_N = Pressure at nozzle in PSI.

After performing additional impact/volume removal testing on two different concrete blocks with 20 mm (0.8 inch) aggregate size and strengths of 17 MPa (2,500 PSI) and 35 MPa (5,000 PSI), Wright determined that the impact calculation could incorporate the potential effect of flow adjusted by the slope ratio of measured performance and expressing the result in terms of surface impact power.

Momber states that cementitious composites are characterized by fracture process zones which occur through progressive softening [10]. With progressive softening, the stress decreases as deformation increases and the fracture zone is surrounded by a non-softening zone, combining to form a non-linear zone. Waterjet impingement in a brittle, tension-softening material, such as concrete, is shown in Figure 2-14. Figure 2-14 shows certain mechanisms that

lead to the formation of the fracture process zone including grain bridging and crack-rim friction behind the crack tip, as well as micro fracturing in front of the crack tip. Momber also notes that fracture behavior is determined by characteristic length, which can be interpreted as the brittleness of a material. Mathematically, it can be estimated by dividing the material's Young's modulus and fracture energy by the tensile strength. This measurement varies between different cementitious materials. For example, the characteristic length in non-reinforced concrete is smaller than that of asphalt due to concrete having a higher measured brittleness [10].

With regards to impingement of cementitious composites, Momber states that the two most important parameters influencing the erosion performance are flow velocity and exposure time. These parameters can be subdivided into an incubation period, or a period of time where no material is removed, and an erosion period where the threshold pressure of the target material has been reached and a volume of material is being removed [37]. A diagram of the incubation period and erosion period during testing by Momber is shown in Figure 2-15. It was also discovered that the threshold pressure has a relationship to the fracture toughness of the target material as shown in Figure 2-16. The results from Figure 2-15 show that concrete began to erode when the flow velocity reached approximately 160 m/s (525 ft/s). Additionally, during testing at a flow velocity of 300 m/s (984 ft/s), there was a jet residence period of approximately 0.01 seconds for concrete before cutting occurred. When cutting began, the eroded volume increased rapidly before tapering off as time went on. Once the threshold pressure is reached, two types of erosion modes were identified by Momber during testing. With Type-I, erosion is comparable to the process of drilling where the cavity is deep, narrow, and regular, and the erosion debris is small. With Type-II, erosion is comparable to the process of crushing, where the cavity is shallow but wide and the debris is large and irregular. Momber found that Type-I erosion was demonstrated in areas of concrete where there were fine grained materials, such as the cement matrix between the aggregate. Type-II erosion was demonstrated in areas with coarse grain structure such as a range of aggregates [37].

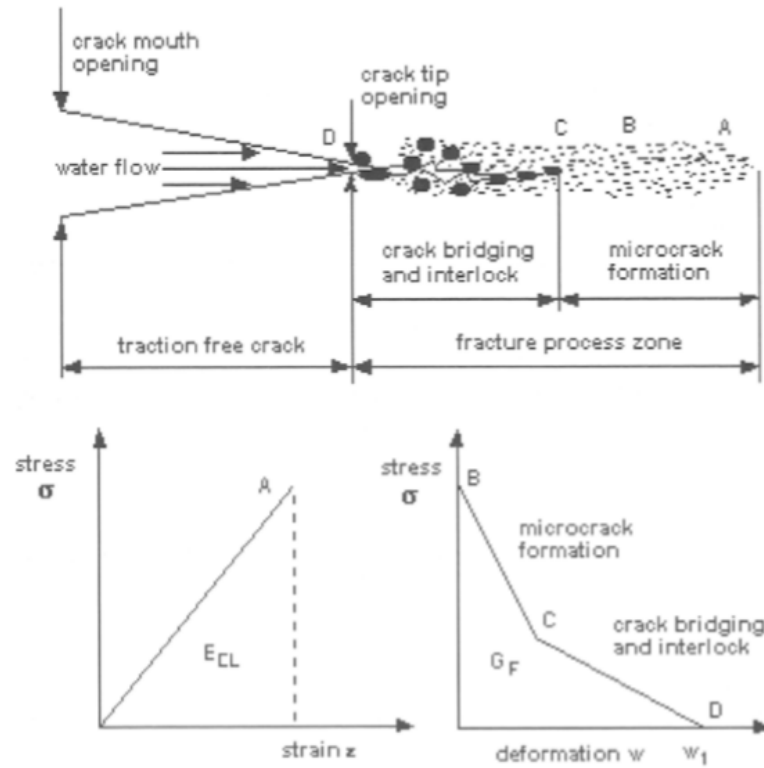


Figure 2-14: Fracture zone produced in tension-softening material [10].

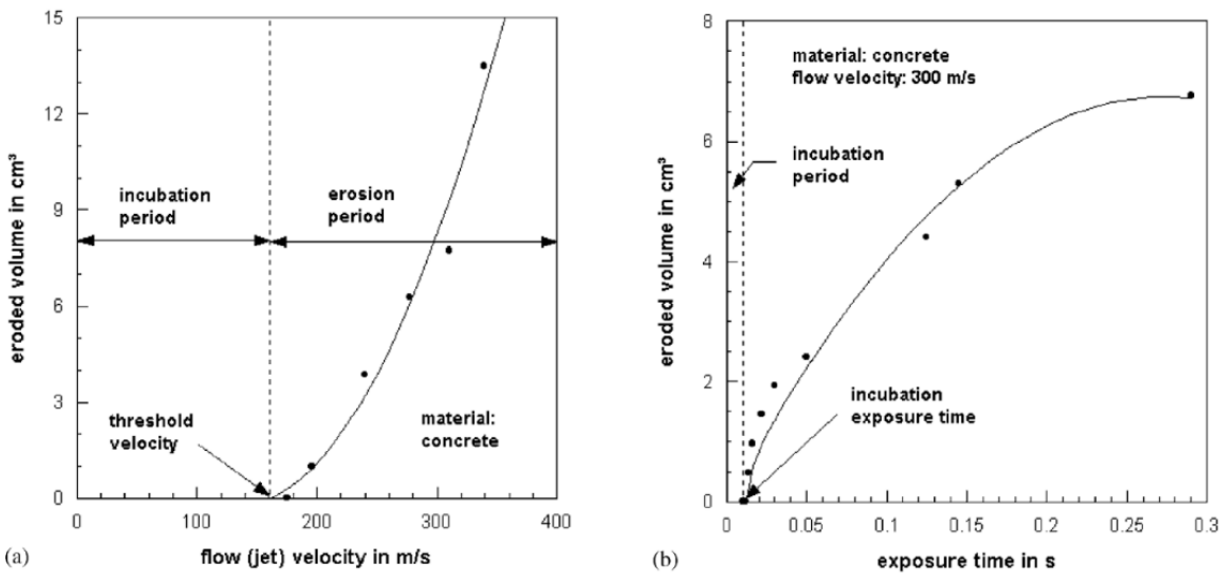


Figure 2-15: Incubation period and erosion period of concrete according to (a) flow velocity and (b) exposure time [37].

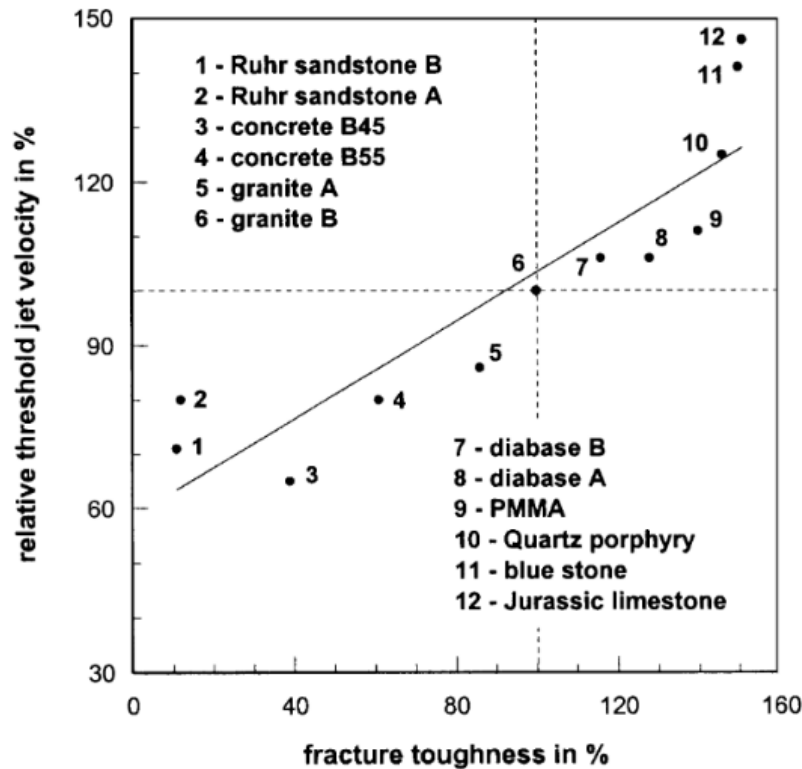


Figure 2-16: Relationship between threshold jet velocity and fracture toughness in varying rock types and concrete [37].

Wright et al state that, when excavating concrete, waterjets act to erode the cement that binds the harder aggregate together while pressurizing micro joints and cracks within the concrete [38]. The use of twin rotating waterjets increases the efficiency of the technology. Rotating jets allow large surface areas to be covered faster due to the jet hitting the surface multiple times, thus speeding up the erosion process. However, during empirical testing on 9.5 mm (3/8-inch) minus aggregate concrete with a minimum UCS of 20.7 MPa (3,000 PSI) it was discovered that there is an optimum rotation speed with regards to efficiency of material removal. Rotation speeds above this optimum range resulted in degradation of the jet as it moved through air while values below the range resulted in poor material removal productivity due to ribs of material being left between jet passes and a decreased depth of cut. Overall, the efficiency of material removal during use of a twin rotating jet system depends not only on the rotation speed but rather an ideal combination of this factor with additional variables such as traverse speed, flow, orifice diameter/orientation, standoff distance, and jet span. The authors noted that it is important to keep the standoff distance as small as possible at higher rotation speeds. Empiric testing by Wright et al demonstrated that two strengths of concrete have different optimum pressures for material removal and the weaker concrete between the two requires less power.

While there have been many attempts to predict the dynamic material removal process due to high speed continuous waterjets, none could achieve a high percentage agreement with

empirical testing across a wide range of materials. In the end, the qualitative model developed by Summers seems to best describe why the process is so difficult to capture [31]. He states that the material removal process is controlled by the initial flaws/cracks present within the sample, as these flaws dictate when crack growth occurs, meaning that jet performance will vary between samples. Momber states that two types of erosion modes exist during jet impingement of concrete with Type-I erosion occurring in fine grained materials such as the cement matrix between the aggregate and Type-II erosion occurring in areas with coarse grain structure such as a range of aggregates. These research findings from Summers and Momber were considered during visual inspection after empiric waterjet testing took place on the support liner panels developed for this research study.

2.8 Visual and Non-Destructive Analysis

At this point in the literature search, background information has been covered for the topics of structural liners, concrete fracture mechanisms associated with impact hammer bits, and instrumentation and fracturing mode for high-pressure waterjet systems. To complete the objectives of this research, it is important to understand how visual and non-destructive analysis can aid in identifying key differences in deterioration of the substrate within the test panels between each excavation method. Numerous visual and non-destructive testing methods have been used to examine possible deterioration within the concrete infrastructure. In the paper “An attempt to describe a relationship between concrete deterioration quantities and bridge deck condition assessment techniques”, Varnavina et al used the methods of visual inspection, core control, Ground Penetrating Radar (GPR), and Ultrasonic Surface Wave (USW) to assess the condition of a concrete bridge deck [39]. The results from each testing method were compared to concrete deterioration quantities collected using LiDAR after hydro demolition took place.

With visual inspection, the top surface of the bridge deck was analyzed, documenting the location of cracks, patches, and any other anomalies. With core control, 51 mm (2 inch) diameter core samples were taken at locations where there was evidence of deterioration and no evidence of deterioration. With GPR, scans were acquired along parallel traverses on the bridge deck oriented parallel to the direction of traffic. Finally, with USW, a Portable Seismic Property Analyzer (PSPA) was used to acquire data from the top surface of the deck at discrete points spaced at 0.61 meter (2 foot) intervals [39]. After each inspection method was completed, the bridge deck was rehabilitated and LiDAR measurements of concrete depth removal were collected to be used as a baseline. After analysis, Varnavina et al concluded that the GPR results showed the best correlation with LiDAR data and suggested that GPR has the best potential to predict concrete repair quantities with good accuracy. A similar investigation was conducted by the Texas A&M Transportation Institute as part of the Transportation Research Board’s Strategic Highway Research Program, sponsored by the U.S. Federal Highway Administration in 2014 [40]. Members of this research group identified non-destructive testing (NDT) techniques that can be used to evaluate the condition of various types of tunnel linings. Analysis of tunnel lining condition includes the assessment of major problems associated with structural integrity, such as water leakage, delamination and spalling of concrete liners due to reinforcing steel corrosion,

voids behind and within the linings, concrete permeability, tiles separating from the liner, and lack of overall integrity of steel reinforcement. After developing tunnel liner specimens and testing various NDT techniques, the research team created a summary of accuracy, detection depth, deterioration mechanisms detected, tunnel lining types, and supplemental information on each testing method as shown in Figure 2-17.

Based on the summary on each of the NDT techniques, ground-coupled GPR appears to be the method that can detect the most deterioration mechanisms, as well as their associated depths, making it the most suitable NDT method for tunnel liner analysis. This is supported by research conducted by Kravitz at CSM, where he determined that GPR was the best method for void detection in a tunnel with a supportive liner and, overall, was a valuable tool in being able to gather large data sets to correlate to known baseline conditions [41]. Research by Lalagüe et al also supports this conclusion, where they utilized GPR systems to inspect stability of existing Norwegian tunnel liners [42]. GPR is an active source geophysical process, where electromagnetic waves (EM) are radiated from a transmitting antenna (TX) to propagate through the subsurface. When the waves hit certain material properties within the subsurface containing EM impedance, the energy is then reflected, traveling back to the surface where it is recorded by a receiving antenna (RX). This process is shown on the left side of Figure 2-18 [43]. As shown on the right side of Figure 2-18, when the EM wave energy is recorded at the receiving antenna, it is stored as a digital signal trace plotting amplitude versus time. Kravitz states that the principles for understanding GPR are found in EM wave theory through which EM waves propagate according to the Maxwell equations [44].

Device	Accuracy	Detection Depth	Deterioration Mechanisms Detected	Tunnel Lining Type	Other Information
Air-coupled GPR	Locates defect within 1 ft of its actual location	Does not measure depth, but indicates areas of high moisture or low density (high air voids). Such areas may represent problems within or behind the tunnel lining.	Tile debonding, delaminations, air-filled voids, water-filled voids, moisture intrusion	Concrete, tile-lined concrete, and shotcrete	This is a scanning tool that can indicate where to conduct testing with in-depth devices.
Thermography (handheld thermal camera)	Locates defect within 1 ft of its actual location	Does not measure depth, but can indicate tile debonding, delaminations up to 1 in., and voids up to 3 in.	Tile debonding, delaminations, air-filled voids, water-filled voids, moisture intrusion	Concrete, tile-lined concrete, and shotcrete	This is a scanning tool that can indicate where to conduct testing with in-depth devices.
SPACETEC scanner	Locates defect within 1 ft of its actual location	Does not measure depth, but can indicate tile debonding, possibly delaminations up to 1 in., and possibly voids up to 3 in.	Tile debonding, delaminations, air-filled voids, water-filled voids, moisture intrusion	Concrete, tile-lined concrete, and shotcrete	This is a scanning tool that can indicate where to conduct testing with in-depth devices. Testing can only be conducted through a service contract.
Ground-coupled GPR	Can determine defect depth within 10% of the actual depth without reference cores—5% if cores are available	Can possibly detect defects at any depth within or immediately behind tunnel linings. However, specimen testing indicates it cannot locate 1-sq-ft voids in steel plates behind tunnel linings.	Delaminations, air-filled voids, water-filled voids, moisture intrusion	Concrete, tile-lined concrete, and shotcrete	Experienced personnel are needed to interpret defect locations and depths from the GPR scans. Specimen testing indicates it cannot locate 1-sq-ft voids in steel plates behind tunnel linings.
Ultrasonic tomography	In concrete, can detect voids within 0.5 in., shallow delaminations within 0.75 in. In shotcrete, can detect air-filled voids within 0.7 in., water-filled voids within 1.21 in., shallow delaminations within 1.88 in.	Can detect defects up to 8 in. deep according to specimen tests. Tunnel tests indicate it can detect possible defects up to 20 in. deep.	Delaminations and voids	Concrete, tile-lined concrete, and shotcrete	This device may not be effective for measuring defects that are 2 in. or less from the lining surface. It may not be accurate enough for measuring defect depths in shotcrete.
Ultrasonic echo	Comparable to the ultrasonic tomography system according to tunnel testing with both devices. Can measure tunnel lining thickness within 3% of the actual thickness	Comparable to the ultrasonic tomography system according to tunnel testing with both devices	Delaminations and voids	Concrete and shotcrete	This device may not be effective for measuring defects that are 2 in. or less from the lining surface. It may not be accurate enough for measuring defect depths in shotcrete. Tunnel tests indicate problems with using this device on tiles.
Portable seismic property analyzer (PSPA) ultrasonic surface waves and impact echo	Ultrasonic surface waves: about 15% of the actual depth for defects up to 6 in. deep Impact echo: 10% for deep delaminations greater than 6 in. deep	Ultrasonic surface waves: up to 6 in. deep Impact echo: up to 18 in. deep	Delaminations and voids	Concrete, tile-lined concrete, and shotcrete	Quantifying the depth of defects that are shallow or extensive may be difficult with this device. It may not get good results when testing on very rough concrete surfaces, oily surfaces, and severely curved surfaces.

Figure 2-17: Summary of non-destructive testing techniques [40].

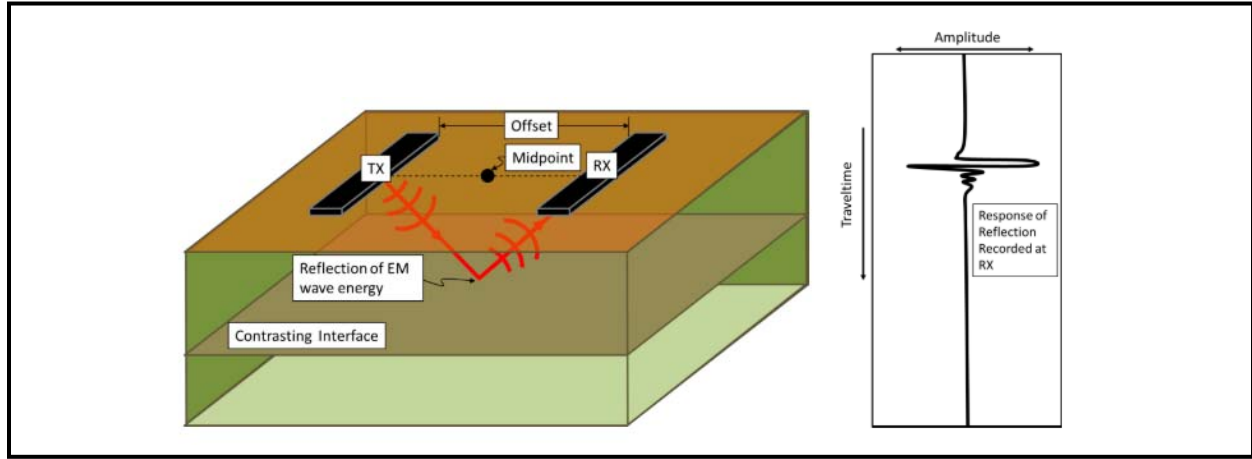


Figure 2-18: Schematic illustrating GPR data collection process [43].

$$\nabla \times e = -\frac{\partial b}{\partial t} \quad (2.18)$$

$$\nabla \times h = j + \frac{\partial d}{\partial t} \quad (2.19)$$

$$\nabla \cdot d = \rho \quad (2.20)$$

$$\nabla \cdot b = 0 \quad (2.21)$$

Where:

e = Electric field strength vector (V/m);
b = Magnetic flux density vector (T);
d = Electric displacement vector (C/m²);
h = Magnetic field intensity (A/m);
j = Electric current density vector (A/m²);
ρ = Electric charge density (C/m²); and
t = Time (s).

The Maxwell equations describe orthogonally oriented changing electric and magnetic fields. The relationship between these equations and material properties describes how EM waves are affected by the material they travel through. Overall, the three material properties to consider during sample analysis are electrical conductivity, dielectric permittivity, and magnetic permeability. Within Kravitz's work, a magnetic permeability of 1 was assumed for the components scanned within tunnel liners, therefore having no effect on the EM wave propagation. From there, effective permittivity and conductivity determines the EM wave velocity, impedance, and attenuation which are all important properties to consider during

analysis of GPR scans. More specifically, these properties effect the return time of a reflected wave off an interface, the amount of energy reflected from that interface, and the amount of energy lost as the wave travels through the material [44]. For reference, dielectric property values of common geomaterials, according to Annan and Soutsos et al, are outlined in Table 2-7 (a) and (b).

Table 2-7(a): Dielectric properties of common geomaterials [44].

Material	ϵ_{eff}	σ_T (mS/m)	u (m/ns)	α (dB/m)
Air	1	0	0.30	0
Distilled water	80	0.01	0.033	2e-3
Fresh water	80	0.5	0.033	0.1
Sea water	80	3000	0.01	103
Dry sand	3-5	0.01	0.15	0.01
Saturated Sand	20-30	1-10	0.06	0.03-0.3
Limestone	4-8	0.5-2	0.12	0.4-1
Shales	5-15	1-100	0.09	1-100

Table 2-7 (b): Dielectric properties of common geomaterials [42].

Material	ϵ_{eff}	σ_T (mS/m)	u (m/ns)	α (dB/m)
Silts	5-30	1-100	0.07	1-100
Clays	5-40	2-1000	0.06	1-300
Granite	4-6	0.01-1	0.13	0.01-1
Dry salt	5-6	0.01-1	0.13	0.01-1
Ice	3-4	0.01	0.16	0.01
Concrete	5-12	0.01-100	0.10	0.01-6

Where:

ϵ_{eff} = Effective permittivity;

σ_T = Conductivity;

u = EM wave velocity; and

α = Attenuation.

According to Alani et al [45], applications of GPR have been used increasingly over recent years by professionals within the fields of Civil Engineering, Geotechnical Engineering, Hydrology, Environmental Science, Geology and more. The non-destructive testing method has proven successful in solving complex engineering and science-based problems within the aforementioned fields of work. More specifically, GPR has been used to successfully monitor bridge decks through identification and integrity assessment of rebar, rebar cover depth, depth of cracks, moisture penetration and delamination, layers of materials within bridge deck, and cavities [45]. A bridge deck was investigated using this method on the Forth Road Bridge in east

central Scotland [45]. The survey was conducted using the RIS HI-Bright Bridge High Resolution Tomography and was performed in an 80 cm (31.5 inch) grid with 10 cm (4 inch) spacing between scans. Alani et al were attempting to gather information regarding thickness of structural layers within the bridge deck, location of shallow utilities and drainage, location and spacing of rebar, and possible moisture penetration and delamination. Surveys were conducted in three different areas on Forth Road Bridge. Alani et al discussed in detail results of processed GPR data in Area 1 as shown in Figure 2-19. The peak curves in the scan show two sets of rebar locations at specific depths as well as an area indicating deterioration due to attenuated amplitude feedback from EM waves. After excavation of the bridge deck, it was confirmed that the deteriorated area had a presence of moisture that penetrated below the upper rebar layer. This deteriorated area is further shown in plan-view sections acquired by the GPR survey in Figure 2-20.

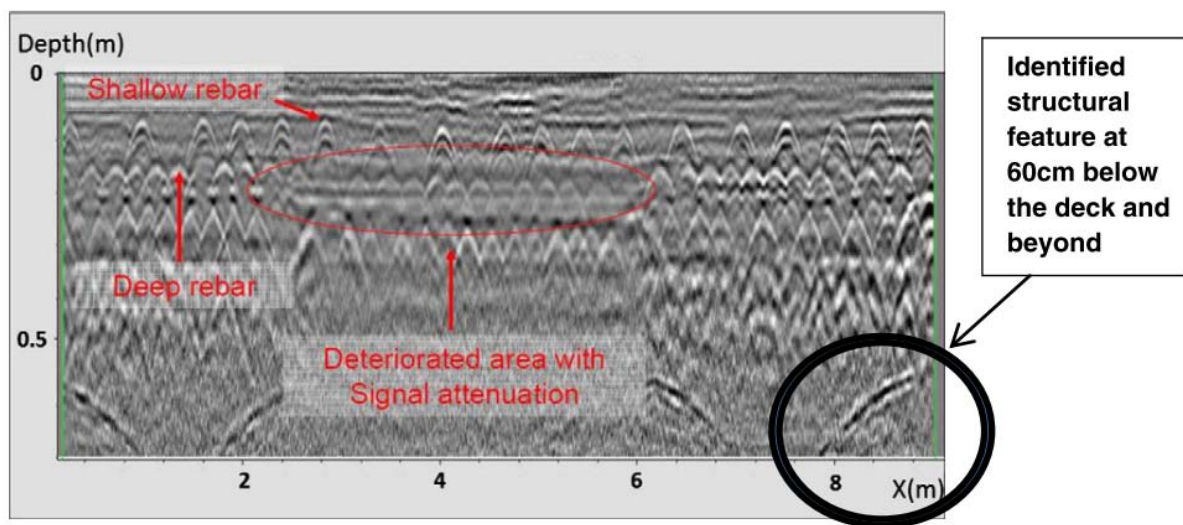


Figure 2-19: Alani et al GPR scan with rebar locations and deteriorated area of bridge deck [45].

The plan-view scans shown in Figure 2-20 indicate that GPR surveys have the ability to identify areas of deterioration, whether it be from moisture content or damage within the substrate. Research conducted by Varnavina et al [46] shows an additional example of bridge deck deterioration below the surface identified by a GPR scan (Figure 2-21). The authors note that the concrete deterioration is identified in the blurred areas of the scan due to an increase in two-way travel time. They also noted that the presence of saline moisture in a concrete bridge deck increases the dielectric constant and conductivity of the concrete. Most importantly, they argued that variations in travel time and signal attenuation are often associated with deterioration or in conditions favorable for the eventual occurrence of deterioration, making it a key characteristic during inspection of GPR processed data.

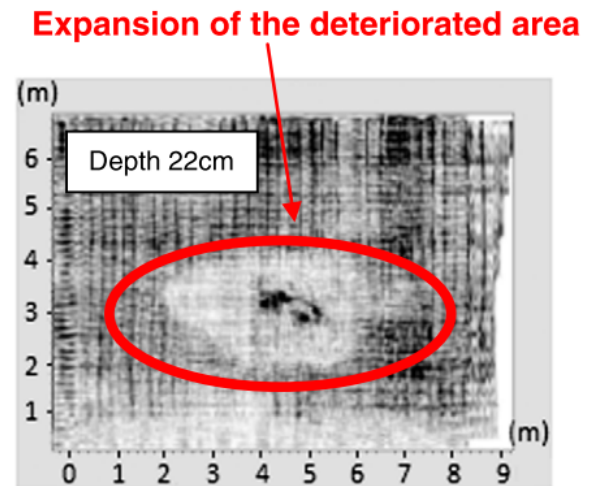
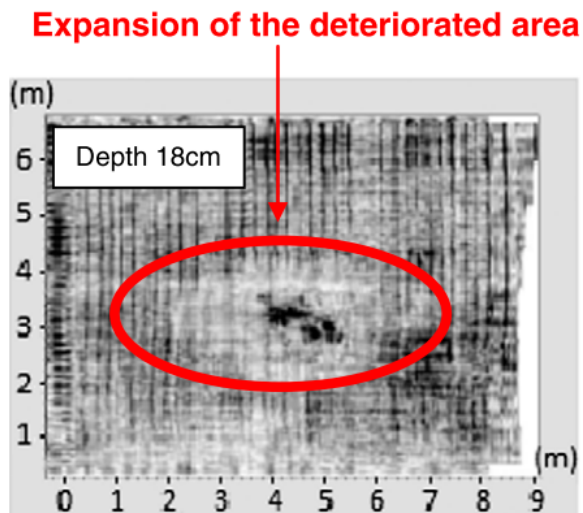
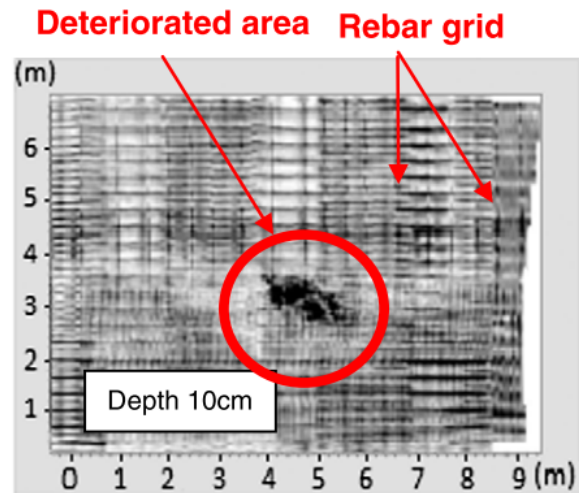
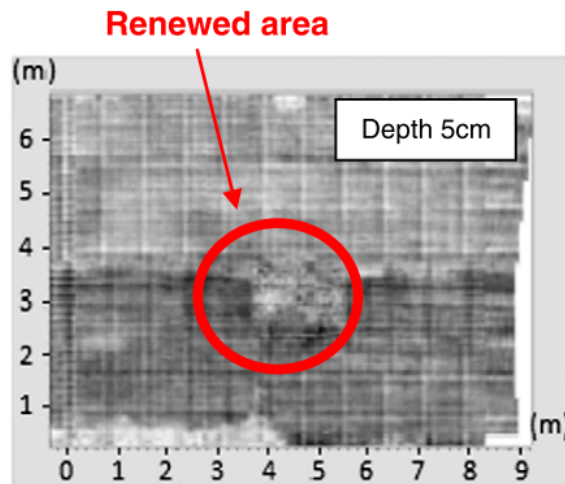


Figure 2-20: Plan-view GPR sections at increasing depths below surface [45].

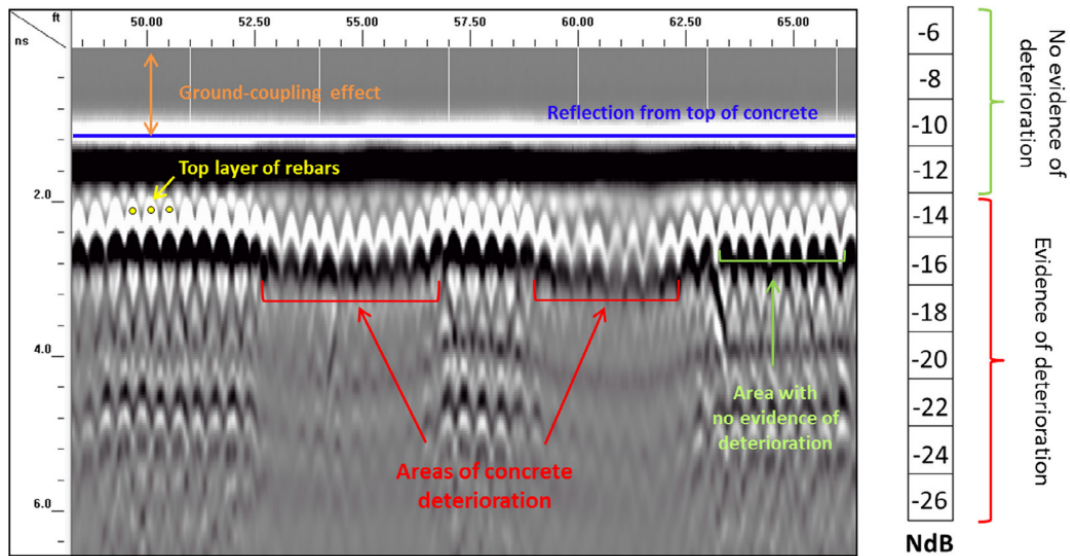


Figure 2-21: GPR scan showing concrete deterioration on bridge deck [46].

Due to the history of GPR use in analysis of integrity and potential defects in bridge decks, it seems prudent to use this NDT method to analyze tunnel/mine drift liners before and after excavation as it is considered to be an effective and efficient tool for analysis of concrete structures. Additionally, data acquired can be analyzed both visually and numerically. Wimsatt et al outline the downsides of using GPR devices as an NDT technique which must be noted while interpreting data. For example, these devices cannot locate 1 square foot voids in steel plates behind structural linings. Additionally, these devices determine defect depth within 10% of the actual depth without reference core samples, meaning that it cannot determine exact location. Most importantly, it is well known that experienced personnel are required to interpret scans acquired from a GPR device [40].

Additional forms of NDT, such as microcomputed tomography (microCT), can be useful in serving as a supplemental form of concrete panel deterioration examination if core samples of the appropriate size are provided. MicroCT is a high resolution form of x-ray computed tomography which is an imaging method that records individual projections from different viewing directions to reconstruct the internal structure of a specific object [47]. This imaging method provides an accurate display of x-ray absorption variation within the studied sample/material. While microCT is often utilized to obtain imaging results with at least 50 to 100 micrometers resolution, the actual desired resolution for a particular sample depends on the microstructural features of interest as well as its shape [47]. According to Nicco [48], there is a trade-off between specimen size and resolution. For example, with a specimen size of 1 to 2 millimeters (0.04 to 0.08 inches) in diameter, the maximum resolution possible with current microCT instrumentation is approximately 0.5 to 1 micrometers. Nicco's dissertation, "Rock Fracturing Under Microwave Irradiation: Development of Analytical Methods and Investigation of the Contribution of Bound Water", demonstrated that this NDT method could be used to characterize cracking induced in granodiorite rock due to microwave irradiation [49].

The success of Nicco's research prompts use of microCT on core samples taken from panels that underwent both impact hammer and waterjet excavation. Use of this method could provide supplemental information that enhances the understanding of substrate damage associated with either excavation tool utilized for shotcrete/concrete removal. Drawbacks associated with the use of microCT for sample analysis are similar to use of GPR in that experienced personnel are required to process data acquired by the equipment. Additionally, use of equipment for this type of investigation is relatively expensive compared to other NDT methods [49].

2.9 Summary

Based on the literature search conducted for this research, the key elements that impact the methodology and objectives include the following:

- Typical liner composition implemented within both the mining and underground construction industries consists of multiple layers of steel reinforced concrete/shotcrete;
- When maintenance and rehabilitation is performed on particular sections of liners, larger areas of defective concrete can be removed either through mechanical impact or by high-pressure water before prepping the surface for a new layer of sprayed concrete;
- The shape of the impact bit, specifically the angle of the wedge, has an influence on depth of penetration and contact stress. It is important to find an optimal wedge angle for the specific material being excavated;
- With issues related to micro-fracturing and loss of structural integrity due to the use of impact hammers, it is important to investigate alternative methods of shotcrete/concrete removal, such as high-pressure waterjet systems;
- The only documented case of waterjets being used for drift/tunnel liner rehabilitation involves a conventional twin orifice rotating, continuous waterjet which selectively removed concrete damaged by a major fire that occurred in the Channel Tunnel linking Britain and France. However, the paper provided no disclosure of operating efficiency, fragmentation dynamics, and other important data through which a quantitative analysis could be made;
- When considering instrumentation of high-pressure waterjet systems, the important design considerations should include not only flow rate, standoff distance, and the dynamics of the jet stream, but also the rock structure, the orientation of impingement, and jet motion. It can be difficult to establish a threshold pressure required to excavate a particular type of rock or concrete due to non-uniform composition between specimens;

- Summers states that the material removal process due to high speed continuous waterjets is controlled by the initial flaws/cracks present within the sample, as these flaws dictate when crack growth occurs, meaning that jet performance will vary between samples;
- Momber states that two types of erosion modes exist during jet impingement of concrete with Type-I erosion occurring in fine grained materials such as the cement matrix between the aggregate and Type-II erosion occurring in areas with coarse grain structure such as a range of aggregates;
- Based on previous empirical studies and equipment availability, the pressure and nominal flow used for this research are approximately 179 MPa (26,000 PSI) and 21.3 lpm (5.6 gpm) respectively;
- Due to the history of GPR use in analysis of integrity and potential defects in bridge decks, it seems prudent to use this NDT method to analyze engineered panels before and after excavation as it is considered to be an effective and efficient tool for analysis of concrete structures; and
- The success of recent research regarding use of microCT to characterize cracking induced in granodiorite rock due to microwave irradiation prompts use of this NDT method on core samples taken from panels that underwent both impact hammer and waterjet excavation. Use of this method could provide supplemental information that enhances the understanding of substrate damage associated with either excavation tool utilized for shotcrete/concrete removal.

These significant findings from the literature search led to the development of the research methodology which is outlined in Chapter 3.

CHAPTER 3 - RESEARCH METHODOLOGY

3.1 Introduction

This analysis is founded on empiric cutting tests performed on engineered and instrumented shotcrete panels designed to quantify vibration and facilitate qualitative comparison of fracture propagation, substrate delamination, and collateral damage associated with the two primary excavation processes. As presented in Chapter 1, the research methodology is comprised into the following tasks:

1. Comprehensive literature review;
2. Established research methodology;
3. Established testing methodology and operating parameters;
4. Laboratory and equipment set-up at EMI and SAI/RAMAX Waterjet Lab;
5. Construction of engineered and instrumented test panels;
6. Development of data acquisition system;
7. Design and assembly of the motion control system;
8. Pre-testing Ground Penetrating Radar (GPR) scanning of test panels;
9. Preliminary testing trials and system modifications;
10. Mechanical impact hammer testing at EMI;
11. Waterjet excavation testing at SAI/RAMAX Waterjet Lab;
12. Post-testing physical inspection of test panels;
13. Post-testing GPR scanning of test panels;
14. Data analysis through visual inspection and sieve analysis of cuttings;
15. Data analysis of vibration during testing for both excavation processes;
16. Data analysis of pre and post testing GPR scans for both excavation processes; and
17. Writing of Final Report, including recommendations for future work.

Under the testing methodology, seven individual composite panels comprised of a steel reinforced concrete substrate with a 10 cm (4 inch) shotcrete layer were developed at the Earth Mechanics Institute (EMI) at the Colorado School of Mines (CSM) in Golden, CO. As part of the research testing plan, six composite panels underwent physical testing; where three of these panels were cut by a twin-orifice, rotating waterjet at the SAI/RAMAX waterjet laboratory in Lancaster, CA and three panels were mechanically excavated by an electric percussive impact hammer at the EMI. One panel was held in reserve for precautionary reasons. For all testing scenarios, the panels were excavated until the tool cut through the entirety of the shotcrete layer, reaching the interface between shotcrete and concrete. Instrumentation of the panels that have been excavated were performed using accelerometers attached to the rebar that reinforced the concrete. Visual fracture/failure examination was conducted on the excavation walls and face, detailing measurement of fractures, delamination, and split aggregate. Non-destructive structural analysis of the panels was performed before and after empiric testing using GPR. GPR data helped visualize differences in substrate damage between each excavation method. For additional fracture analysis, core samples were taken from two panels, one excavated by the

impact hammer and one by the waterjet, and examined using microCT. It is anticipated that the resulting data will service as the foundation for subsequent research activities.

3.2 Experimental Setup

Test panels were designed to simulate a shotcrete tunnel liner and the concrete substrate. Similarly, the design of the test setup attempted to simulate operating conditions that would normally be found in industrial applications. This includes the test panels, the waterjet system, and the manually operated impact hammer. Prior to excavation, all the panels underwent a GPR survey to facilitate comparison. Three panels were mechanically excavated at the EMI using a hand operated electric demolition hammer. Vibration data was taken during excavation. After excavation, these panels were scanned again with GPR and visually inspected for fracture/failure, delamination, and percentage split aggregate at the face. Three additional panels were transported to the SAI/RAMAX waterjet lab, where vibration data was collected during waterjet excavation. Upon completion of testing, each panel was transported back to the EMI for GPR scans and visual inspection performed in the same manner as the panels excavated with the impact hammer. Finally, two 35 mm (1-3/8-inch) core samples were taken from a mechanically excavated panel and a waterjet excavated panel for microCT analysis which aided in visualizing fractures within the substrate due to testing.

3.2.1 Test Panel

The test panels measure 76 cm (30 inches) by 61 cm (24 inches) by 25 cm (10 inches) thick, weighing approximately 227 kilograms (500 pounds) per panel. The concrete substrate is 15 cm (6 inches) thick and reinforced with #3 rebar (0.95 cm or 3/8 inches). The rebar is positioned in the middle of the concrete layer in a cross pattern on 20 cm (8 inch) spacing. Three segments of rebar run along the short-axis and two extend along the long-axis in each sample. The concrete/shotcrete and steel reinforcing materials are housed by a wood panel form. Holes were drilled in the sides of the wooden panel form to hold the rebar at the appropriate location within the panel, 7.6 cm (3 inches) up from the plywood bottom. The rebar was placed in the holes and protruded out of each panel siding to mount the accelerometers for vibration measurements. The concrete is type I/II 31 MPa (4,500 PSI (min)) commercial ready mix with 20 mm (¾ inch) aggregate and 28-day compressive strength of 45.4 MPa (6,590 PSI). The batch had a water to cement ratio of 0.45, slump of 10.2 centimeters (4 inches), air content of 5.7%, was mixed and delivered by a local ready-mix company to the EMI, and was poured in the seven wood panel forms. The concrete mix composition and list of physical properties are found in Appendix B-1. A standard electric vibrator was used on the concrete after it was poured to eliminate the potential for air voids in the batch within each panel. After the concrete cured for four weeks, the shotcrete layer was poured. The shotcrete layer is 10 cm (4 inches) thick with a 4-gauge welded wire mesh positioned 5 cm (2 inches) above the substrate. To facilitate GPR usage and provide uniform shotcrete layering on the test panels, Quikrete sand/topping mix was used as a shotcrete simulant. This was necessary because the size of the test panels did not allow for consistent placement of shotcrete from a pneumatic nozzle.

Quikrete sand/topping mix was deemed appropriate as a shotcrete simulant due to its material properties, fast setting time of 4 to 6 hours, and 28-day compressive strength of 34.5 MPa (5,000 PSI). The texture of the shotcrete simulant is similar to that of shotcrete used for underground structural liners due to the use of ASTM C-33 sand as the aggregate, resulting in a finer cured material with relatively smaller maximum grain size compared to that of the concrete substrate. The material data sheet and particle distribution of un-cured Quikrete sand/topping mix used in this research is provided in Appendix B-1. A water content of 2.8 to 4.3 liters per 60-pound bag was used during mixing. It is important to note that the Quikrete sand/topping mix does differ in that the aggregate is relatively smaller than a typical maximum aggregate size used in shotcrete. As noted in Chapter 2, maximum aggregate size used in a shotcrete mix can reach up to between 10 and 12 mm (0.4 and 0.5 in). The sieve analysis of the Quikrete mix used as a shotcrete simulant in this research had a maximum aggregate size of around 2.5 mm (0.1 in), making it a relatively finer material than shotcrete typically used in underground support liners.

The steel (rebar and wire mesh) placement and density as well as the materials used in the substrate and shotcrete simulant were selected to replicate design parameters consistent with underground support liners. These parameters were reviewed and verified by both a licensed professional structural engineer and an experienced civil contractor. Panel dimensions (in inches) are shown in Figure 3-1 and panel properties are outlined in Table 3-1.

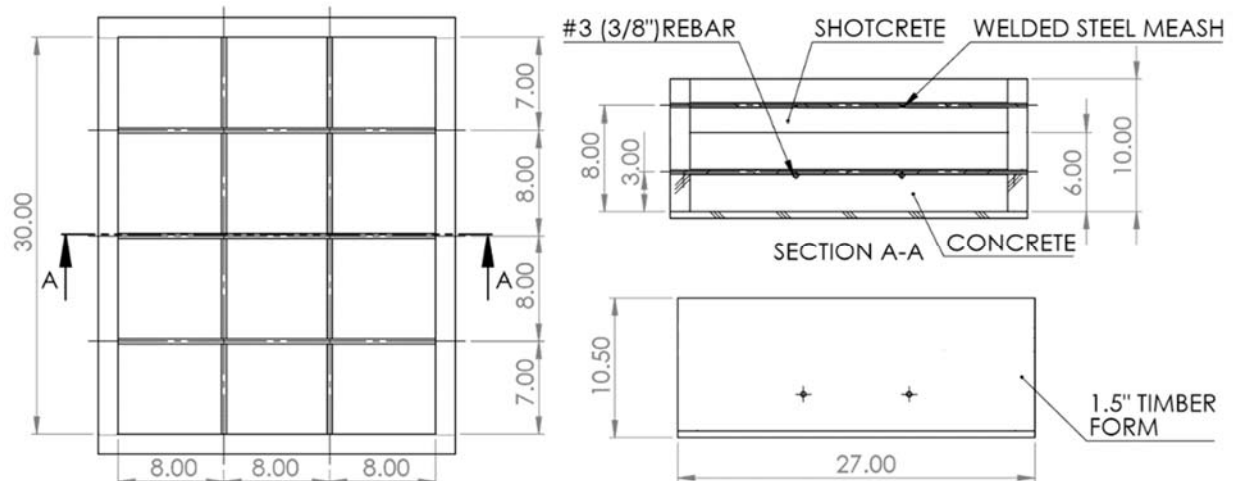


Figure 3-1: Composite panel dimensions (shown in inches) used for experimentation.

Table 3-1: Composite panel properties used for experimentation.

Panel Component	Material Volume, cm³ (in³)	% of Panel
Type I/II 4,500 PSI Concrete	70,553 (4,305.4)	59.8
Quikrete Sand/Topping Mix	47,111 (2,874.9)	39.9
#3 (3/8") Rebar	239 (14.6)	0.2
Welded Steel Mesh	84 (5.1)	0.1
Sum	117,987 (7,200)	100

*Welded steel mesh nominal diameter of 4 gauge – 4.7 mm (0.187")

The panels are designed to facilitate transportation and be forklift compatible. The forms are left in place and wooden rails were added to fit forks and pallet jacks. This allowed lab personnel to easily move the panels as necessary. The wood form provided some protection from shock loadings and damage during transportation and testing.

3.2.2 Mechanical Excavation

Mechanical excavation was conducted at the EMI using an electric rotary hammer. The sample was turned on end, so the exposed concrete face was vertical in order to better simulate repairs to the rib. A Bauer 40 mm (1-9/16-inch) rotary hammer (1643E-B) was used. It was rated at 3,780 beats per minute for impact rate with a force of up to 6.6 foot-pounds per impact. The impact energy associated with this tool is comparable to the hand-held hammers used commercially to manually excavate shotcrete and concrete tunnel liners and is far smaller than the potential impact energy of a hammer attached to the boom of conventional rubber-tired equipment. Therefore, with regards to this research project, the resulting data acquired during empiric testing of the mechanical hammer are representative of hand-held equipment and its associated impact energy. The primary disadvantage of the 1643E-B was thermal limits to its duty cycle. After approximately 15 minutes of operation, the tool became hot and required time to cool. Overall, the excavation time was brief enough that long term tool reliability was not an issue.

Excavation was conducted using a 1-inch (2.54 cm) concrete spade chisel. Bit rotation was disabled to allow for better operator control of the chisel location and orientation and to simulate common repair practice. A rectangular cavity was cut in the center of each panel and excavated to the top of the concrete layer. The process was slow, physically taxing, and extremely labor intensive. When possible, the wire mesh was left intact, although it was often inadvertently damaged by the concrete chisel. The mechanical excavation process is shown in Figure 3-2.



Figure 3-2: Process of mechanical excavation using Bauer impact hammer.

3.2.3 Waterjet Excavation

Waterjet excavation of the panels was conducted at the SAI/RAMAX laboratory near Lancaster, California. The panels that underwent waterjet impingement testing were transported from the EMI to California in an enclosed utility trailer. Panels were placed on a manually operated hydraulic lift. This provided vertical movement of the sample and was utilized to elevate the panel relative to the jet assembly. Horizontal movement during sample cutting was accomplished by an air actuated linear slide. Due to the long air hoses and the compressible nature of air, there was significant dwell time whenever the slide was reversed between passes.

The pressurized flow for waterjet testing was generated by a KOBE high-pressure triplex, positive displacement pump. This pump was a Size-4 model with 180 nominal HP and 15.9 mm (5/8-inch) diameter plungers. It possessed a designed maximum operating pressure of 207 MPa (30,000 PSI) as well as a theoretical fixed displacement of 28.1 lpm (7.4 gpm). The KOBE was powered by a 150 HP electric AC motor. During testing, the system operating pressure was 189.6 MPa (27,500 PSI), which was measured at the pump discharge manifold. Calculations that estimate the energy loss between the pump and the nozzle are presented in Appendix B-2. Due to the occurrence of slippage internally within the pump at pressure, the actual nozzle flow rate during testing was significantly less than the theoretical operating flow rate. It is common for the actual volumetric output of a high-pressure pump to differ from a manufacturer's specifications due to wear and deterioration of dynamic and static seal assemblies and machined components. Empiric testing was previously conducted to determine the pump's true discharge efficiency with accordance to increasing fluid pressure as shown in Table 3-2. To determine the variance in nozzle flow rate empirically, flow meters were used to directly measure fluid pressure and flowrate through the inlet feedline to the pump, low-pressure drains, and discharge lines from the flow controls to the tank and atmosphere.

During operation of the waterjet system for testing, a low-pressure priming pump was used to supply the Kobe pump at a flow rate of 22.8 lpm (6 gpm) at 0.45 MPa (65 PSI). The system also included a 250-gallon water storage tank and inlet line filters. The waterjet system diagram is shown in Figure 3-3.

Table 3-2: Variance in nozzle flow rate due to slippage and leakage through the system's flow controls.

Fluid Pressure (PSI)	Volume Discharge (GPM)	Efficiency (%)
1,000	7.4	100
5,000	7.2	97
10,000	6.8	92
20,000	6.2	84
26,500	5.7	77
28,000	5.6	76
30,000	5.4	73

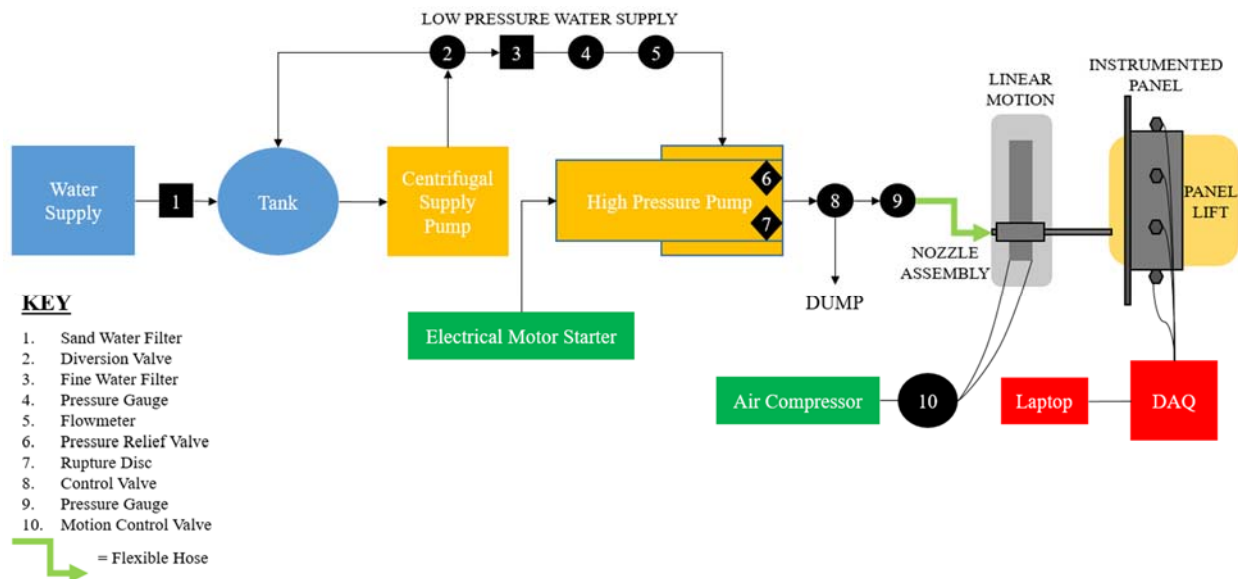


Figure 3-3: Waterjet instrumentation and cutting setup at SAI/RAMAX waterjet laboratory.

The nozzle assembly was connected to the pump accumulator via a 3.7-meter (12-foot) long, 5 mm (0.2-inch) ID, 275.8 MPa (40,000 PSI) high-pressure flexible hose. The system includes a bypass valve at the pump which was designed to regulate flow and pressure. For safety considerations, a pressure relief valve and rupture disc assembly were plumbed into the system.

System pressure was measured using a gauge located at the pump accumulator. On startup, the output from the KOBE pump was dumped at low-pressure. Cutting started when the dump valve was closed, pressurizing the nozzle assembly.

The KOBE pump required an organic lubricant in the form of a soluble gear oil mixture, which was mixed into the water supply (2% by volume). It is assumed that the addition of the oil into the system possessed negligible effects on the thermal and dynamic properties of the fluid, such as intermolecular cohesion, compressibility, and vapor pressure. Physical properties associated with the pumping fluid at 100 degrees Fahrenheit are as follows:

- Weight density of 62.1 lbf/cft
- Kinematic viscosity of 1.50 centistokes
- Vapor pressure of 138.2 lbf/sq.ft
- Surface tension of 0.0048 lbf/ft
- Bulk modulus of 545,000 psi (at 30 KSI)
- Compressibility of $18.35 \times 10^{-7} \text{ psi}^{-1}$
- Acoustic velocity of 6,380 ft/s

A manually operated hydraulic lift was used to prop and orient the test panels in front of the jet for testing. In order for the jet to traverse across the stationary panel, the nozzle assembly was securely fastened to a rigid structure housing a traversing mechanism powered by a compressor. The standoff distance could be manually adjusted by either adjusting the position of the panel or the traverse mount. A standoff distance of 121 nozzle diameters, or 8.9 cm (3.5 inches), was used when initially cutting into a panel. This standoff distance increased as material was removed until reaching the shotcrete/concrete interface, giving a standoff distance range of 121 to 259 nozzle diameters, or 8.9 to 19.1 cm (3.5 to 7.5 inches). The maximum traverse speed achievable by the laboratory setup was 17.8 cm per second (7.0 inches per second).

A twin orifice nozzle rotary head jet system was used for waterjet excavation to create a cutting profile similar to that in literature developed by Momber shown in Figure 3-4 [10]. This rotary system utilized two commercially purchased 0.74 mm (0.029 inch) inner diameter stainless steel AP4 6.4 mm (¼-inch) NPT leach walker type design nozzles with vane flow straighteners. These nozzles were chosen based on their pressure and flow ratings of 151.7 MPa (22,000 PSI) and 12.9 lpm (3.4 gpm) respectively. Both nozzles were placed within a self-rotating swivel tool. All parts for the nozzle system were purchased from StoneAge. Overall, the size and design of the nozzles used for this research was chosen based on convenience and the need to maintain jet stagnation pressures above the threshold pressures of the target material. While there is an increase in friction loss within a twin orifice nozzle rotary head jet system compared to that of a single nozzle jet orifice, the additional surface exposure from the second jet outweighs any inefficiencies due to increased friction to the system.

With regards to the strategy governing the selection of the jet parameters, it is important to reiterate that the purpose of testing was to investigate empirical relationships between the

properties of continuous high-pressure waterjets and the failure mechanisms of shotcrete/concrete upon fluid impingement. More importantly, the intent was not to optimize the material removal process, making it less critical to define parameters that would generate an ideal specific energy for operation. The only parameters of relative significance in this research project were fluid pressure at the nozzle, standoff distance, and nozzle speed through traverse and rotation of the head jet system. All of the chosen operating parameters were based on prior empiric experience through experimentation at the SAI/RAMEX waterjet lab. No parametric testing/analysis was conducted prior to waterjet excavation of the engineered panels. Overall, it was important to ensure that the fluid pressure at the nozzle was well above the threshold pressure of the target material, based on previous cutting tests identified for concrete in the literature search, and that the standoff distance kept the target material within the core jet zone during initial impingement. A summary of operating parameters used during continuous waterjet impingement on the test panels is outlined in Table 3-3. These parameters were first used to cut the shotcrete layer in Panel TEST in order to determine if any changes needed to be made. Once this process was found to be successful with the original chosen operating parameters, cutting resumed for the remaining panels. Cutting operations at the SAI/RAMEX waterjet lab are shown in Figure 3-5. During the Summer of 2018, the Kobe pump cracked a piston while cutting the 3rd panel, so waterjet cutting was stopped prematurely. The pump was repaired in Fall 2019 for further experimentation.

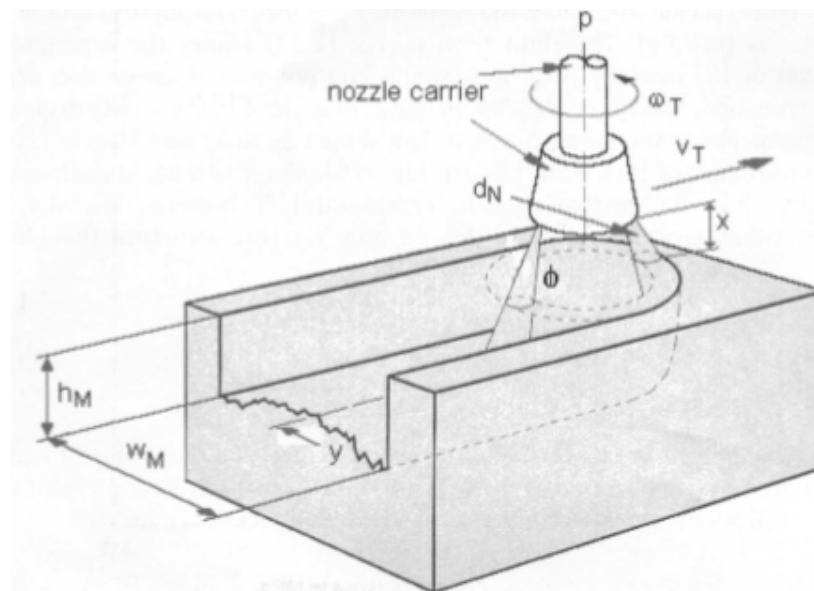


Figure 3-4: Target parameters associated with a twin orifice nozzle rotary head jet system [10].

Table 3-3: Continuous waterjet testing parameters.

Jet Parameter	Value	Units
Fluid Pressure at Pump	189.6 (27,500)	MPa (PSI)
Fluid Pressure at Nozzle	179.0 (25,966)	Mpa (PSI)
System Pressure Loss	10.6 (1,534)	Mpa (PSI)
Pump Flow	21.2 (5.6)	LPM (GPM)
Nozzle Diameter	0.74 (0.029)	mm (in)
Nozzle Exit Velocity	539 (1,768)	m/s (ft/s)
Standoff Distance	88.9 – 190.5 (3.5 – 7.5)	mm (in)
Traverse Rate	25.4 – 152.4 (1.0 – 6.0)	mm/s (in/s)
Impingement Angle	10	deg
Rotation of Nozzle Assembly	300	RPM



Figure 3-5: Waterjet excavation – SAI/RAMAX Laboratory set-up (upper left) start of slot in panel (upper right) kerf in panel (bottom left) close-up of kerf in panel (bottom right).

3.2.4 Vibration Data Acquisition

The data acquisition system (DAQ) recorded vibration readings from seven accelerometers. The accelerometers were mounted on the exposed ends of the rebar in the test panels. A USB DAQ and LabVIEW were used to process and save the collected data to a laptop. The accelerometers used were a prosumer product from Sparkfun, the ADXL337 which is shown in Figure 3-6. The ADXL337 is a triple axis analog accelerometer with a range of ± 200 G. The X, Y, Z, ground and +3.3 V connections were soldered to the wiring harness. The ground and +3.3 V were supplied by the National Instruments USB-6211 DAQ. The Z axis and the X axis were used on each accelerometer due to the limited number of analog channels available. The Z axis was normal to the sample surface with +Z pointing towards the excavation equipment. The X axis ran parallel to the edge of the sample.



Figure 3-6: Accelerometer mount (left) and ADXL337 (right).

The accelerometers were mounted in enclosed 3D printed ABS sensor mounts (Figure 3-6). The ADXL337 was attached to the accelerometer mount by four screws. A cutaway was left in the base of the sensor mount for the wiring harness. The sensor mounts were pressed onto the rebar. To ensure a tight fit, the rebar was wrapped with electrical tape. The hexagonal tops of the sensor mounts were parallel to the surface of the panel. Seven sensor mounts were used during testing. These were arranged in a counter clockwise pattern around the sample starting with accelerometer 1 on the bottom right rebar end. There were three accelerometers on the right side of the sample, two on the top of the sample, and two on the left side of the sample. The sensor arrangement is shown in Figure 3-7.

The accelerometers were connected to the DAQ by CAT5 and CAT7 cables. CAT5 cable was soldered to the accelerometers. This was then spliced into a shielded CAT7 cable. The wiring harness for each accelerometer ran to a terminal block for the signal channels busses for +3.3 V and the ground. CAT7 cable provides four twisted pairs. The temperature and 3rd axis channels were not used so the +3.3 V, ground, and the two used signal channels ran on their own twisted

pair. All wiring between the terminal block and the DAQ was done with shielded CAT7 cable. Early prototypes used unshielded cables and had cross talk noise equivalent to ± 20 G.

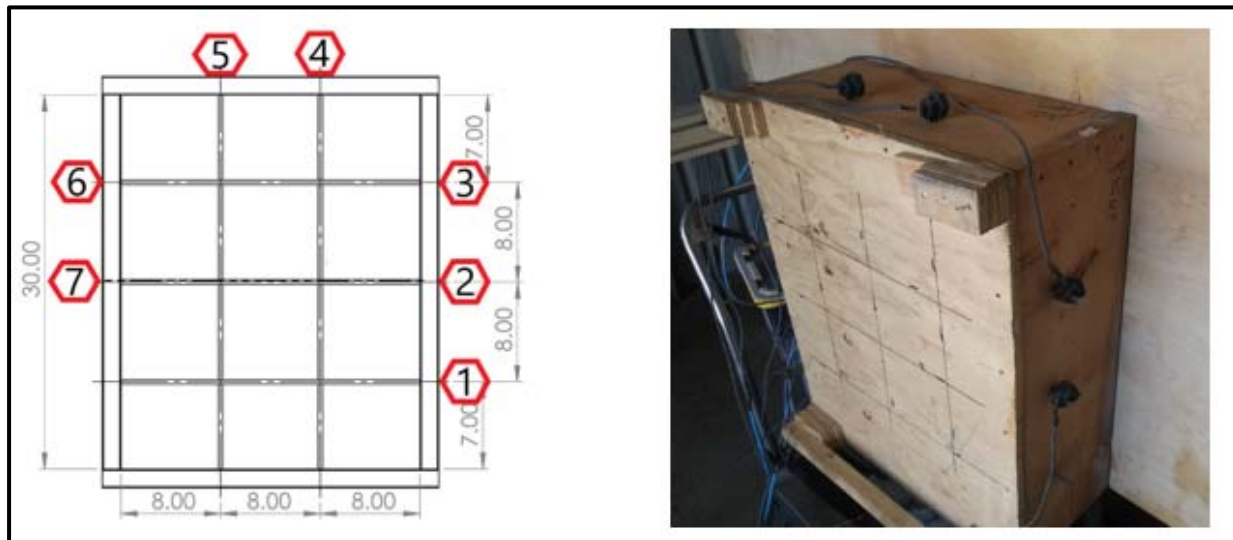


Figure 3-7: Accelerometer locations (left) accelerometers on actual panel (right).

A National Instruments USB-6211 DAQ was used to read the analog signals from the accelerometers. This DAQ supported sixteen analog channels. Fourteen of the channels were used for accelerometer data, one was used to monitor the accelerometer power supply voltage, and the remaining analog channel was not used. The specified maximum impact rate of the Bauer rotary hammer (1643E-B) was 3900 impacts per minute (65 HZ). Thermal and operating considerations lead to the hammer being operated at frequencies well below the maximum (below 50 HZ).

The sample rate of the DAQ was 100 HZ which translates to a recorded reading for each accelerometer in the X and Z direction every 0.01 seconds. This was sufficient to exceed the Nyquist frequency of the hammer at plausible operating conditions. Due to the recording sample rate, most cutting runs lasted approximately 210 seconds at which point recording stopped and the values for the readings per every 0.01 second were output in excel format. With this time constraint per run in the DAQ, each panel required multiple testing runs in order to excavate through the entirety of the shotcrete layer until reaching the shotcrete/concrete interface. For example, it took seven runs to reach the shotcrete/concrete interface in Panel 2, which was excavated using the impact hammer. It is possible that some peaks were missed or underestimated due to the sample rate.

The signal from the ADXL337 accelerometers had noise that typically ranged from 0.25 G to 0.5 G. This slightly exceeds the specification but was negligible when compared to mechanical

cutting (some readings in excess of 100 G). In some waterjet cuts, the vibrations from cutting were indistinguishable from ± 0.5 G noise. During waterjet cutting, the sensor mounts were shielded with a plywood fence to prevent spray and mist from infiltrating the pods. The DAQ board was in a water-resistant box. Despite these precautions, water still damaged the USB cable to the computer and one of the accelerometer wiring harnesses. The wet joints resulted in voltage drift of $\frac{1}{2}$ G to 1 G in several runs. Once detected, wet connections were dried and repaired.

The data acquisition program was written in LabVIEW. The virtual instrument (VI) read the analog voltages from the accelerometers as shown in Figure 3-8. The voltage data was then converted into acceleration by the VI. Each accelerometer channel had to be individually calibrated inside the VI. The 0 G voltage was the primary calibration variable changed. While running, the VI graphed the output of every accelerometer for calibration purposes.

The accelerometers were calibrated to near zero for every test period. The VI wrote its collected data to disk every 30 seconds to prevent loss in the event of a system crash. The data from each cut was saved as an Excel file. The data files were post processed in Excel and MATLAB. The average acceleration of each channel was found and used as 0 since field calibration was only accurate to ± 0.5 G.

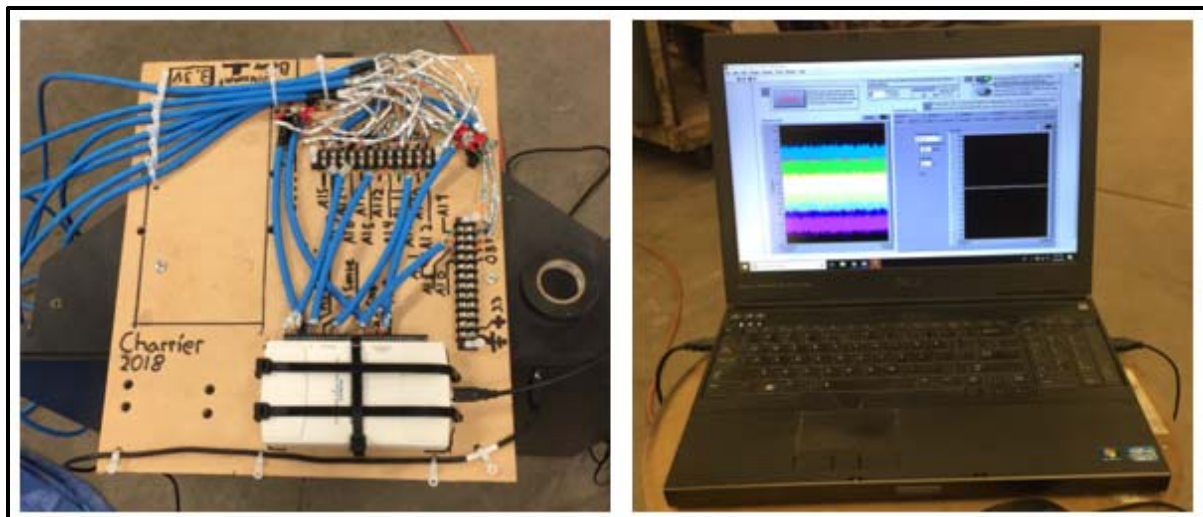


Figure 3-8: Data acquisition setup.

3.2.5 Visual Inspection and Examination of Cuttings

Visual inspection was performed after excavation was completed on each panel. This process was accomplished in sections to analyze the entirety of the excavation profile including the left, upper, right, and bottom walls, as well as the face where exposed aggregate was located. Before inspection took place, each panel's excavation profile was rinsed thoroughly with water

to provide a clean, wet surface which aided in fracture/failure visibility to the naked eye. When each section was examined, areas of fracture/failure were noted. These areas either had a single fracture or a network of failure which were manually measured in millimeters using measuring tape. All of these areas were identified, measured, and summarized for each excavation section. Figure 3-9 gives an example of a specific section analyzed in Panel 2, which was tested upon using the impact hammer.

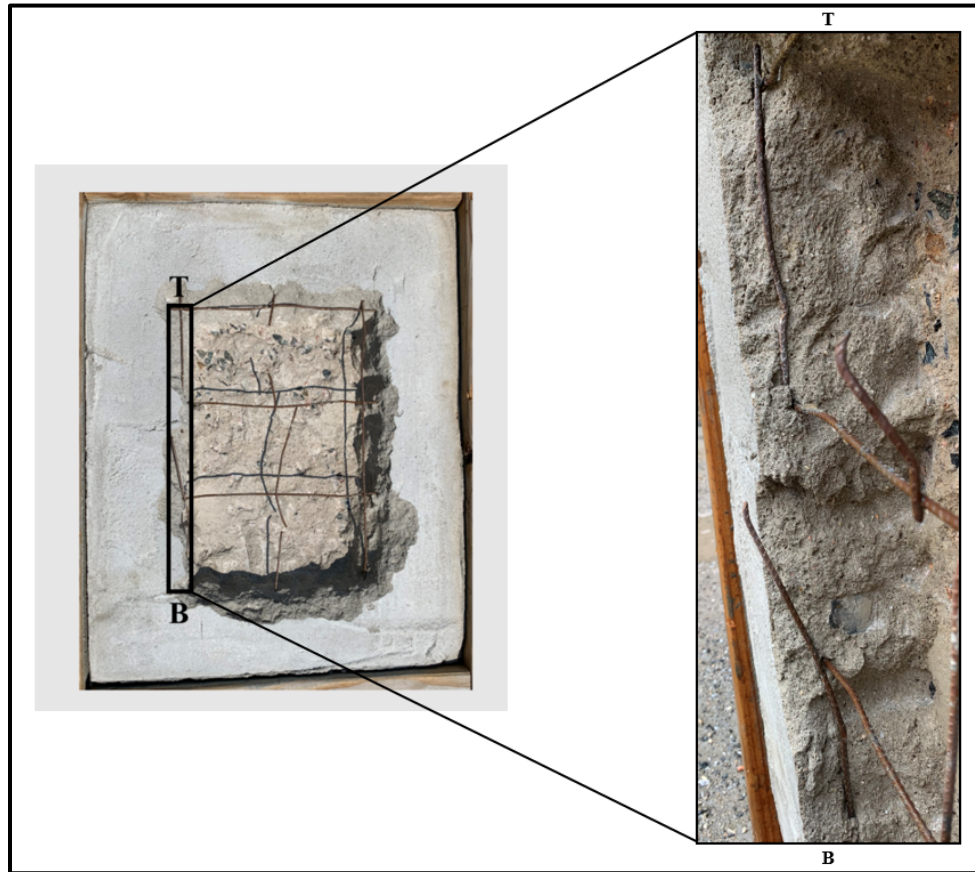


Figure 3-9: Example of visual inspection scenario for left face of panel 2.

During inspection of a particular section, if damage to wire mesh was present, it was noted for final comparison between each testing method. Delamination was also measured in millimeters if it was present in the analyzed division of the excavation profile. Finally, for the face section, split aggregate was counted and divided by the total exposed aggregate to give a percentage of split aggregate at the face due to testing as shown in Equation 3.1.

$$P_{SpA} = \frac{N_{SpA}}{N_A} \times 100 \quad (3.1)$$

Where:

P_{SpA} = Percent split, exposed aggregate on excavation face;

N_{SpA} = Number of split, exposed aggregate on excavation face; and

N_A = Total number of exposed aggregate on excavation face.

Shotcrete simulant cuttings were collected during testing on all panels for examination. Impact hammer cuttings were analyzed at the EMI through three 500-gram (1.1 pound) samples which were poured through a sieve set of 48, 28, 14, 8, and 4 Tyler mesh with additional 12.7 mm (½ inch) and 25.4 mm (1 inch) mesh sieves for larger chip sizes. For each impact hammer sample, the sieve set was placed into a Model RX-29 Tyler sieve shaker, as shown in Figure 3-10, for dry screening, running for 15 minutes, after which each sieve was weighed and recorded. These recorded weights were used to generate a plot for cumulative percentage retained according to each sieve size. Waterjet cuttings were analyzed at the SAI/RAMAX laboratory through measurement of grains collected during testing. Due to the nature of waterjet testing, not all of the generated cuttings could be contained, resulting in a smaller sample size compared to that of impact hammer testing.



Figure 3-10: Model RX-29 Tyler sieve shaker used for sieve analysis of impact hammer cuttings.

3.2.6 Ground Penetrating Radar

GPR was used to perform non-destructive inspection of the panels before and after testing. This inspection includes analysis of rebar and wire mesh location, fractures and voids within the substrate and shotcrete simulant, moisture penetration, and possible delamination between the substrate and shotcrete simulant due to mechanical/waterjet impact. The GPR

system gathered real-time non-destructive testing data in the form of DZT files. The data was collected using two GPR systems, a 2600 MHz radar antenna coupled with a SIR 3000 radar system control unit and a 1600 MHz radar antenna coupled with a SIR 4000 radar system control unit (Figure 3-11). Both sets of equipment were rented from Exploration Instruments, LLC, a geophysical instrumentation company located in Austin, TX. Parameters of the concrete samples, specifically through approximate ten-inch thickness and concrete/shotcrete material composition, led to selection of the 2600 and 1600 MHz radar antennas.



Figure 3-11: 2600 MHz radar antenna connected to SIR 3000 radar system control unit (left) 1600 MHz radar antenna coupled with SIR 4000 radar system control unit.

These particular antennas are typically used to inspect concrete structures, as well as locate embedded rebar, which fits with the specifications of the test samples. In general, the higher the antenna frequency, the shallower the penetration depth and the greater the resolution. In this case, the 2600 MHz system provided a higher resolution basis of knowledge to determine any pre-existing voids or deficiencies within the panels and identify key differences in components due to excavation. The 1600 MHz system provided a lower resolution analysis of key differences in panel composition due to excavation. In the end, the use of two GPR systems proved to be a benefit in that they provided a comparative analysis between different GPR operating systems for assessing the support liner.

Equipment specifications for the 2600 MHz radar antenna include a center frequency of 2600 MHz, a depth range of 0 to 30.5 cm (0 to 12 inches), and a weight of 1.8 kilograms (4 pounds) [59]. Equipment specifications for the 1600 MHz radar antenna include a center frequency of 1600 MHz, a depth range of 0 to 45.7 centimeters (0 to 18 inches), and a weight of 1.8 kilograms (4 pounds) [60]. Before conducting any scans, the input parameters in Table 3-4 and Table 3-5 were selected within the SIR 3000 and SIR 4000 control units respectively. No filters were used for control unit setup. These parameters were selected based on consultation from Mr. Roy Bowling, Geophysical Engineer for Collier Consulting, for a 25.4 cm (10 inch) thick concrete/shotcrete sample with embedded wire mesh and rebar. A scanning grid criterion was developed for each sample based on the width dimension of the radar antenna. The radar antenna rolling chassis has a width of 17.8 cm (7 inches), making this the dimension appropriate

for the grid spacing chosen. The samples were scanned on the top shotcrete face, the front timber form face, the right timber form face, the left timber form face, the back-timber form face, and the bottom plywood/concrete face. Examples of these faces with drawn grid lines for the top shotcrete face and bottom plywood/concrete face is shown in Figure 3-12.

Table 3-4: SIR 3000 control unit input parameters.

<i>Input Category</i>	<i>Input Sub-Category</i>	<i>Input Parameter</i>	<i>Value</i>	<i>Unit</i>
COLLECT	RADAR	ANTENNA	2.6	GHz
		T_RATE	100	kHz
		MODE	Distance	
		GPS	None	
	SCAN	SAMPLES	2048	
		FORMAT	16	Bits
		RANGE	10	nS
		DIEL	6.25	
		RATE	32	
		SCN/UNIT	4	
		GAIN	0	dB
	GAIN	SETTING	Auto	
		POINTS	3	
	POSITION	SETTING	Manual	
		OFFSET	10.87	
		SURFACE	10.00	%

Table 3-5: SIR 4000 control unit input parameters.

<i>Input Category</i>	<i>Input Sub-Category</i>	<i>Input Parameter</i>	<i>Value</i>	<i>Unit</i>
COLLECT	RADAR	ANTENNA	1.6	GHz
		T_RATE	100	kHz
		MODE	Distance	
		GPS	None	
	SCAN	SAMPLES	2048	
		FORMAT	16	Bits
		RANGE	10	nS
		DIEL	6.4	
		RATE	47	
		SCN/UNIT	4	
		GAIN	0	dB
	GAIN	SETTING	Manual	
		POINTS	3	
	POSITION	SETTING	Manual	
		OFFSET	12.18	
		SURFACE	10.00	%

Each sample followed the same scanning procedure. For the top shotcrete face, the radar antenna started on the bottom left corner, as shown in Figure 3-12, and took scans from bottom to top. Once a scan was completed, the radar antenna would move to the next grid space to the right and take the next scan. The top shotcrete face had room for three full width grid spaces, followed by a remaining space that did not reach full width. When the radar antenna would reach this 4th smaller grid space, the right wheels would be moved to the shotcrete edge, meeting the timber form, and a bottom to top scan would be taken from there. The radar antenna would then be moved to the bottom right corner of the top face and face left, taking scans from right to left for four full grid widths. This scan sequencing is shown in Figure 3-13. The direction of the single scan taken at each sample's front, right, left and back face is shown.

For the front, right, left and back timber form face, a single scan was taken by lining up the wheels with the top edge of the wood form and moving in the direction indicated above. For the bottom plywood/concrete face, the scan sequencing is similar to that of the top shotcrete face. However, the sizing of the wooden form allowed for four even scans both bottom to top and right to left, as shown in Figure 3-14. The scanning procedures described were intended to gather data for each sample before mechanical and waterjet testing took place. This would establish a baseline for wire mesh and rebar location within each sample, as well as any pre-existing voids that were a result of the mix composition and casting process. After mechanical and waterjet testing took place, the scanning procedures for front face, right face, left face, back face and bottom plywood/concrete plan face were performed again to gather data representing each sample after mechanical/waterjet impact.

Scans collected by the radar antenna were stored in the control unit as DZT files and named in the order in which they were taken (File___001, File___002, etc.). During testing, each file name was matched with its particular sample sequence number. After testing, each file was collected on a USB from the control unit, and transferred to a computer. The software program GPR Mapper [61], which operates through MATLAB, was used for 2D data interpretation of GPR scans while OpendTect was used for 3D visual analysis. A model of each tested panel was developed in AutoCAD to provide figures of section plane views depicting the panel components and excavated profile that each GPR scan was recording.



Figure 3-12: Top shotcrete face with GPR gridlines (top left) back timber form face to receive one GPR scan (top right) front timber form face to receive one GPR scan (bottom left) bottom plywood/concrete face with GPR gridlines (bottom right).

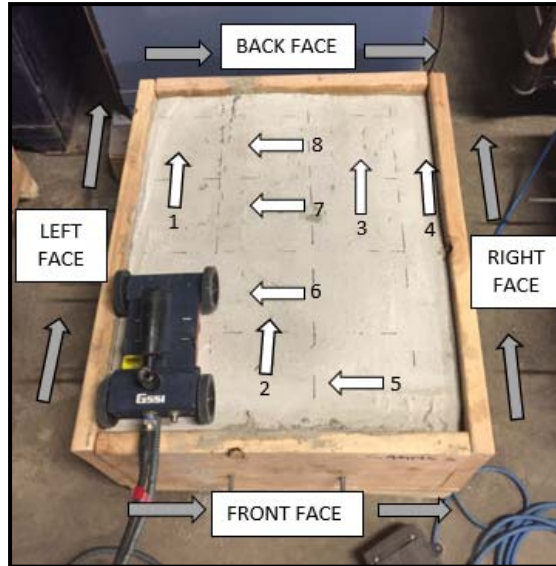


Figure 3-13: GPR scan sequencing for top shotcrete face along with directions of single scan for sample's front, right, left, and back-timber form face.



Figure 3-14: GPR scan sequencing for bottom plywood/concrete plan face.

3.2.7 Coring and Microcomputed Tomography

MicroCT was used to perform non-destructive inspection of cores taken from two panels after testing. This inspection includes analysis of micro-fractures present in the core samples due to each excavation method. Two cores were taken from a panel excavated by impact hammer, as well as a panel excavated by waterjet to give a total of four cores for analysis. Panel 4 and Panel 7 were chosen to be the representative panels for coring as shown in Figure 3-15. The two

black “X” marks indicate the proposed locations for potential micro-fracture examination. A forklift was utilized to lift the core drill above each sample to drill into the panels. For each panel, one core sample was taken from the excavation face, directly under where testing occurred, and a second core sample was taken just outside the excavation profile to investigate whether or not significant collateral damage occurred due to the testing method. For fair examination, the first core samples were taken in approximately the same location on each panel’s excavation face and the second core samples for each panel were both taken 38.1 millimeters (1.5 inches) outside the excavation profile. Table 3-6 gives the measured locations of each core for Panels 4 and 7. It’s important to note that the actual locations of each core differed slightly to the proposed locations due to avoidance of steel reinforcement (wire mesh and rebar) as well as human error through misalignment during operation of the forklift.

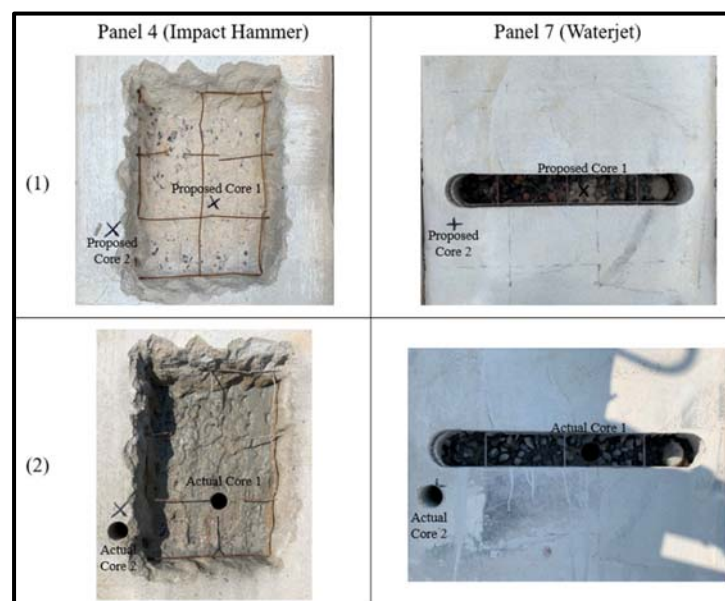


Figure 3-15: Coring process showing (1) proposed locations of cores and (2) actual locations of cores.

A Milwaukee 4094 dymodrill was used with a 41.3 mm (1-5/8-inch) diamond core bit as shown in Figure 3-16. This provided 35 mm (1-3/8-inch) core samples for microCT analysis. Each core was taken until the bit reached the plywood bottom of the panel, at which point, the bit retreated and the samples were removed. All four cores, as well as their associated lengths, are shown in Figure 3-17. In order to fit into the microCT scanner, each core had to be cut into 76 mm (3 inch) long segments using a continuous rim circular diamond saw blade.

Table 3-6: Proposed and actual core locations on panel 4 and panel 7.

		Panel 4	Panel 7
Proposed Core 1	X direction (from bottom right corner of panel plan view)	-317.5 mm (-12.5 in)	-317.5 mm (-12.5 in)
	Y direction (from bottom right corner of panel plan view)	370.8 mm (14.6 in)	370.8 mm (14.6 in)
Proposed Core 2	X direction (from bottom left corner of panel plan view)	139.7 mm (5.5 in)	101.6 mm (4 in)
	Y direction (from bottom left corner of panel plan view)	304.8 mm (12 in)	304.8 mm (12 in)
Actual Core 1	X direction (from bottom right corner of panel plan view)	-330.2 mm (-13 in)	-298.5 mm (-11.75 in)
	Y direction (from bottom right corner of panel plan view)	336.6 mm (13.25 in)	368.3 mm (14.5 in)
Actual Core 2	X direction (from bottom left corner of panel plan view)	142.2 mm (5.6 in)	91.4 mm (3.6 in)
	Y direction (from bottom left corner of panel plan view)	260.4 mm (10.25 in)	287.0 mm (11.3 in)

The scanner used for microCT analysis was a MicroXCT-400, as shown in Figure 3-18, operated by the Department of Geophysics at CSM. Each 76 mm (3 inch) long core sample required approximately 45 minutes of preparation through alignment onto the platform within the MicroXCT-400, as well as three hours to complete a full scan. The process of acquiring a microCT scan is shown in Figure 3-19. Through consultation with Kurt Livo, a graduate student at CSM who operates the scanning equipment within the Department of Geophysics, a resolution of approximately 25 microns was utilized for analysis of the 35 mm (1-3/8-inch) diameter cores with a step size of 0.1 degrees. This resolution was deemed appropriate due to the intention of the scans, which was to identify fractures due to testing. Due to availability of the scanning equipment within the Department of Geophysics, only Core 1 from Panel 7 and Panel 4 were examined while Core 2 from both panels were held in reserve for future research.



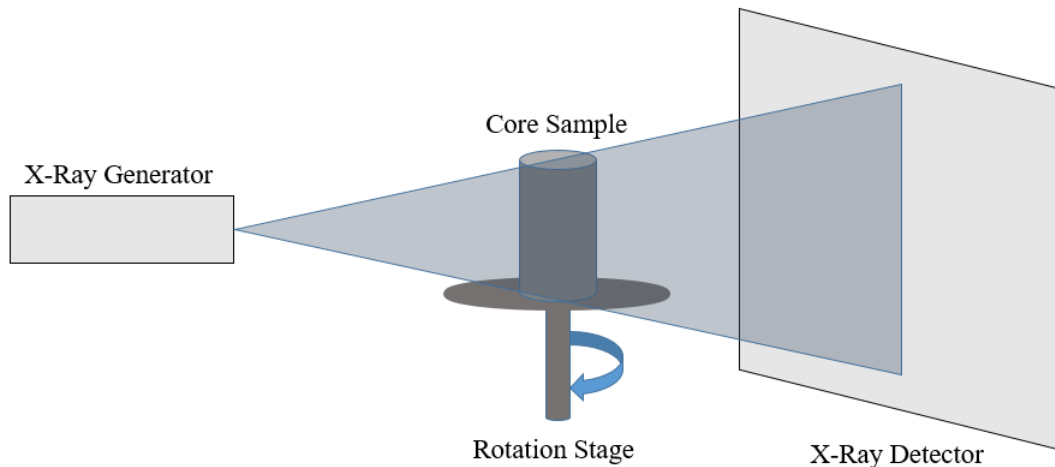
Figure 3-16: Core drill and bit set-up with forklift at EMI.



Figure 3-17: Cores and their respective lengths. Lettering “T” indicates the top of the core while “B” indicates the bottom of the core.



Figure 3-18: MicroXCT-400 equipment used for microCT analysis of core segments.



Process of Acquiring MicroCT Scan

1. X-rays are transmitted through sample
2. X-rays are recorded by the detector as 2D projection image
3. Sample is rotated a fraction of a degree
4. Repeat steps 1 through 3 until rotated 360 degrees
5. 2D projection images are reconstructed into cross sectional images of sample

Figure 3-19: Process of acquiring a microCT scan.

Scanning Core 1 from both panels allowed for investigation of the concrete substrate directly beneath where excavation occurred. Since these cores were cut into 76 millimeter (3 inch) long segments, four cores (two for Core 1 of Panel 7 and two for Core 1 of Panel 4) underwent examination after being labeled accordingly to designate proper orientation. The MicroXCT-400 operated under the following scanning resolutions for each core segment:

- 26.75 μm for top half of Core 1, Panel 4
- 28.02 μm for bottom half of Core 1, Panel 4
- 27.50 μm for top half of Core 1, Panel 7
- 28.27 μm for bottom half of Core 1, Panel 7

During operation, the MicroXCT-400 would output cross sectional images of the core in resolution size increments as TIF files. The nature of the X-ray imaging process led to chosen focus areas shown in Figure 3-20. Table 3-7 provides measurements for the designated areas of analysis for each core. The same focus zone locations were chosen for Core 1 of each panel to provide fair comparison of the internal structure of the substrate generated by each testing method.

Table 3-7: Measurements for designated scan area for each core sample.

	Total Length of Core Sample, mm (inches)	Scanning Resolution Used for Core Sample (μm)	Number of Cross-Sectional Images Generated	Total Length of Reconstruction Imaging Focus Area, mm (inches)	Midpoint of Reconstruction Imaging from Core Sample Bottom, mm (inches)
Core 1 Panel 7 Top Half	76.2 (3.0)	26.75	507	13.6 (0.5)	31.8 (1.3)
Core 1 Panel 7 Bottom Half	73.0 (2.9)	28.02	507	14.2 (0.6)	54.0 (2.1)
Core 1 Panel 4 Top Half	73.0 (2.9)	27.50	507	13.9 (0.5)	38.1 (1.5)
Core 1 Panel 4 Bottom Half	76.2 (3.0)	28.27	507	14.3 (0.6)	57.2 (2.3)

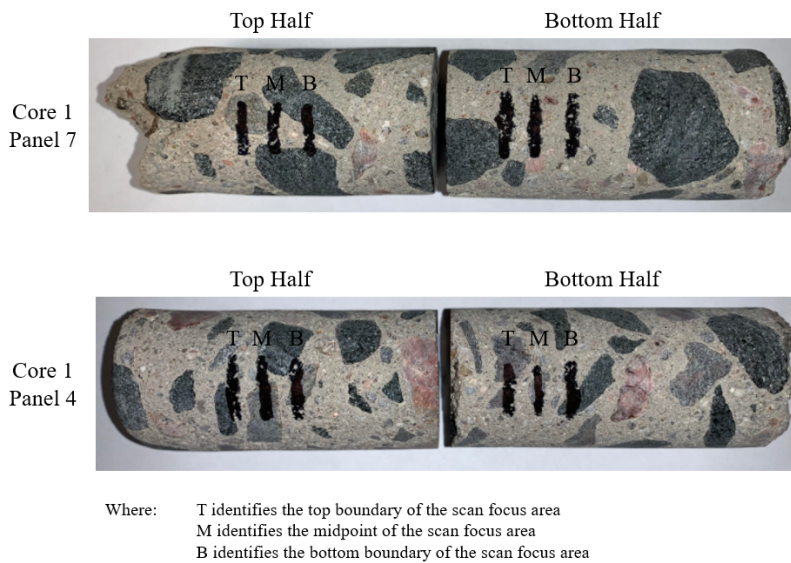


Figure 3-20: Location of focus areas for microCT scans of each core sample.

Therefore, through the chosen focus areas, these four core samples allowed for examination of ranges 28 to 51 mm (1.1 to 2 inches) and 85 to 102 mm (3.3 to 4 inches) below the shotcrete/concrete interface. During scanning, each file name was matched with its particular core label identification marked on the smooth cut surface. Each batch of TIF files according to the core sample were then collected on a USB memory stick from the control unit, and transferred to a computer for analysis.

CHAPTER 4 - TESTING RESULTS WITH RAW AND PROCESSED DATA

4.1 Introduction

This chapter covers results of the data collected during testing outlined in the Research Methodology as well as an analysis of raw and processed data. These results and analysis are broken into four sections according to Table 4-1, covering investigation of waterjet system operating parameters necessary to cut the shotcrete layer, investigation of fracture mechanisms imposed by the waterjet system to cut the shotcrete layer, verification that waterjets can successfully be used as an alternative shotcrete removal tool, and validation of the hypothesis that waterjet removal of concrete/shotcrete liners will result in less collateral damage than conventional methods. Findings of raw and processed data are briefly covered while a more detailed analysis of the significance behind acquired data with relation to the research objectives is discussed in Chapter 5. For clarification purposes, the designed panels along with their testing method are shown in Table 4-1.

Table 4-1: Panel number and associated testing method.

Panel	Testing Method
2	Impact Hammer
3	Impact Hammer
4	Impact Hammer
1	Waterjet
7	Waterjet
TEST	Waterjet

Note: One of the panels is named “TEST” due to it being the first panel completed with the particular specifications outlined in the Research Methodology for waterjet testing.

4.2 Investigation of Waterjet System Operating Parameters Necessary to Cut Shotcrete Layer

The waterjet system operating parameters used to cut the shotcrete layer were documented during empiric testing at the SAI/RAMAX laboratory near Lancaster, California. This section covers how variations in operating parameters caused changes in the cutting behavior within the shotcrete layer. In addition, the waterjet cutting process is compared to the excavation process followed using the manual impact hammer.

4.2.1 Changes in Waterjet System Operating Parameters During Testing

Waterjet excavation was completed on three of the developed panels. As stated in the Research Methodology, testing was conducted in a manner that required multiple runs to excavate the entirety of the shotcrete layer to reach the shotcrete/concrete interface. Notes

were taken during every testing run for each panel in order to document how adjustments in parameters caused changes in cutting behavior through the shotcrete layer. Throughout the entirety of waterjet operation, the 150 HP primary pump consistently operated at 189.6 MPa (27,500 PSI), which was measured at the pump discharge manifold, with a flow rate of 21.3 lpm (5.6 gpm). Additionally, a low-pressure priming pump was used to supply the primary pump at a flow rate of 22.8 lpm (6 gpm) at 0.45 MPa (65 PSI). Upon every startup, the output from the primary pump was dumped at low-pressure and cutting started when the dump valve was closed, pressurizing the nozzle assembly. Table 4-2 shows the notes taken during every run of each panel excavated using the waterjet system.

As previously stated, the intent of this research was not to find the optimum operating parameters for shotcrete excavation. If that were the case, different pressure and flow values would have been used in order to isolate an ideal pump configuration. Instead, this research looked to identify how the system operates while cutting shotcrete.

Table 4-2: Notes taken regarding operating parameters during waterjet excavation.

Panel Number	Run Number	Notes
1	1	Changed standoff distance from 139.7mm to 88.9mm (5.5" to 3.5"), about 15 passes in each direction, kerf penetrated substrate top in some areas, vibration magnitude increased to about +/- 4g when stalled at each end of traverse, mesh showing in kerf.
	2 3 4	Lowered sample to finish upper cut. Performed runs 2, 3, and 4 back to back. 1/3 kerf overlap with earlier run, stopped momentarily after 3 passes in each direction due to muck gumming up traverse, high vibrations appeared to be dependent on jet location kerf geometry, vibrations visibly peaked when the jet traversed points where it had previously stalled.
	5	Killed off rib in kerf. Had high G forces in end regions where standoff distance was low, 5 passes in each direction, high vibrations occurred when stalled, likely caused by jet moving over ribs.
7	1	5 passes in each direction, HP leak detected, started motion prematurely, 38.1mm (1.5") cut from 5 back and forth passes with 88.9mm (3.5") standoff.
	2	15 passes in each direction, 69.9mm (2.75") kerf depth, as standoff increased the cutting depth did not decrease, pump feels hot to touch (decided to let it cool down before next run), 127mm (5") standoff distance due to previous cut, wire showing from previous cut.
	3 4 5 6	88.9mm (3.5") standoff. Performed runs 3, 4, 5, and 6 back to back, overall performed 25 passes in each direction, cut deep into substrate, saw light through pinhole in substrate, never had a reading above 6g.

Note: No notes were taken during waterjet excavation of Panel TEST as it was used primarily for DAQ and waterjet system calibration purposes.

The notes in Table 4-2 indicate the following key behaviors:

- There was no notable difference in cutting depth when standoff distance was between 88.9 and 190.5 mm (3.5 and 7.5 inches)
- Relatively higher vibrations occurred during the following conditions:
 - Standoff distance was below 88.9 mm (3.5 inches);
 - When the nozzle of the jet was stalled at the endpoints of the traverse; and
 - When the nozzle traversed across areas of kerf geometry where additional free-surfaces existed because of adjacent kerfs.
- It is possible for the muck, which is generated by accumulation of cuttings and water, to limit the traverse of the nozzle due to collecting on the linear slide.

4.2.2 Comparing Waterjet Excavation Process to Impact Hammer Excavation Process

While both the waterjet and impact hammer excavation processes are fundamentally different from each other, it is important to comparatively analyze them with respect to factors related to operation, health, and safety. This comparison is shown in Table 4-3. It's important to note that the factors shown in Table 4-3 are in direct reference to empiric observations made during testing.

The waterjet system used for excavation was remotely operated while impact hammer excavation was a manual process. Due to these differing exposure scenarios, each material removal method has differing probabilities and severities related to health and safety hazards. For example, with waterjet excavation, there is a very low probability that the nozzle jet stream would come into contact with human body parts, however, if it did, the severity would be high as it would likely result in a serious injury and possible death. Comparatively, with impact hammer excavation, the probability of injury from pinch points during operation is higher than that of a waterjet injury but the severity would most likely be lower than that inflicted by a high-pressure waterjet.

Table 4-3: Observations made during each testing method that consider mode of operation and health and safety hazards.

Factor	Waterjet Excavation	Impact Hammer Excavation
Equipment Used	Water supply, supply pump, high-pressure pump, pump breaker, valve, pressure dump, pressure gauge, high-pressure hosing, compressor, linear motion system, lance, nozzle, PPE	Bauer 40 millimeter (1-9/16-inch) rotary hammer (1643E-B), 1-inch concrete spade chisel, PPE
Mode of Operation	Switch valve on water supply to let water flow to supply pump, run the supply pump, run the high-pressure pump (running at low pressure from supply pump), close the dump valve to pressurize the nozzle assembly and begin excavation of target material, run the compressor to linearly traverse the dual orifice rotating nozzle assembly across the panel	Insert concrete spade chisel into Bauer rotary hammer, plug Bauer rotary hammer into outlet, excavate target material by manually pressing into it while running hammer
Health Hazards	Loud noise (high decibel) exposure due to operation of high-pressure pump	Loud noise (high decibel) exposure due to operation of Bauer rotary hammer, respiratory hazard through shotcrete/concrete dust generation, physically taxing due to manual operation, hand-arm vibration exposure
Safety Hazards	High-pressure leak in waterjet system or body part being in line of fire of high-pressure stream coming out of nozzle, flying target material from cutting process, handling of chemicals associated with waterjet solution used to cut	Flying target material from cutting process, pinch points during operation, tripping/falling during operation

4.3 Investigation of Fracture Mechanisms Imposed by Waterjet Shotcrete Cutting

The waterjet system fracture mechanisms that occurred during removal of the shotcrete layer were documented during empiric testing at the SAI/RAMAX laboratory. This section covers how the material removal geometry differed between excavation methods. In addition, cuttings generated from both testing methods are compared and contrasted.

4.3.1 Material Removal Geometry for Both Excavation Methods

Figure 4-1 shows the difference in excavation kerf and the damage of steel infrastructure between the two testing methods. With impact hammer excavation, the kerf was developed by chipping into the shotcrete layer, causing inconsistency in the path of the hammer. This resulted in a cut that was difficult to navigate even though the operator could choose where they wished to remove material. There was also resulting damage to the steel wire mesh during impact hammer testing. The operator attempted to leave the wire mesh intact however it was, at times, unavoidable. Another example is shown in Figure 4-2, where a section of the wire mesh was accidentally cut. This means that the operator would need to remove more area in order to replace the wire mesh section before applying a new layer of shotcrete, which would prove problematic and time consuming in many industrial applications.

Figure 4-2 also shows the inconsistent kerf generated by the impact hammer where the chipping process caused sections of the cutting edge to remove material outside of the desired cutting zone. There are also visible areas of aggregate exposure on the concrete face which could be useful as a bonding surface, however a high percentage of the exposed aggregate was split by the impact hammer which is discussed further in Section 4.5. With waterjet cutting, the kerf was developed as the twin orifice rotating jets made multiple passes over the same surface, rapidly eroding weakness within the cement binder between ASTM C-33 sand particles, leaving a clean-cut slot with significantly smoother walls compared to that left by the impact hammer. The resulting slot left in the panels excavated by the waterjet is similar to that of the diagram developed by Momber [10] as shown in Figure 4-3.



Figure 4-1: Photos taken at panel face showing cutting geometry and bond surface left after impact hammer testing (left) and waterjet testing (right).

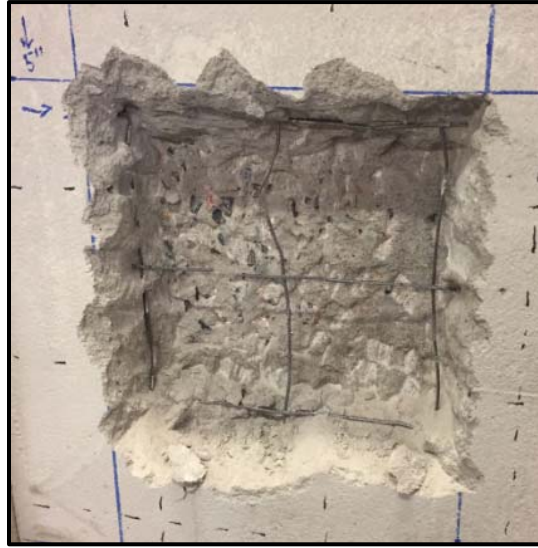


Figure 4-2: Example of inconsistent kerf and damage to steel infrastructure during impact hammer testing.

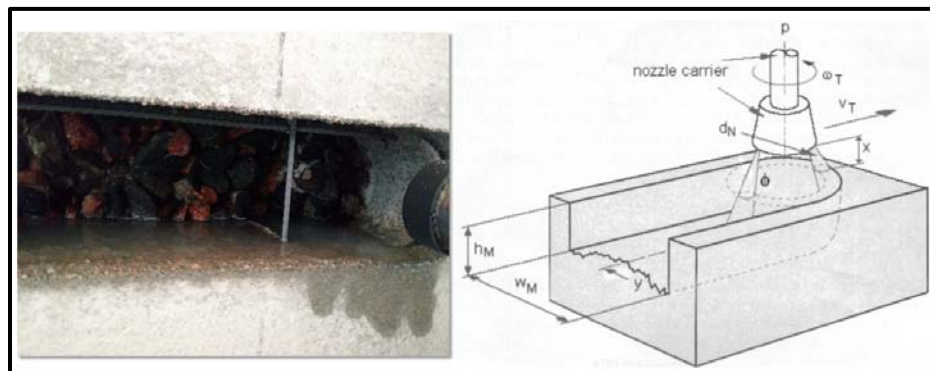


Figure 4-3 Comparison of shotcrete cutting with twin orifice rotating waterjet to Momber's diagram [10]

The kerf itself is much cleaner and uniform than that of impact hammer excavation. Additionally, the wire mesh was left completely intact and cleaned of shotcrete. This is especially important due to the fact that there is no longer any need for the replacement of steel infrastructure when performing rehabilitation work with high-pressure waterjet equipment. While the waterjet system parameters used for this research were successful in leaving the wire mesh intact, it is important to note that it is possible to cut steel infrastructure, depending on the combined pressure and flow used during operation, so caution should be used when selecting the waterjet operating parameters. When reaching the concrete layer, the waterjet rapidly eroded weakness within the cement binder between the 2 cm ($\frac{3}{4}$ inch) aggregate, leaving the aggregate intact.

On Panel TEST, ribs of shotcrete were left between jet passes. This occurred at the ends of the traverse when the jet assembly was stalled and air was draining out of the system. This needed to take place in order for the assembly to translate in the opposite direction. Overall, stalling of the jet at the ends of the traverse resulted in an inconsistency of material removal in these transitional areas. This is shown in Figure 4-4. While this did not adversely impact the results of the testing, it does reiterate the importance of designing a more responsive traverse assembly that correlates to the rotational velocity of the nozzle in order to avoid these edge effects.



Figure 4-4: Ribs of shotcrete left on edges of panel TEST due to traverse limitations in reversing direction.

4.3.2 Examination of Cuttings Generated by Both Excavation Methods

For the cuttings generated by the impact hammer, three 500-gram (1.1 pound) samples underwent sieve analysis. The results of all three sieve tests is shown in Table 4-4. Figure 4-5 graphically shows the results of the sieve tests presented in Table 4-4 in semi-logarithmic form.

Table 4-4: Results of impact hammer cuttings sieve tests.

Sieve Test 1: 500.13 gram sample						
Sieve Size Range, Tyler (in)	Sieve Size Range, μm	Sieve Fractions		Nominal Aperture Size (μm)	Cumulative %	
		wt (g)	wt %		undersize	oversize
(1)	+25400	36.51	7.3	25400	92.7	7.3
(1/2)	-25400 to +12700	128.96	25.8	12700	66.8	33.2
4 (0.185)	-12700 to +4899	104.66	21.0	4899	45.9	54.1
8 (0.093)	-4899 to +2362	34.83	7.0	2362	38.9	61.1
14 (0.048)	-2362 to +1168	28.83	5.8	1168	33.1	66.9
28 (0.0234)	-1168 to +595	45.10	9.0	595	24.1	75.9
48 (0.0117)	-595 to +297	55.62	11.1	297	12.9	87.1
-48 (+0.0117)	-297	64.51	12.9			

Table 4-4: Results of impact hammer cuttings sieve tests (cont.).

Sieve Test 2: 500.00 gram sample

Sieve Size Range, Tyler (in)	Sieve Size Range, μm	Sieve Fractions		Nominal Aperture Size (μm)	Cumulative %	
		wt (g)	wt %		undersize	oversize
(1)	+25400	35.06	7.0	25400	93.0	7.0
(1/2)	-25400 to +12700	99.78	20.0	12700	72.9	27.1
4 (0.185)	-12700 to +4899	120.16	24.1	4899	48.8	51.2
8 (0.093)	-4899 to +2362	39.35	7.9	2362	40.9	59.1
14 (0.048)	-2362 to +1168	36.23	7.3	1168	33.6	66.4
28 (0.0234)	-1168 to +595	53.99	10.8	595	22.8	77.2
48 (0.0117)	-595 to +297	57.09	11.5	297	11.3	88.7
-48 (+0.0117)	-297	56.46	11.3			

Sieve Test 3: 500.01 gram sample

Sieve Size Range, Tyler (in)	Sieve Size Range, μm	Sieve Fractions		Nominal Aperture Size (μm)	Cumulative %	
		wt (g)	wt %		undersize	oversize
(1)	+25400	57.29	11.5	25400	88.5	11.5
(1/2)	-25400 to +12700	131.29	26.3	12700	62.2	37.8
4 (0.185)	-12700 to +4899	89.22	17.9	4899	44.3	55.7
8 (0.093)	-4899 to +2362	33.35	6.7	2362	37.6	62.4
14 (0.048)	-2362 to +1168	33.05	6.6	1168	31.0	69.0
28 (0.0234)	-1168 to +595	49.54	9.9	595	21.1	78.9
48 (0.0117)	-595 to +297	53.06	10.6	297	10.4	89.6
-48 (+0.0117)	-297	52.04	10.4			



Figure 4-5: Semi-logarithmic plot of impact hammer sieve analysis tests.

For the cuttings that were able to be captured during waterjet testing, 100 percent measured less than 8350 microns (0.25 inches) with 75 percent of that sample being smaller than 2540 microns (0.1 inches).

4.4 Verification of Waterjet Effectiveness as an Alternative Shotcrete Removal Tool

This section covers post-testing physical inspection of the test panels to identify whether the waterjet system can facilitate material removal in a manner comparable to the use of mechanical impact hammers.

4.4.1 Post-Excavation Physical Inspection of Test Panels

Once excavation was completed, pictures were taken to visualize and document differences in the finished process, specifically at the concrete/open air interface. Inspection of the bonding surface helped identify whether waterjet testing would be a technically viable alternative to impact tools in these applications. Photographs were taken at the cutting face at each panel to analyze the resulting bond surface. Figure 4-1 provides validation that the waterjet system can complete the same material removal task as an impact hammer. Based on the bond surface left after testing, the waterjet system also shows that it leaves a better surface for application of a new shotcrete layer due to it being rough with exposed aggregate that was not split by the excavation tool. The finished surface on the excavation face located at the shotcrete/concrete interface from impact hammer testing is smooth compared to that of waterjet testing. Additionally, there is visible delamination and loose concrete chips shown at the interface after impact hammer testing. Visibly, this delamination shows that there were potentially higher magnitudes of vibration induced by the impact hammer tool compared to the waterjet. This is backed up by accelerometer data collected during testing, which is discussed further in Section 4.5.

4.5 Validation of Hypothesis that Waterjet Removal of Concrete/Shotcrete Liners will Result in Less Collateral Damage than Conventional Methods

Empiric evidence indicates that waterjets are capable of selectively removing damaged areas of support liners without structurally compromising or adversely impacting intact material around the area being repaired. This section covers the visual fracture/failure examination conducted on the walls and face of the excavated kerf, detailing measurement of fractures, delamination, and split aggregate of each tested panel, the vibration comparison based on results gathered by the data acquisition system (DAQ), the Ground Penetrating Radar (GPR) scan comparison of substrate damage, and investigation of potential micro-fractures within the substrate through microcomputed tomography (microCT) analysis of core samples taken from two panels.

4.5.1 Visual Inspection Comparison of Kerf and Damage of Steel Infrastructure

Visual inspection was performed after excavation was completed on each panel through analysis of the entirety of the excavation profile including the left, upper, right, and bottom walls, as well as the face where exposed aggregate was located. Each section of the excavation profile was inspected individually for areas of fracture/failure, delamination, damage of steel wire mesh, and, for the excavation face, percentage of split aggregate.

Panels 2, 3, 4, 7, and TEST were examined (Appendix B-3) at the Earth Mechanics Institute (EMI). Panel 1 was not visually inspected as it is currently being held at the SAI/RAMAX laboratory for future testing. For comparison, examples of upper wall excavation inspections for panels tested using an impact hammer and waterjet are shown in Figure 4-6 and Figure 4-7. With Figure 4-7, there were no areas of fracture/failure or delamination so there are no singled-out regions similar to that of Figure 4-6. Results of visual inspection measurements for all panels are shown in Table 4-5.

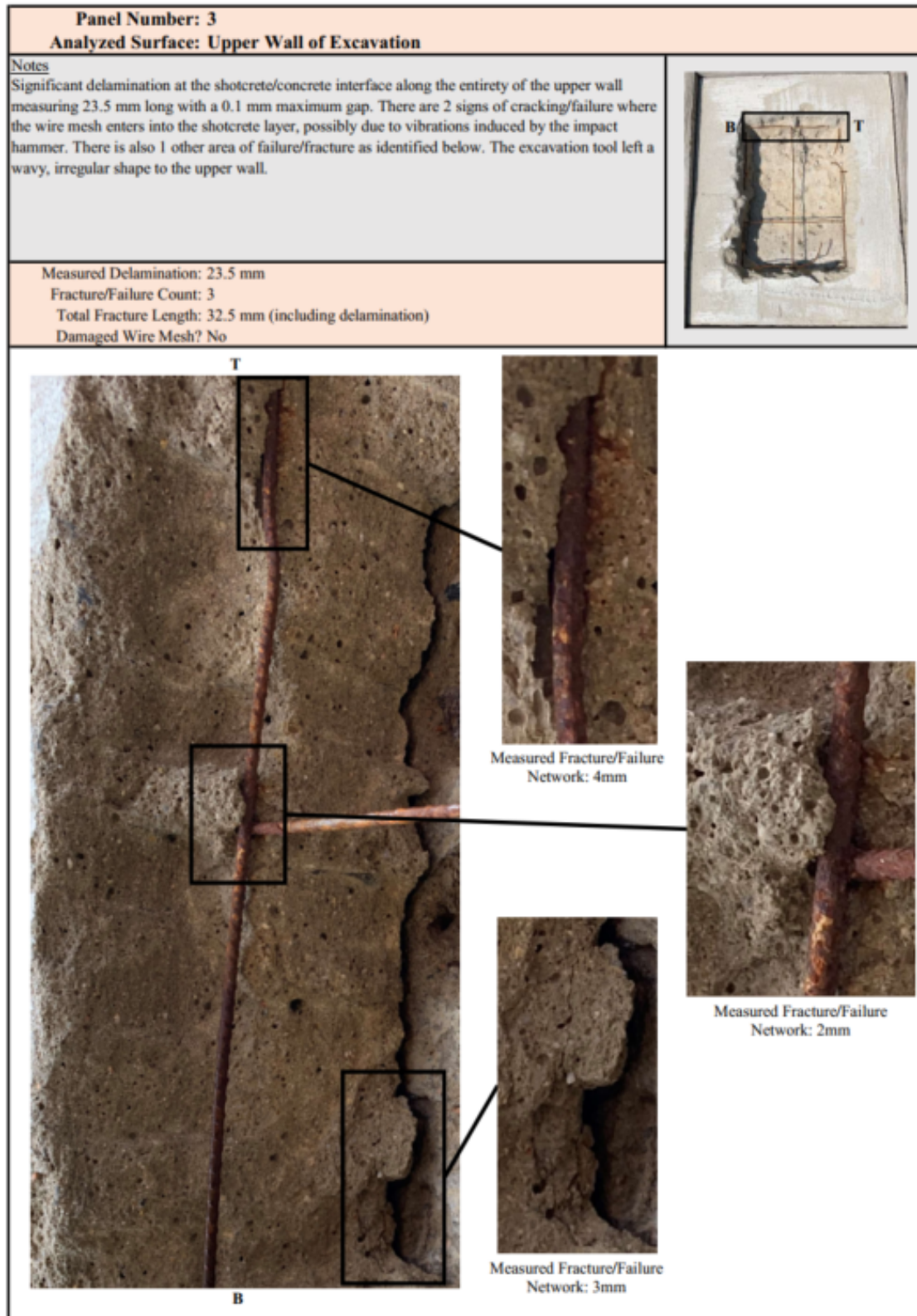


Figure 4-6: Impact hammer excavation upper wall profile visual inspection on panel 3.



Panel Number: 7 Analyzed Surface: Upper Wall of Excavation	
<u>Notes</u> There are no visible signs of delamination. Sections that look like delamination are areas where jet cut slightly into the wall and a shadow is cast over it. Waterjet left a very clean cut across the upper wall, no deviations or wavy nature.	
Fracture/Failure Count: 0 Total Fracture Length: 0 mm Damaged Wire Mesh? No	
<div style="text-align: center;">T</div>  <div style="text-align: center;">B</div>	

Figure 4-7: Waterjet excavation upper wall profile visual inspection on panel 7.

Table 4-5: Results of fracture/failure count and measured distance, measured delamination, and percent split aggregate (exposed).

Panel	Excavation Method	Fracture/Failure Count						Total Fracture / Failure Count	Total Measured Fracture / Failure Distance, mm (in)	Total Measured Delamination Distance, mm (in)	Percent Split Aggregate (Exposed)
		Left Wall	Upper Wall	Right Wall	Lower Wall	Excavation Face	Outside Excavation Profile				
2	Impact Hammer	3	1	3	2	1	3	13	66.5 (2.6)	0	62.7
3	Impact Hammer	7	3	6	4	0	2	22	165 (6.5)	131.5 (5.2)	62.5
4	Impact Hammer	4	3	2	0	0	2	11	57.5 (2.3)	92 (3.6)	80.7
7	Waterjet	1	0	0	0	0	1	2	19 (0.7)	0	0
TEST	Waterjet	1	1	1	0	0	1	4	23.5 (0.9)	0	

Panel 3 resulted in the highest measured fracture/failure, as well as the highest measured delamination while Panel 4 measured the highest percentage of split exposed aggregate at the excavation face. Percentage of split exposed aggregate was at least above 60 percent for all impact hammer panels. Both Panel 7 and Panel TEST resulted with no measured delamination, no damage to the steel wire mesh, and had less measured fracture/failure than all of the impact hammer tested panels. In addition to the absence of damage to galvanized wire mesh, there was no occurrence of flash rust due to waterjet testing. Overall, rust on exposed wire mesh was not observed for six months after waterjet testing. Panel TEST did not fully excavate to the substrate layer, resulting in zero exposed aggregate at the face, however, Panel 7 reached into the concrete layer and did not split any aggregate even though it had the highest exposed count.

4.5.2 Vibration Comparison from DAQ Results

The DAQ recorded acceleration from seven accelerometers during both impact hammer and waterjet excavation testing. The recording sample rate was 100 HZ which translated to a recorded reading for each accelerometer in the X and Z direction every 0.01 seconds.

The data from each run was saved as an Excel file, where post processing took place. The Excel data for each run was processed to plot all seven accelerometer's X and Z readings as well as peak acceleration values for the entire run. Due to the recording sample rate, most cutting runs lasted approximately 210 seconds. It took multiple runs to complete the excavation of a panel to reach the concrete layer. All panels listed in Table 4-1 were monitored with accelerometers during testing.

A sample of processed DAQ acceleration readings from an impact hammer run is shown in Figure 4-8 and a sample from a waterjet run is shown in Figure 4-9. For these particular examples, run 1 of Panel 2, which was cut by an impact hammer, had an overall peak acceleration of 80.8 g, while run 1 of Panel 7, which was cut by a waterjet, had an overall peak acceleration of 2.2 g. It should be noted that accelerometer 3 was damaged during waterjet testing when water saturated the USB cable to the computer and one of the accelerometers wiring harnesses. This led to omitted data for waterjet testing from accelerometer 3 in the X and Z direction for Panel 1, Panel TEST, as well as omitted data for waterjet testing from accelerometer 3 in the X direction for Panel 7. Outside of these occurrences, no data was omitted. All of the runs for each panel are presented in Appendix B-4.

During both forms of testing, acceleration in the Z direction typically exhibited higher magnitudes as a consequence of the Z direction being normal to the panel surface. Some of the higher magnitude acceleration values in the X direction during impact hammer testing could be contributed to when the angle of the chisel was changed from perpendicular to the excavation surface to having an attack angle in order to remove material in the X direction with relation to the panel face. Accelerometer results of waterjet testing generally appear as static noise with consistent vibration when excavating surfaces that do not have irregular geometry. Comparatively, results of impact hammer testing show frequent peaks in all accelerometers at

values never once reached during waterjet testing, and thereby showing far less consistency with much higher vibration.

All accelerometer data for every run of each panel was compiled in MATLAB to provide an easier comparison of vibration during testing using both forms of excavation. The results showed significant differences in overall induced vibration from the cutting tool and are shown in Figure 4-10 through Figure 4-15. To provide a fair comparison, the y axis for the aforementioned figures is set to 120/-120 g which accounts for the highest accelerometer reading throughout all excavation testing.

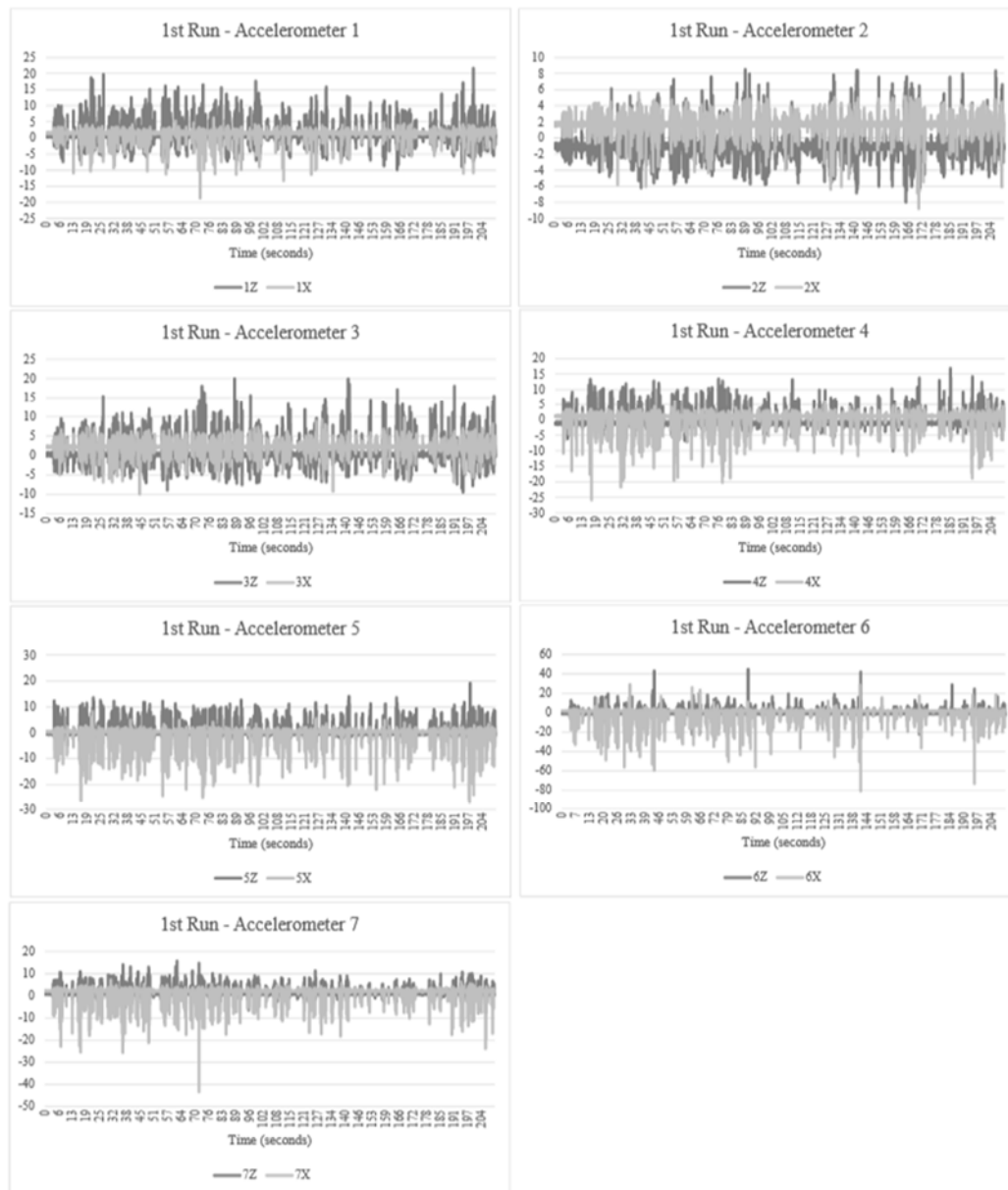
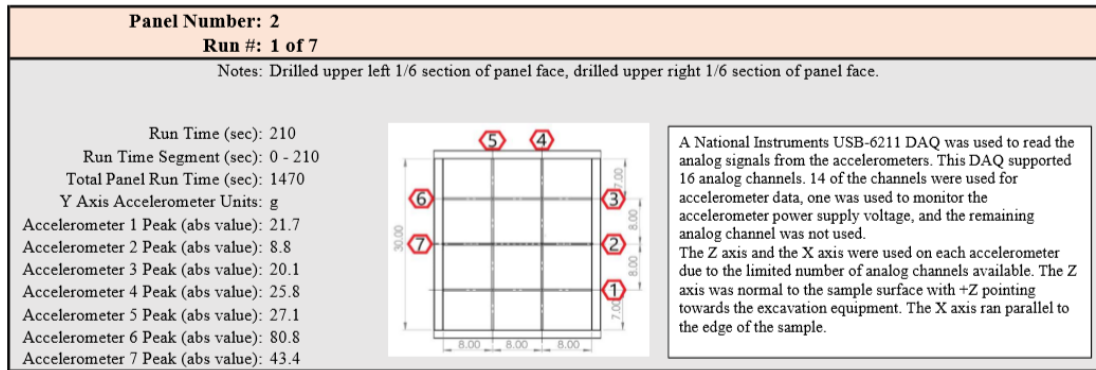


Figure 4-8: Impact hammer testing, Panel 2, Run 1 of 7.

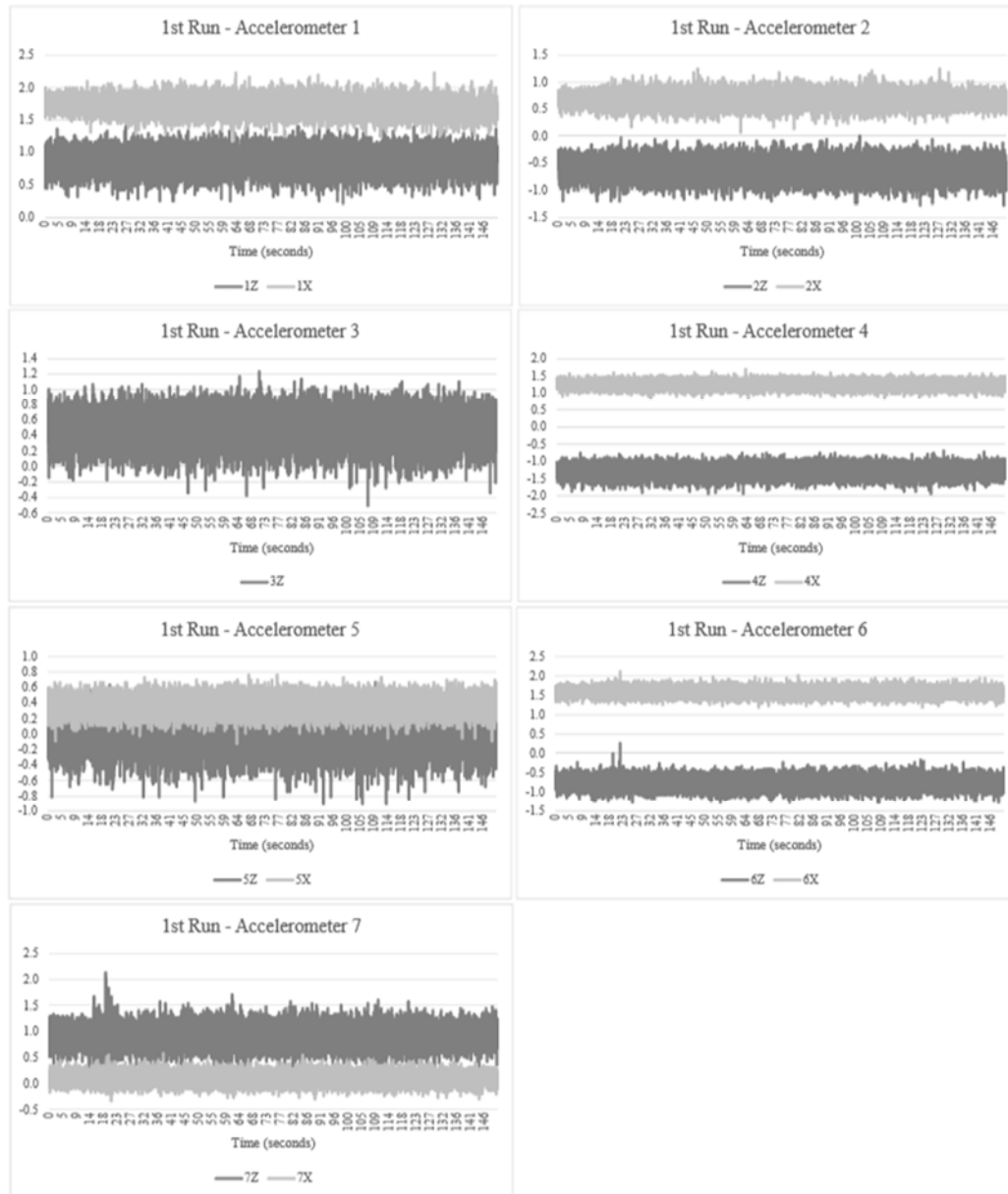
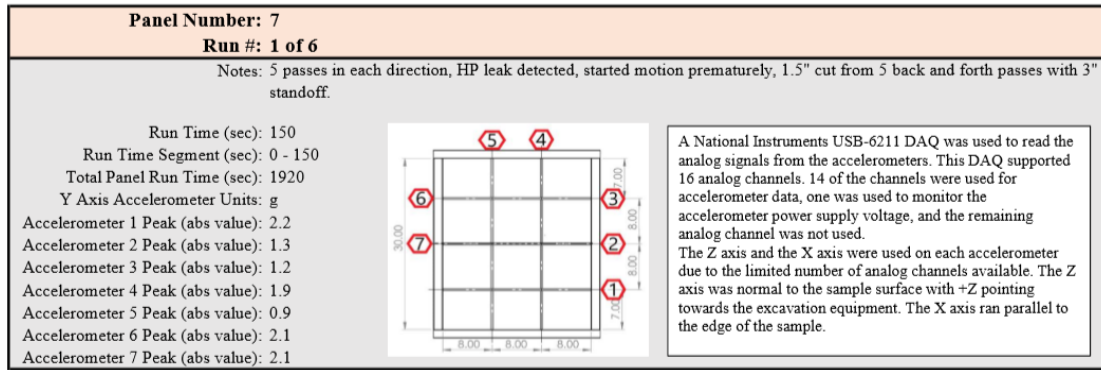


Figure 4-9: Waterjet testing, Panel 7, Run 1 of 6.

Positive and negative peak acceleration values reached during testing on each panel are shown in Table 4-6. For Panel 7, acceleration readings during waterjet excavation never reached above 6 g. With Panel 1, there were instances when accelerations between 10 and 20 g were recorded when the jet stalled at the end of a traverse before reversing direction or when the nozzle traversed across areas of kerf geometry where additional free-surfaces existed because of adjacent kerfs. The longest period of time that the nozzle assembly stalled at the end of a traverse was approximately 15 seconds. This could be avoided in future applications by utilizing hydraulics to traverse the nozzle assembly rather than air compression. Overall, even with these relatively infrequent spikes in recorded acceleration, values never exceeded 20 g during waterjet testing.

Figures for impact hammer testing show that vibrations are significantly higher across all accelerometers during the entirety of testing compared to that of waterjet testing. A section of Panel 4 was excavated using hand hammering with the chisel and a sledge hammer, instead of using the Bauer tool, to draw a comparison of different impact techniques. These results are shown in Run 3 of Panel 4 in Appendix B-4 and during the 7 to 10.5-minute time interval on Figure 4-12. During hand hammering, acceleration peaks between 17-72.5 g were recorded which were comparatively lower than typical peaks reached with the Bauer tool however, still significantly higher than that of the waterjet system.

The higher vibrations induced through impact hammer testing are likely the cause of delamination at the interface of the shotcrete/concrete layer shown in Figure 4-1 after visual inspection. There is no visual indication of delamination in the panels excavated using the waterjet system. Deterioration within the panel, specifically in the concrete section was further analyzed using GPR and microCT.

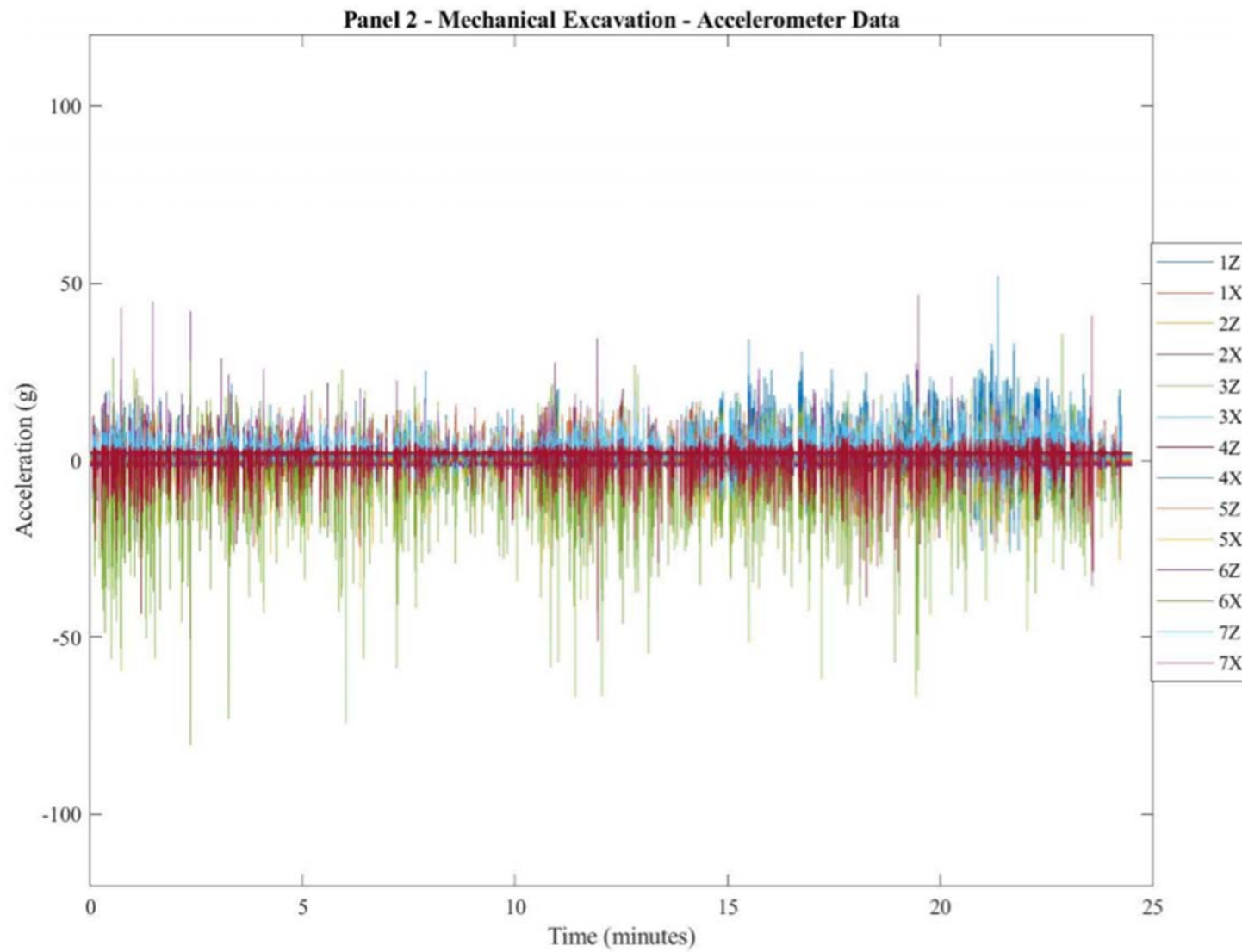


Figure 4-10: Vibration data acquired from accelerometers during impact hammer testing on panel 2.

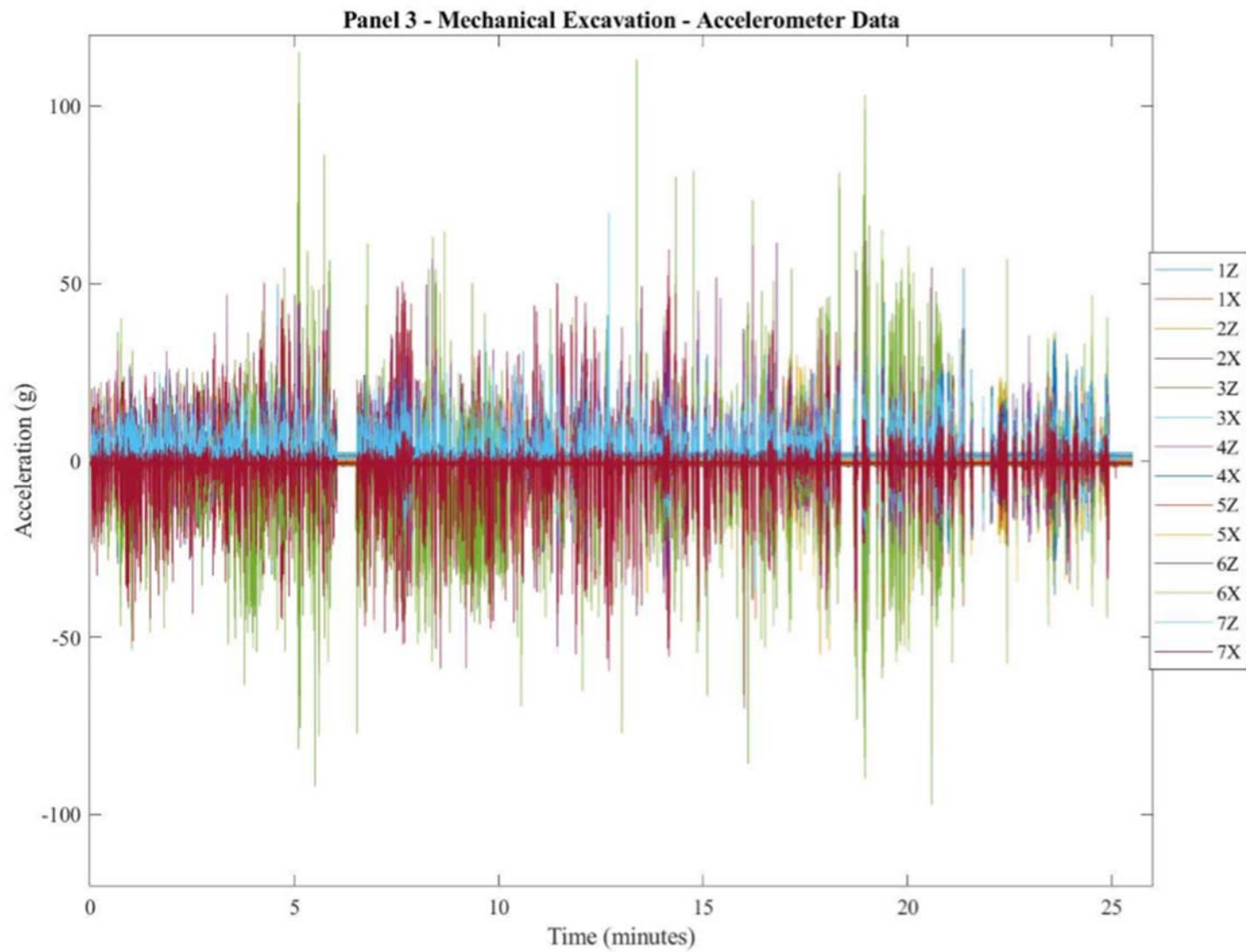


Figure 4-11: Vibration data acquired from accelerometers during impact hammer testing on panel 3.

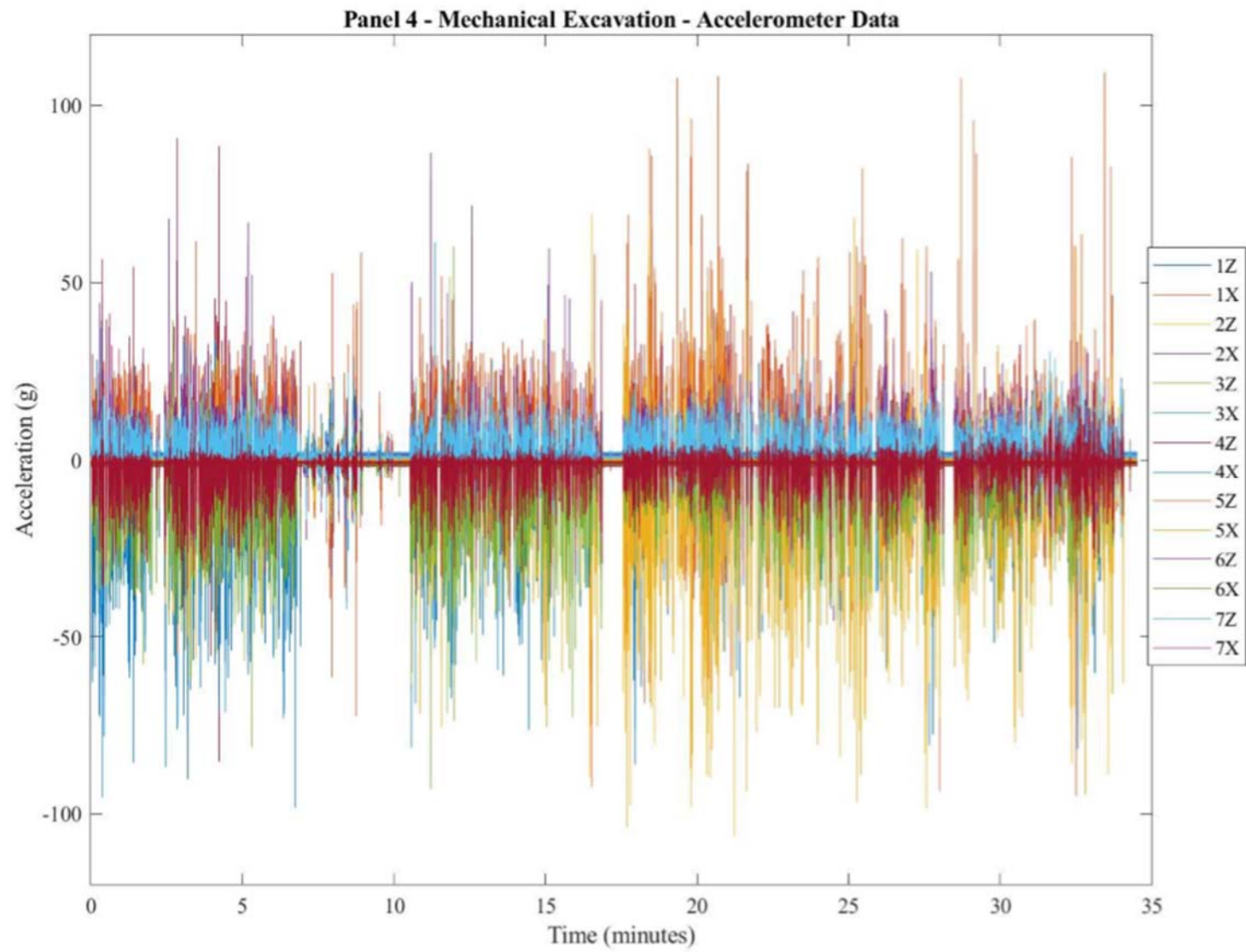


Figure 4-12: Vibration data acquired from accelerometers during impact hammer testing on panel 4.

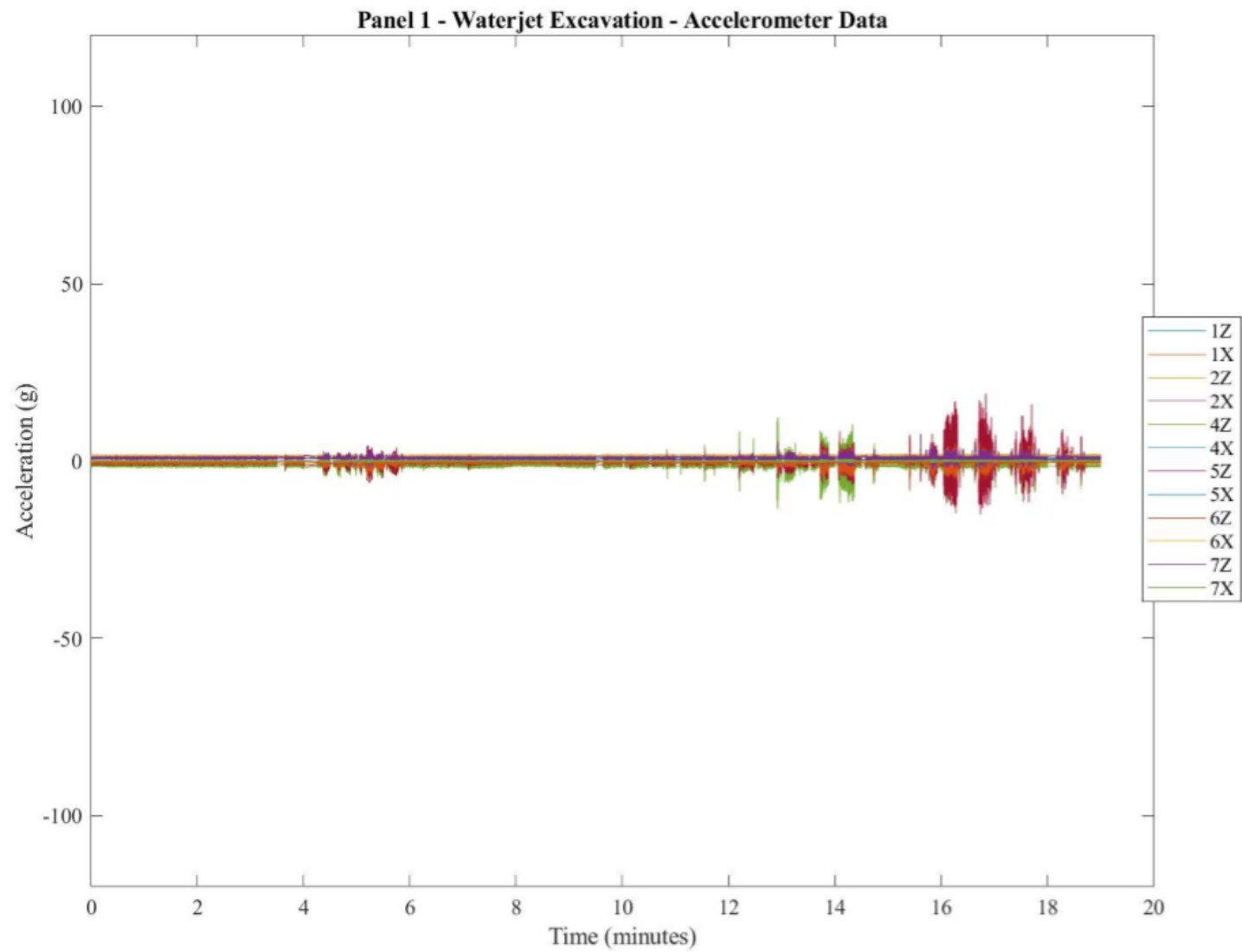


Figure 4-13: Vibration data acquired from accelerometers during waterjet testing on panel 1.

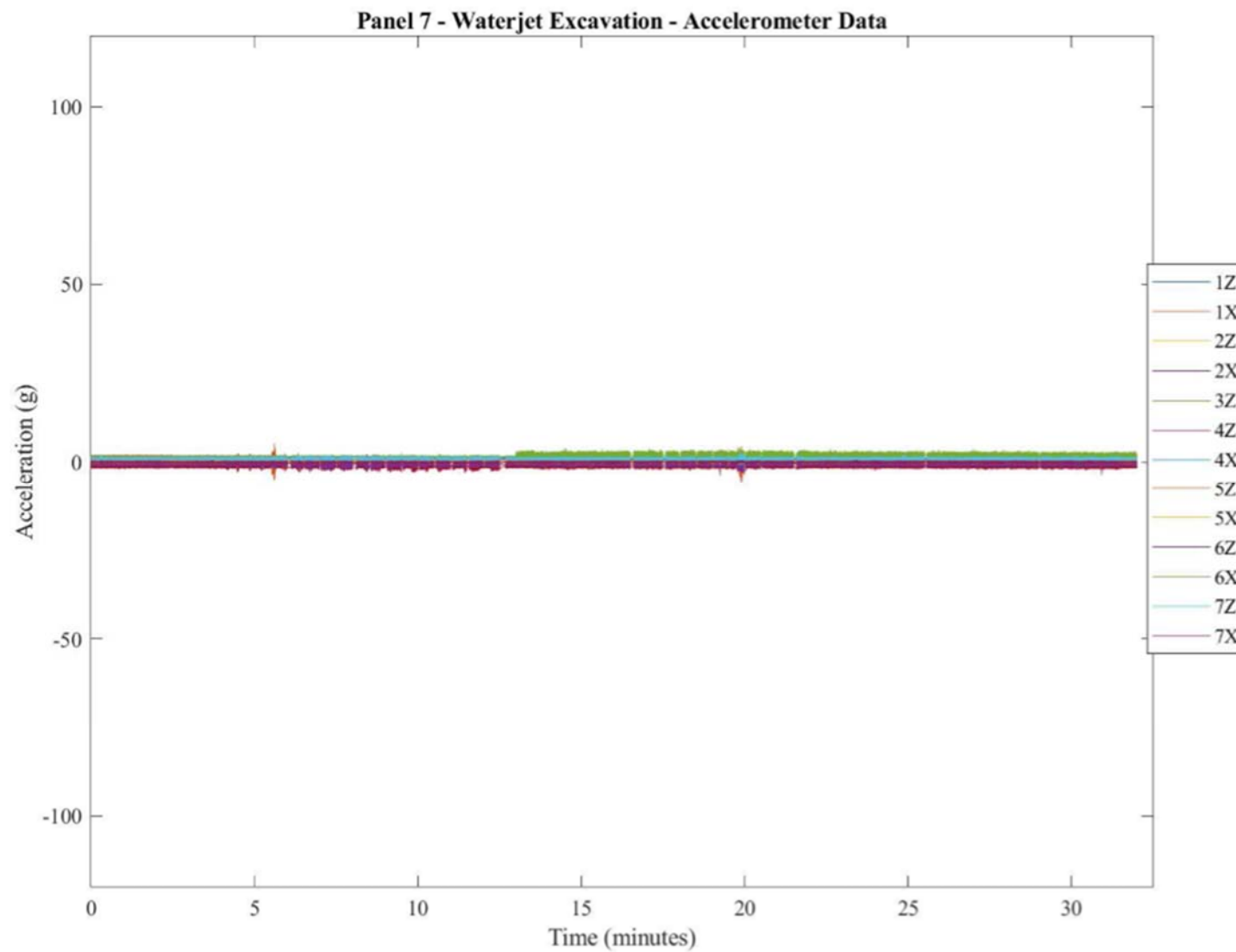


Figure 4-14: Vibration data acquired from accelerometers during waterjet testing on panel 7.

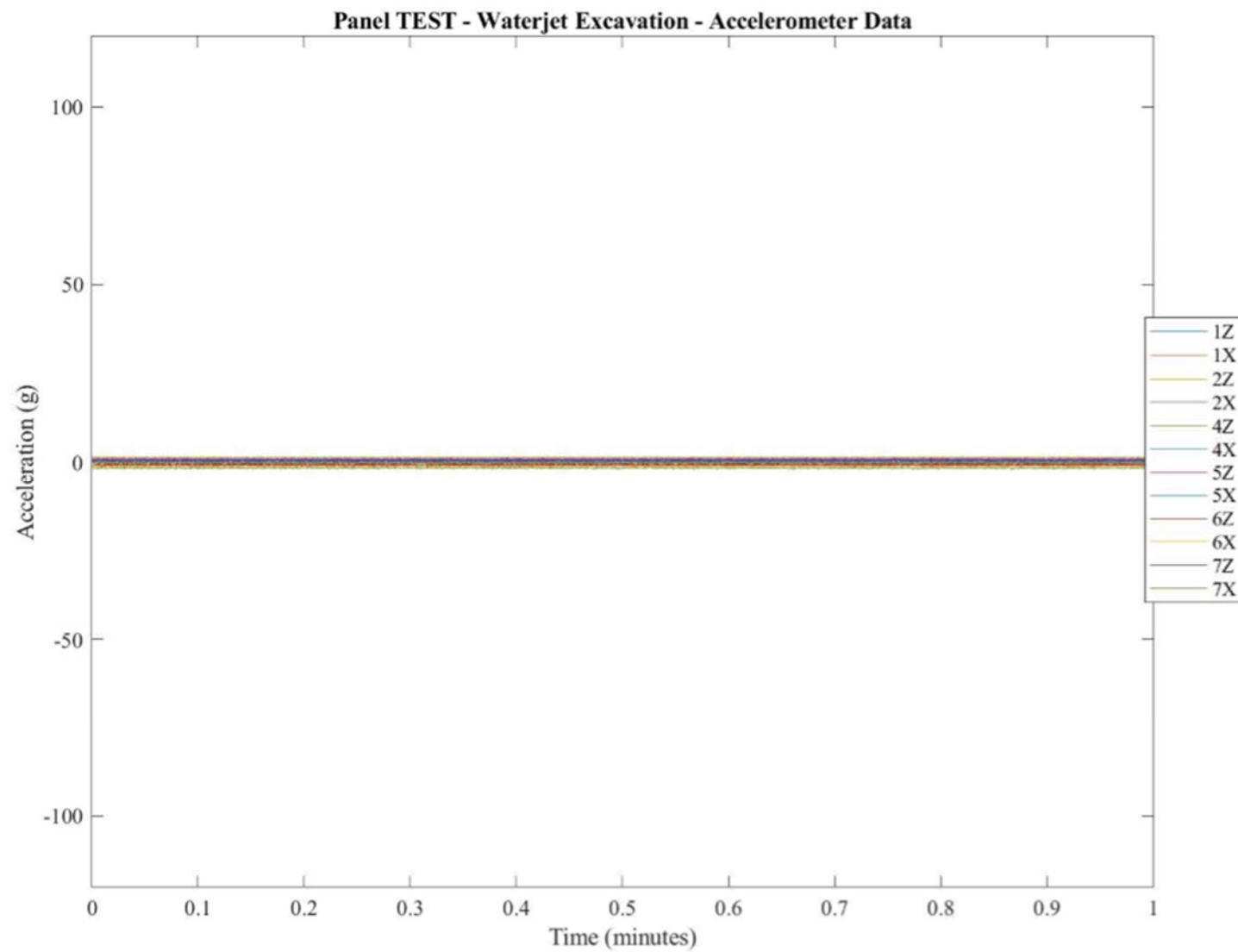


Figure 4-15: Vibration data acquired from accelerometers during waterjet testing on panel TEST.

Table 4-6: Positive and negative peak acceleration values (g) reached during impact hammer and waterjet excavation according to each accelerometer.

	Panel 2		Panel 3		Panel 4		Panel 1		Panel 7		Panel TEST	
	Positive Peak	Negative Peak	Positive Peak	Negative Peak	Positive Peak	Negative Peak	Positive Peak	Negative Peak	Positive Peak	Negative Peak	Positive Peak	Negative Peak
1Z	52.1	26.1	54.2	26.9	32.1	15.9	4.1	1.8	2.2	0.3	1.4	
1X	9.4	19.0	53.7	44.8	20.1	20.7	2.2		2.2	1.7	1.8	
2Z	14.7	16.5	84.6	77.2	18.0	16.6	2.7	3.2	1.2	2.8	-	-1.2
2X	9.8	18.7	39.4	22.8	16.5	34.8	1.8	1.1	2.5	1.2	0.9	-
3Z	21.7	15.4	115.3	89.9	23.1	19.3	OM	OM	4.5	3.2	OM	OM
3X	14.2	19.1	33.7	31.2	22.3	41.5	OM	OM	OM	OM	OM	OM
4Z	20.4	12.3	60.8	55.5	91.0	85.3	12.3	13.5	3.1	5.7		-2.0
4X	9.1	25.8	34.3	38.0	61.2	98.3	3.3	1.1	2.2		1.3	
5Z	19.1	12.2	55.8	22.1	109.4	95.1	19.0	15.0	5.3	5.1	0.3	1.0
5X	16.4	36.4	19.6	54.8	69.6	106.4	4.1	3.7	1.1	0.4	0.6	0.2
6Z	46.8	35.6	62.0	43.8	86.8	48.5	5.3	5.5	2.2	3.0		-1.3
6X	35.5	80.8	113.2	97.3	60.1	93.1	3.0		4.0	1.1	1.9	
7Z	20.3	29.4	70.1	36.1	30.5	42.2	5.0	2.8	2.9	0.9	1.5	
7X	40.8	51.0	24.0	70.1	56.6	55.3	0.7	0.7	0.7	0.5	0.2	0.5

Note: OM means the data was omitted due to water damage to the particular accelerometer

“-” means there was no positive or negative peak for the accelerometer

4.5.3 Non-Destructive Analysis from Processed GPR Scan Comparison

With regards to the timeline through which each antenna was utilized for inspection of the developed panels, a 2600 MHz antenna gathered pre-excavation scans on all of the panels at the EMI in May 2018. Impact hammer testing was conducted within the same week of pre-excavation scans so post impact hammer testing scans were taken on Panels 2, 3, and 4 with the same 2600 MHz system. After waterjet testing in October, 2018, a 1600 MHz antenna was used to gather post excavation scans on all panels at the EMI. In order to conduct an analysis of conditions within each panel before and after testing took place, only the GPR scans from the bottom face could be compared due to destruction of the top face. Using GPR Mapper within MATLAB [50], each scan acquired through both the 2600 and 1600 MHz antennas went through the processing flow shown in Figure 4-16. Time zero correction was used to crop all data to the first negative peak in the trace for consistent starting points. In this case, the starting point of the scan is the plywood bottom of the panel which is half an inch thick. DeWow was used to filter out the low frequency energy associated with the close proximity of the receiver and transmitter [51]. Fourier filtering manipulated the specific frequency components of the signal by taking the Fourier transform of the signal, amplifying a specific range, and inverse transforming the result. If a 2600 MHz antenna was being used, the range of 1300-3900 MHz was amplified for the Fourier filter. If a 1600 MHz antenna was being used, the range of 800-2400 MHz was amplified for the Fourier filter. Time gain was used to equalize amplitude throughout the depth of the scan due to the fact that radar signals rapidly attenuate as they propagate into the target material. Finally, background removal was used to remove instances of antenna ringing by taking the mean of all traces in a section and subtracting it from each trace [52]. Each step within post collection processing is shown with a sample scan in Figure 4-17 and is further detailed in Appendix B-5.

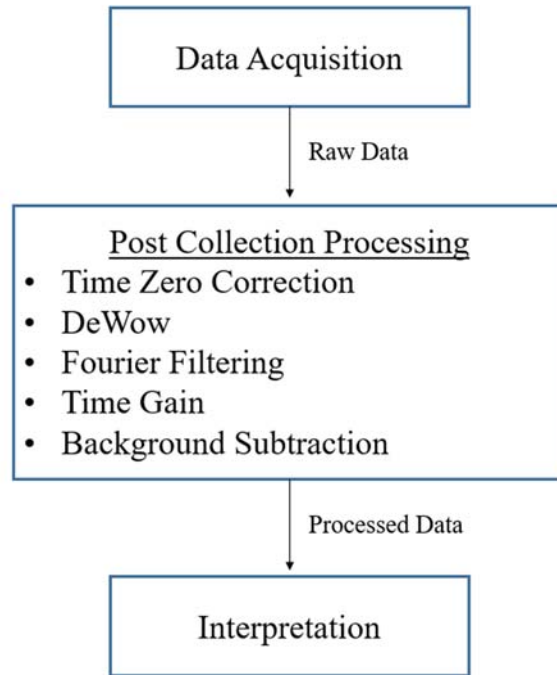


Figure 4-16: GPR scan processing flow.

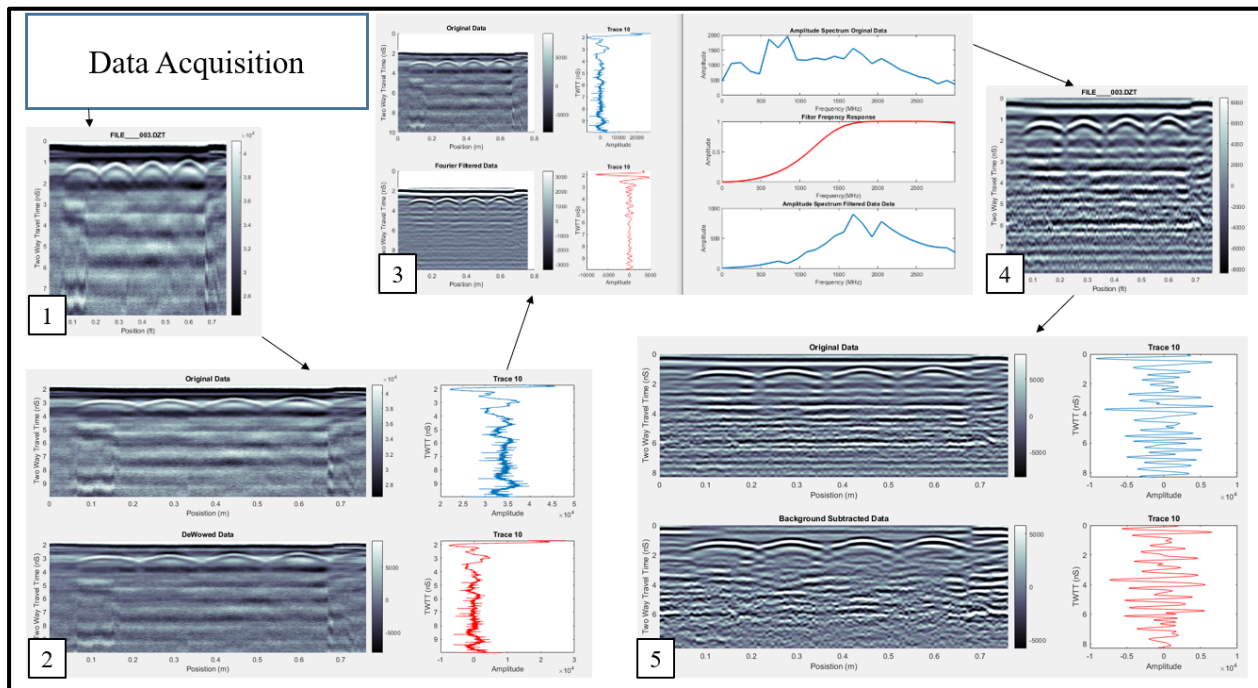


Figure 4-17: Sample scan that goes through time zero correction (1) DeWow (2) Fourier filtering (3) time gain (4) and background subtraction (5).

After processing was completed, the 2D scans of each panel gathered using the 2600 MHz antenna before testing were lined up for analysis. An AutoCAD model was developed for each panel to help visualize the location of each individual scan. These 2D scans along with their location within each panel are shown in Appendix B-5. It is important to note that a significant portion of the scan obtained from the radar and antenna was open air. Equation 4.1 and Equation 4.2 were used to identify the different panel components according to travel time to help focus on key aspects of each scan.

$$ns = \frac{d_{comp.}}{v_c} * 2 \quad (4.1)$$

Where:

ns = Two-way travel time (nanoseconds)

$d_{comp.}$ = Distance to panel component

v_c = Radar velocity

$$v_c \approx \frac{c}{\sqrt{D}} \quad (4.2)$$

Where:

c = Speed of light

D = Dielectric constant of concrete/shotcrete

The permittivity method was used to approximate the radar velocity used in this scenario which would be applied through the entirety of the shotcrete/concrete layers. A dielectric constant of 6 was used to approximate the radar velocity (0.12 m/ns) which was then used to determine the distance to each panel component from the plywood bottom in nanoseconds as shown in Table 4-7.

Table 4-7: Distance in nanoseconds to panel components from plywood bottom.

	inches	meters	nanoseconds
Distance to Rebar	3.50	0.09	1.46
Distance to Concrete/Shotcrete Interface	6.50	0.17	2.71
Distance to Wire Mesh	8.50	0.22	3.55
Distance to Shotcrete/Air Interface	10.50	0.27	4.38

It is also important to consider the reflection coefficients for materials within the engineered panels. Reflection coefficient at the boundary of two materials can be calculated or approximated using Equation 4.3.

$$R = \frac{Z_2 - Z_1}{Z_2 + Z_1} \approx \frac{v_2 - v_1}{v_2 + v_1} \quad (4.3)$$

Where:

R = Reflection coefficient

Z = Impedance

v = EM velocity

Equation 4.3 uses the impedance of each material for a more precise calculation while the approximation uses EM velocity of each material. The approximation can be used for near-surface applications, including this research on panel segments, and was used to get a general idea of reflected energy and possible phase reversal between panel materials during scan interpretation. Approximate reflection coefficients are shown in Table 4-8. Effective permittivity and EM wave velocity values for air and water were used from Table 2-7. A schematic of how an EM wave reacts when coming in contact with a material boundary is shown in Figure 4-18. A material with a coefficient of 1 would be the greatest amount of reflected energy. In this case, an EM wave traveling through concrete/shotcrete and reflecting off air would give a reflection coefficient of 0.43 which would indicate a moderate amount of energy and the returned signal would have no phase reversal. If the EM wave travels through concrete/shotcrete and reflects off water, there would be a coefficient of -0.57 which indicates a slightly stronger amount of energy, compared to that of air, with a phase reversal.

Table 4-8: EM properties and reflection coefficients of materials in GPR scans.

EM Properties of Materials in Ground Penetrating Radar Scans

Material	ϵ_{eff}	v (m/ns)
Concrete/Shotcrete	6	0.12
Air	1	0.3
Water	80	0.033

Reflection Coefficients for Materials in Ground Penetrating Radar Scans

		Material 2		
		Concrete/Shotcrete	Air	Water
Material 1	Concrete/Shotcrete	0.00	0.43	-0.57
	Air	-0.43	0.00	-0.80
	Water	0.57	0.80	0.00

A primary objective of the scan interpretation was the detection of air voids or delamination within the concrete substrate due to excavation testing. Kravitz states that, according to Chen and Scullion, when air voids of small thickness relative to wavelength are present within a sample, the reflected waves coming off the top and bottom of the void combine with each other and induce positive interference, leading to an increase in amplitude of the returned EM signal and therefore, amplifies the strong reflection shown on the 2D scan [44]. Additionally, Clemeña et al state that the reflected waves coming off the top and bottom of air voids would overlap due to the relatively small thickness, making it difficult to estimate time separation [53].

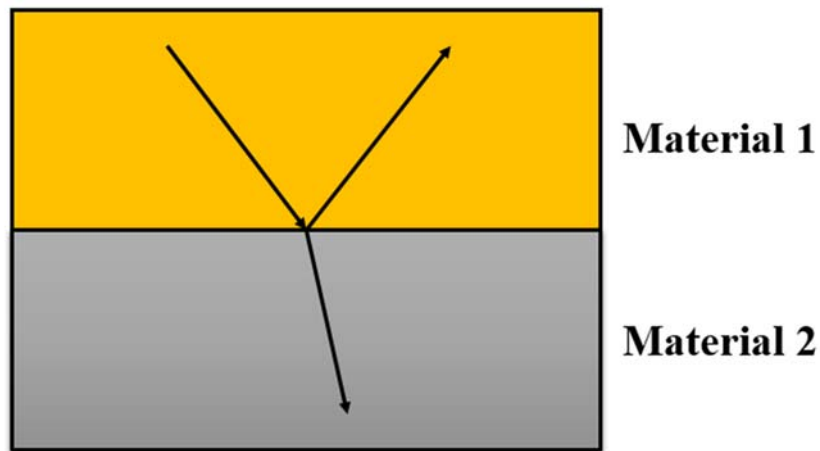


Figure 4-18: Schematic showing path of EM wave at interface of two materials.

According to Clemeña, Figure 4-19 illustrates how a microwave reflection profile for concrete pavement differs when a void is present. Resolution of the GPR system plays a key role in identifying whether the thickness of the void can be determined or not. Vertical resolution determines how large the vertical distance between discontinuities needs to be in order to be detectable by the GPR system and can be calculated using Equation 4.4 and Equation 4.5 [54].

$$R_V = \frac{1}{4}\lambda \quad (4.4)$$

Where:

R_V = Vertical resolution

λ = Wavelength

$$\lambda = \frac{v_c}{f} \quad (4.5)$$

Where:

v_c = Radar velocity
 f = Antenna frequency

If a 2600 MHz antenna was utilized with a radar velocity of 0.12 m/ns, the vertical resolution is 1.2 cm (0.47 inches). If a 1600 MHz antenna was utilized with a radar velocity of 0.12 m/ns, the vertical resolution is 1.9 cm (0.74 inches). This means that if an air void or delamination has vertical spacing of less than 1.2 cm for a 2600 MHz antenna or 1.9 centimeters for a 1600 MHz antenna, the radar will not be able to identify a top and bottom. However, as previously stated, the waves coming off the top and bottom of these smaller voids would overlap/combine and still amplify the reflection.

Overall, the location of the air void is important. Within this research, the air voids of interest would have a top material boundary of concrete/air and a bottom material boundary of air/concrete which would result in an initial reflection coefficient of 0.43 and a closely followed second reflection coefficient of -0.43. The upper envelope scans would return both these reflections as an increase in amplitude and could help locate areas of micro-fracturing within the concrete layer.

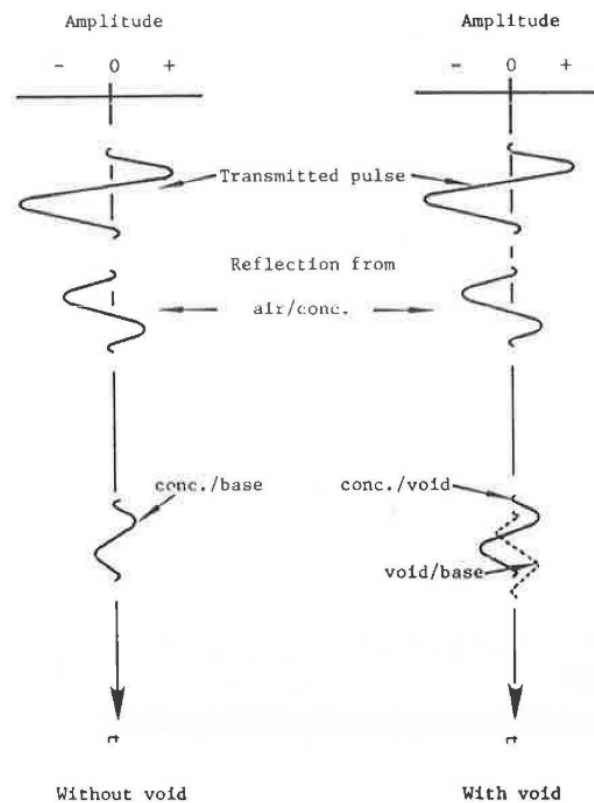


Figure 4-19: Microwave reflection profile for concrete pavement without a void and with a void [53].

With the background knowledge known for approximate travel time to panel components, the EM properties and reflective coefficients for each material within the panels, and vertical resolution according to each radar antenna, the pre-excavation scans recorded by the 2600 MHz antenna were processed further in MATLAB to return the upper envelope of the input sequence, x , as the magnitude of its analytic signal. The analytic signal of x is found using the discrete Fourier transform as implemented in Hilbert. This procedure was completed to provide a better visual for identifying changes in amplitude within each individual scan. Figure shows a processed scan before and after returning the upper envelope. With the particular example in Figure 4-20, it's easily noticeable that something is causing the amplitude of the first identified rebar to drop significantly at the center of the hyperbola. In this case, it's possible that a piece of aggregate within the concrete interfered with the path of the EM wave. These are things that need to be considered during scan interpretation.

Since the purpose of non-destructive analysis through GPR data was to identify differences in panel deterioration, specifically within the concrete layer, due to the method of testing, the upper envelope scans were then cropped to the zone between the plywood bottom and approximately 1.2 nanoseconds past the concrete/shotcrete interface. The cropped boundary extends past the concrete/shotcrete interface for two reasons; (1) the panel component locations are approximate calculations through use of the permittivity method, and (2) a full view of the reflections given off from the concrete/air boundary was desired which was sometimes so strong that it extended 1.2 nanoseconds past the concrete/shotcrete interface. These cropped, 2D processed and upper envelope scans were lined up and stacked with their location in the panel according to the AutoCAD model (Appendix B-5).

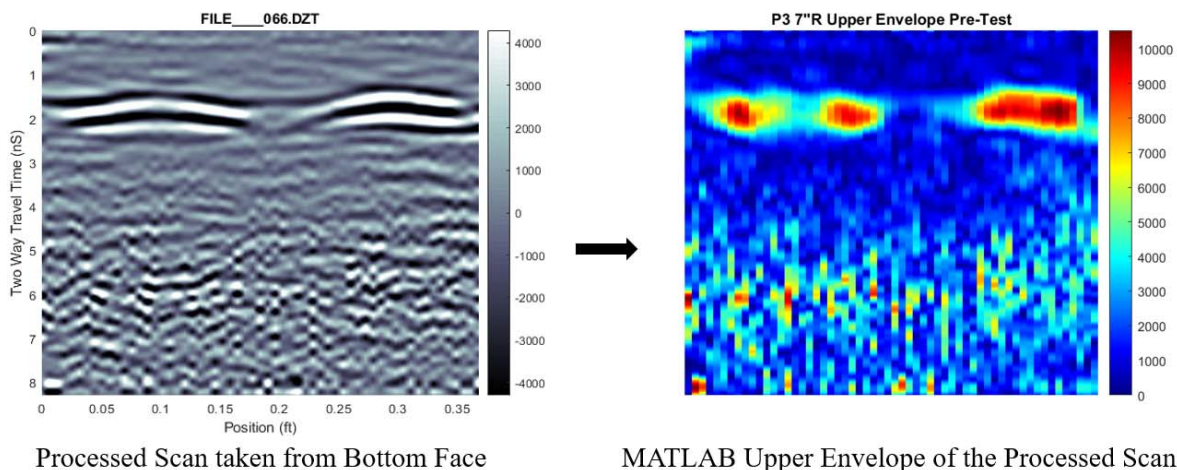


Figure 4-20: Example of processed GPR scan before and after returning the upper envelope in MATLAB.

Post excavation GPR scans were recorded using a 1600 MHz radar antenna. As stated in Chapter 3, in general, the lower the frequency of the antenna, the greater the penetration depth

and the lower the resolution. While there is a lower resolution with the 1600 MHz antenna, it was important to analyze the panels with two different antennas to see if varying frequency helps identify additional areas of potential panel deterioration. For example, according to Kravitz, if a maximum threshold frequency antenna is used, the steel reinforcement and high strength concrete could attenuate the signal before returning to the receiver, whereas if a minimum threshold frequency antenna is used, the wavelength may be too large to pass through the steel reinforcement [44]. Similar to the pre-excavation radargrams, each scan was processed to return the upper envelope and the resulting 2D scans of each panel were lined up and stacked with their location in the panel according to the AutoCAD model. The end results are shown in Figure 4-21 through Figure 4-30. The shaded area shown on each AutoCAD model's cross section outlines the location of the scan acquired from the bottom face of the panel. Observations during interpretation of the post analysis scans gathered using the 1600 MHz radar antenna are found in Appendix B-6.

To serve as an additional form of visual analysis on the 1600 MHz post-excavation scans, OpendTect, an open source seismic interpretation system created by dGB Earth Sciences, was utilized to examine the positioning of processed scans in 3D for each panel. These figures are provided in Appendix B-6. These 3D models of each panel's scan sequence were useful in providing a general comparison of visualizing properties of scans inside and outside of the excavation profile generated by each cutting tool. In addition, these models helped provide additional insight into whether or not delamination could be identified by the 1600 MHz antenna at the shotcrete/concrete interface for scans located outside the excavation profile.

PANEL 2 - POST IMPACT HAMMER EXCAVATION SCANS FROM SOUTH TO NORTH ON BOTTOM FACE BETWEEN PLYWOOD BOTTOM AND 1.2 NANSECONDS PAST SHOTCRETE/CONCRETE INTERFACE USING 1600 MHZ ANTENNA

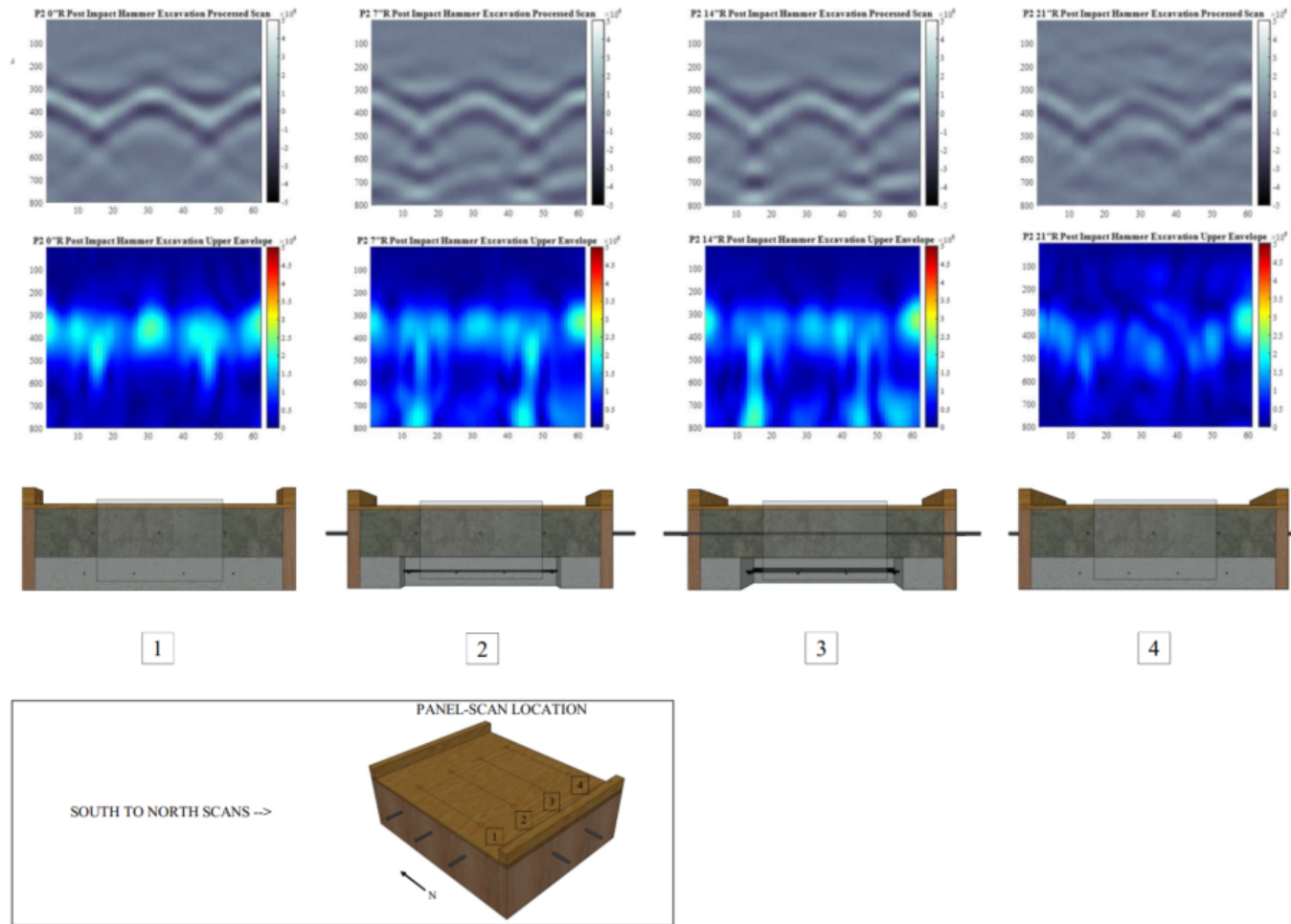


Figure 4-21: 1600 MHz post excavation south to north scans on panel 2 showing the lowest recorded amplitude increase within the substrate for a panel cut by the impact hammer.

PANEL 2 - POST IMPACT HAMMER EXCAVATION SCANS FROM EAST TO WEST ON BOTTOM FACE BETWEEN PLYWOOD BOTTOM AND 1.2 NANSECONDS PAST SHOTCRETE/CONCRETE INTERFACE USING 1600 MHZ ANTENNA

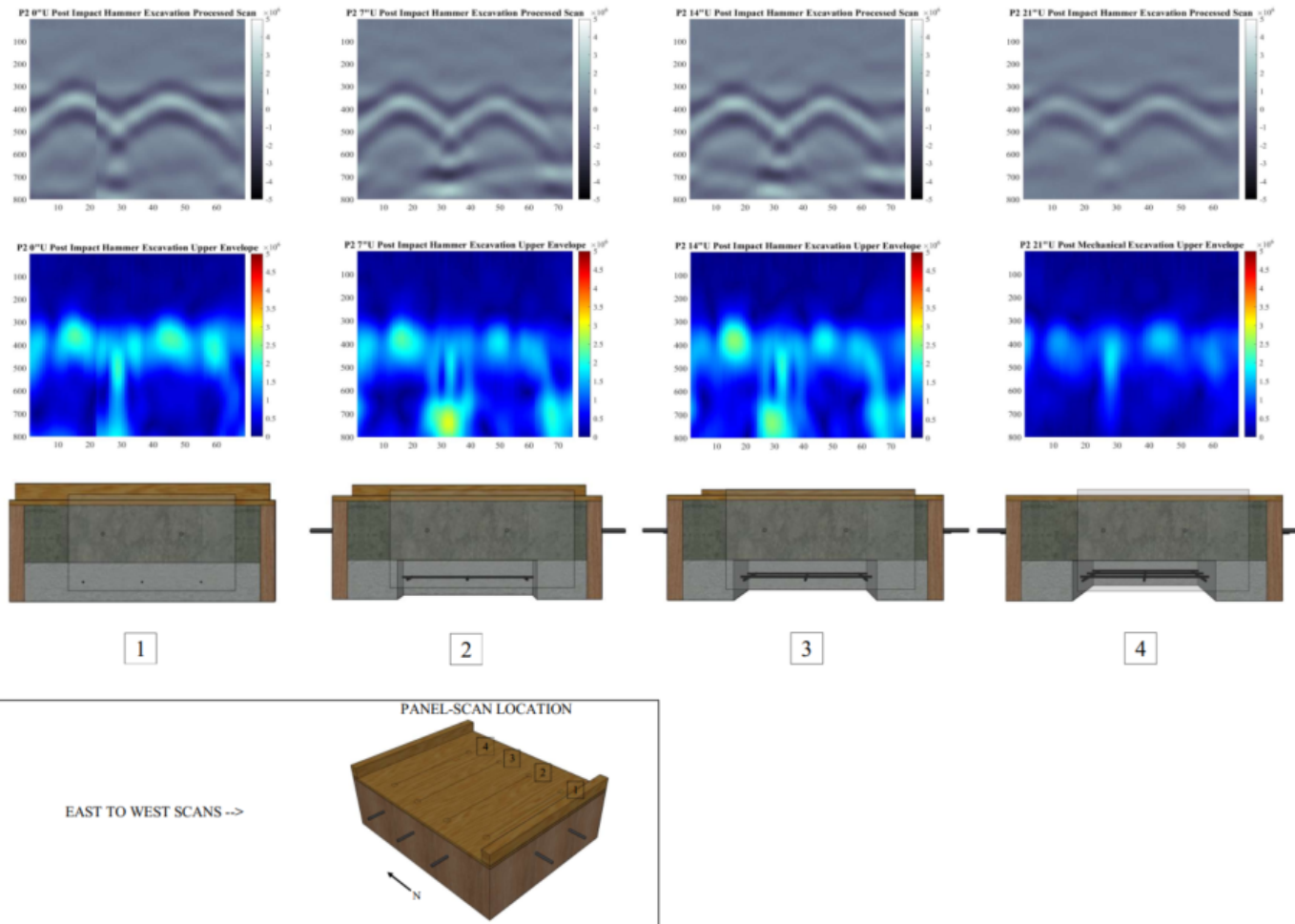


Figure 4-22: 1600 MHz post excavation east to west scans on panel 2 showing the lowest recorded amplitude increase within the substrate for a panel cut by the impact hammer.

PANEL 3 - POST IMPACT HAMMER EXCAVATION SCANS FROM SOUTH TO NORTH ON BOTTOM FACE BETWEEN PLYWOOD BOTTOM AND 1.2 NANSECONDS PAST SHOTCRETE/CONCRETE INTERFACE USING 1600 MHZ ANTENNA

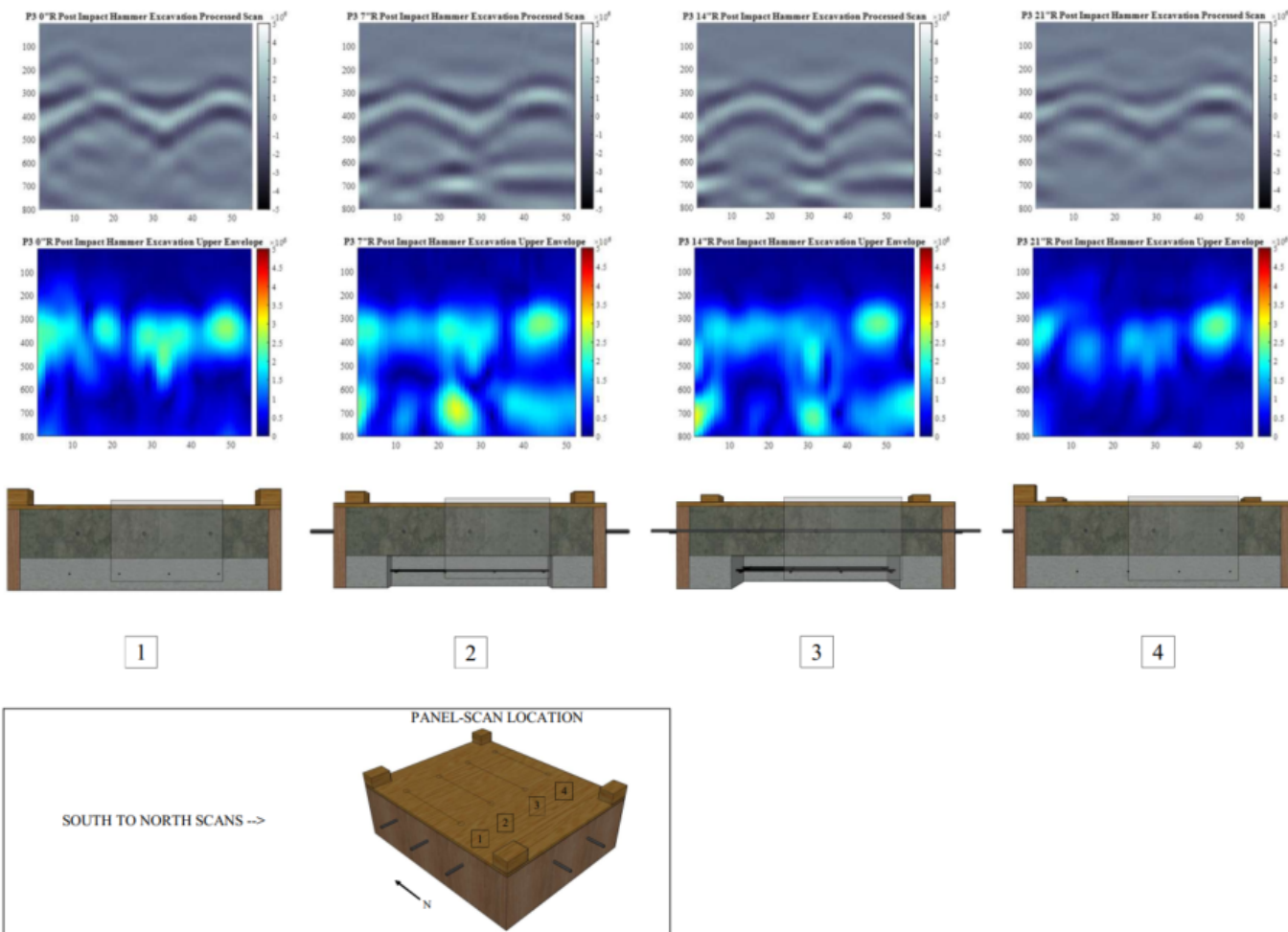


Figure 4-23: 1600 MHz post excavation south to north scans on panel 3 showing the second highest recorded amplitude increase within the substrate for a panel cut by the impact hammer.

PANEL 3 - POST IMPACT HAMMER EXCAVATION SCANS FROM EAST TO WEST ON BOTTOM FACE BETWEEN PLYWOOD BOTTOM AND 1.2 NANSECONDS PAST SHOTCRETE/CONCRETE INTERFACE USING 1600 MHZ ANTENNA

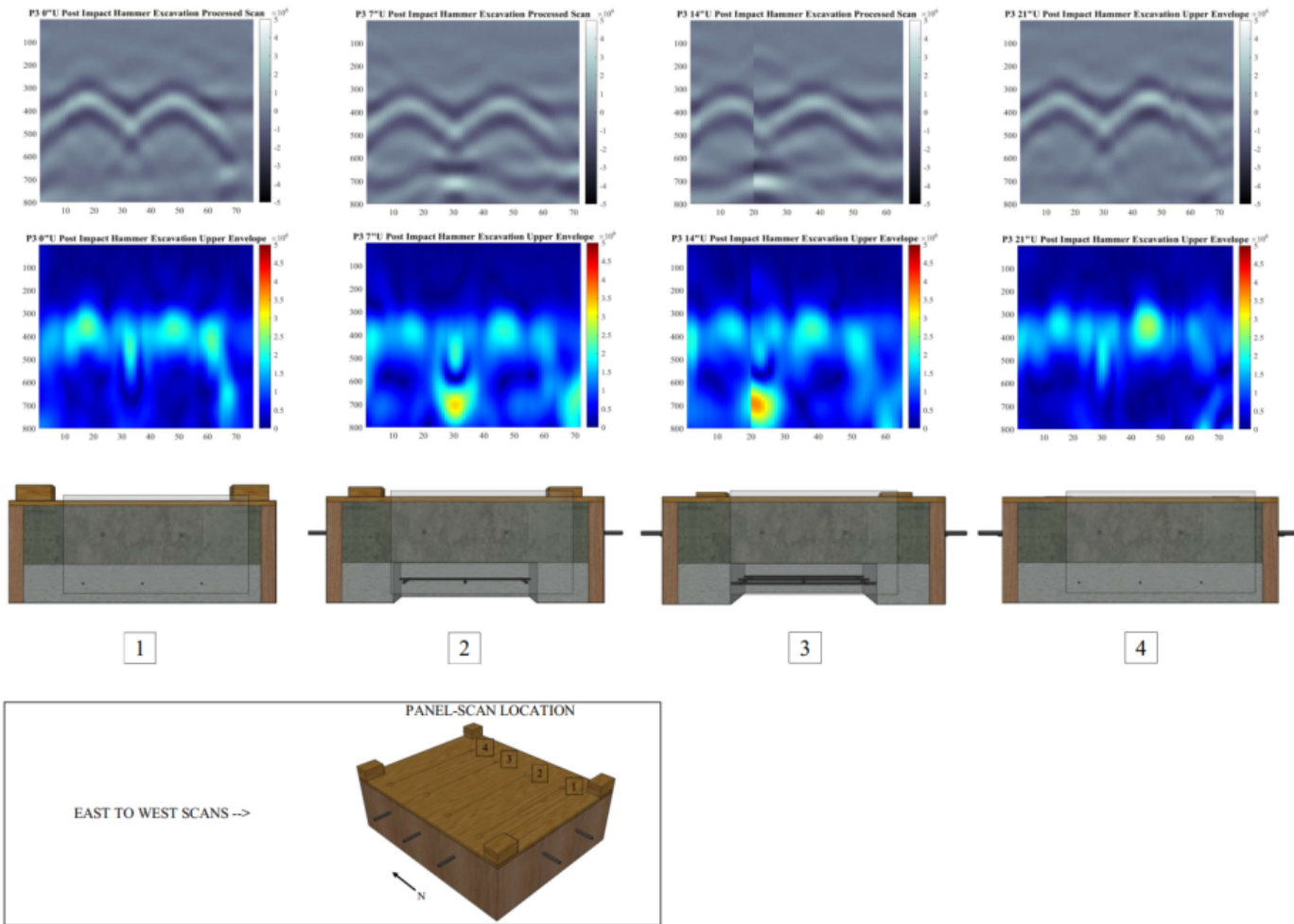


Figure 4-24: 1600 MHz post excavation east to west scans on panel 3 showing the second highest recorded amplitude increase within the substrate for a panel cut by the impact hammer.

PANEL 4 - POST IMPACT HAMMER EXCAVATION SCANS FROM SOUTH TO NORTH ON BOTTOM FACE BETWEEN PLYWOOD BOTTOM AND 1.2 NANSECONDS PAST SHOTCRETE/CONCRETE INTERFACE USING 1600 MHZ ANTENNA

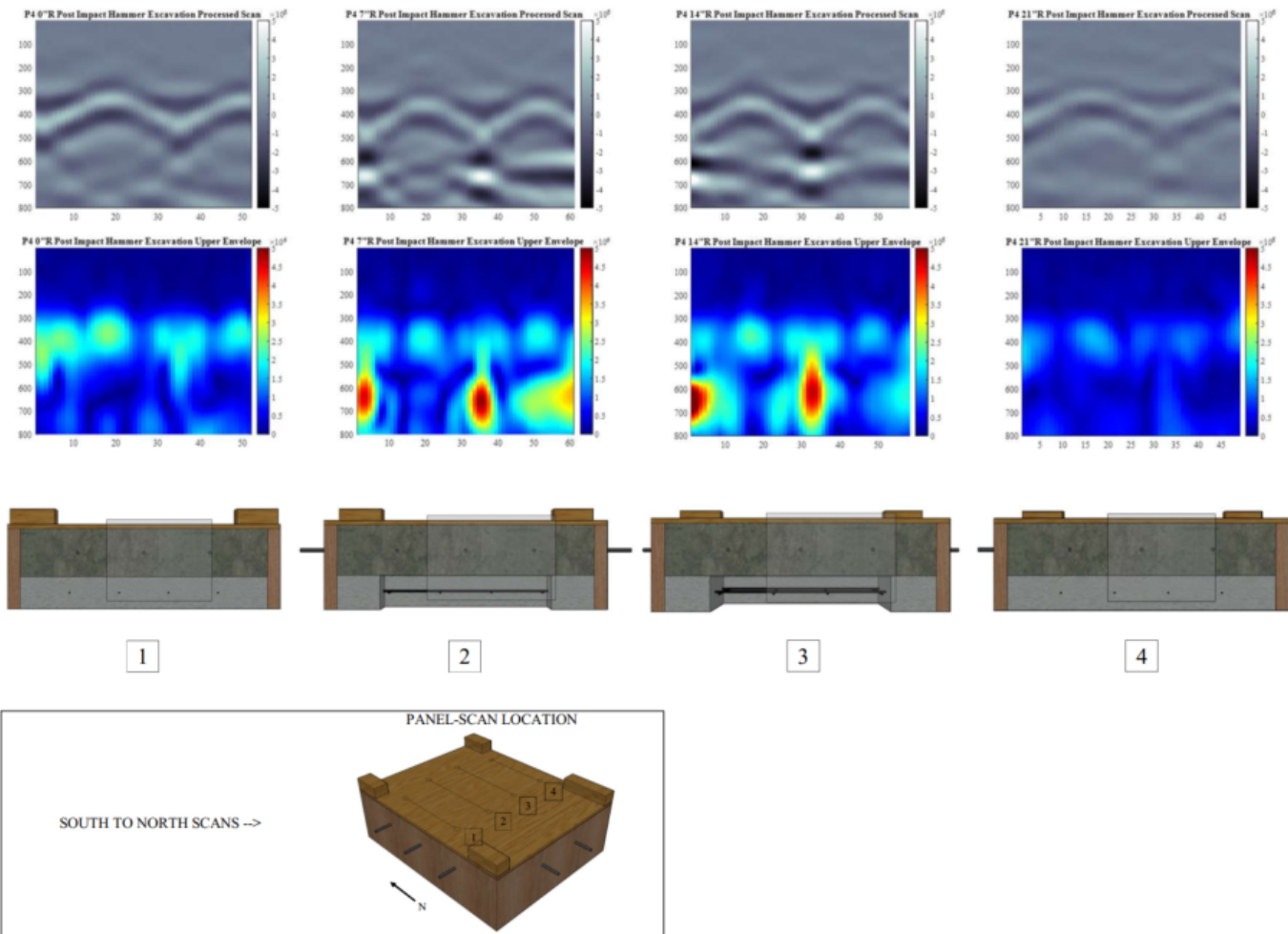


Figure 4-25: 1600 MHz post excavation south to north scans on panel 4 showing the highest recorded amplitude increase within the substrate for a panel cut by the impact hammer.

PANEL 4 - POST IMPACT HAMMER EXCAVATION SCANS FROM EAST TO WEST ON BOTTOM FACE BETWEEN PLYWOOD BOTTOM AND 1.2 NANSECONDS PAST SHOTCRETE/CONCRETE INTERFACE USING 1600 MHZ ANTENNA

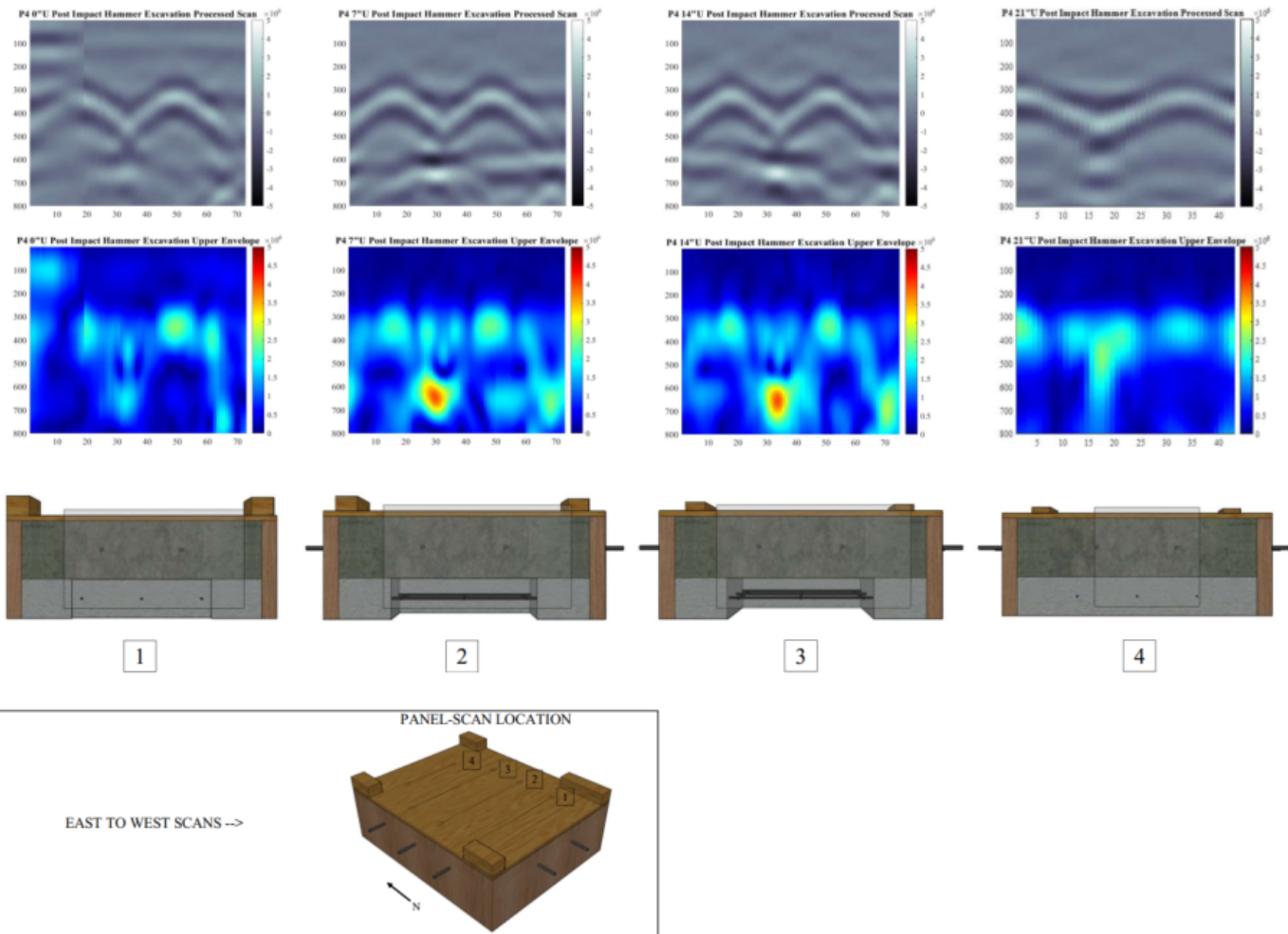


Figure 4-26: 1600 MHz post excavation east to west scans on panel 4 showing the highest recorded amplitude increase within the substrate for a panel cut by the impact hammer.

**PANEL 7 - POST WATERJET EXCAVATION SCANS FROM SOUTH TO NORTH ON BOTTOM FACE BETWEEN PLYWOOD
BOTTOM AND 1.2 NANSECONDS PAST SHOTCRETE/CONCRETE INTERFACE USING 1600 MHZ ANTENNA**

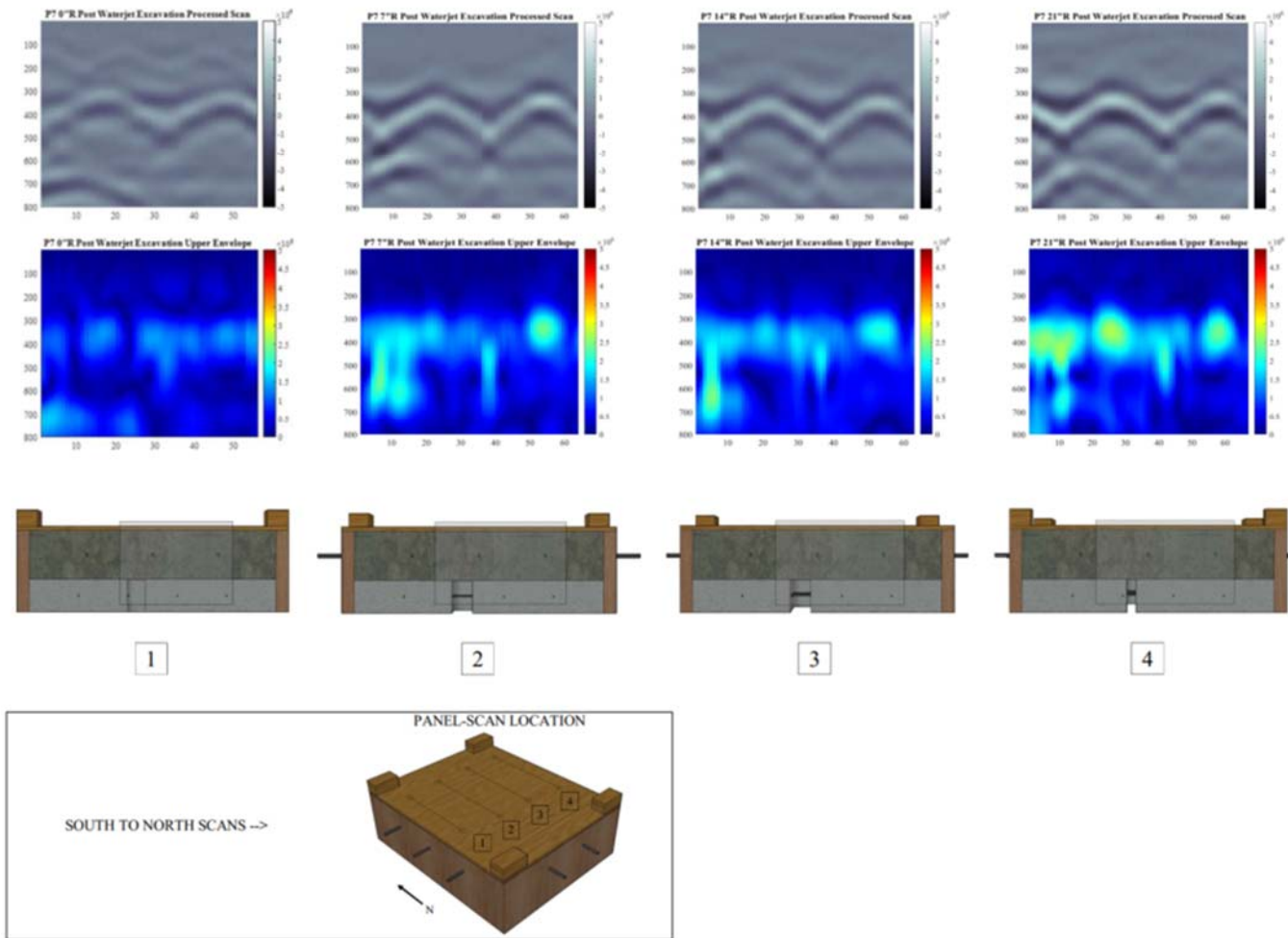


Figure 4-27: 1600 MHz post excavation south to north scans on panel 7 showing the highest recorded amplitude increase within the substrate for a panel cut by the waterjet system with notably lower amplitude increase than any of the impact hammer panels.

**PANEL 7 - POST WATERJET EXCAVATION SCANS FROM EAST TO WEST ON BOTTOM FACE BETWEEN PLYWOOD
BOTTOM AND 1.2 NANOSECONDS PAST SHOTCRETE/CONCRETE INTERFACE USING 1600 MHZ ANTENNA**

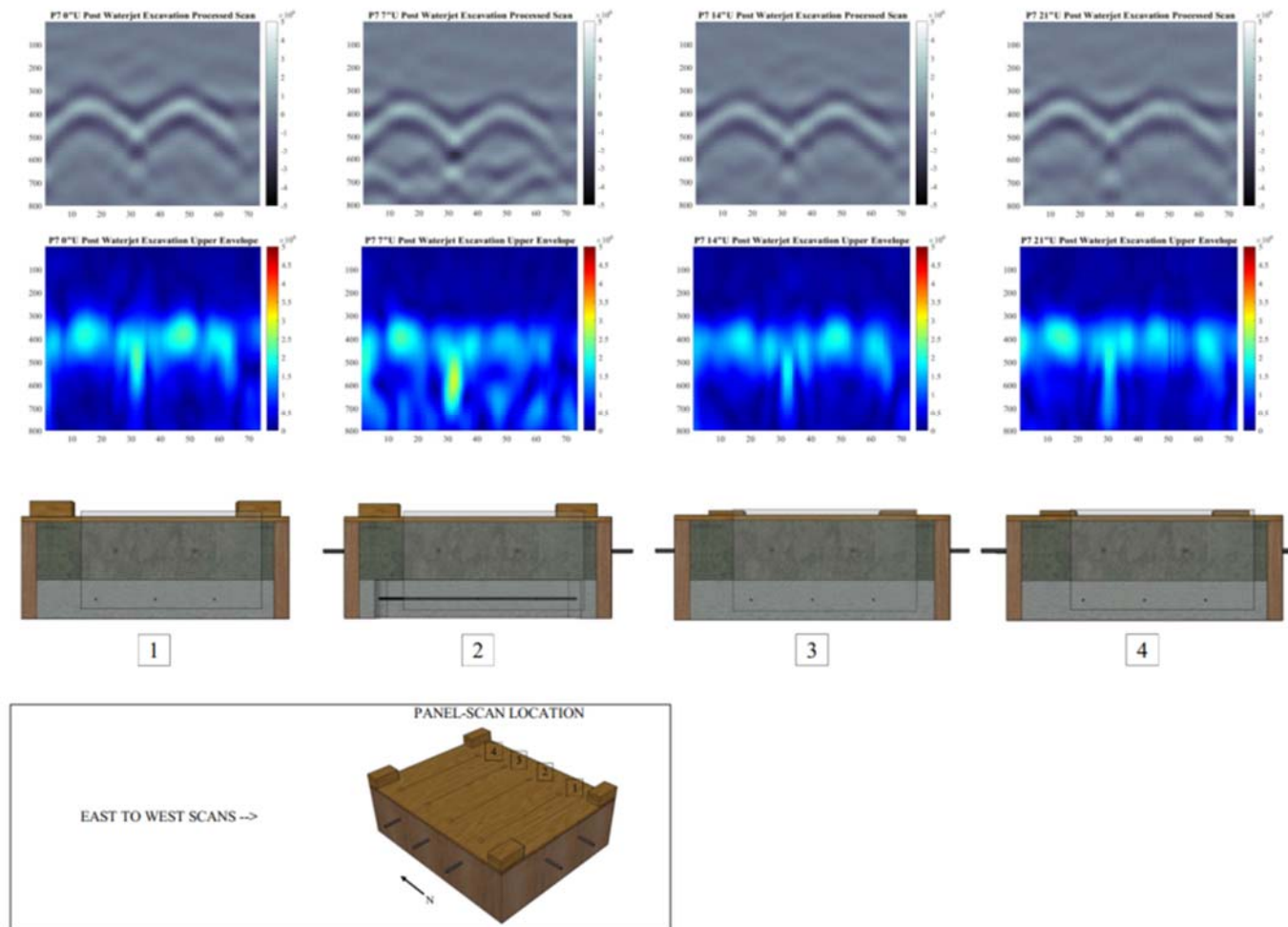


Figure 4-28: 1600 MHz post excavation east to west scans on panel 7 showing the highest recorded amplitude increase within the substrate for a panel cut by the waterjet system with notably lower amplitude increase than any of the impact hammer panels.

PANEL TEST - POST WATERJET EXCAVATION SCANS FROM SOUTH TO NORTH ON BOTTOM FACE BETWEEN PLYWOOD BOTTOM AND 1.2 NANSECONDS PAST SHOTCRETE/CONCRETE INTERFACE USING 1600 MHZ ANTENNA

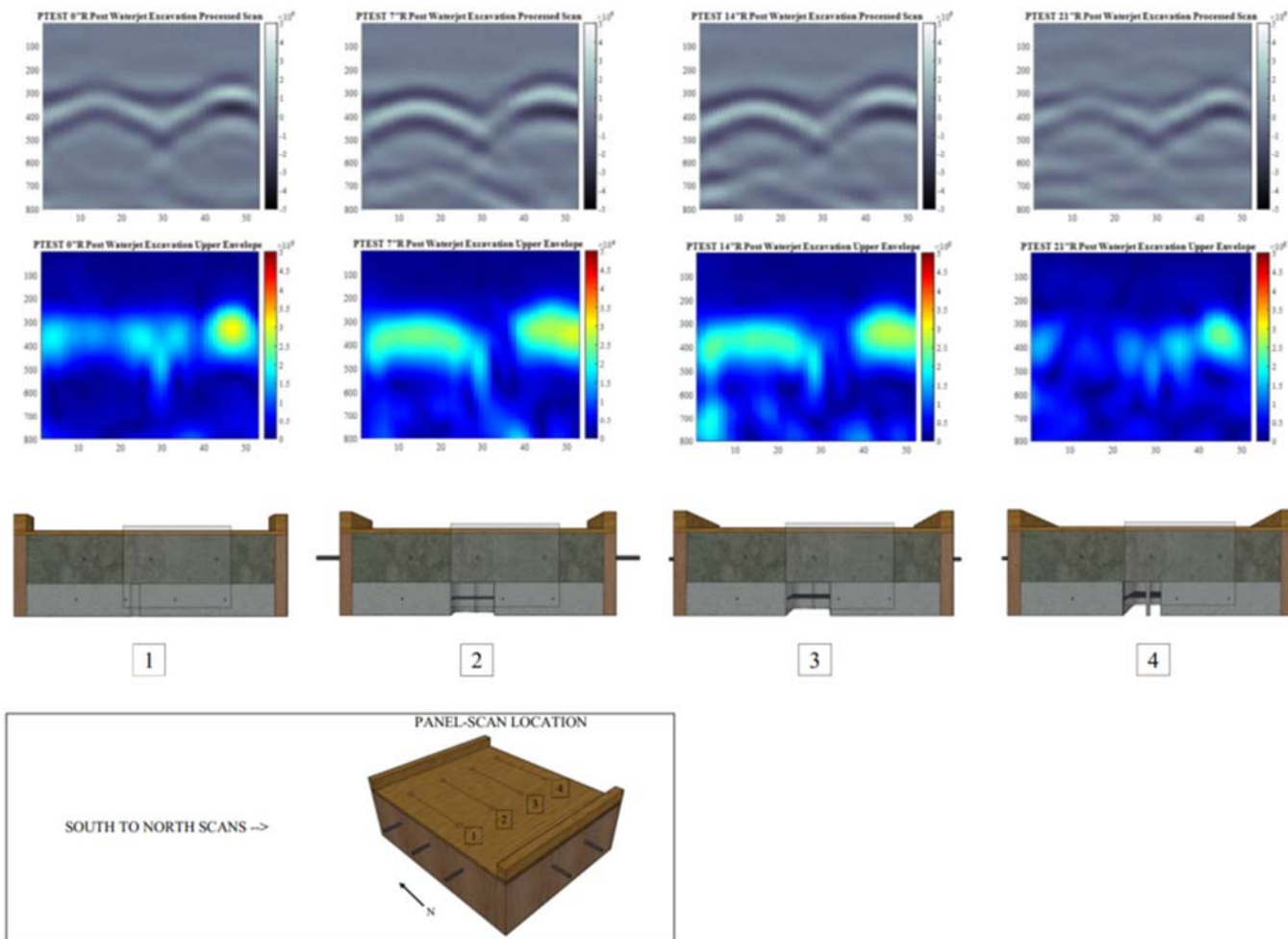


Figure 4-29: 1600 MHz post excavation south to north scans on panel TEST showing the lowest recorded amplitude increase within the substrate for a panel cut by the waterjet system with notably lower amplitude increase than any of the impact hammer panels.

**PANEL TEST - POST WATERJET EXCAVATION SCANS FROM EAST TO WEST ON BOTTOM FACE BETWEEN PLYWOOD
BOTTOM AND 1.2 NANOSECONDS PAST SHOTCRETE/CONCRETE INTERFACE USING 1600 MHZ ANTENNA**

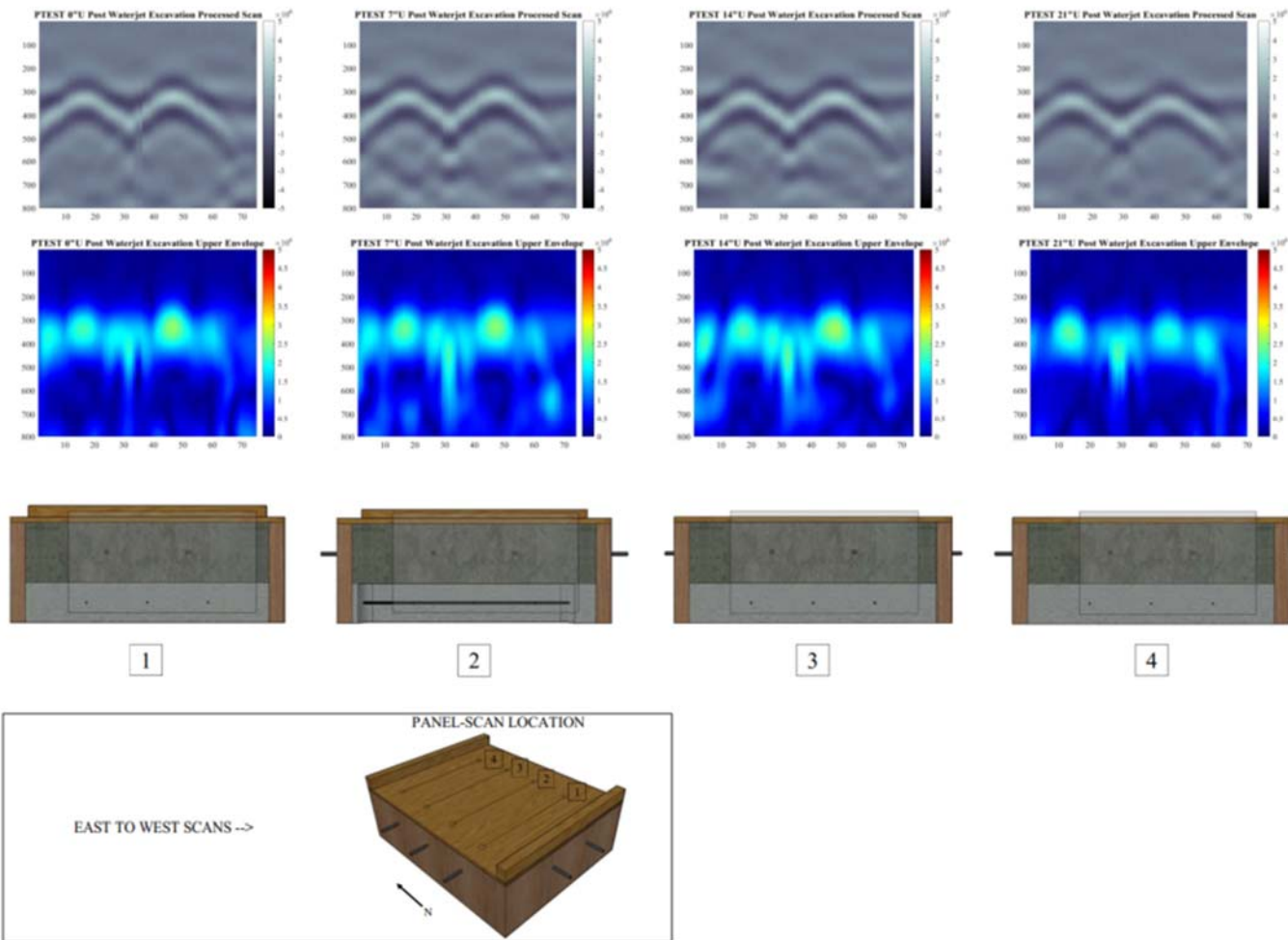


Figure 4-30: 1600 MHz post excavation east to west scans on panel TEST showing the lowest recorded amplitude increase within the substrate for a panel cut by the waterjet system with notably lower amplitude increase than any of the impact hammer panels.

4.5.4 Non-Destructive Analysis from microCT Scans of Cores from Panel 4 and Panel 7

Due to availability of the scanning equipment within the Department of Geophysics, only Core 1 from Panel 7 and Panel 4 were examined. During the scanning process for each core sample, 507 cross-sectional images were generated through reconstruction. Six cross-sectional images were chosen for analysis of each core to inspect potential fractures generated due to the testing method. These six images were chosen based on spanning above and below the midpoint of the focus area, leading to the chosen cross sectional ID's of 213, 233, 253, 254, 274, and 294 for each core's batch of scans, as shown in Figure 4-31 through Figure 4-34. In addition to the six cross-sectional images chosen from each core sample for analysis, Audio Video Interleave (AVI) files were created using ImageJ, a Java-based image processing program, to present all images of every core in movie format and are available in electric format in Appendix B-6.

Due to the varying densities of components that constitute concrete, one can visually distinguish between aggregate, cement matrix, and cavities on a cross-sectional image generated by the MicroXCT-400 as they contain their own relative X-Ray attenuation rates [55]. Within the greyscale cross-sections reconstructed for this research, the aggregate is the light blocky material, due to it having the highest density compared to the rest of the constituents, the cement matrix is darker than the aggregate, and the cavities are the darkest shade. During interpretation, it is important to note that both voids and fractures exhibit the same X-Ray attenuation rate, meaning that air cavities and material failure due to testing would be the same dark shade within the greyscale image. Therefore, investigating the geometry of the cavity is crucial when determining if its occurrence is natural to the concrete sample or a result of excavation. For example, entrapped air cavities natural to the concrete appear as black circles of varying diameters, while a fracture/failure would appear as a hairline that extends from one point to another.

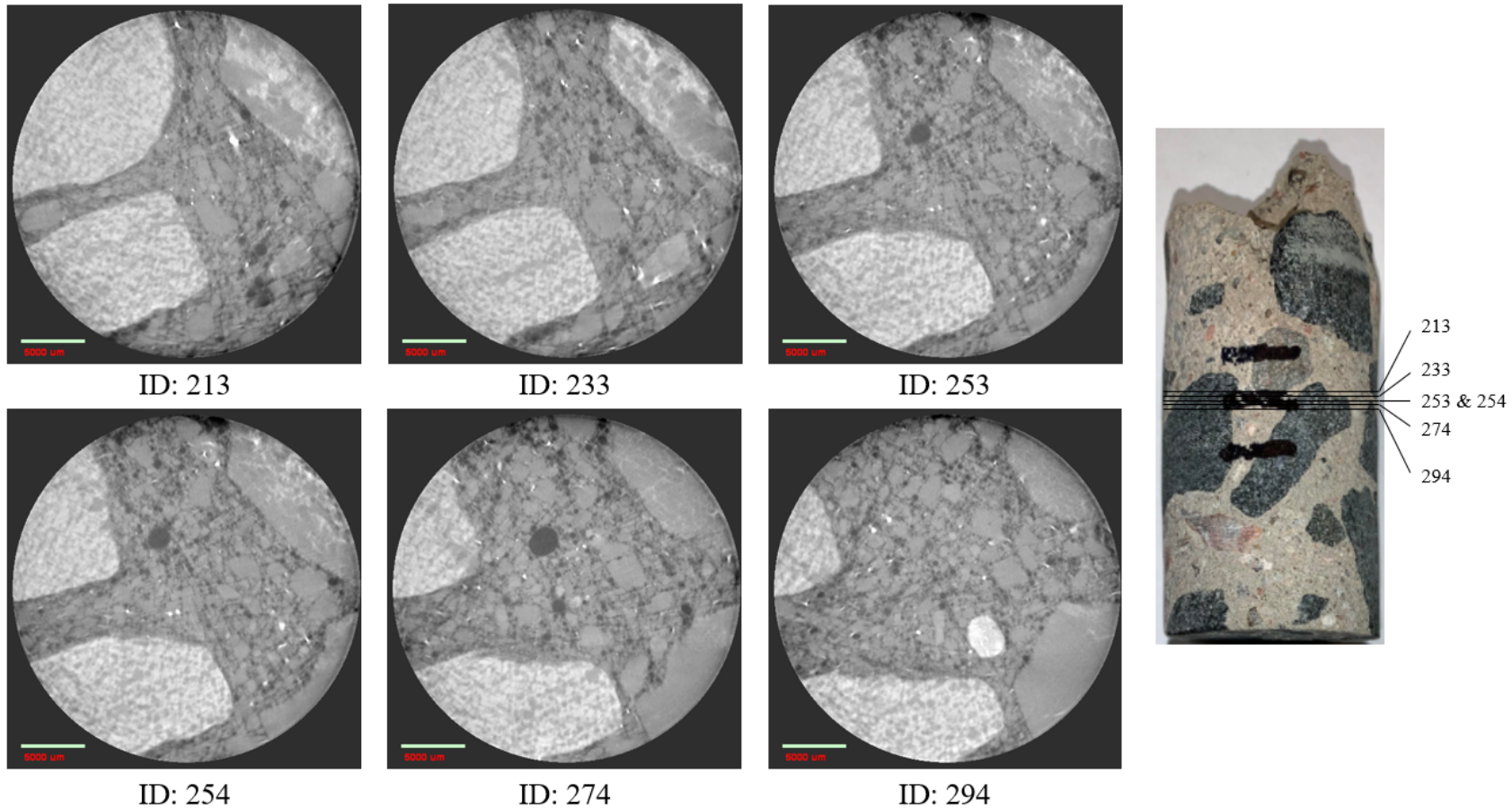


Figure 4-31: Core 1, panel 7 top half microCT scan sections with reference on core sample.

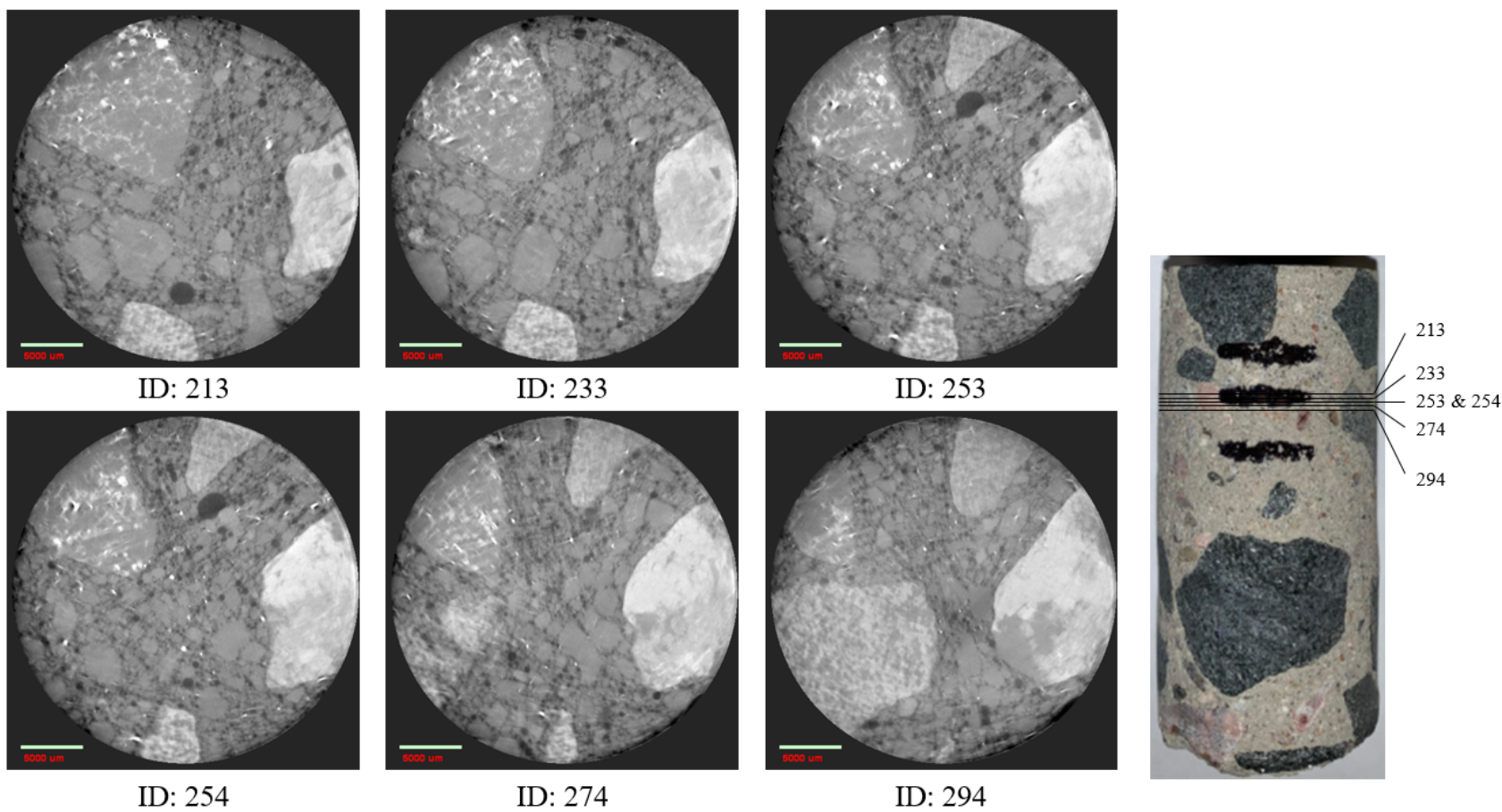


Figure 4-32: Core 1, panel 7 bottom half microCT scan sections with reference on core sample.

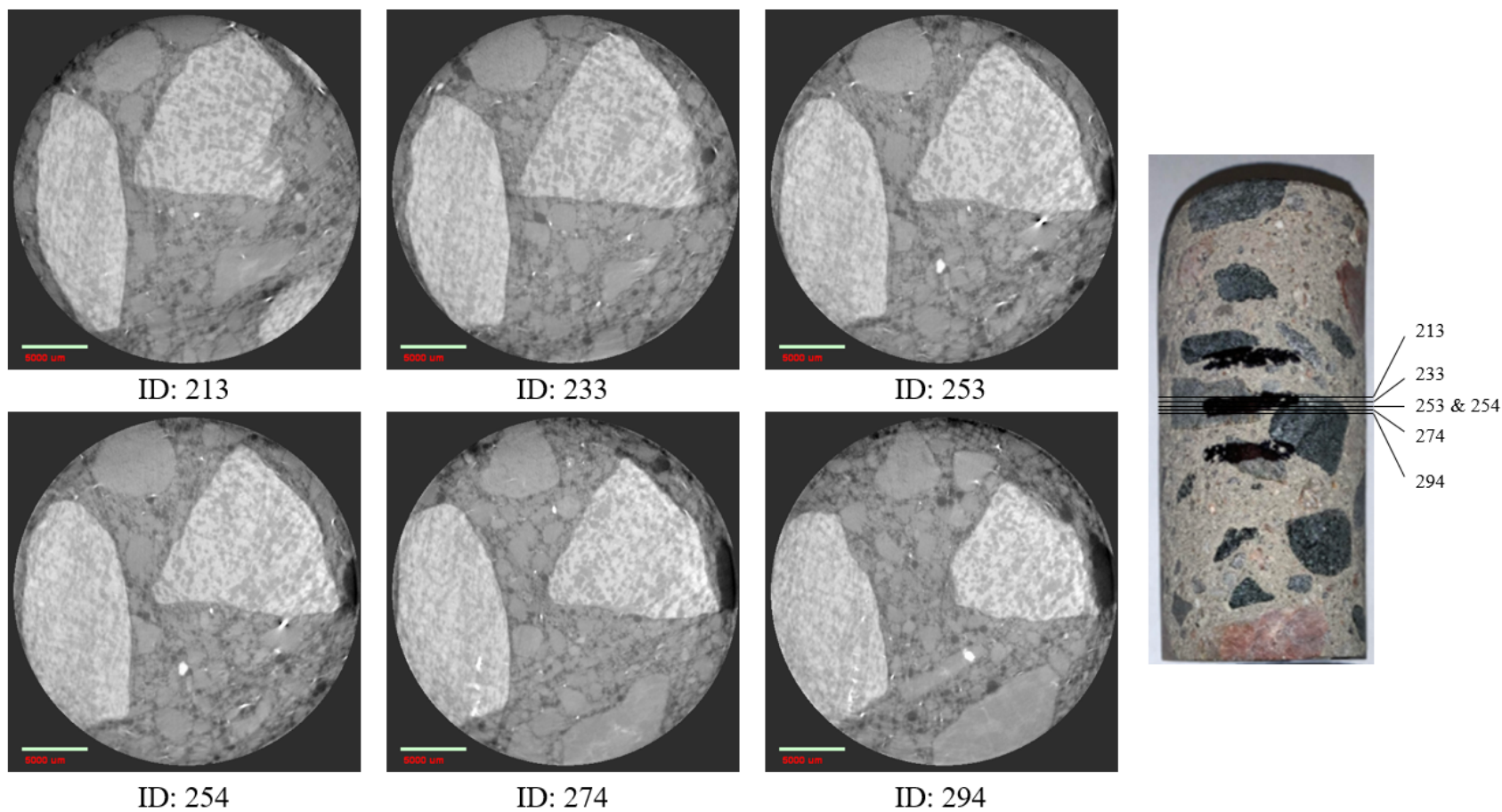


Figure 4-33: Core 1, panel 4 top half microCT scan sections with reference on core sample.

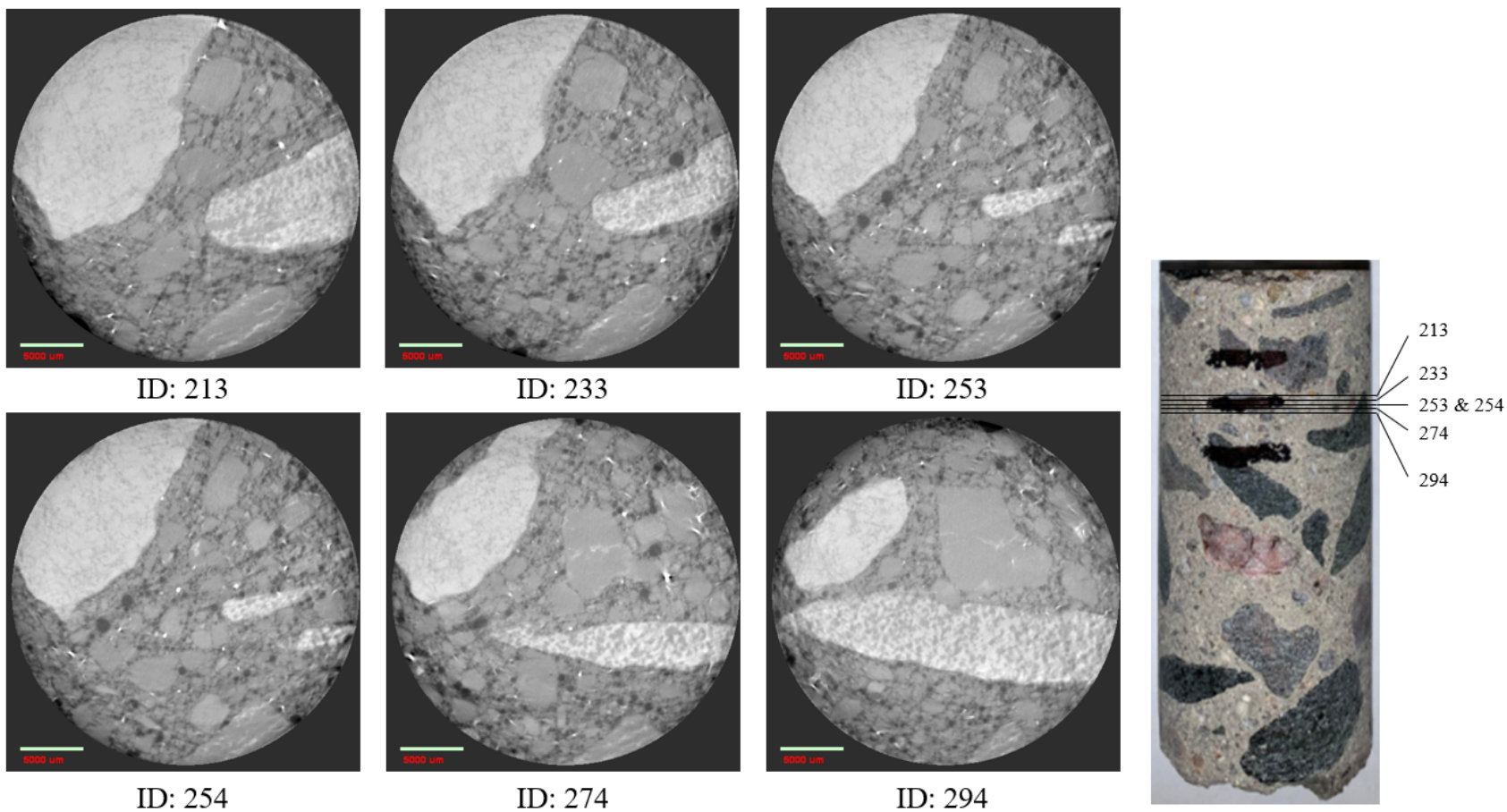


Figure 4-34: Core 1, panel 4 bottom half microCT scan sections with reference on core sample.

CHAPTER 5 - DISCUSSION OF RESEARCH RESULTS

5.1 Introduction

The research objectives outlined in Chapter 1 are as follows:

- Investigate waterjet system operating parameters necessary to cut the shotcrete layer;
- Investigate the fracture mechanisms associated with waterjet cutting of the shotcrete layer;
- Verify that waterjets can successfully be used as an alternative shotcrete removal tool; and
- Validate the hypothesis that waterjet removal of these liners will likely result in less collateral damage than those produced by conventional methods.

The results and observations associated with the particular steps taken within the research methodology to complete these objectives are outlined in Chapter 4. This chapter discusses the research results, summarizing completion of the research objectives through empirical comparison of excavation methods, as well as an analysis of the proposed hydroexcavation technology.

5.2 Investigation of Waterjet System Operating Parameters Needed to Cut Shotcrete Layer

There is no one combination of waterjet system operating parameters required to cut shotcrete in a manner specific to the requirements of this research project. Therefore, it is important to point out that the results that follow are not the optimum parameters for this type of work. They are a starting point in research that investigates the failure of shotcrete under waterjet impingement. While the pump pressure, measured at the pump discharge manifold, was 189.6 MPa (27,500 PSI), pressure losses throughout the waterjet system led to a calculated pressure of 179.0 MPa (25,966 PSI) at the nozzle, giving an overall system pressure loss of 10.6 MPa (1,534 PSI). This total pressure loss is a product of flow rate and system components, such as fluid friction in the flexible hoses and high-pressure fittings, the manifold and directional control valves, swivel components, and nozzle assembly (Appendix B-2). Due to the dimensions of the nozzle and applied value of 0.9 for coefficient of discharge, the velocity of the waterjet stream out of the nozzle was 538.9 m/s (1,768 ft/s). The kerf depth of the impinging jet into the shotcrete material was 0.8 cm (0.3 inches) for every complete pass of the nozzle assembly when the standoff distance was 8.9 cm (3.5 inches). Once the standoff distance increased to 12.7 cm (5 inches), the kerf depth recorded around 0.5 cm (0.2 inches) for every complete pass and was consistently at this cutting depth until the standoff distance reached 19.1 cm (7.5 inches). This is important for the operator to understand when using these specific waterjet parameters as the jet is making its final passes before reaching the target cutting depth. For example, there were some instances where the jet cut into the substrate layer. While this may be beneficial in some

instances where the operator wants to cut into the substrate to create an ideal bonding surface, cutting too deep into the substrate may not be desired.

Higher vibrations were recorded from accelerometers during specific modes of operation, such as when standoff distance was below 8.9 cm (3.5 inches), when the nozzle of the jet was stalled on one area while reversing direction, and when the nozzle traversed across areas of kerf geometry where additional free-surfaces existed because of adjacent kerfs. These instances can all be observed and adjusted by the operator to further reduce the induced vibration from the excavation tool. Due to the empiric testing, it is now known that a standoff distance of less than 8.9 cm (3.5 inches) is not ideal for this particular operating scenario. Additionally, the impinging jet should keep a consistent attack angle, without an additional angle of tilt, while avoiding instances of stalling on one area during operation. Traverse and rotation of the nozzle assembly are critical components of exposing weakness within the cement binder of shotcrete/concrete and limiting vibration induced through the entire panel.

5.3 Investigation of Fracture Mechanisms Associated with Waterjet Cutting of the Shotcrete Layer

Excavation of the kerf during waterjet testing was developed using conventional, commercially available cleaning accessories that included a twin orifice rotating nozzle assembly. As prescribed by the testing methodology, the nozzle assembly made multiple passes over the surface of the shotcrete using a pneumatic linear traverse, rapidly eroding the cement binder between ASTM C-33 sand particles, generating a clean-cut slot with relatively smooth walls compared to the kerf created by the impact hammer. During the waterjet cutting tests, the wire mesh within the shotcrete layer was not cut and left completely intact. Additionally, when in the path of the waterjet, the wire mesh was cleaned, with no occurrence of flash rust, and shotcrete was removed around the surface area of the steel reinforcement to continue excavation below its plane of orientation. However, it was noticed that, near the edges of the cut, the wire mesh tended to block the path of the waterjet in such a way that shotcrete was not able to be completely eroded to the wall of the slot where wire mesh was not present (Figure 5-1). This phenomenon should be considered when steel reinforcement is present within the desired excavation path. As stated in Chapter 4, while the waterjet system parameters used for this research were successful in leaving the wire mesh intact with no occurrence of flash rust, it is important to note that it is possible to cut the steel reinforcement with a waterjet, depending on the combined pressure and flow rate used. While the system parameters needed to cut the steel reinforcement would be far in excess of those required to excavate either the shotcrete or concrete substrate, caution is warranted when selecting the operating parameters to prevent any unintended damage to the mesh or rebar.

When reaching the concrete layer, the waterjet rapidly eroded the cement binder between the 2 cm ($\frac{3}{4}$ inch) aggregate, leaving the aggregate intact. Testing on Panel 7 showed that if the jet only cut slightly into the substrate, exposing the initial layer of aggregate while leaving it bonded with cement on its bottom face, the excavation surface would become a prime area for application of a new shotcrete layer. This is due to the aggregate being left completely

intact (not split as observed with the mechanical impact tool) providing a rough, undamaged surface to adhere to.



Figure 5-1: Example of edge effect caused by wire mesh, blocking erosion by waterjet, leaving shadow of shotcrete behind steel reinforcement.

Empiric waterjet testing of Panel TEST illustrated that there is an optimal relationship between translation of the jet assembly and the rotation rate of the swivel head for a given set of operating parameters, including flow rate, jet velocities, standoff distance, and the angle of the jet orifices from horizontal. Given the research objectives, it is important to note that no attempt was made to optimize these relationships.

With regards to the shotcrete simulant cuttings generated by the waterjet, 100 percent of the captured material measured less than 8,350 microns (0.25 inches), with 75 percent being smaller than 2,540 microns (0.1 inches). Comparatively, three sieve tests of cuttings generated by the impact hammer resulted in an approximate range of 53 to 63 percent passing at 8,350 microns, as well as an approximate range of 37 to 41 percent passing at 2,540 microns. Therefore, with the waterjet system and operating parameters used for this research, the cuttings generated will be significantly finer overall than those of an impact hammer and, more specifically, will not produce large chips of shotcrete. These results support the contention that vacuum removal (mucking) systems can be integrated into the waterjet excavation process to mitigate the need for material re-handling during the mucking of excavated shotcrete and other materials. This is consistent with what was observed in the Conjet project to repair the damaged concrete liner after a fire in the Chunnel Rail Tunnel. It is also important to note that, undamaged aggregate will comprise part of the cuttings generated during waterjet excavation. While the aggregate in this case for the shotcrete simulant was ASTM C-33 sand, which is relatively small compared to aggregate used for a type I/II commercial ready concrete, one should be aware that cuttings from continuous waterjet excavation will contain whatever size aggregate present within the

shotcrete/concrete mix, if the jetting process completely erodes the cement matrix around the intact particles.

5.4 Verification that Waterjets can Successfully be Used as an Alternative Shotcrete Removal Tool

The overall objective of the empiric testing process was to excavate the shotcrete layer until the interface between the shotcrete and concrete layer was reached. This would be the scenario in the field during liner rehabilitation, maintenance, and repair. The variables of time and volume of material removed were not important in this testing process, although they were still documented. Therefore, if the waterjet was capable of removing a section of the shotcrete layer in the panel until reaching concrete, it would be deemed as a successful alternative shotcrete removal tool.

Based on the results shown in Section 4.4.1, the waterjet effectively removed the shotcrete layer until reaching the concrete layer through incremental volumes during each pass of the dual orifice rotating nozzle system. The waterjet system configured for this research is fully capable of completing the job typically executed by conventional methods, such as the use of an impact hammer. This is critically important in advancing a research agenda for this scope of work because it proves that waterjets are a viable excavation tool for liner rehabilitation. Empiric testing should now focus on parametric analysis using structural liners that are damaged and require repair. As with this research initiative, it is critical that operating parameters simulate the actual operating environment and best operating practices.

Additional testing can also be conducted to investigate ways to reduce time required to cut slots into shotcrete using a high-pressure waterjet system. Within the scope of this research, issues encountered with regards to the amount of time required to excavate a given volume of material directly related to the nozzle dwell time that occurred whenever the traverse slide was reversed between passes. The significant dwell time was a function of the long air hoses, the type of high-speed traverse used, and the compressible nature of air in pneumatic motion systems. If an efficient traverse system was developed, the productivity of the waterjet system would not only be far more productive, but would also result in further reduction in the vibrations induced into the target material because of the elimination of nozzle stalling.

5.5 Validation of the Hypothesis that Waterjet Liner Excavation will likely result in Less Collateral Damage than that Produced by Conventional Methods

Visual inspection of Panels 2, 3, 4, 7, and TEST exemplified stark differences between measurement of fracture/failure, delamination, damage to steel wire mesh, and percentage of split aggregate due to each testing method. Table 4-5 of Chapter 4 shows that impact hammer excavation caused more counts of fracture/failure, compared to that of waterjet cutting, along the excavation profile and surrounding shotcrete layer with 13, 22, and 11 for Panels 2, 3, and 4 respectively. Panels 7 and TEST resulted in fracture/failure counts of 2 and 4. While the panels

tested upon by the waterjet system did result in measured fracture/failure, there was no visual record of delamination, damage to wire mesh, or split exposed aggregate. This is especially important because the panels tested upon by the impact hammer contained damaged wire mesh, measured delamination in two of the three panels, and measured over 50% split exposed aggregate for all panels. The highest measured delamination within the excavation profile of a panel subjected to impact hammer testing was 131.5 mm (5.2 inches) from Panel 3, which also had the highest recorded vibration from accelerometers.

Accelerometer data gathered during testing of Panels 2, 3, 4, 1, 7, and TEST illustrated significant difference in vibrations induced by the chosen excavation tools with the impact hammer consistently recording acceleration far higher than that of the waterjet. The range of measured acceleration according to the positive and negative peaks gathered in Table 4-6 are illustrated in Figure 5-2. Within this figure, the labeling of each panel is preceded by the testing method used where “IH” stands for “Impact Hammer” and “WJ” stands for “Waterjet”.

This data clearly demonstrates that use of a high-pressure waterjet systems will translate substantially less vibrations to the embedded steel reinforcement. The high readings of acceleration shown in Panel 1 can be reduced through adjustment of operating parameters, specifically avoidance of stalling the nozzle assembly while keeping a consistent traverse speed and avoiding standoff distances of less than 8.9 centimeters (3.5 inches). It’s important to note that, while particularly high acceleration was recorded for Panel 3, experienced use of the impact hammer could result in lower readings like that of Panel 2, however, these are still considerably higher than data gathered for all waterjet panels.

The post excavation 1600 MHz GPR scans provided sufficient quantitative evidence outlining differences in the substrate damage as a result of each testing method. However, it is crucial to point out commonalities between each scan due to the behavior of the antenna. The overlapping of reflection from individual rebar within each sample was consistent during analysis of each scan. This overlap of hyperbola would occur as one or multiple streaks located between the level of the rebar and the level of the shotcrete/concrete interface. This is important to recognize because, initially, in the upper envelope figures, it may appear like an increase in amplitude due to testing, designating a potential area for micro-fractures within the substrate. However, this is not the case as the overlap of reflection hyperbola were present in almost every scan, even in scans where no excavation occurred. It is also important to recognize that steel reinforcement, while easy to identify using GPR, acts as a perfect reflector, where nearly 100% of the emitted energy from the antenna is reflected [42], making it difficult to analyze an area beneath it. With regards to the scans gathered for this research, most increases in amplitude due to excavation were located in areas of substrate between the rebar, even if the excavated profile extended along the entirety of the GPR scan, thus correlating with the fact that steel acts as a perfect reflector. Due to this occurrence, it was expected that areas of potential substrate damage would not be easily identifiable directly beneath the rebar.

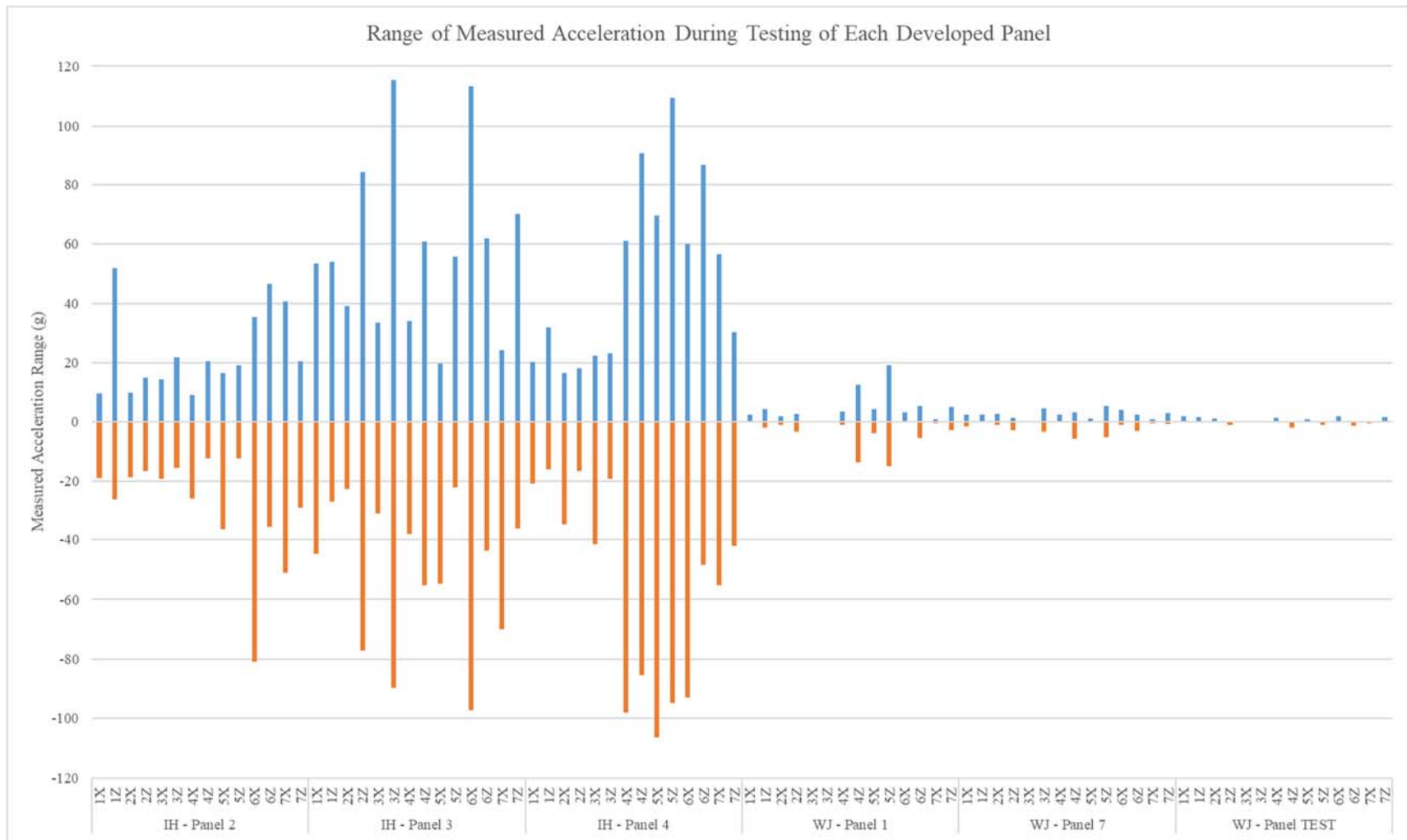


Figure 5-2: Range of measured acceleration during testing of each developed panel.

With the aforementioned commonalities described for each acquired scan, there were differences in amplitude strength increase within the substrate for panels excavated using an impact hammer as compared to that of the waterjet system. This is particularly evident for post excavation scans of Panel 4 which demonstrated the highest degree of amplitude increase that spanned from the shotcrete/concrete interface to the level of the rebar as shown in Figure 4-25. As discussed in Chapter 4, an increase in amplitude within each scan after testing is identified as a potential area of substrate damage due to previous research which showed that reflected waves coming off the top and bottom of voids combine with each other and induce positive interference, leading to an increase in amplitude of the returned EM signal and thereby, intensifying the reflection shown on the 2D scan [44]. The pre-excavation scans acquired from the 2600 MHz antenna helped verify that there were increases in amplitude due to testing as the upper envelope scans had no significant sign of reflection within the substrate other than where the rebar is located. Table 5-1 outlines peak amplitude measured by the upper envelope scans for each panel.

Table 5-1: Peak amplitude measured by upper envelope scans of each panel.

Panel	Peak Measured Upper Envelope Amplitude
2	3509300
3	4711000
4	5965100
7	2873200
TEST	3124200

The strength of amplitude spanning into the substrate of Panels 3 and 4, which were excavated by impact hammers, is far higher than that of Panels 7 and TEST, which were excavated by waterjets. This leads to the belief that there may be more micro-fractures, or instances of concrete deterioration, present within the substrate of panels tested using the impact hammer. For additional analysis, amplitude was measured at the vertex of each located rebar's reflection hyperbole within every panel's scans to compare with peak levels shown in Table 5-1. These findings, along with each panel's average measured rebar amplitude, are given in Table 5-2.

Table 5-2: Post excavation rebar amplitude measurements.

Panel	Scan ID	Identified Rebar (Fully in Scan)	Measured Upper Envelope Amplitude
2	0”R	1	2300000
	7”R	1	1742000
	14”R	1	1621000
	21”R	1	1143000
	0”U	1	2289000
		2	2235000
	7”U	1	2289000
		2	1760000
	14”U	1	2542000
		2	1921000
	21”U	1	1391000
		2	1642000
AVERAGE			1906250
3	0”R	1	2146000
		2	2570000
	7”R	1	1652000
		2	2490000
	14”R	1	1662000
		2	2421000
	21”R	1	796300
		2	2406000
	0”U	1	2447000
		2	2229000
	7”U	1	1668000
		2	1912000
	14”U	1	1894000
		2	1979000
	21”U	1	1931000
		2	2658000
AVERAGE			2053831
4	0”R	1	2514000
		2	2042000
	7”R	1	2003000
		2	1969000

Table 5-2: Post excavation rebar amplitude measurements (cont.).

Panel	Scan ID	Identified Rebar (Fully in Scan)	Measured Upper Envelope Amplitude
4	14”R	1	2142000
		2	1617000
	21”R	1	1542000
		2	1203000
	0”U	1	2030000
		2	2472000
	7”U	1	2171000
		2	2365000
	14”U	1	2242000
		2	2369000
	21”U	1	2400000
2		1856000	
AVERAGE			2058563
7	0”R	1	1356000
		2	1372000
	7”R	1	1722000
		2	2359000
	14”R	1	1694000
		2	2030000
	21”R	1	2698000
		2	2411000
	0”U	1	2066000
		2	2276000
	7”U	1	2243000
		2	1572000
	14”U	1	1873000
		2	2036000
	21”U	1	2166000
2		1814000	
AVERAGE			1980500
TEST	0”R	1	1383000
		2	3124200
	7”R	1	2455000
		2	2879000
	14”R	1	2288000
		2	2757000
	21”R	1	732800
		2	2447000
	0”U	1	2205000
		2	2583000
	7”U	1	2323000
		2	2535000
	14”U	1	2237000
		2	2638000
	21”U	1	2310000
2		2049000	
AVERAGE			2309125

The data in Table 5-2 shows that peak measured amplitude for panels excavated by the impact hammer far exceeded the readings from reflections given by the rebar. Peak amplitude reached for panels tested upon by the waterjet were either much closer or exactly the same as reflection readings given by the rebar. For example, the peak amplitude reached by Panel 7 was 2873200 and a rebar reflection reading for scan 21”R was 2698000. The peak amplitude reached by Panel TEST was 3124200 which is exactly the rebar reflection reading in scan 0”R. This shows that the strength readings within the substrate recorded as a result of impact hammer testing are consistently higher than those gathered during waterjet excavation.

Due to the timing of GPR equipment rentals in May, 2018, post excavation scans were acquired with a 2600 MHz antenna on panels excavated by the impact hammer. Due to these panels having scans gathered before and after testing with the same strength antenna, it was possible to generate figures visualizing the subtraction of amplitude, meaning the difference would show how amplitude changed in specific areas due to testing. Therefore, the difference in amplitude at the shotcrete/concrete interface and within the concrete layer between pre and post testing GPR scans of Panels 2, 3, and 4 were analyzed (Appendix B-6). MATLAB was utilized to subtract the upper envelope scans at each panel location. Future research could be conducted to acquire similar subtraction figures on the waterjet tested panels using a 2600 MHz antenna for continued comparison of substrate condition as a result of each form of excavation. All figures generated for the purpose of this research are available for additional interpretation in order to further this field of work.

Use of the MicroXCT-400 provided high resolution cross-section images of cores drilled into the concrete substrate from the excavation face of Panel 7 and Panel 4 which were tested using the waterjet system and impact hammer respectively. The use of microCT allowed for inspection of ranges 28 to 51 millimeters (1.1 to 2.0 inches) and 85 to 102 millimeters (3.3 to 4.0 inches) below the shotcrete/concrete interface. While the scans were useful in identifying constituents of the concrete at these specific locations below the interface, there was no indication of fracture/failure within any of the generated images. Therefore, there was no difference in internal structure at these specific locations within the substrate of Panel 4 and Panel 7. These core samples are available for future analysis, including the cores taken outside of the excavation face of both Panel 4 and Panel 7. It is suggested that microCT scans be acquired through the entire length of each core for complete analysis of potential micro-fractures generated by each excavation tool. Additionally, different scanning resolutions can be utilized to inspect every core sample in varying detail.

The impact energy associated with the handheld mechanical excavation tool used for this research was 6.6 foot-pounds, which is relatively smaller than the potential impact energy of a hammer attached to the boom of conventional rubber-tired equipment. This indicates that the induced vibration and collateral damage associated with impact hammer excavation in this field of work could potentially be even higher and more severe than the measured results seen in this study. This further reiterates the positive effects waterjet technology can facilitate as a substitute

to an impact hammer for rehabilitation work through improvements in both worker safety and structural integrity of underground shotcrete/concrete structural liners.

The results obtained from visual inspection, accelerometer data, and GPR scans of the panels correlate with observations made in the literature favoring the use of hydrodemolition in bridge deck removal and repair work [56], specifically those identifying structural benefits to its use including:

- Providing a rough surface profile for excellent mechanical bond to repair materials;
- Eliminating surface micro-fracturing;
- Not fracturing exposed aggregates;
- Minimizing vibration; and
- Cleaning steel reinforcement and leaving it undamaged.

The data collected for this research project provides supplemental validation of the benefits of hydrodemolition. According to Asadi et al, the Federal Highway Administration reported that 11% of the bridges in the United States are rated as structurally deficient and over 30% of existing bridges have exceeded their 50-year design life [54]. This means that bridge deck analysis and rehabilitation work will substantially increase in the years to come. The findings from this research, specifically through the reduction of vibration to embedded steel reinforcement and avoidance of cutting the aggregate within the concrete layer for an improved bonding surface to the new overlay material, can be used to further advance the knowledge and use of high-pressure waterjet systems for bridge deck rehabilitation.

Overall, these results provide a baseline for a research agenda that will move towards implementing use of high-pressure waterjet systems in the tunneling, mining, and heavy construction industries for repair of compromised sections of structural liners. In May, 2020, Society for Mining, Metallurgy & Exploration (SME) Mining Engineering published the T&UC tunnel demand forecast, compiled by Jonathan Klug, David R. Klug & Associates, stating that over 1.6 million feet in length of tunnels are forecasted for development in the United States and Canada alone [4]. Major proposed underground mining projects such as Resolution in Arizona, Twin Metals in Minnesota, Black Butte in Montana, and Elk Creek Project in Nebraska, as well as extensions to current operating underground operations such as the Henderson Mine in Colorado, Eagle Mine in Michigan, and multiple operations in Nevada encompass development supported by shotcrete liners. With the current forecast of structural liner development and threat of shotcrete failure from multiple environmental and operational sources, it seems prudent to consider excavation equipment that will provide as safe a working environment as possible while keeping the structural integrity of the support system during repair.

CHAPTER 6 – SUMMARY AND CONCLUSIONS

6.1 Introduction

This chapter discusses the conclusions of this study and recommendations related to specific areas of research that require further investigation.

6.2 Summary and Conclusions

The objectives of this research were to characterize the excavation process associated with removal of damaged or structurally compromised shotcrete liners associated with repair and maintenance using waterjet technology. Additionally, this research sought to validate the hypothesis that waterjet removal of these liners would result in less collateral damage than conventional methods, such as impact hammers, and to provide a basis for in-field empiric testing of jetting parameters.

In pursuit of these objectives, testing and examination spanned a wide breadth of subjects, including: composition of underground structural liners, fracture mechanisms of impact bits, instrumentation of high-pressure waterjet systems, hydraulic fracturing excavation systems and fracture mode, instrumentation of accelerometers and a data acquisition system (DAQ) for vibration analysis, and non-destructive analysis of concrete structures, including methods such as visual inspection, ground penetrating radar (GPR), and microcomputed tomography (microCT). The following is a synopsis of the key technical conclusions identified over the duration of this study.

6.2.1 Characterizing the Excavation Process Associated with Removal of Deteriorated Shotcrete Using Waterjet Technology

For every pass of the nozzle assembly, the average kerf depth created by the impinging jet into the shotcrete material was 0.8 cm (0.3 inches) at a standoff distance of 8.9 cm (3.5 inches). Once the standoff distance increased to 12.7 cm (5 inches), the kerf depth decreased to approximately 0.5 cm (0.2 inches) for every complete pass. The cutting depth remained consistent until the standoff distance reached 19.1 cm (7.5 inches). Therefore, at an operating pressure of 189.6 MPa (27,500 PSI), measured at the pump discharge manifold, and a flow rate of 21.2 lpm (5.6 gpm), there is little to no change in the cutting depth when the standoff distance changes between the aforementioned values. Future testing should vary the operating pressure and flow parameters to investigate whether these have a greater influence on cutting depth.

Higher vibrations were recorded from accelerometers during specific modes of waterjet operation. These include situations where the standoff distance was less than 8.9 cm (3.5 inches), the nozzle assembly was stalled while the jet direction was reversed at the ends of the linear traverse, and when the nozzle trajectory was adjacent to previously excavated kerfs. Through proper system design, these modes of operation can all be avoided to further reduce

the incidence of vibration within the embedded steel reinforcement of the structural liner. During empiric testing, it was discovered that traverse and rotational velocity of the nozzle assembly are critical components of exposing weakness within the cement binder of shotcrete/concrete and limiting vibration induced through the entire panel.

The wire mesh within the shotcrete layer was left undamaged and completely intact during waterjet testing. Additionally, flash rust was not observed on the exposed wire mesh after testing. When in the path of the waterjet, the wire mesh was cleaned and shotcrete was removed around the surface area of the steel reinforcement to continue excavation below its plane of orientation. However, it was noticed that, near the edges of the cut, the wire mesh tended to block the path of the waterjet in such a way that shotcrete was not able to be completely eroded to the wall of the slot where wire mesh was not present. Based on previous observations, it is believed that a jet utilizing a higher flow rate will mitigate this issue.

With regards to the method of fragmentation when reaching the concrete substrate, the waterjet rapidly eroded the cement binder between the 2 cm ($\frac{3}{4}$ inch) aggregate, leaving the aggregate intact. The profile of the intact aggregate should provide an excellent bonding surface for the application of a new layer of shotcrete. This observation could result in the improved structural integrity of a particular section of the liner requiring repair, as compared to an excavation cut with an impact hammer, which does split aggregate at the excavation interface.

An analysis of the shotcrete cuttings generated by the waterjet resulted in a distribution where 100 percent of the captured material measured less than 8350 microns (0.25 inches) with 75 percent being smaller than 2540 microns (0.1 inches). Comparatively, three sieve tests of cuttings generated by the impact hammer resulted in an approximate range of 53 to 63 percent passing at 8,350 microns, as well as an approximate range of 37 to 41 percent passing at 2,540 microns. Therefore, with the waterjet system and operating parameters used for this research, the cuttings generated will be significantly finer overall than those of an impact hammer and, more specifically, will not produce large chips of shotcrete.

The waterjet system used for this research effectively removed the shotcrete layer until reaching the concrete layer through incremental cuts associated with each pass of the dual orifice rotating nozzle system. Therefore, the research demonstrates that waterjet systems are fully capable of achieving the required outcomes executed by conventional methods, such as use of mechanical impact hammers.

6.2.2 Validating the Hypothesis that Waterjet Excavation of Deteriorated Liners Will Result in Less Collateral Damage than Conventional Methods

After empiric testing, visual inspection of the kerf shows that, compared to waterjet cutting, the use of an impact hammer for shotcrete excavation caused damage to the embedded wire mesh, as well as more counts of fracture/failure along the excavation profile and surrounding shotcrete layer. Additionally, waterjet cutting did not result in any instances of

delamination at the shotcrete/concrete interface or split any aggregate exposed at the excavation face. These differences in the resulting profile generated by each excavation method during empiric testing shows that, from a perspective of the excavation surface, the impact hammer caused more damage to the liner during material removal and the waterjet system creates a better bonding surface for application of new shotcrete.

Accelerometer data gathered during testing illustrated significant difference in vibrations induced by the excavation tools, where the impact hammer consistently recording acceleration far higher than that of the waterjet. The readings of acceleration shown in the panels excavated by the waterjet system can be further reduced through adjustment of operating parameters, specifically avoidance of stalling the nozzle assembly while reversing direction and avoiding standoff distances of less than 8.9 cm (3.5 inches). It is also important to note that the impact energy of the mechanical hammer used for this research (6.6 foot-pounds) is comparable to those handheld units utilized in commercial applications and would be far less than the impact energy generated by a hammer attached to the boom of rubber-tired equipment. As compared to the later, the vibrations induced by conventional rubber-tired mechanical excavation equipment would likely be far greater than the data acquired in this research.

Use of a 1600 MHz GPR antenna proved useful for identifying differences in amplitude increase within the substrate of individual developed panels according to each testing method. With regards to the scans gathered for this research, most increases in amplitude due to excavation were located in areas of substrate between the rebar, even if the excavated profile extended along the entirety of the GPR scan. This is likely the result of the steel reinforcement acting as a perfect reflector. The strength of amplitude spanning into the substrate of Panels 3 and 4, which were excavated by mechanical impact hammers, is far higher than that of Panels 7 and TEST, which were excavated by waterjets. This leads to the belief that there may be more voids or micro-fractures present within those impact hammer tested panels.

The use of microCT allowed for inspection of ranges 28 to 51 mm (1.1 to 2.0 inches) and 85 to 102 mm (3.3 to 4.0 inches) below the shotcrete/concrete interface. While the scans were useful in identifying constituents of the concrete at these specific locations below the interface, the results were inconclusive regarding the ability to delineate fractures/failure within any of the generated images.

6.3 Recommendations for Additional Work

The conclusions derived from this research will provide the basis for further work focused on conducting empiric parametric testing conducted using a concrete structural liner in the field. Once a set of operating parameters have been established, the next step of this research agenda would be to adapt the waterjet system used at SAI/RAMAX to an existing tunnel or mine site, where large sections of an existing support liner could be excavated as part of a full-scale pilot test. Based on the vibration analysis conducted in this study, accelerometers could be embedded into sections of support liner for continued collection of data during future empiric testing.

Depending on the thickness of the liner, 2600 MHz and 1600 MHz ground coupled GPR should be utilized as a non-destructive testing (NDT) method to analyze the substrate of compromised sections requiring rehabilitation in the following order of scenarios:

- Before rehabilitation work with the waterjet takes place;
- After rehabilitation work with the waterjet takes place; and
- After application of a new shotcrete layer to the repaired section.

It is important to continually acquire additional scans of engineered panels or actual concrete support liners in operating environments using 2600 MHz and 1600 MHz antennas, specifically of structures that have been excavated either by an impact hammer or high-pressure waterjets in order to further characterize the substrate of a liner that has undergone repair work. With regards to additional techniques to analyze potential substrate damage due to the use of varying excavation tools, ultrasonic shear-wave tomography should also be considered as a NDT method as it has been successfully used to accurately detect horizontal cracks or delamination in continuously reinforced concrete pavement [57].

To enhance visual inspection of the excavation profile developed in a shotcrete layer, liquid penetrant inspection (LPI) could also be utilized for detection of impact failure/fracture. Advantages to use of LPI include the following:

- Easy to use and requires a minimal amount of training;
- Has high sensitivity to small surface discontinuities;
- Cost effective; and
- Can be used to inspect large areas and volumes through simple application.

Potential disadvantages of using LPI in these applications may include:

- Requires thorough cleaning of surface before use;
- Surface finish and roughness can affect sensitivity of penetrant;
- A relatively porous surface can cause the inspection method to be ineffective; and
- The method is sensitive to surface failure/fracture only.

Concerning core analysis of future testing applications, microCT should continue to be tested at varying resolutions as a possible method of fracture analysis due to waterjet impingement on the shotcrete and substrate. It is suggested that microCT scans be acquired through the entire length of each core generated in order for complete analysis of potential micro-fractures generated by each excavation tool. Pull tests should also be performed on cores taken from liners that have had a new layer of applied shotcrete in order to quantify typical bond strength between the substrate and new shotcrete layer after each excavation process.

Finally, the proposed research could also be used to optimize the jet's specific energy for fragmentation. Through this process, the time required to remove a volume of shotcrete could be characterized in hopes of increasing the excavation rate as compared to conventional mechanical methods. For commercial application, a cost-benefit and safety analysis between

waterjet systems and traditional tools, such as impact hammers, would be beneficial for advancing the commercial relevance of the technology in specific industrial applications.

REFERENCES

- [1] I. Galan, A. Baldermann, W. Kusterle, M. Dietzel, and F. Mittermayr, "Durability of shotcrete for underground support– Review and update," *Constr. Build. Mater.*, vol. 202, pp. 465–493, 2019.
- [2] L. Luo, X. Li, M. Tao, and L. Dong, "Mechanical behavior of rock-shotcrete interface under static and dynamic tensile loads," *Tunn. Undergr. Sp. Technol.*, vol. 65, pp. 215–224, 2017.
- [3] M. Gharouni-Nik, M. Naeimi, S. Ahadi, and Z. Alimoradi, "Reliability analysis of idealized tunnel support system using probability-based methods with case studies," *Int. J. Adv. Struct. Eng.*, 2014.
- [4] J. Klug and D. R. Klug, "Tunnel Demand Forecast," *Min. Eng.*, vol. 72, no. 5, pp. 61–62, 2020.
- [5] L. Malmgren, E. Nordlund, and S. Rolund, "Adhesion strength and shrinkage of shotcrete," *Tunn. Undergr. Sp. Technol.*, vol. 20, no. 1, pp. 33–48, Jan. 2005.
- [6] Bourgeois, J., Miller, H. & Steele, J., B., Charrier, E., & Asbury, B., "The Characterization of Delamination Processes with Respect to Waterjet Shotcrete Removal during Tunnel Liner Repair and Maintenance", 2019 TBR Workshop Performance of Underground Transportation Infrastructure: Opportunities and Challenges, 2019 TRB Annual Meeting, Washington DC, January 2019.
- [7] "Chunnel Repairs Call On Conjet Hydrodemolition Robots," SME Mining Engineering, Tunneling & Underground Construction News Article, Society for Mining, Metallurgy & Exploration (SME), page 37, June 2009.
- [8] A. Thomas, *Sprayed Concrete Lined Tunnels*, Second Edition, CRC Press, 2020.
- [9] E. C. Poeck, "Analyzing the Potential for Unstable Mine Failures with the Calculation of Released Energy in Numerical Models." Colorado School of Mines, Dissertation, Mining Engineering, ISBN 9781369484380, 2016.
- [10] A. W. Momber, *Hydrodemolition of Concrete Surfaces and Reinforced Concrete Structures*. Elsevier Ltd, 2005.
- [11] M. Luna, D. Arcos, and L. Duro, "Effects of grouting, shotcreting and concrete leachates on backfill geochemistry," *SKB Rapp.*, no. R-06-107, p. 51, 2006.

- [12] L. A. Martin, C. C. Clark, J. B. Seymour, and M. A. Stepan, *Shotcrete Design and Installation Compliance Testing: Early Strength, Load Capacity, Toughness, Adhesion Strength, and Applied Quality*. Spokane, WA: Department of Health and Human Services, Centers for Disease Control and Prevention, National Institute for Occupational Safety and Health, 2014.
- [13] A. Darby and M. Leggett, "Use of shotcrete as the permanent lining of tunnels in soft ground," 1997.
- [14] A. M. Neville, "Properties of Concrete," 5th Edition, Pearson Publ., 1995.
- [15] L. A. Martin, "Field-Use Early-Strength Shotcrete Test System," 2011.
- [16] M. Raffaldi, D. Benton, L. Martin, J. Johnson, and M. Stepan, "Assessing the mechanical behavior of large-scale shotcrete panels," *2016 SME Annu. Conf. Expo Futur. Min. a Data-Driven World*, no. February 2016, pp. 464–473, 2016.
- [17] R. A. Cummings, "Identification of Mine Roof Susceptibility to Air Slacking," *Int. J. Coal Geol.*, vol. 8, no. 4, pp. 315–324, 1987.
- [18] "Fundamental Research on Percussion Drilling : Improved rock mechanics analysis , advanced simulation technology , and full- scale laboratory investigations," 2005.
- [19] U. M. Rao Karanam and B. Misra, *Principles of Rock Drilling*. A.A. Balkema/Rotterdam/Brookfield, 1998.
- [20] C. Zha, G. Liu, J. Li, Y. Li, Y. Xi, and B. Guo, "Combined Percussive-Rotary Drilling to Increase Rate of Penetration and Life of Drill Bit in Drilling Hard Rock Formation," *Chem. Technol. Fuels Oils*, vol. 53, no. 2, pp. 254–262, 2017.
- [21] T. C. Marshall, "Comparison Between Hydraulic and Pneumatic Rockdrills," *J. South African Inst. Min. Metall.*, vol. 75, no. 7, pp. 181–184, 1975.
- [22] B. Paul and D. L. Sikarskie, "A preliminary model for wedge penetration in brittle materials," *Trans. Am. Inst. Min. Eng.*, vol. 232, pp. 372–383, 1965.
- [23] P. K. Dutta, "A theory of percussive drill bit penetration," *Int. J. Rock Mech. Min. Sci.*, vol. 9, pp. 543–567, 1972.
- [24] N. Bilgin, H. Copur, and C. Balci, *Mechanical Excavation in Mining and Civil Industries*. CRC Press Taylor & Francis Group, 2014.

- [25] J. D. Wenzlick, "Hydrodemolition and Repair of Bridge Decks," Missouri Department of Transportation, Development & Technical Division Report, 12 pgs, 2002.
- [26] I. Tanikura, R. Shintani, A. Sainoki, S. Watanabe, and Y. Obara, "Quantitative comparison of chipping- and hydrodemolition-induced microscopic damage evolution in concrete substrates," *Constr. Build. Mater.*, vol. 164, pp. 193–205, 2018.
- [27] E. C. Poeck and M. Kuchta, "A Performance Evaluation of Various Nozzle Designs for Waterjet Scaling in Underground Excavations," Colorado School of Mines, 2008.
- [28] H. El Naggar and A. R. Sabouni, "State-of-the-Art Review for the Application of Shotcrete in Tunnel Lining Rehabilitation," *AHU J. Eng. Appl. Sci.*, no. January, 2009.
- [29] H. B. Miller and F. D. Wang, "The Characterization of Rock Failure Induced by High Frequency Modulated Fluid Jets in Crystalline Rock," WJTA Conference, Houston, TX, 2007.
- [30] D. Wright and S. Hardy, "Configuring a Waterblast System," WJTA Conference, Houston, TX, 2009.
- [31] H. B. Miller, "The Characterization of Crack Propagation and Brittle Failure Induced by Discrete, High Velocity Waterjet Impacts in Crystalline Rocks," Colorado School of Mines, Mining Engineering, Dissertation, 1996.
- [32] M. M. Vijay, "Fluid Mechanics of Jets," in *Waterjet Technology: Basics and Beyond Short Course*, WJTA, 2019.
- [33] D. A. Summers, *Waterjetting Technology*. CRC Press, 2003.
- [34] D. Wright, J. Wolgamott, and G. Zink, "Nozzle Performance in Rotary Applications," WJTA Conference, Houston, TX, 1999.
- [35] D. Wright, J. Wolgamott, and G. Zink, "Waterjet Nozzle Material Types," WJTA Conference, Houston, TX, 2003.
- [36] D. A. Summers, "A Historical Perspective on Waterjet Development," in *Waterjet Technology: Basics and Beyond Short Course*, WJTA, 2019.
- [37] A. W. Momber, "Wear of rocks by water flow," *Int. J. Rock Mech. Min. Sci.*, 2003.
- [38] D. Wright, J. Wolgamott, and G. Zink, "A Study of Rotary Jets for Material Removal," WJTA Conference, Houston, TX, 1997.

- [39] A. V. Varnavina, L. H. Sneed, A. K. Khamzin, E. V. Torgashov, and N. L. Anderson, "An attempt to describe a relationship between concrete deterioration quantities and bridge deck condition assessment techniques," *J. Appl. Geophys.*, vol. 142, pp. 38–48, 2017.
- [40] A. Wimsatt *et al.*, "Mapping Voids, Debonding, Delaminations, Moisture, and Other Defects Behind or Within Tunnel Linings," Transportation Research Board, SHRP2, Report S2-R06G RR1, 33 pgs, 2014.
- [41] B. Kravitz, "Non-Destructive Evaluation of Two-Component Backfill Grouting Behind Segmental Tunnel Linings," Colorado School of Mines, Dissertation, 2018.
- [42] A. Lalagüe, M. A. Lebens, I. Hoff, and E. Grøtv, "Detection of Rockfall on a Tunnel Concrete Lining with Ground-Penetrating Radar (GPR)," *Rock Mech. Rock Eng.*, vol. 49, no. 7, pp. 2811–2823, 2016.
- [43] R. D. Bowling, "Applications of Ground Penetrating Radar to Structural Analysis of Carbonate Terraces on the Island of Bonaire, Caribbean Netherlands," Texas A&M University, Dissertation, 2017.
- [44] B. Kravitz, M. Mooney, J. Karlovsek, I. Danielson, and A. Hedayat, "Void detection in two-component annulus grout behind a pre-cast segmental tunnel liner using Ground Penetrating Radar," *Tunn. Undergr. Sp. Technol.*, vol. 83, no. October 2018, pp. 381–392, 2019.
- [45] A. M. Alani, M. Aboutalebi, and G. Kilic, "Applications of ground penetrating radar (GPR) in bridge deck monitoring and assessment," *J. Appl. Geophys.*, vol. 97, pp. 45–54, 2013.
- [46] A. V. Varnavina *et al.*, "Concrete bridge deck assessment: Relationship between GPR data and concrete removal depth measurements collected after hydrodemolition," *Constr. Build. Mater.*, vol. 99, pp. 26–38, Nov. 2015.
- [47] S. R. Stock, *MicroComputed Tomography: Methodology and Applications*, 2nd ed. CRC Press, 2019.
- [48] M. Nicco, E. A. Holley, P. Hartlieb, R. Kaunda, and P. P. Nelson, "Methods for Characterizing Cracks Induced in Rock," *Rock Mech. Rock Eng.*, vol. 51, no. 7, pp. 2075–2093, 2018.
- [49] M. Nicco, "Rock Fracturing Under Microwave Irradiation: Development of Analytical Methods and Investigation of the Contribution of Bound Water," Colorado School of Mines, Mining Engineering, Dissertation, 2019.
- [50] C. E. Stanford and R. D. Bowling, "GPR_Mapper." 2018.

- [51] P. Annan, "Electromagnetic principles of ground penetrating radar," in *Ground Penetrating Radar*, Elsevier, 2009, pp. 1–40.
- [52] N. Cassidy, "Ground penetrating radar data processing, modelling and analysis," in *Ground Penetrating Radar*, Elsevier, 2009, pp. 141–176.
- [53] G. G. Clemena, M. M. Sprinkel, and R. R. Long, "Use of Ground-Penetrating Radar for Detecting Voids Under a Jointed Concrete Pavement.," *Transp. Res. Rec.*, vol. 1109, pp. 1–10, 1987.
- [54] A. Q. Adetunji, "Mapping the Internal Structure of Sand Dunes in the Jafurah Sand Sea of Eastern Saudi Arabia using Ground Penetrating Radar," King Fahd University of Petroleum & Minerals, 2008.
- [55] C. M. Loeffler, Y. Qiu, B. Martin, W. Heard, B. Williams, and X. Nie, "Detection and segmentation of mechanical damage in concrete with X-Ray microtomography," *Mater. Charact.*, vol. 142, no. March, pp. 515–522, 2018.
- [56] P. Winkler, "Guide for the Preparation of Concrete Surfaces for Repair Using Hydrodemolition Methods," Introduction to ICRT Technical Guideline, No. 310.3R-2014, 4 pgs., 2004.
- [57] P. Choi, D. H. Kim, B. H. Lee, and M. C. Won, "Application of ultrasonic shear-wave tomography to identify horizontal crack or delamination in concrete pavement and bridge," *Constr. Build. Mater.*, vol. 121, pp. 81–91, 2016.

APPENDIX A – TECHNOLOGY TRANSFER ACTIVITIES

1 Accomplishments

The primary objectives of this research were to compare and contrast the unintended damage caused to a structural liner and underlying substrate by both conventional impact hammers and waterjet excavation methods during empiric testing. This analysis involved physical cutting on instrumented shotcrete panels designed to quantify fracture propagation, substrate delamination, and stress distribution. Through empiric testing, this research also sought to validate the hypothesis that waterjet removal of these support systems will result in greater selectivity and less unintended damage than conventional removal methods, where the intent is to develop a viable technology that will reduce the collateral damage caused to surrounding liners during excavation, improve the adhesion between shotcrete and the substrate for longer lasting ground support, and improve overall safety for workers in underground environments.

The major accomplishments stemming from this research have helped to facilitate a better understanding of the dynamic excavation processes associated with the repair and rehabilitation of reinforced shotcrete and concrete liners used in tunneling and underground construction. These contributions will also aid future research activities, in hopes of developing a prototype system applicable for field testing. In addition, the research provided valuable insights related to nondestructive testing of the test panels using ground penetrating radar (GPR) and microcomputed tomography (microCT), as well as the instrumentation of the panels for quantifying induced vibrations in within the structural elements. A complete discussion of the research outcomes and accomplishments can be found in Chapter 6 of this report.

Since its inception, this project has actively sought to engage undergraduate and graduate students as part of its research and educational objectives. Integral to the pursuit of this research has been the involvement of two Ph.D. students, Erik Charrier and Josef Bourgeois, and an undergraduate student researcher, Devon Reason. All three students were actively engaged in all phases of the research and assumed areas of responsibility associated with specific tasks. In addition, these students have participated in regular project meetings and planning. The graduate students participating in the research designed and constructed the laboratory equipment and test panels. Mr. Charrier designed the data acquisition system and constructed it with the assistance of the faculty advisors and Mr. Reasoner. Mr. Bourgeois planned and conducted the visual analysis, the GPR scans, and microCT of the test panels. These students also planned and conducted the mechanical excavation of the test panels. Mr. Charrier participated in all activities associated with the use of the SAI/RAMAX Laboratory in California and assisted with the waterjet cutting tests. Both Mr. Charrier and Mr. Bourgeois led efforts to analyze the test data, prepare the final project report, and give conference presentations.

1.1 What was done? What was learned?

The methodology associated with this research consisted of an extensive number of definitive steps and included the integration of numerous different technologies. In addition, the research required significant logistical planning due to the use of two separate laboratories located 2,500 km apart. A complete description of the research methodology can be found in Chapter 1.4 and Chapter 3.1. In summary, the project team developed a research plan based upon specific objectives and a comprehensive literature search. This included the adaptation and set-up of two different experiments (waterjet and mechanical impact hammers) at each of these laboratories, and the development of the motion control systems, instrumented test panels, the data acquisition system, the processes and technology needed to quantify the impact of the empiric testing, and data analysis. Beyond the conclusions derive from the research (as discussed in Chapter 6 and Appendix A 1), the critical role that students played in facilitating this project is important because it represents a unique learning opportunity that this research provided. Each step in the research methodology provided for team discussions, problem-solving activities, exposure to new technologies and knowledge, the development of professional skill-sets, and opportunities for scientific creativity. All of these are important for the professional development of research engineers and scientists. By any criteria, the project was extremely successful.

1.2 How have the results been disseminated?

The results of this research have been disseminated through numerous venues to a variety of technical audiences. This includes several UTC-UTI Workshops, conference presentations, graduate seminars, technical short-courses focused on subjects related to mining and waterjet technology, and a Ph.D. dissertation. It is anticipated that several journal publications will be submitted once the dissertation has be completed.

2 Participants and Collaborating Organizations

The following participants and collaborating organizations provided financial and material support over the duration of this project:

Name: RAMAX, LLC
Location: Lancaster, CA
Contribution: Provided use of their waterjet laboratory, equipment and staff. The estimated cost of \$50,000 was provided as cost match to a research project funded by UTC-UTI.

Name: IET Waterjet Foundation; CSM Foundation
Location: Golden, CO
Contribution: Provided more than \$20,000 in support of travel and student scholarship.

Name: CSM Earth Mechanics Institute
Location: Golden, CO
Contribution: Provided use of laboratory facilities for the project funded by UTC-UTI. Estimated cost match is \$10,000.

3 Outputs

Thesis

J. P. Bourgeois, *Characterizing the Excavation Process Associated with the Removal of Shotcrete Reinforced Underground Structural Liners Using Waterjet Technology*, Ph. D. Dissertation, Mining Engineering, Colorado School of Mines, Defended October 1, 2020, Projected Graduation December 2020.

Presentations

- 1) Miller, H.B., Invited Panelist, CDC National Occupational Research Agenda (NORA), Mining Sector Priorities, “Underground Metal Mining”, Denver, CO, Feb. 22, 2017.
- 2) Charrier, E., Miller, H., Steele, J. & Asbury, B., Bourgeois, J., “The Characterization of Delamination Processes with Respect to Waterjet Shotcrete Removal during Tunnel Liner Repair and Maintenance”, First Workshop of the University Transportation Center for Underground Transportation Infrastructure, Colorado School of Mines, Feb. 19, 2018.
- 3) Charrier, E., Miller, H. & Steele, J., “Efforts to Characterize and Mitigate Hot Work Accidents in Mining & Mineral Processing”, 2018 SME Annual Meeting, Coal & Energy Division, Mine Safety II, Minneapolis, MN, Feb. 28, 2018
- 4) Miller, H.B., Colorado Mining Association Panelist, “Industry Educational Collaborations”, Denver, CO, April 4, 2018;
- 5) Miller, H.B., “Occupational Health Issues in Mining & Excavation”, Colorado State University, Industrial Hygiene/Public Health Graduate Seminar, April 20, 2018.
- 6) Miller, H.B., Steele, J., Asbury, B., Charrier, E., Bourgeois, J. “The Characterization of Delamination Processes with Respect to Waterjet Shotcrete Removal During Liner Repair and Maintenance – Empiric Test Results”, UTC-UTI Tunneling Fundamentals, Practice & Innovations, Golden, CO, Oct. 18, 2018.
- 7) Bourgeois, J., Miller, H. & Steele, J., B., Charrier, E., & Asbury, B., “The Characterization of Delamination Processes with Respect to Waterjet Shotcrete Removal during Tunnel Liner

Repair and Maintenance”, 2019 TBR Workshop Performance of Underground Transportation Infrastructure: Opportunities and Challenges, 2019 TRB Annual Meeting, Washington DC, January 2019.

- 8) Bourgeois, J., “The Characterization of Delamination Processes with Respect to Waterjet Shotcrete Removal during Tunnel Liner Repair and Maintenance”, Mining Engineering Graduate Seminar, CSM, January 30, 2019.
- 9) Charrier, E., Miller, H. & Steele, J., B., Bourgeois, J., & Asbury, B., “The Characterization of Waterjet Shotcrete Removal during Liner Repair and Maintenance”, 2019 SME Annual Meeting, Mining & Exploration: Innovations & Technologies: Emerging Technologies and Engineering Advancements: Challenging the Status Quo II, Denver, CO, Feb. 26, 2019

Major reports

Miller, H.B., Steele, J.P.H., Asbury, B., Charrier, E., Bourgeois, J., “The Characterization of Delamination Processes with Respect to Waterjet Shotcrete Removal During Tunnel Liner Repair and Maintenance”, Final Project Report, University Transportation Center for Underground Transportation Infrastructure (UTC-UTI), Colorado School of Mines, Oct. 2020.

Workshops

- 1) First Workshop of the University Transportation Center for Underground Transportation Infrastructure, Colorado School of Mines, Feb. 19, 2018.
- 2) UTC-UTI Workshop, Tunneling Fundamentals, Practice & Innovations, Golden, CO, Oct. 18, 2018.

Short-Courses

- 1) Miller, H.B., “Waterjet Technology: Basics & Beyond”, 2017 WJTA-IMCA Conference and Expo, Equipment Considerations, New Orleans, LA, Oct. 24, 2017.
- 2) Miller, H.B., U.S. National Defense College, The Eisenhower School, “Mine Design Considerations & Economics”, Washington DC, Jan. 17-19, 2018
- 3) Miller, H.B., Caterpillar, “Underground Mine Design & Operations”, Peoria, IL, April 13, 2018;
- 4) Miller, H.B., Caterpillar, “Mining Fundamentals – Economics, Cost Drivers & Challenges”, Tanja Hills (CAT Proving Grounds), Green Valley, AZ, May 2, 2018;

- 5) Miller, H.B., “An Introduction to Mining Fundamentals & Resource Extraction”, US Geologic Survey & Dept. of Commerce, Afghan Capacity Building, AGS & MoM, Delhi, India, Oct. 21-24, 2018
- 6) Miller, H.B., “The Fundamentals of Resource Extraction”, US Geologic Survey & U.S. Dept. of Commerce, Afghan Capacity Building, AGS & MoM, Istanbul, Turkey, June 24-30, 2019.
- 7) Miller, H.B., “Waterjet Technology: Basics & Beyond”, 2019 WJTA-IMCA Conference and Expo, Equipment Considerations, New Orleans, LA, Oct. 24, 2019.

4 Outcomes

The most significant outcomes of this research were associated with the completion of a Ph.D. dissertation and confirming the hypothesis that hydroexcavation of shotcrete and tunnel liners represents a potentially viable technology that possesses unique fragmentation characteristics that appear to mitigate the detrimental characteristics associated with using mechanical impact hammers.

6 Impacts

The impact of this research is far reaching and will serve to help facilitate advancements of the technology towards possible commercialization. Analysis of the data obtained from empiric testing clearly demonstrates the potential to develop a viable tool that could mitigate the likelihood of inducing inadvertent damage to the structural liner adjacent to areas undergoing repair and rehabilitation. There are direct ramifications of this research to the safety of underground construction and tunnel workers, as well as for increasing the productivity and durability associated with these repairs.

APPENDIX B – PROJECT DATA & CALCULATIONS

Section B-1: Concrete and Quikrete Specification

Concrete Mix Design Report

Mix ID #:CD4570Laboratory Trial #:90437Lab Trial Date:9/13/2019Class/Use:CDOT Class B and D - Hand

Material	Cubic Yard	Unit	Product/Source	ASTM Std
Cement	520	lbs	Cement	C 150
Fly Ash	95	lbs	Class C Fly Ash	C 618
Sand	1315	lbs	Martin Marietta Washed Concrete Sand	C 33
57/67	1710	lbs	Martin Marietta 5767	C 33
AEA	2.2	oz.	Air Entraining Admixture	C 260
MRWR	49.2	oz.	Water Reducing Admixture	C 494
HS	0.0	oz.	Hydration Stabilizer	C 494
Water	76.8	lbs	Municipal Water	C 94

The above w

aturated, surface dry condition. Batch plant corrections must be made for aggregates that vary from these moisture conditions. AEA adjustments at plant and on site may be required to achieve proper air entrainment. Air adjustments may be made with either liquid or Fritz air entrainment and Fritz Air Minus or Sika Perfin. Admixtures are used as needed in order to obtain specified mix design properties and will not exceed manufacturer recommended maximum dosage.

Physical Properties (as tested):			Specified Physical Properties:		
Unit Weight:	143.8	pcf	Compressive Strength:	4500	psi (min)
(w/cm) Ratio:	0.45		(w/cm) Ratio:	0.45	(max)
Slump:	4.00	in	Slump:	3.00 - 5.00	in
Air Content:	5.7	%	Air Content:	5.0 - 8.0	%
Relative Yield:	1.01	cy	Relative Yield:	0.99 - 1.02	cy
Yield:	27.24	cf	Yield:	26.73 - 27.54	cf
Percent Fly Ash:	15	%	Percent Fly Ash:	50	% (max)

Compressive Strength Data

Trial #	90437		
Age	psi		
7 Day	5440		
7 Day	5250	Average	5350
28 Day	6680		
28 Day	6610		
28 Day	6490	Average	6590



CEMENT & CONCRETE PRODUCTS™

SAND/TOPPING MIX

PRODUCT NO. 1103

DIVISION 3

Concrete Topping
03 53 00

PRODUCT DESCRIPTION

QUIKRETE® Sand/Topping Mix consists of a uniformly blended mixture of Portland cement and commercial grade sands, used for repairing and topping damaged horizontal concrete surfaces less than 2" (51 mm) thick.

PRODUCT USE

QUIKRETE® Sand/Topping Mix is formulated for placing concrete overlays less than 2" (51 mm) thick. It is also used for patching and leveling steps, walks and floors. Other applications for QUIKRETE® Sand/Topping Mix include:

- Chimney caps
- Large crack repairs
- Thick setting beds for ceramic floor tile
- Filling cores in masonry block or brick

SIZES

- QUIKRETE® Sand/Topping Mix –
 - 80 lb (36.3 kg) bags
 - 60 lb (27.2 kg) bags
 - 40 lb (18.1 kg) bags
 - 10 lb (4.5 kg) bags
 - 25 kg (55 lb) bags
 - 30 kg (66 lb) bags

YIELD

- 80 lb (36.3 kg) bag - Approximately 0.66 cu ft (19 L)
- 60 lb (27.2 kg) bag - Approximately 0.5 cu ft (14 L)
- 40 lb (18.1 kg) - Approximately 0.37 cu ft (10 L)

TECHNICAL DATA

APPLICABLE STANDARDS

ASTM International - ASTM C387 Standard Specification for Packaged, Dry, Combined Materials for Mortar and Concrete
QUIKRETE® Sand/Topping Mix exceeds the compressive strength requirements for high strength mortars per ASTM C387. Typical compressive strengths are:

- 3000 psi (20.7 MPa) at 7 days
- 5000 psi (34.5 MPa) at 28 days

INSTALLATION

SURFACE PREPARATION

When using Sand/Topping Mix to resurface damaged concrete surfaces 1/2" - 2" (12.7 - 51 mm) thick dig a small trench along the edge of the damaged surface so that forms can be set in place level with the old concrete surface. It is important to form a solid base for the new topping.



Remove all broken and loose concrete. Clean the surface thoroughly with QUIKRETE® Concrete & Asphalt Cleaner.

ADMIXTURES

For patches less than 1" (25.4 mm) thick, replace part of the mixing water with QUIKRETE® Concrete Acrylic Fortifier #8610 for improved bonding. Add the QUIKRETE® Concrete Acrylic Fortifier directly to the mix at the rate of 3 pt (1.4 L) per 60 lb (27.2 kg) bag or 1/2 gal (1.9 L) per 80 lb (36.3 kg) bag.

MIXING

NOTE:

- For applications 1" - 2" (25.4 - 51 mm) thick, use specified bonding agent
- For applications less than 1" (25.4 mm) thick, use specified admixture

MACHINE MIXING

QUIKRETE® Sand/Topping Mix can be mixed in a barrel type concrete mixer or a mortar mixer. Choose the mixer size most appropriate for the size of the job. Allow at least 1 cu ft (28 L) of mixer capacity for each 80 lb (36.3 kg) bag of QUIKRETE® Sand/Topping Mix to be mixed at one time

- For each 80 lb (36.3 kg) bag of QUIKRETE® Sand/Topping Mix to be mixed, add approximately 8 pt (3.8 L) of fresh water to the mixer
- Turn on the mixer and begin adding bags of Sand/Topping Mix to the mixer

- If the material becomes too difficult to mix, add additional water until a workable mix is obtained

Note - Final water content should be 8 - 12 pt (3.8 - 5.7 L) of water per 80 lb (36.3 kg) bag of Sand/Topping Mix. For other bag sizes, use Table 1 to determine water content.

HAND MIXING

- Empty Sand/Topping Mix bags into a suitable mixing container
- For each 80 lb (36.3 kg) bag of mix, add approximately 8 pt (3.8 L) of clean water. Work the mix with a shovel, rake or hoe

- Add additional water as needed to obtain a workable plastic-like consistency
- Note - Final water content should be 8 - 12 pt (3.8 - 5.7 L). Be sure all material is wet. Do not leave standing puddles. For other bag sizes, use Table 1 to determine water content.

TABLE 1 MIX WATER REQUIREMENTS FOR QUIKRETE® SAND/TOPPING MIX		
Package size	Starting water content	Final water content
80 lb (36.3 kg)	8 pt (3.8 L)	8-12 pt (3.8-5.7 L)
60 lb (27.2 kg)	6 pt (2.8 L)	6-9 pt (2.8-4.3 L)
40 lb (18.1 kg)	4 pt (1.9 L)	4-6 pt (1.9-2.8 L)

APPLICATION

- Using 2 × 4s and stakes, construct a form around the old sidewalk or slab. Use a level to make sure that the forms are set at the correct height and that there is adequate slope for drainage
- If the area to be resurfaced requires topping from 1" - 2" (25.4 - 51 mm) in thickness, first coat the damaged area with QUIKRETE® Concrete Bonding Adhesive (#9902)
- Allow the Bonding Adhesive to dry before proceeding. Concrete Bonding Adhesive should not be used when Sand/Topping Mix contains Acrylic Fortifier
- Place the Sand/Topping Mix onto the damaged area and trowel the surface smooth using a steel finishing trowel or wood float
- Edge using a concrete edging tool if desired
- If the topping is placed over an existing concrete joint, it is important to tool a joint into the Sand/Topping Mix directly over the existing joint
- Use a trowel or jointer to form the joint at least half the depth of the patch

FINISHING

QUIKRETE® Sand/Topping Mix can be broom finished or hand trowel finished. Power finishing is not recommended. Specialty finishes, such as stamping, adding color or staining, are also acceptable.

CURING

General

Curing is one of the most important steps in the use of Sand/ Topping Mix. Proper curing increases the strength and durability of the repair, and a poor curing job can ruin an otherwise well-done project. Proper water content and temperature are essential for good curing. In near freezing temperatures, the hydration process slows considerably. When weather is too hot, dry or windy, water is lost by evaporation from the repair and hydration stops, resulting in finishing difficulties and cracks. The ideal circumstances for curing are ample moisture and moderate temperature and wind conditions. Curing should start as soon as possible and should continue for a period of 5 days in warm weather at minimum 70°F (21°C) or higher, or for 7 days in colder weather at 50 - 70°F (10 - 21°C).

Specific Curing Methods

- QUIKRETE® Acrylic Cure & Seal – Satin Finish (#8730) provides the easiest and most convenient method of curing. Apply by spray, brush or roller soon after the final finishing operation when the surface is hard. The surface can be damp, but not wet, when applying the curing compound. Complete coverage is essential
- Other methods of providing proper curing include covering the surface with wet burlap, keeping the surface wet with a lawn sprinkler and covering the surface with plastic sheeting or waterproof paper to prevent moisture loss
- If burlap is used, it should be free of chemicals that could weaken or discolor the concrete. New burlap should be washed before use. Place it when the concrete is hard enough to withstand surface damage and sprinkle it periodically to keep the concrete surface continuously moist
- Water curing with lawn sprinklers, nozzles or soaking hoses must be continuous to prevent interruption of the curing process
- Curing with plastic sheets is convenient. They must be laid flat, thoroughly sealed at joints and anchored carefully along edges

PRECAUTIONS

- Curing compounds should not be applied if rain or temperatures below 50°F (10°C) are expected within 24 hours
- Curing with plastic or burlap can cause patchy discoloration of the repair
- For repairs to colored surfaces, wet curing or the use of QUIKRETE® Acrylic Cure & Seal – Satin Finish (#8730) is recommended
- Do not use curing compounds during late fall on surfaces where de-icers will be used to melt ice and snow. Using curing compounds at that time can prevent proper air curing of the repair, which is necessary to enhance its resistance to damage caused by de-icers
- Protect Sand/Topping Mix from freezing during the first 48 hours. Plastic sheeting and insulation blankets should be used if temperatures are expected to fall below 32°F (0°C)
- Mixes that contain Concrete Acrylic Fortifier do not require extensive curing. No curing is required except in especially hot, dry or windy conditions. Under such conditions, the repair should be moist cured for 24 hours

WARRANTY

NOTICE: Obtain the applicable LIMITED WARRANTY: at www.quikrete.com/product-warranty or send a written request to The Quikrete Companies, LLC, Five Concourse Parkway, Atlanta, GA 30328, USA. Manufactured under the authority of The Quikrete Companies, LLC. © 2018 Quikrete International, Inc.

* Refer to www.quikrete.com for the most current technical data, SDS, and guide specifications

Quikrete Particle Analysis

Sieve Test 1: 500.87 gram sample

Sieve Size Range, Tyler (in)	Sieve Size Range, μm	Sieve Fractions		Nominal Aperture Size (μm)	Cumulative %	
		wt (g)	wt %		undersize	oversize
8 (0.093)	+2362	26.80	5.4	2362	94.6	5.4
14 (0.048)	-2362 to +1168	95.06	19.2	1168	75.4	24.6
28 (0.0234)	-1168 to +595	92.32	18.7	595	56.7	43.3
48 (0.0117)	-595 to +297	103.84	21.0	297	35.7	64.3
-48 (+0.0117)	-297	176.81	35.7			

Sieve Test 2: 500.09 gram sample

Sieve Size Range, Tyler (in)	Sieve Size Range, μm	Sieve Fractions		Nominal Aperture Size (μm)	Cumulative %	
		wt (g)	wt %		undersize	oversize
8 (0.093)	+2362	29.54	5.9	2362	94.1	5.9
14 (0.048)	-2362 to +1168	96.72	19.5	1168	74.6	25.4
28 (0.0234)	-1168 to +595	93.08	18.7	595	55.8	44.2
48 (0.0117)	-595 to +297	104.19	21.0	297	34.8	65.2
-48 (+0.0117)	-297	173.01	34.8			

Sieve Test 3: 500.17 gram sample

Sieve Size Range, Tyler (in)	Sieve Size Range, μm	Sieve Fractions		Nominal Aperture Size (μm)	Cumulative %	
		wt (g)	wt %		undersize	oversize
8 (0.093)	+2362	27.40	5.5	2362	94.5	5.5
14 (0.048)	-2362 to +1168	97.63	19.6	1168	74.9	25.1
28 (0.0234)	-1168 to +595	95.54	19.2	595	55.6	44.4
48 (0.0117)	-595 to +297	104.30	21.0	297	34.7	65.3
-48 (+0.0117)	-297	172.46	34.7			

Note: For each un-cured Quikrete sample, the sieve set was placed into a Model RX-29 Tyler sieve shaker for dry screening, running for 10 minutes, after which each sieve was weighed and recorded. These recorded weights were used to generate a plot for cumulative percentage retained according to each sieve size.

Section B-2: Fluid and System Parameters

Nozzle Specifications

The nozzle specifications for the twin orifice rotary head jet system include the following:

- Stainless steel material type;
- Conventional Leach and Walker design; and
- Circular orifice.

These characteristics led to an assumed coefficient of discharge (C_d) of 0.90.

Pressure Losses

In order to determine the exit velocity of the jet fluid out of the nozzle, pressure losses that occur throughout the system need to be quantified. In order to calculate these pressure losses, energy loss was estimated at three specific points including:

- Point 1: the pump accumulator;
- Point 2: at the end of the flexible high-pressure hose prior to the nozzle assembly; and
- Point 3: within the nozzle assembly before exiting the orifice.

It is important to note that 100% of the flow generated by the pump was directed through the nozzle and leakage through the controls was assumed to be negligible.

Point 1: The pump accumulator

Nozzle diameter – 0.74 millimeter (0.029 inch)

Fluid pressure – 189.6 MPa (27,500 psi) (measured at gauge)

Flow rate = 21.2 lpm (5.6 gpm) (from pump specifications)

Total pressure loss at Point 1 = 0 MPa (0 PSI)

Point 2: At the end of the flexible high-pressure hose prior to the nozzle assembly

Pressure loss component 1 – 3.7-meter (12 foot), 5 millimeter (0.20 inch) internal diameter flexible hose with 14.3 millimeter (9/16 inch) end fittings (Rogan and Shanley, model 4005 ST).

∴ Pressure loss (P_L) from manufacturer's curves is equivalent to 5.1 MPa (740 PSI).

Pressure loss component 2 – 3 way, 2 stem manifold valve, 14.3 millimeter (9/16 inch) outside diameter connectors, 3.2 millimeter (0.125 inch) internal orifice, vee-stem, autoclave engineers (model 30VM9075).

Where:

- Flow rate (Q) = 21.2 lpm (5.6 gpm)
- Fluid specific gravity (SG) = 0.995
- Exit flow diameter (d) = 3.2 millimeter (0.125 inch)
- Valve flow coefficient (C_v) = 0.955

Using the calculation for volumetric flow rate combined with the coefficient of volumetric discharge, pressure loss in the manifold valve becomes:

$$P_L = \left[\frac{Q}{29.91 C_V d_2^2} \right]^2$$

$$\therefore P_L = 1.1 \text{ MPa (160 PSI)}$$

Pressure loss component 3 – 304 stainless steel tubing, pressure rated for 275.8 MPa (40,000 PSI), 30.5 centimeters (12 inches) long, 6.4 millimeter (0.250 inch) internal diameter.

Where: Reynolds number (R) = 47,225
Hydraulic (equivalent) diameter (De) = 6.4 millimeters (0.25 inches)
Length of tubing (L) = 30.5 centimeters (1 foot)

$$P_L = (0.0043) \left[\frac{Q^2}{D_e^5 R^{0.25}} \right] (L)$$

$$\therefore P_L = 62.1 \text{ kPa (9 PSI)}$$

Total pressure loss from Point 1 to Point 2 = 6.3 MPa (909 PSI)

Fluid pressure at Point 2 = 189.6 MPa (27,500 PSI) – 6.3 MPa (909 PSI) = 183.3 MPa (26,591 PSI)

Point 3: Within the nozzle assembly before exiting the orifice

Pressure loss component 1 – flow straightener

The flow straightener was part of the flow path as they have empirically demonstrated substantial free-stream improvements in coherency, throw, and power relative to not using these components at all. This pressure loss was previously determined experimentally as 4.3 MPa (625 PSI) through laboratory testing [31].

$$\therefore P_L = 4.3 \text{ MPa (625 PSI)}$$

Total pressure loss from Point 2 to Point 3 = 4.3 MPa (625 PSI)

Fluid pressure at Point 3 = 183.3 MPa (26,591 PSI) – 4.3 MPa (625 PSI) = 179.0 MPa (25,966 PSI)

Summary:

Nozzle Orifice Diameter, mm (in)	Jet Fluid Pressure, MPa (PSI)		
	Point 1	Point 2	Point 3
0.74 (0.029)	189.6 (27,500)	183.3 (26,591)	179.0 (25,966)

Nozzle Velocity






Calculation of jet velocity out of a nozzle requires a modification of Equation 2.11 from Chapter 2. Equation 2.11 assumes a velocity coefficient (C_v) of unity, however, to account for friction and turbulence caused by fluid impedance through the nozzle, the coefficient of discharge is incorporated, resulting in the following equation:

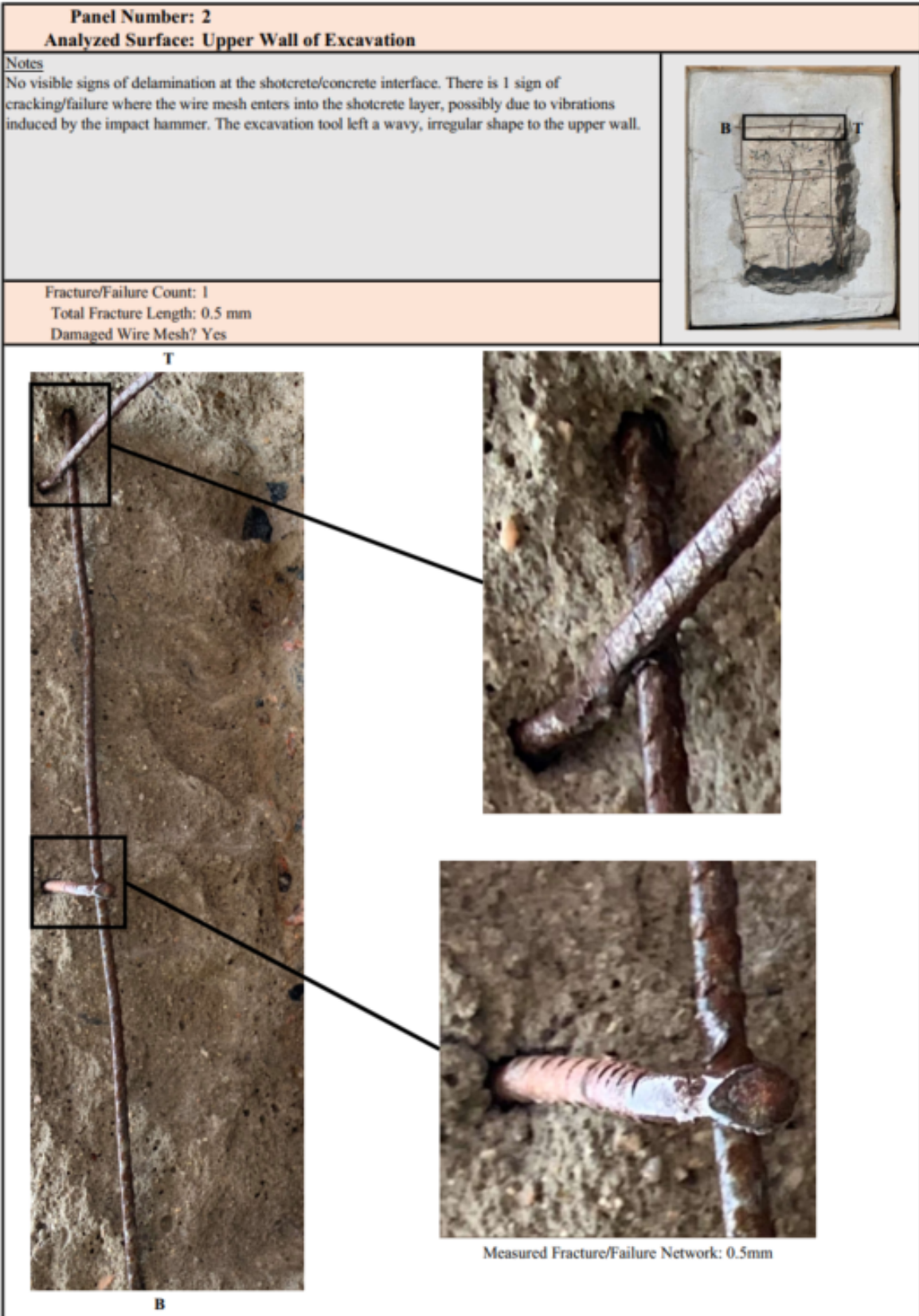
$$V_2 = 12.19C_d \sqrt{\frac{(p_1 - p_2)}{1 - \frac{d_2^4}{d_1^4}}}$$


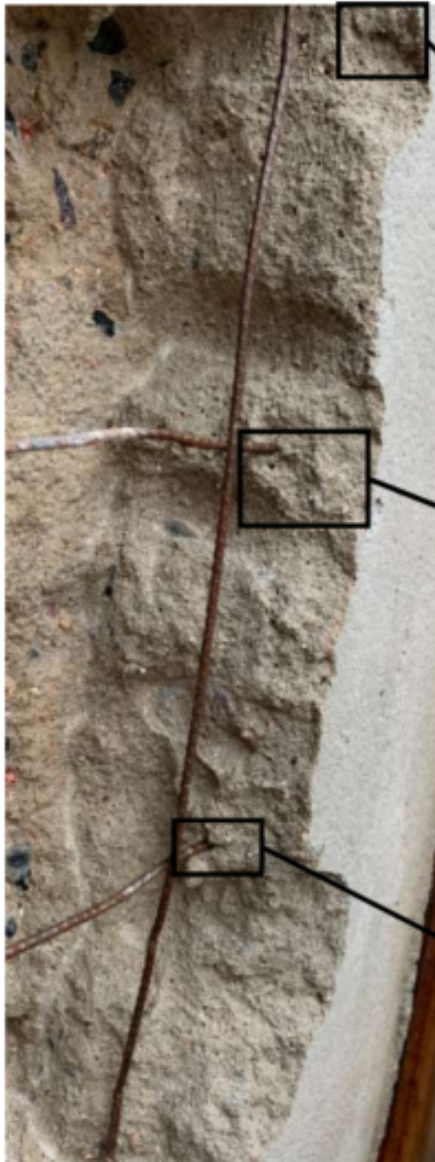



Where:




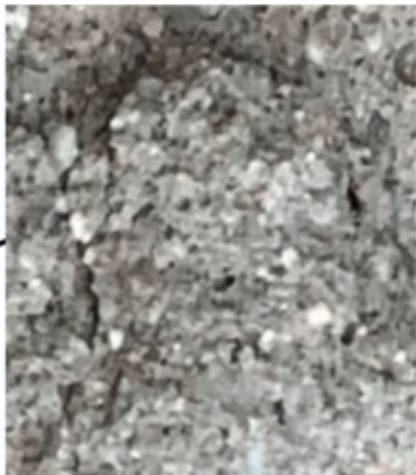
- Coefficient of discharge (C_d) = 0.90
- Fluid pressure at Point 3 (p_1) = 179.0 MPa (25,966 PSI)
- Fluid pressure in free stream (p_2) = 0 MPa (0 PSI)
- Nozzle entrance diameter (d_1) = 5.6 millimeters (0.220 inches)
- Nozzle orifice diameter (d_2) = 0.74 millimeters (0.029 inches)
- ∴ Jet Velocity (V_2) = 538.9 meters/second (1,768 feet/second)



Section B-3: Visual Inspection of Panels After Excavation


Panel Number: 2 Analyzed Surface: Left Wall of Excavation	
<p>Notes</p> <p>No visible signs of delamination at the shotcrete/concrete interface. There are 2 signs of cracking/failure where the wire mesh enters into the shotcrete layer, possibly due to vibrations induced by the impact hammer. There is also 1 other area of failure/fracture as identified below. The excavation tool left a wavy, irregular shape to the left wall.</p>	
<p>Fracture/Failure Count: 3</p> <p>Total Fracture Length: 12.5 mm</p> <p>Damaged Wire Mesh? Yes</p>	
<p style="text-align: center;">T</p> <div></div> <p style="text-align: center;">B</p> <div><p>Measured Fracture/Failure Network: 1mm</p><p>Measured Fracture/Failure Network: 2.5mm</p><p>Measured Fracture/Failure Network: 9mm</p></div>	





Panel Number: 2 Analyzed Surface: Right Wall of Excavation	
<p>Notes</p> <p>No visible signs of delamination at the shotcrete/concrete interface. There are 2 signs of cracking/failure where the wire mesh enters into the shotcrete layer, possibly due to vibrations induced by the impact hammer. There also appears to be slight fracturing on the upper right section of the wall near the top of the shotcrete layer. The excavation tool left a wavy, irregular shape to the right wall.</p>	
<p>Fracture/Failure Count: 3</p> <p>Total Fracture Length: 9 mm</p> <p>Damaged Wire Mesh? Yes</p>	
<div><div></div><div><p>Measured Fracture/Failure Network: 1.5mm</p><p>Measured Fracture/Failure Network: 5.5mm</p><p>Measured Fracture/Failure Network: 2mm</p></div></div>	

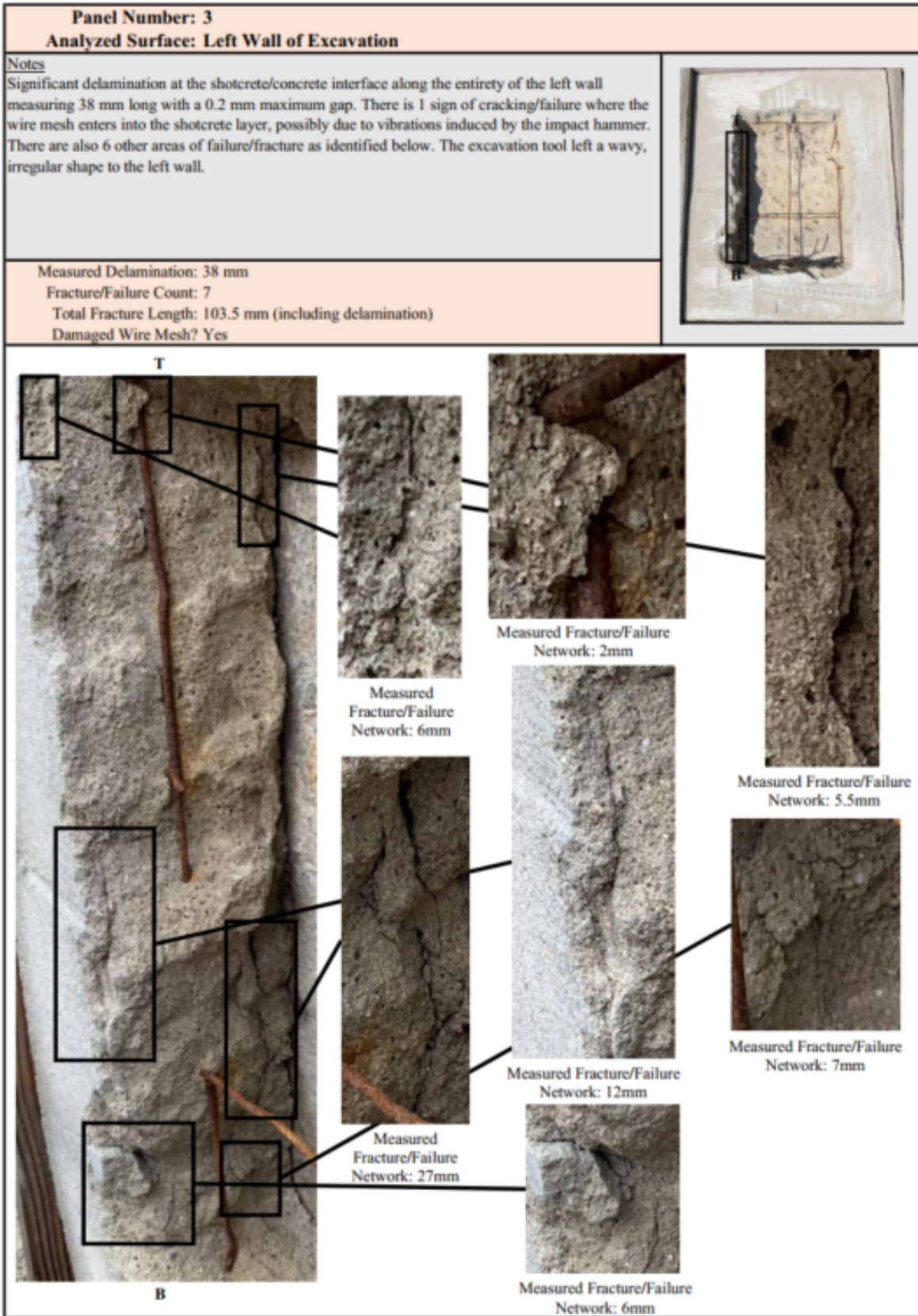
Panel Number: 2 Analyzed Surface: Lower Wall of Excavation	
<div>Notes</div> <div>No visible signs of delamination at the shotcrete/concrete interface. There also appears to be 2 areas of fracture/failure as highlighted below. The excavation tool left a wavy, irregular shape to the bottom wall.</div>	
<div>Fracture/Failure Count: 2</div> <div>Total Fracture Length: 4.5 mm</div> <div>Damaged Wire Mesh? Yes</div>	
<div>T</div> <div></div> <div><div>Measured Fracture/Failure Network: 1mm</div></div> <div><div>Measured Fracture/Failure Network: 3.5mm</div></div> <div>B</div>	




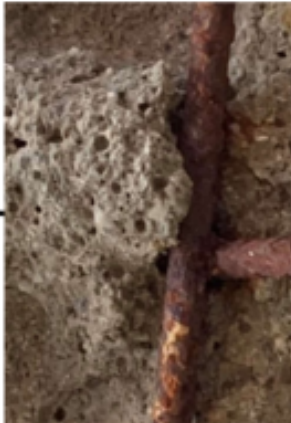

Panel Number: 2 Analyzed Surface: Area Outside Excavated Profile	
Notes 3 areas of failure were discovered along the shotcrete face surrounding the excavation profile. The fracture in the upper section identified above measures 13 mm, the fracture in the mid right section measures 11 mm, and the fracture identified in the lower left corner measures 8 mm.	
Fracture/Failure Count: 3 Total Fracture Length: 32 mm	
 <div data-bbox="954 636 1347 1203" data-label="Image"> </div> <div data-bbox="971 1209 1331 1234" data-label="Caption"> <p>Measured Fracture/Failure Network: 13mm</p> </div> <div data-bbox="716 1360 1338 1614" data-label="Image"> </div> <div data-bbox="847 1621 1208 1646" data-label="Caption"> <p>Measured Fracture/Failure Network: 11mm</p> </div> <div data-bbox="254 1455 701 1770" data-label="Image"> </div> <div data-bbox="305 1776 656 1801" data-label="Caption"> <p>Measured Fracture/Failure Network: 8mm</p> </div>	

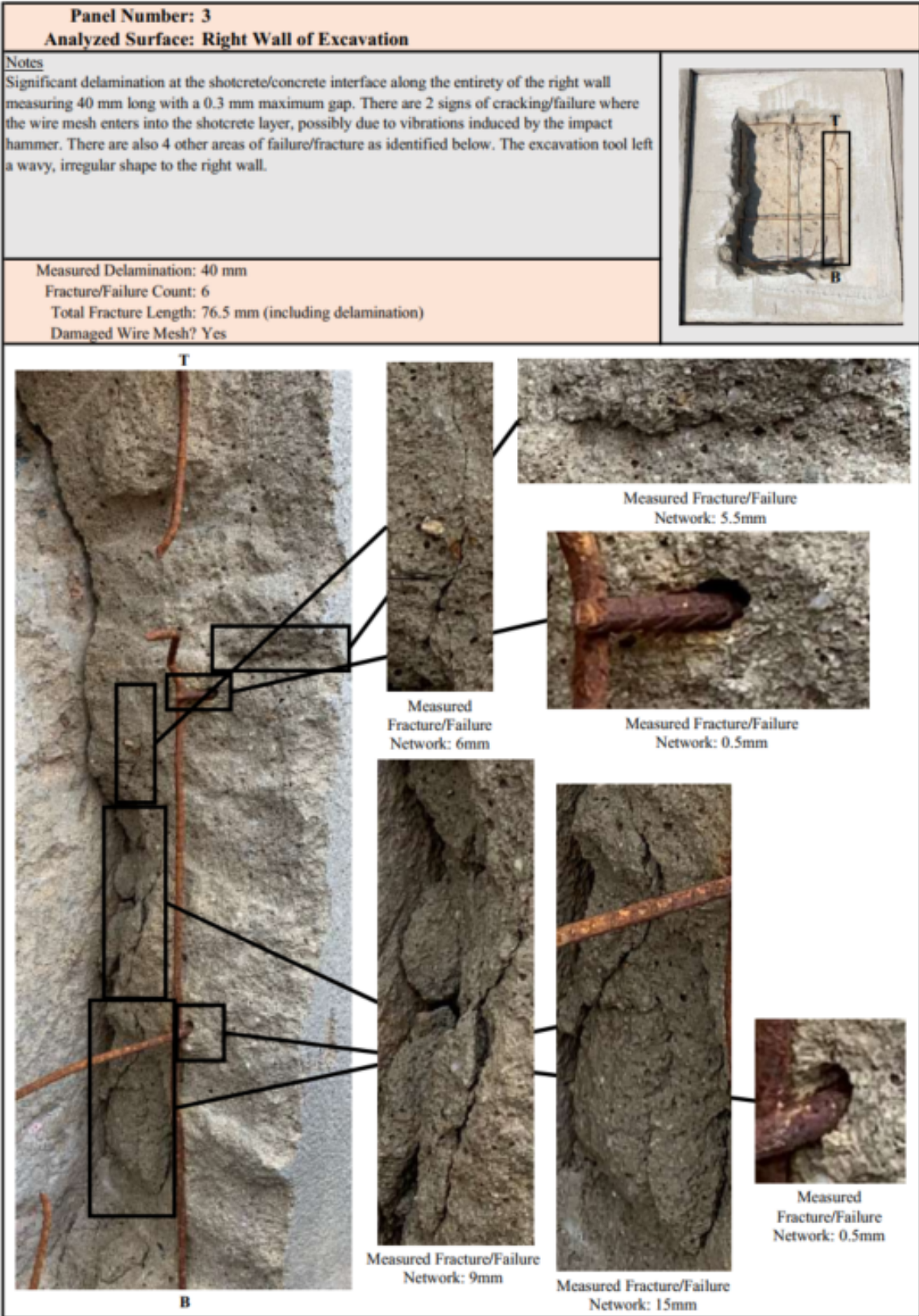
Panel Number: 2	
Analyzed Surface: Excavation Face	
Notes	
A large percentage of the exposed aggregate was fractured by the impact hammer. There is 1 area of the excavation face that shows failure around the perimeter of a piece of aggregate.	
Exposed Aggregate Count: 51 Percentage Aggregate Split: 32 split = 62.7% Fracture/Failure Count: 1 Total Fracture Length: 8 mm	










Measured Fracture/Failure Network: 8mm





Panel Number: 3 Analyzed Surface: Upper Wall of Excavation	
Notes Significant delamination at the shotcrete/concrete interface along the entirety of the upper wall measuring 23.5 mm long with a 0.1 mm maximum gap. There are 2 signs of cracking/failure where the wire mesh enters into the shotcrete layer, possibly due to vibrations induced by the impact hammer. There is also 1 other area of failure/fracture as identified below. The excavation tool left a wavy, irregular shape to the upper wall.	
Measured Delamination: 23.5 mm Fracture/Failure Count: 3 Total Fracture Length: 32.5 mm (including delamination) Damaged Wire Mesh? No	
<div style="display: flex; align-items: center;"> <div style="flex: 1;">  </div> <div style="flex: 1;">  <p>Measured Fracture/Failure Network: 4mm</p> </div> <div style="flex: 1;">  <p>Measured Fracture/Failure Network: 2mm</p> </div> <div style="flex: 1;">  <p>Measured Fracture/Failure Network: 3mm</p> </div> </div>	




Panel Number: 3 Analyzed Surface: Lower Wall of Excavation	
Notes Significant delamination at the shotcrete/concrete interface along the entirety of the lower wall measuring 30 mm long with a 0.1 mm maximum gap. There are 4 areas of failure/fracture as identified below. The excavation tool left a wavy, irregular shape to the left wall.	
Measured Delamination: 30 mm Fracture/Failure Count: 4 Total Fracture Length: 66 mm (including delamination) Damaged Wire Mesh? Yes	
	 Measured Fracture/Failure Network: 2mm  Measured Fracture/Failure Network: 3mm  Measured Fracture/Failure Network: 9mm  Measured Fracture/Failure Network: 22mm

Panel Number: 3 Analyzed Surface: Area Outside Excavated Profile	
<p>Notes</p> <p>2 areas of failure were discovered along the shotcrete face surrounding the excavation profile. The fracture in the the middle right area measures 7 mm while the fracture in the lower left corner measures 11 mm.</p>	
<p>Fracture/Failure Count: 2 Total Fracture Length: 18 mm</p>	





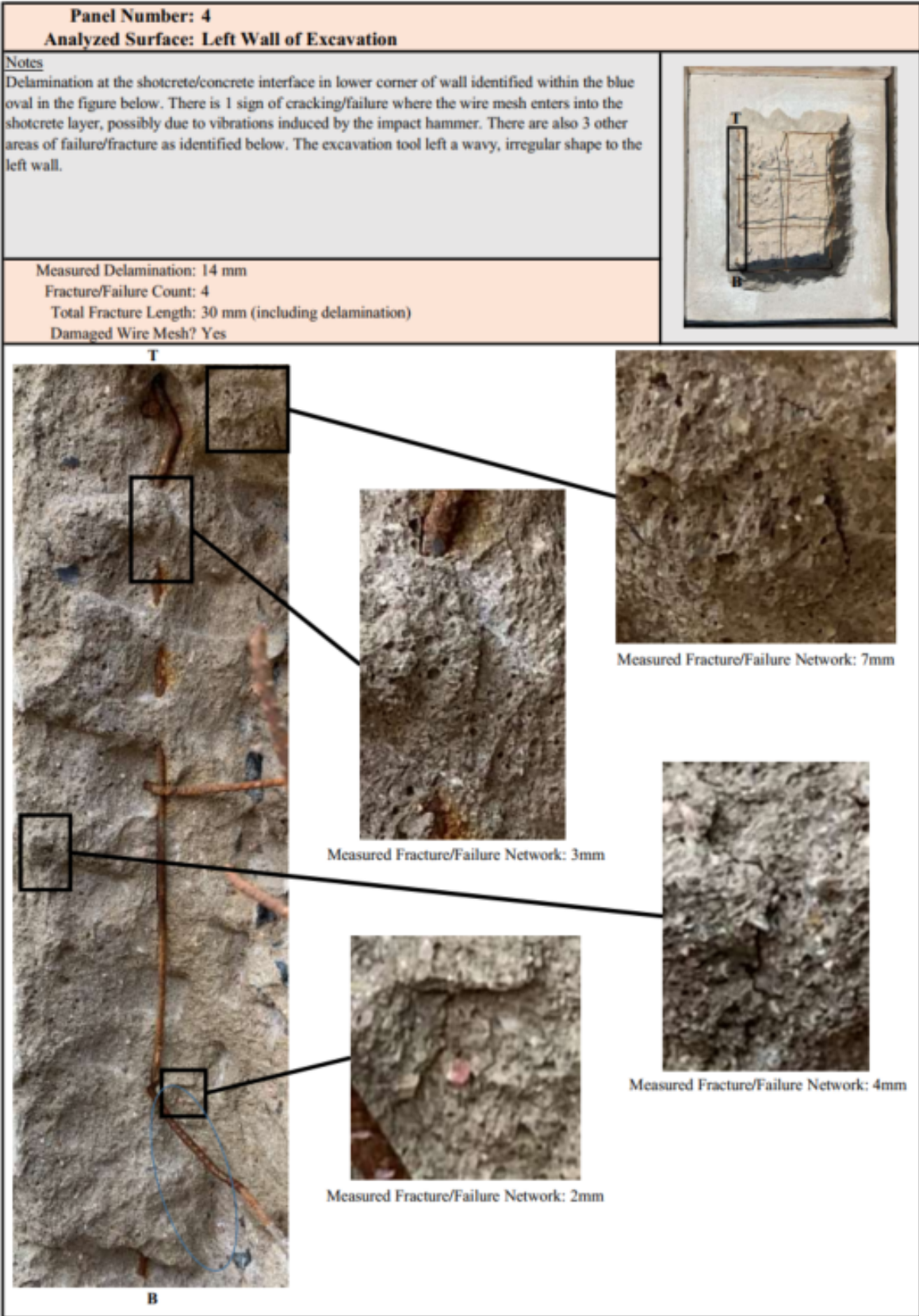


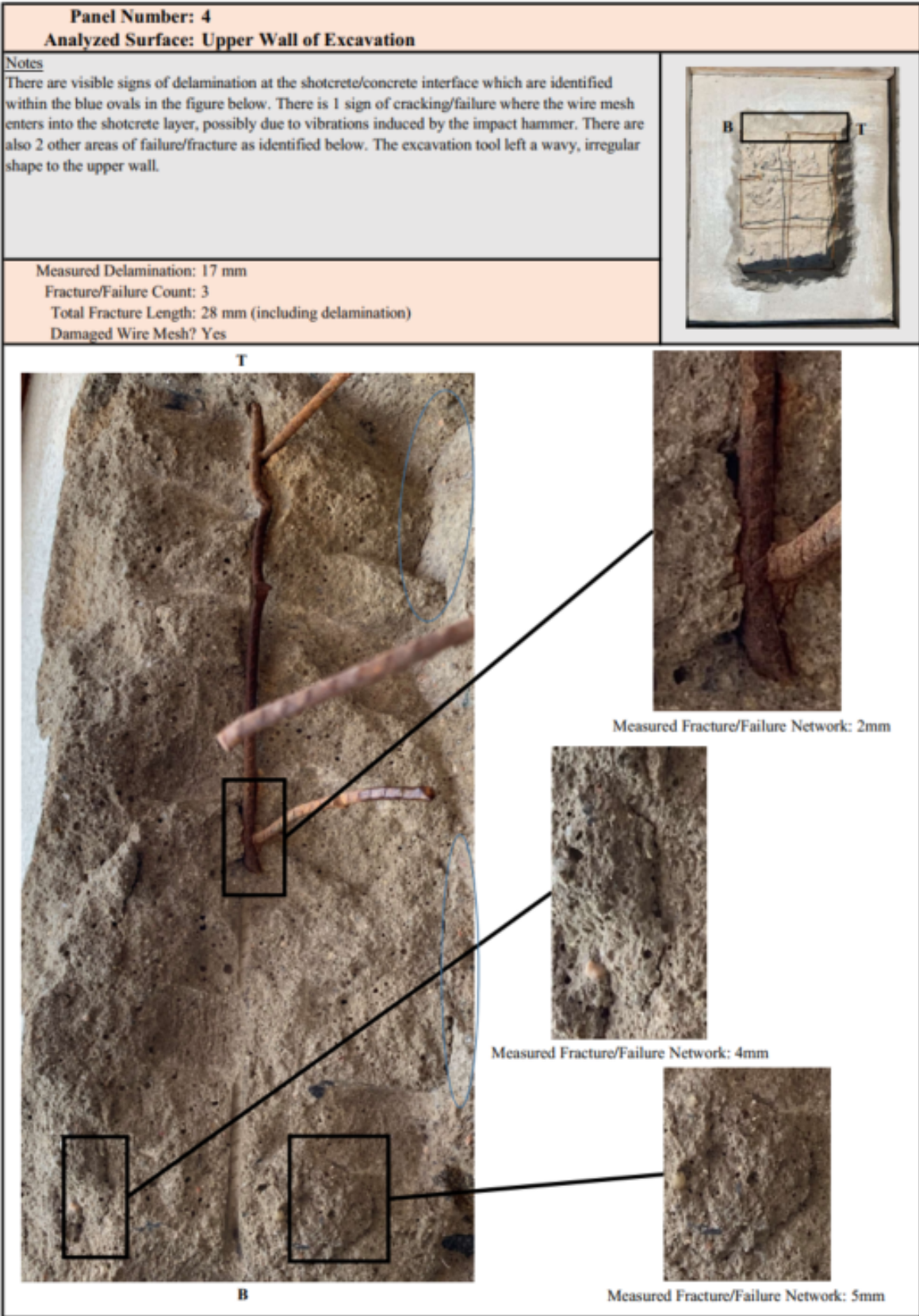
Measured Fracture/Failure Network: 7mm



Measured Fracture/Failure Network: 11mm

Panel Number: 3 Analyzed Surface: Excavation Face	
<u>Notes</u> While there was not a lot of exposed aggregate after excavation of this particular sample, a large percentage was still fractured by the impact hammer.	
Exposed Aggregate Count: 16 Percentage Aggregate Split: 10 split = 62.5% Fracture/Failure Count: 0 Total Fracture Length: 0 mm	
	







Panel Number: 4 Analyzed Surface: Right Wall of Excavation	
<p>Notes</p> <p>There are visible signs of delamination at the shotcrete/concrete interface which are identified within the blue ovals in the figure below. There is 1 sign of cracking/failure where the wire mesh enters into the shotcrete layer, possibly due to vibrations induced by the impact hammer. There is also 1 other area of failure/fracture as identified below. The excavation tool left a wavy, irregular shape to the right wall.</p>	
<p>Measured Delamination: 39 mm</p> <p>Fracture/Failure Count: 2</p> <p>Total Fracture Length: 42.5 mm (including delamination)</p> <p>Damaged Wire Mesh? Yes</p>	


T

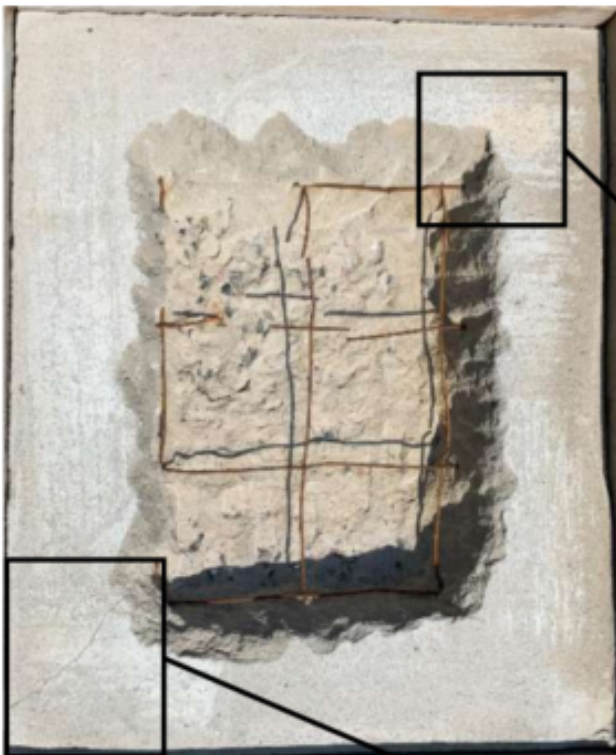
B

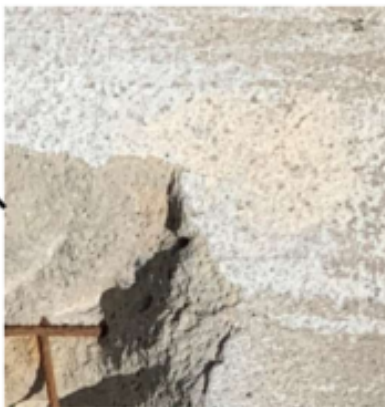
Measured Fracture/Failure Network: 0.5mm

Measured Fracture/Failure Network: 3mm


Panel Number: 4 Analyzed Surface: Lower Wall of Excavation	
Notes There are visible signs of delamination at the shotcrete/concrete interface identified within the blue oval in the figure below. The excavation tool left a wavy, irregular shape to the lower wall.	
Measured Delamination: 22 mm Fracture/Failure Count: 0 Total Fracture Length: 22 mm (including delamination) Damaged Wire Mesh? No	
<div style="text-align: center;">T</div>  <div style="text-align: center;">B</div>	

Panel Number: 4 Analyzed Surface: Area Outside Excavated Profile	
<p>Notes</p> <p>2 areas of failure was discovered along the shotcrete face surrounding the excavation profile. The fracture in the the lower left corner measures 16 mm and the fracture on the upper right corner measures 11 mm.</p>	
<p>Fracture/Failure Count: 2</p> <p>Total Fracture Length: 27 mm</p>	










Measured Fracture/Failure Network: 11mm



Measured Fracture/Failure Network: 16mm

Panel Number: 4 Analyzed Surface: Excavation Face	
Notes A large percentage of the exposed aggregate was fractured by the impact hammer.	
Exposed Aggregate Count: 57 Percentage Aggregate Split: 46 split = 80.7% Fracture/Failure Count: 0 Total Fracture Length: 0 mm	
	

Panel Number: 7 Analyzed Surface: Left Wall of Excavation	
Notes No visible signs of delamination at the shotcrete/concrete interface. There is 1 area of failure/fracture as identified below. At this edge of the cut, 1 rib of material were left between jet passes, resulting in 1 inconsistency.	
Fracture/Failure Count: 1 Total Fracture Length: 10 mm Damaged Wire Mesh? No	
<div style="text-align: center;">T  B</div> <div style="text-align: center;"> Measured Fracture/Failure Network: 10mm</div>	

Panel Number: 7
Analyzed Surface: Upper Wall of Excavation



Notes



There are no visible signs of delamination. Sections that look like delamination are areas where jet cut slightly into the wall and a shadow is cast over it. Waterjet left a very clean cut across the upper wall, no deviations or wavy nature.








Fracture/Failure Count: 0
Total Fracture Length: 0 mm
Damaged Wire Mesh? No



Panel Number: 7 Analyzed Surface: Right Wall of Excavation	
<u>Notes</u> No visible signs of delamination at the shotcrete/concrete interface. Waterjet left a very clean cut across the right wall, one slight rib deviation with no wavy nature.	
Fracture/Failure Count: 0 Total Fracture Length: 0 mm Damaged Wire Mesh? No	
<div style="text-align: center;">T</div>  <div style="text-align: center;">B</div>	

Panel Number: 7 Analyzed Surface: Lower Wall of Excavation	
<u>Notes</u> There are no visible signs of delamination. Waterjet left a very clean cut across the upper wall, no deviations or wavy nature.	
Fracture/Failure Count: 0 Total Fracture Length: 0 mm Damaged Wire Mesh? No	
<p style="text-align: center;">T</p>  <p style="text-align: center;">B</p>	

Panel Number: 7 Analyzed Surface: Area Outside Excavated Profile	
<p><u>Notes</u></p> <p>1 area of failure was discovered along the shotcrete face surrounding the excavation profile. The fracture measures 9 mm.</p>	
<p>Fracture/Failure Count: 1</p> <p>Total Fracture Length: 9 mm</p>	
<div><p>Measured Fracture/Failure Network: 9mm</p></div>	

Panel Number: 7 Analyzed Surface: Excavation Face	
<u>Notes</u> For this panel, the waterjet cut through the shotcrete/concrete interface to expose aggregate. Out of all the exposed aggregate, the jet did not cut or split any and, instead, eroded the cement binder between it. The figure below is a combination of multiple pictures taken at the face. This was done to provide a clearer, close up visual of the exposed aggregate. This also explains why the wire mesh isn't exactly alligned.	
Exposed Aggregate Count: 122 Percentage Aggregate Split: 0 split = 0% Fracture/Failure Count: 0 Total Fracture Length: 0 mm	
	

Panel Number: TEST
Analyzed Surface: Left Wall of Excavation



Notes



While this sample did not cut through the entirety of the shotcrete layer, there are no visible signs of delamination. There is 1 area of failure/fracture as identified below. At this edge of the cut, ribs of shotcrete were left between jet passes due to the system stalling while air bled out of the traverse in order to reverse direction.



Fracture/Failure Count: 1
Total Fracture Length: 13 mm
Damaged Wire Mesh? No








Measured Fracture/Failure Network: 13mm

Panel Number: TEST Analyzed Surface: Upper Wall of Excavation	
<u>Notes</u> While this sample did not cut through the entirety of the shotcrete layer, there are no visible signs of delamination. The section that looks like delamination is an area where the jet cut slightly into the wall and a shadow is cast over it. Waterjet left a very clean cut across the upper wall, no deviations or wavy nature.	
Fracture/Failure Count: 1 Total Fracture Length: 0 mm Damaged Wire Mesh? No	
<div style="text-align: center;">T</div>  <div style="text-align: center;">B</div>	

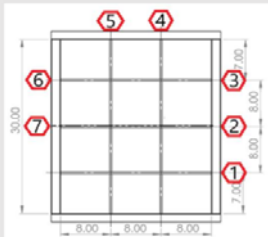
Panel Number: TEST Analyzed Surface: Right Wall of Excavation	
Notes While this sample did not cut through the entirety of the shotcrete layer, there are no visible signs of delamination. There is 1 area of failure/fracture as identified below. At this edge of the cut, ribs of shotcrete were left between jet passes due to the system stalling while air bled out of the traverse in order to reverse direction.	
Fracture/Failure Count: 1 Total Fracture Length: 5 mm Damaged Wire Mesh? No	
<div style="text-align: center;"> T  B </div>	

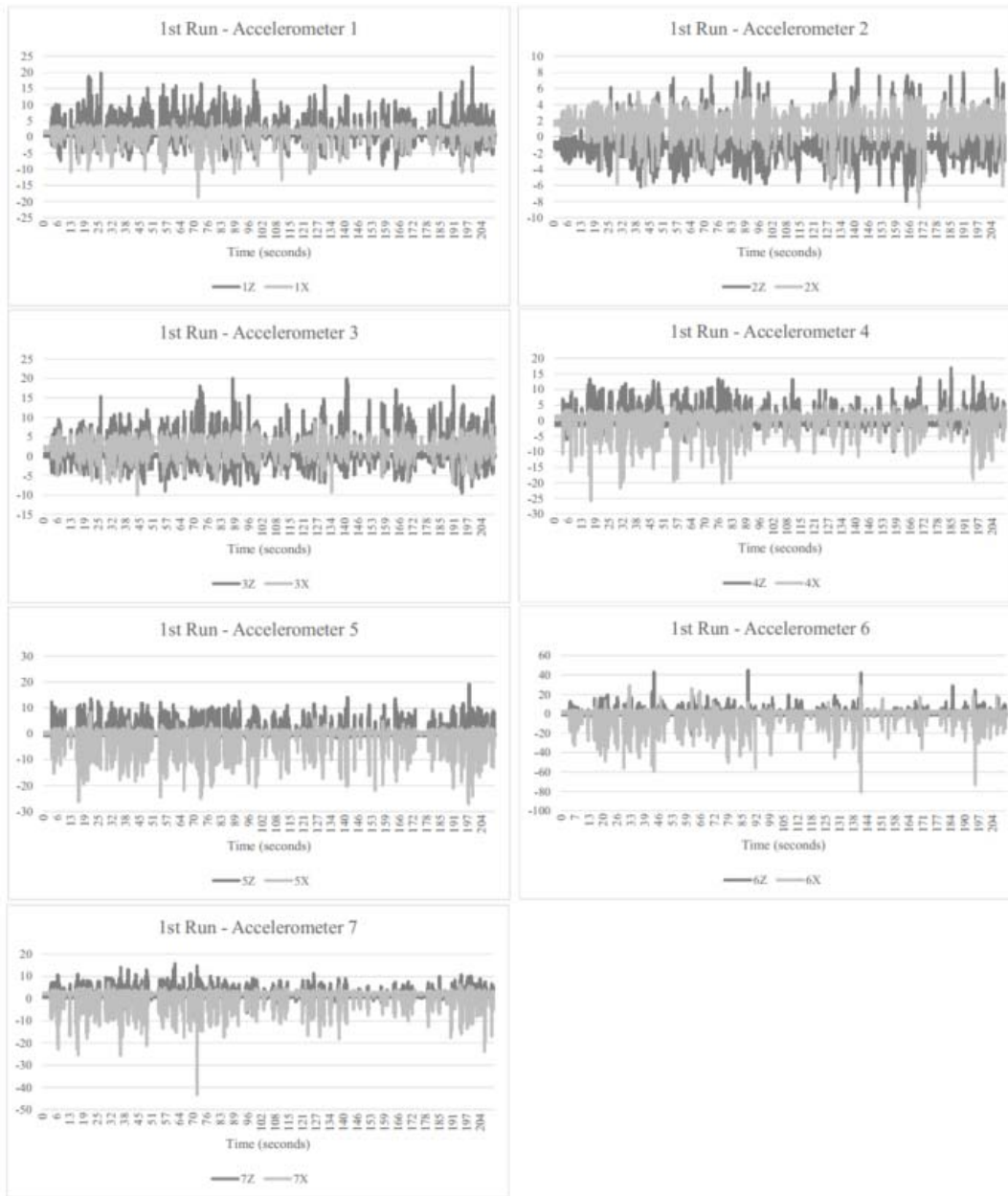
Panel Number: TEST Analyzed Surface: Lower Wall of Excavation	
<p><u>Notes</u></p> <p>While this sample did not cut through the entirety of the shotcrete layer, there are no visible signs of delamination. Waterjet left a clean cut across the lower wall, with one slight deviation but no wavy nature.</p>	
<p>Fracture/Failure Count: 0</p> <p>Total Fracture Length: 0 mm</p> <p>Damaged Wire Mesh? No</p>	
<div style="text-align: center;">T</div>  <div style="text-align: center;">B</div>	

Panel Number: TEST Analyzed Surface: Area Outside Excavated Profile	
<u>Notes</u> 1 area of failure was discovered along the shotcrete face surrounding the excavation profile. The fracture measures 5.5 mm.	
Fracture/Failure Count: 1 Total Fracture Length: 5.5 mm	
	
	
Measured Fracture/Failure Network: 5.5mm	

Panel Number: TEST Analyzed Surface: Excavation Face	
<u>Notes</u> For this panel, the waterjet did not cut through the entirety of the shotcrete layer so there was no exposed aggregate.	
Exposed Aggregate Count: 0 Percentage Aggregate Split: - Fracture/Failure Count: 0 Total Fracture Length: 0 mm	
	

Section B-4: Accelerometer Data

Panel Number: 2	
Run #: 1 of 7	
Notes: Drilled upper left 1/6 section of panel face, drilled upper right 1/6 section of panel face.	
Run Time (sec): 210	
Run Time Segment (sec): 0 - 210	
Total Panel Run Time (sec): 1470	
Y Axis Accelerometer Units: g	
Accelerometer 1 Peak (abs value): 21.7	
Accelerometer 2 Peak (abs value): 8.8	
Accelerometer 3 Peak (abs value): 20.1	
Accelerometer 4 Peak (abs value): 25.8	
Accelerometer 5 Peak (abs value): 27.1	
Accelerometer 6 Peak (abs value): 80.8	
Accelerometer 7 Peak (abs value): 43.4	
A National Instruments USB-6211 DAQ was used to read the analog signals from the accelerometers. This DAQ supported 16 analog channels. 14 of the channels were used for accelerometer data, one was used to monitor the accelerometer power supply voltage, and the remaining analog channel was not used. The Z axis and the X axis were used on each accelerometer due to the limited number of analog channels available. The Z axis was normal to the sample surface with +Z pointing towards the excavation equipment. The X axis ran parallel to the edge of the sample.	

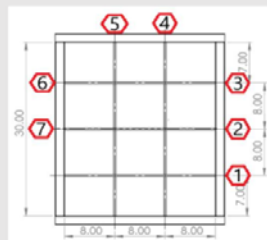


Panel Number: 2

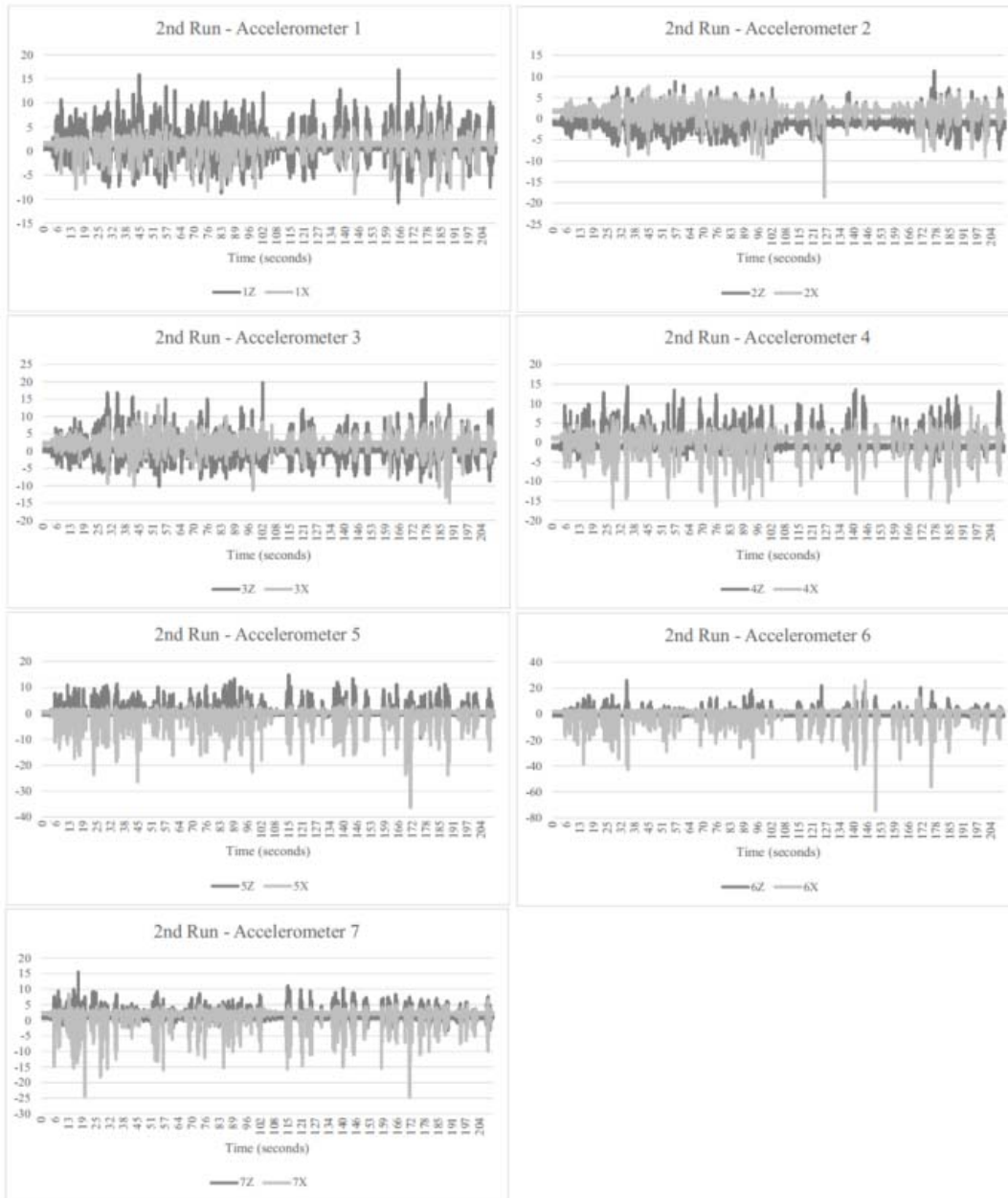
Run #: 2 of 7

Notes: Drilled upper right 1/6 section of panel face, got past wire mesh.

Run Time (sec): 210
Run Time Segment (sec): 210 - 420
Total Panel Run Time (sec): 1470
Y Axis Accelerometer Units: g
Accelerometer 1 Peak (abs value): 16.9
Accelerometer 2 Peak (abs value): 18.6
Accelerometer 3 Peak (abs value): 19.8
Accelerometer 4 Peak (abs value): 17.0
Accelerometer 5 Peak (abs value): 36.4
Accelerometer 6 Peak (abs value): 74.4
Accelerometer 7 Peak (abs value): 24.7



A National Instruments USB-6211 DAQ was used to read the analog signals from the accelerometers. This DAQ supported 16 analog channels. 14 of the channels were used for accelerometer data, one was used to monitor the accelerometer power supply voltage, and the remaining analog channel was not used. The Z axis and the X axis were used on each accelerometer due to the limited number of analog channels available. The Z axis was normal to the sample surface with +Z pointing towards the excavation equipment. The X axis ran parallel to the edge of the sample.

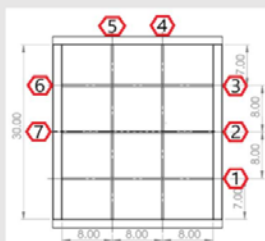


Panel Number: 2

Run #: 3 of 7

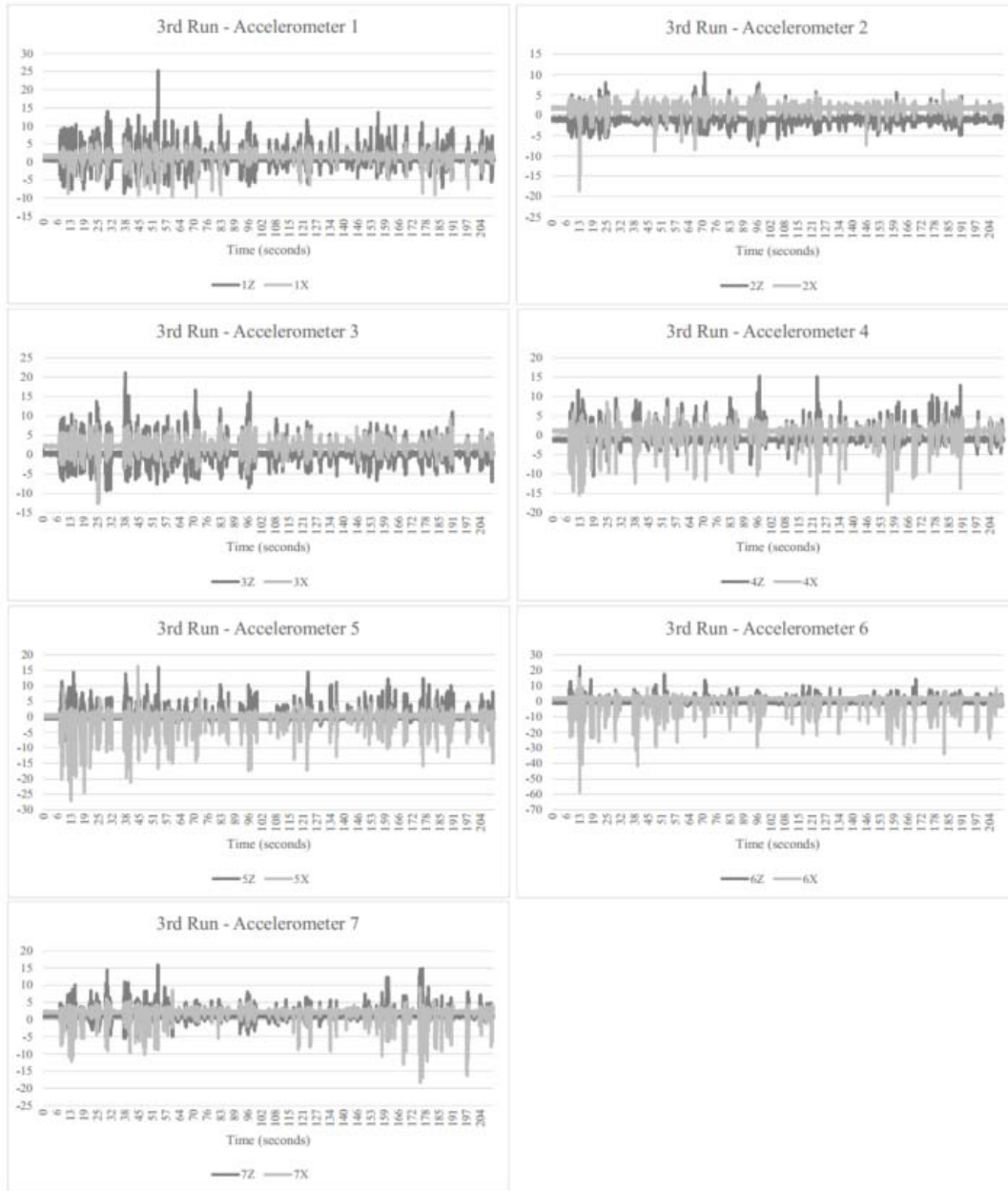
Notes: Drilled upper left 1/6 section of panel face, got past wire mesh.

Run Time (sec): 210
 Run Time Segment (sec): 420 - 630
 Total Panel Run Time (sec): 1470
 Y Axis Accelerometer Units: g
 Accelerometer 1 Peak (abs value): 25.3
 Accelerometer 2 Peak (abs value): 18.7
 Accelerometer 3 Peak (abs value): 21.2
 Accelerometer 4 Peak (abs value): 17.8
 Accelerometer 5 Peak (abs value): 27.1
 Accelerometer 6 Peak (abs value): 58.8
 Accelerometer 7 Peak (abs value): 18.3



A National Instruments USB-6211 DAQ was used to read the analog signals from the accelerometers. This DAQ supported 16 analog channels. 14 of the channels were used for accelerometer data, one was used to monitor the accelerometer power supply voltage, and the remaining analog channel was not used.

The Z axis and the X axis were used on each accelerometer due to the limited number of analog channels available. The Z axis was normal to the sample surface with +Z pointing towards the excavation equipment. The X axis ran parallel to the edge of the sample.

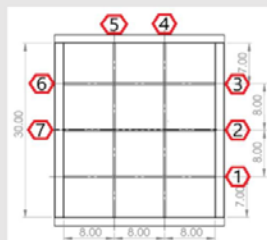


Panel Number: 2

Run #: 4 of 7

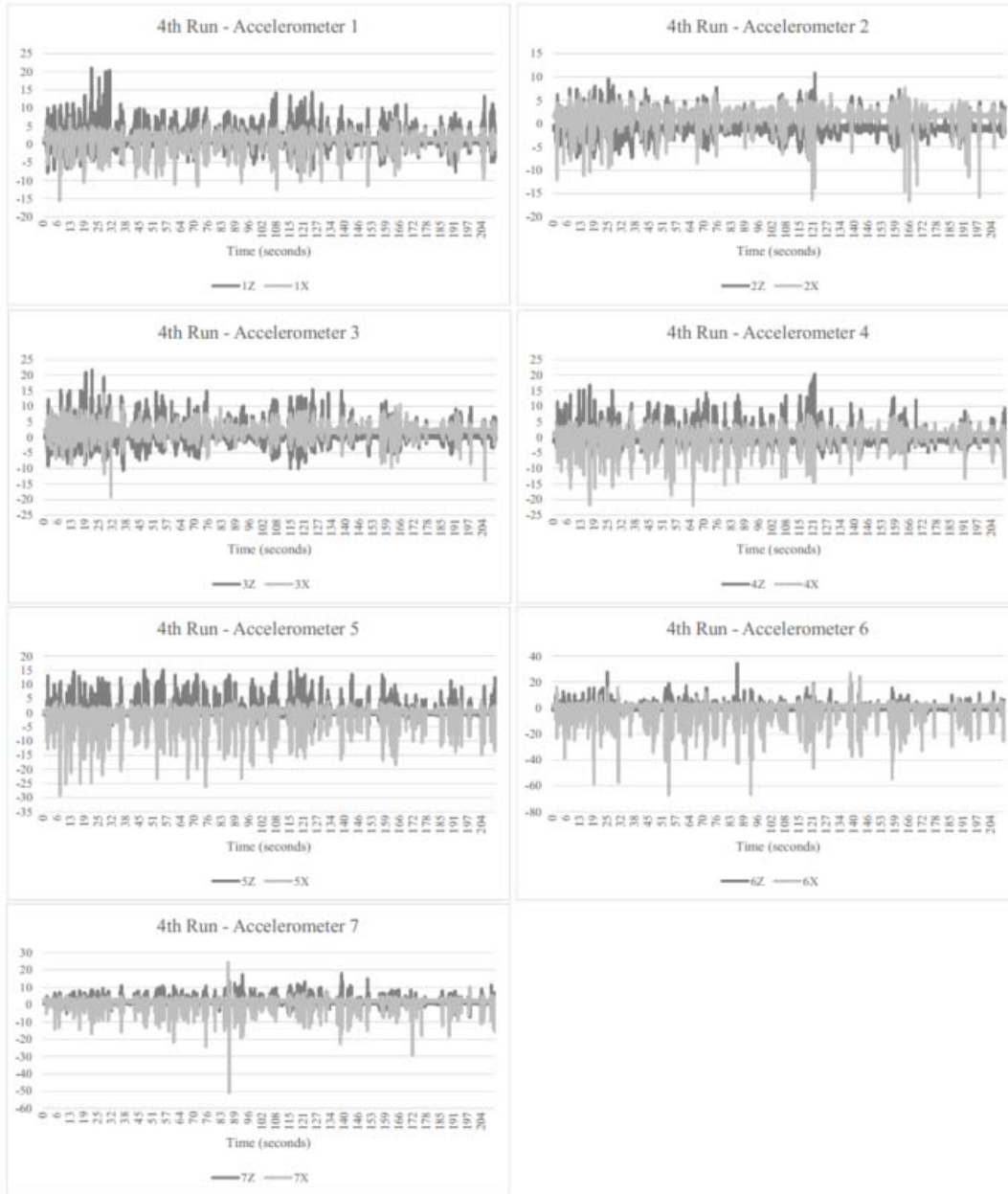
Notes: Drilled middle left 1/6 section of panel face.

Run Time (sec): 210
 Run Time Segment (sec): 630 - 840
 Total Panel Run Time (sec): 1470
 Y Axis Accelerometer Units: g
 Accelerometer 1 Peak (abs value): 21.0
 Accelerometer 2 Peak (abs value): 16.7
 Accelerometer 3 Peak (abs value): 21.7
 Accelerometer 4 Peak (abs value): 22.1
 Accelerometer 5 Peak (abs value): 29.3
 Accelerometer 6 Peak (abs value): 67.0
 Accelerometer 7 Peak (abs value): 51.0



A National Instruments USB-6211 DAQ was used to read the analog signals from the accelerometers. This DAQ supported 16 analog channels. 14 of the channels were used for accelerometer data, one was used to monitor the accelerometer power supply voltage, and the remaining analog channel was not used.

The Z axis and the X axis were used on each accelerometer due to the limited number of analog channels available. The Z axis was normal to the sample surface with +Z pointing towards the excavation equipment. The X axis ran parallel to the edge of the sample.

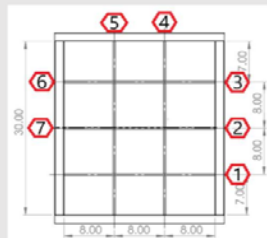


Panel Number: 2

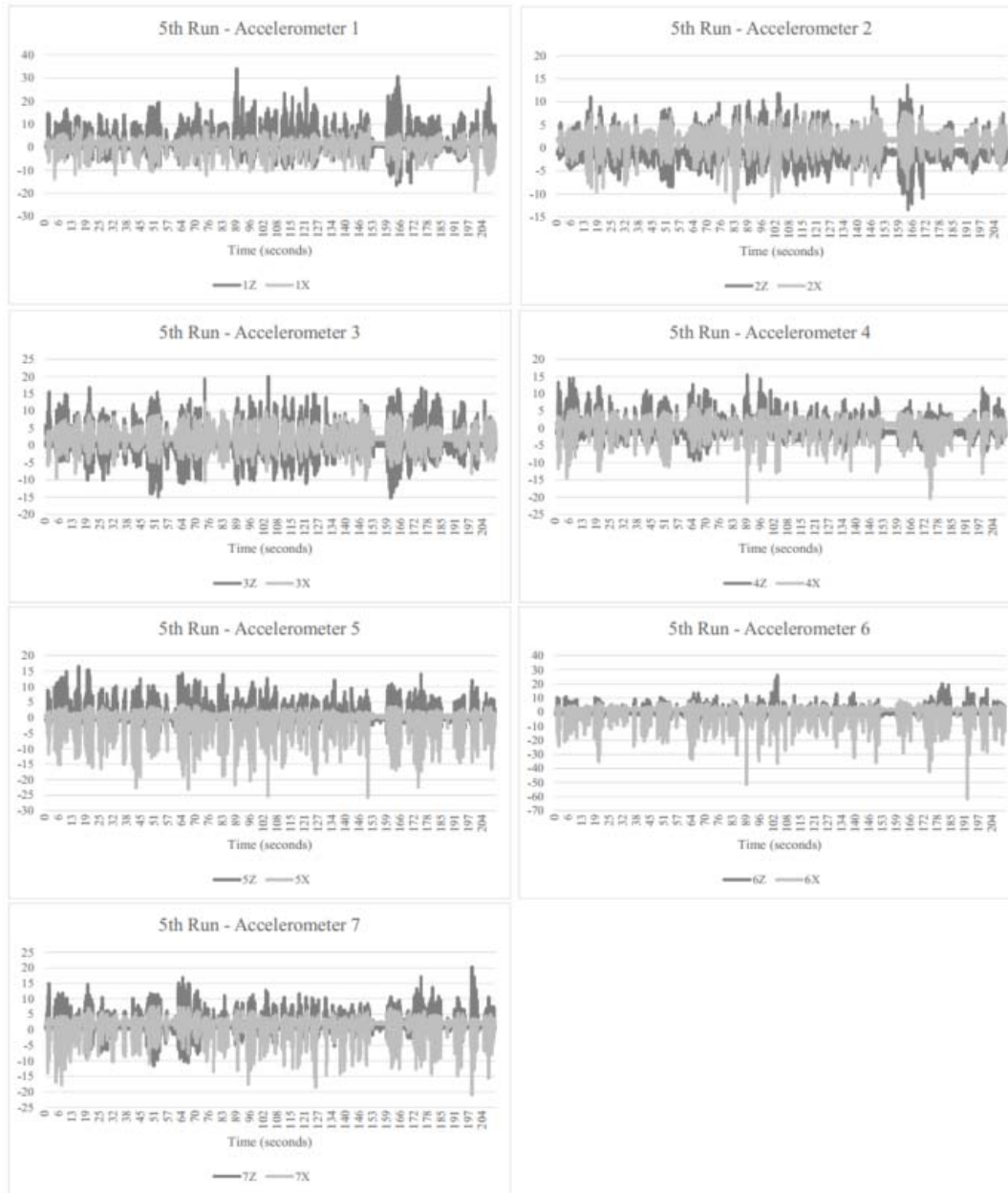
Run #: 5 of 7

Notes: Drilled middle right 1/6 section of panel face.

Run Time (sec): 210
 Run Time Segment (sec): 840 - 1050
 Total Panel Run Time (sec): 1470
 Y Axis Accelerometer Units: g
 Accelerometer 1 Peak (abs value): 34.1
 Accelerometer 2 Peak (abs value): 13.7
 Accelerometer 3 Peak (abs value): 20.0
 Accelerometer 4 Peak (abs value): 21.6
 Accelerometer 5 Peak (abs value): 25.8
 Accelerometer 6 Peak (abs value): 61.7
 Accelerometer 7 Peak (abs value): 21.0



A National Instruments USB-6211 DAQ was used to read the analog signals from the accelerometers. This DAQ supported 16 analog channels. 14 of the channels were used for accelerometer data, one was used to monitor the accelerometer power supply voltage, and the remaining analog channel was not used. The Z axis and the X axis were used on each accelerometer due to the limited number of analog channels available. The Z axis was normal to the sample surface with +Z pointing towards the excavation equipment. The X axis ran parallel to the edge of the sample.

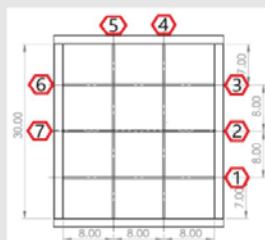


Panel Number: 2

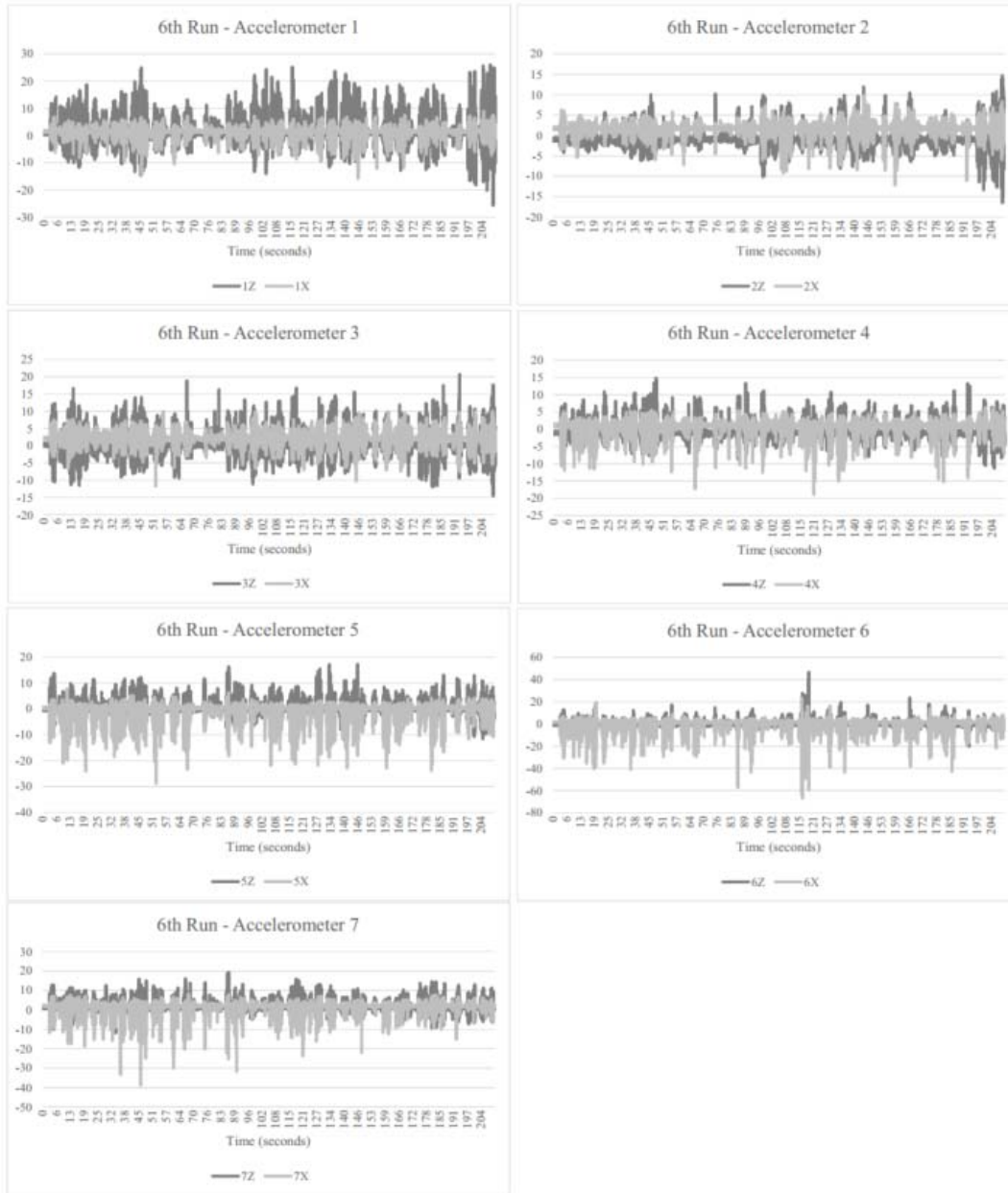
Run #: 6 of 7

Notes: Drilled bottom right and left 1/6 section of panel face. Got past wire mesh on middle right 1/6 section of panel face (delamination during testing).

Run Time (sec): 210
 Run Time Segment (sec): 1050 - 1260
 Total Panel Run Time (sec): 1470
 Y Axis Accelerometer Units: g
 Accelerometer 1 Peak (abs value): 26.0
 Accelerometer 2 Peak (abs value): 16.5
 Accelerometer 3 Peak (abs value): 20.7
 Accelerometer 4 Peak (abs value): 18.9
 Accelerometer 5 Peak (abs value): 28.7
 Accelerometer 6 Peak (abs value): 66.9
 Accelerometer 7 Peak (abs value): 38.8



A National Instruments USB-6211 DAQ was used to read the analog signals from the accelerometers. This DAQ supported 16 analog channels. 14 of the channels were used for accelerometer data, one was used to monitor the accelerometer power supply voltage, and the remaining analog channel was not used. The Z axis and the X axis were used on each accelerometer due to the limited number of analog channels available. The Z axis was normal to the sample surface with +Z pointing towards the excavation equipment. The X axis ran parallel to the edge of the sample.

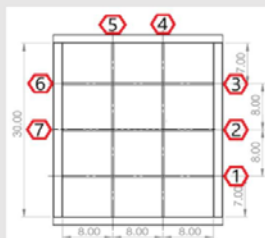


Panel Number: 2

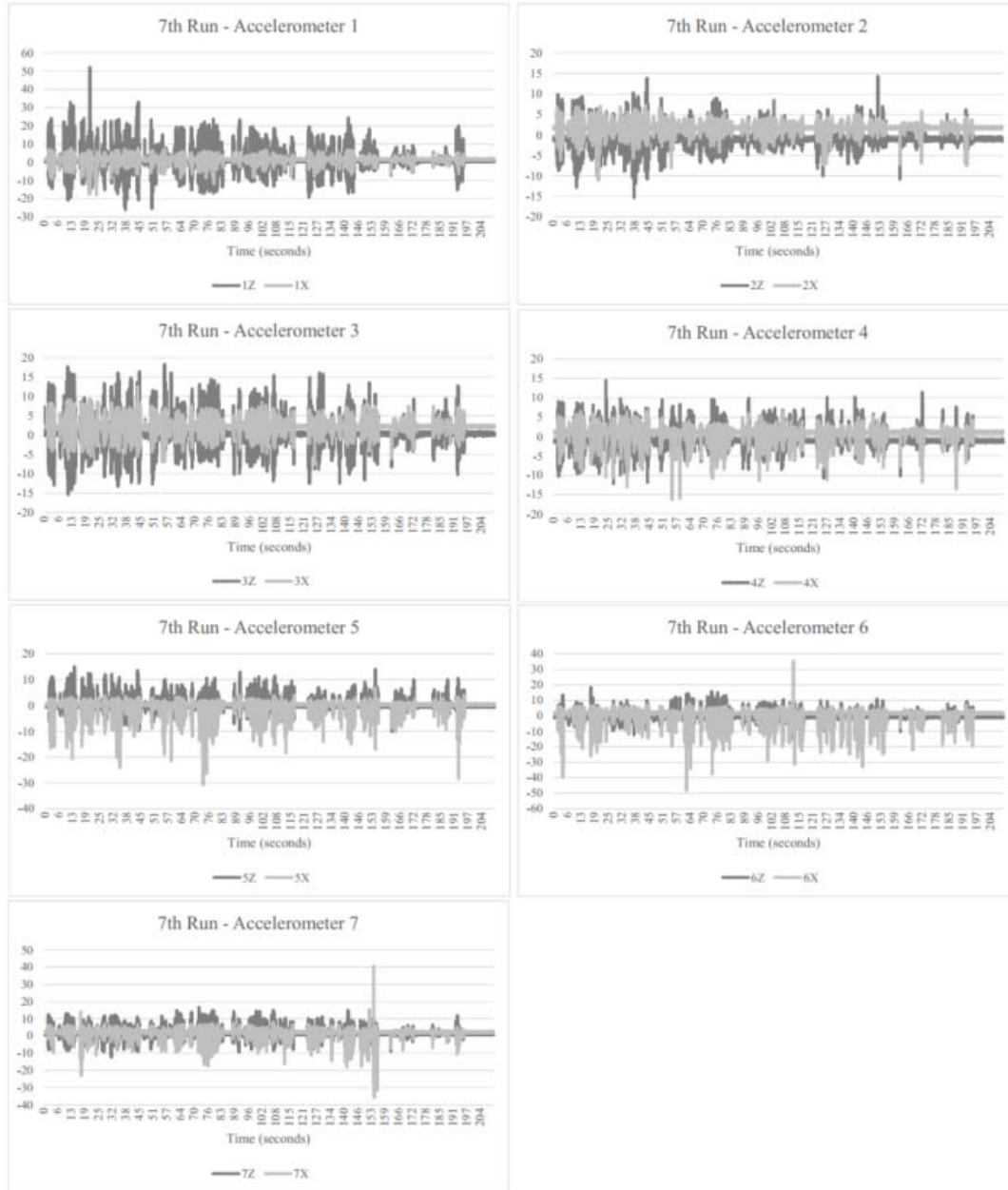
Run #: 7 of 7

Notes: Drilled and finished bottom right and left 1/6 section of panel face.

Run Time (sec): 210
 Run Time Segment (sec): 1260 - 1470
 Total Panel Run Time (sec): 1470
 Y Axis Accelerometer Units: g
 Accelerometer 1 Peak (abs value): 52.1
 Accelerometer 2 Peak (abs value): 15.4
 Accelerometer 3 Peak (abs value): 18.3
 Accelerometer 4 Peak (abs value): 16.3
 Accelerometer 5 Peak (abs value): 30.9
 Accelerometer 6 Peak (abs value): 48.3
 Accelerometer 7 Peak (abs value): 40.8



A National Instruments USB-6211 DAQ was used to read the analog signals from the accelerometers. This DAQ supported 16 analog channels. 14 of the channels were used for accelerometer data, one was used to monitor the accelerometer power supply voltage, and the remaining analog channel was not used. The Z axis and the X axis were used on each accelerometer due to the limited number of analog channels available. The Z axis was normal to the sample surface with +Z pointing towards the excavation equipment. The X axis ran parallel to the edge of the sample.

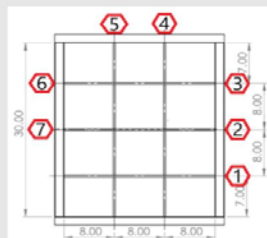


Panel Number: 3

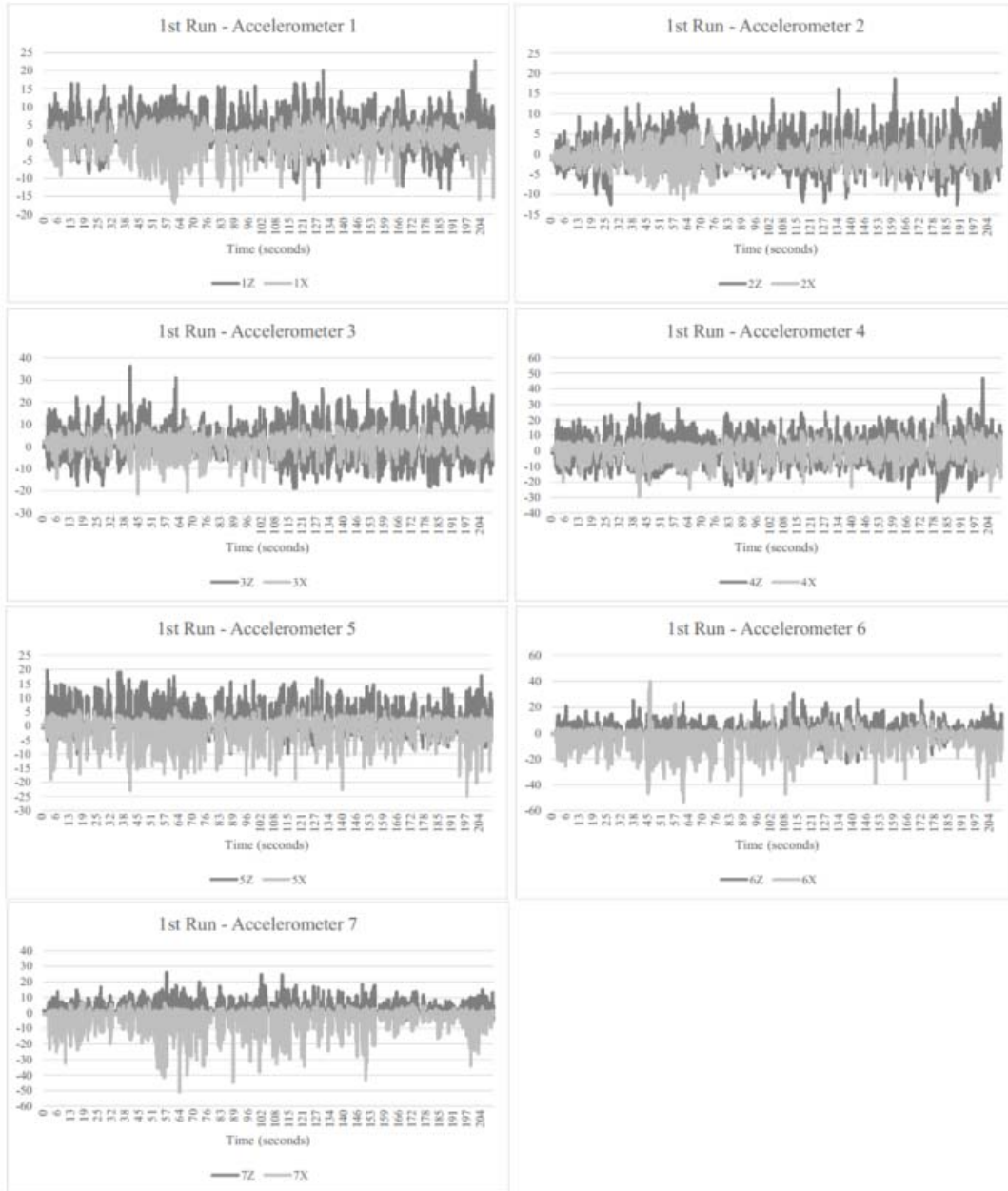
Run #: 1 of 8

Notes: Drilled upper left 1/6 section of panel face, drilled upper right 1/6 section of panel face.

Run Time (sec): 210
Run Time Segment (sec): 0 - 210
Total Panel Run Time (sec): 1530
Y Axis Accelerometer Units: g
Accelerometer 1 Peak (abs value): 22.9
Accelerometer 2 Peak (abs value): 18.7
Accelerometer 3 Peak (abs value): 36.3
Accelerometer 4 Peak (abs value): 46.8
Accelerometer 5 Peak (abs value): 24.8
Accelerometer 6 Peak (abs value): 53.5
Accelerometer 7 Peak (abs value): 51.0



A National Instruments USB-6211 DAQ was used to read the analog signals from the accelerometers. This DAQ supported 16 analog channels. 14 of the channels were used for accelerometer data, one was used to monitor the accelerometer power supply voltage, and the remaining analog channel was not used. The Z axis and the X axis were used on each accelerometer due to the limited number of analog channels available. The Z axis was normal to the sample surface with +Z pointing towards the excavation equipment. The X axis ran parallel to the edge of the sample.

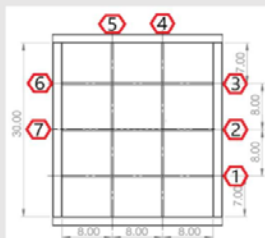


Panel Number: 3

Run #: 2 of 8

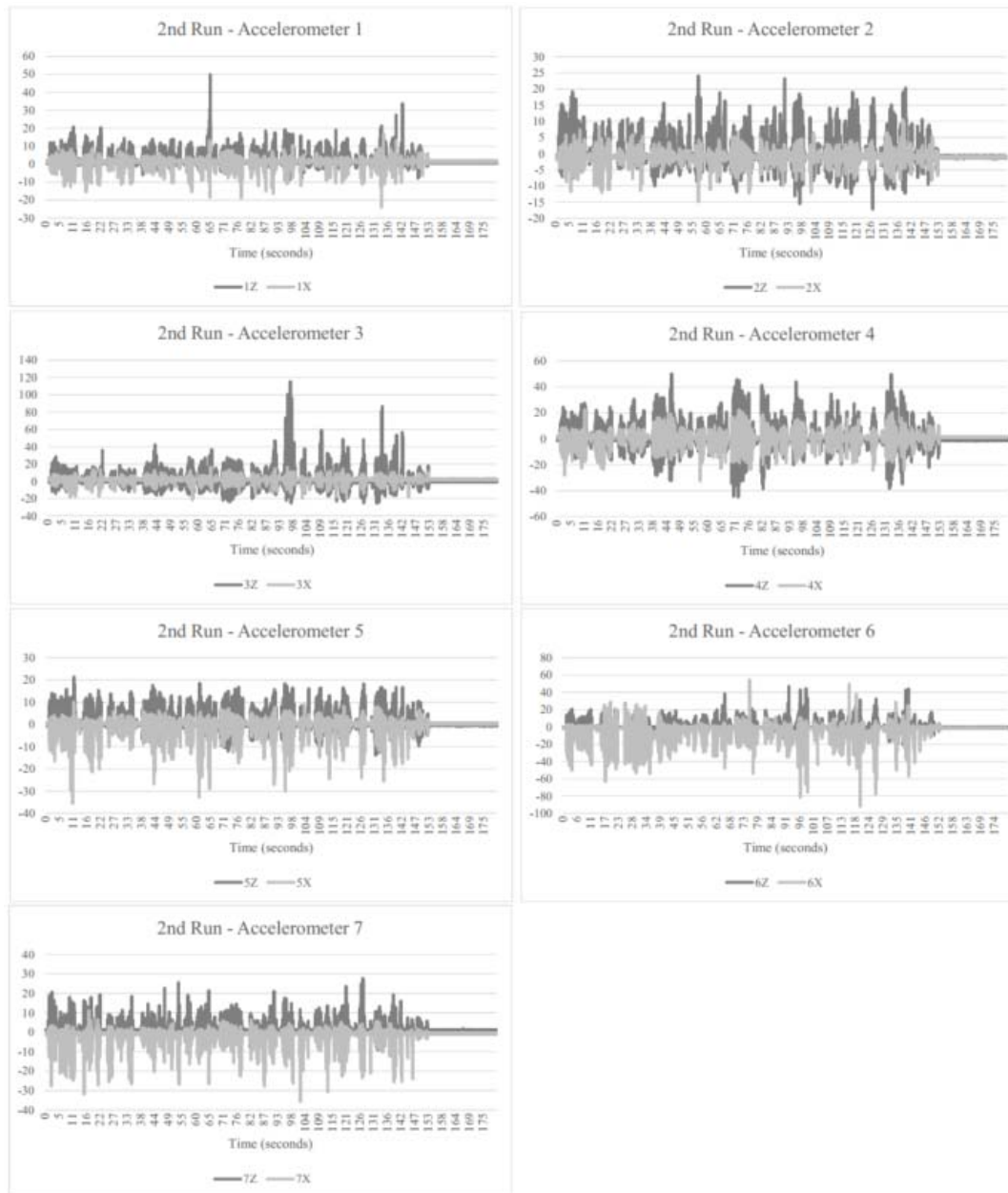
Notes: Drilled upper right 1/6 section of panel face, got past wire mesh.

Run Time (sec): 180
Run Time Segment (sec): 210 - 390
Total Panel Run Time (sec): 1530
Y Axis Accelerometer Units: g
Accelerometer 1 Peak (abs value): 49.9
Accelerometer 2 Peak (abs value): 24.1
Accelerometer 3 Peak (abs value): 115.3
Accelerometer 4 Peak (abs value): 50.1
Accelerometer 5 Peak (abs value): 35.6
Accelerometer 6 Peak (abs value): 92.1
Accelerometer 7 Peak (abs value): 35.7



A National Instruments USB-6211 DAQ was used to read the analog signals from the accelerometers. This DAQ supported 16 analog channels. 14 of the channels were used for accelerometer data, one was used to monitor the accelerometer power supply voltage, and the remaining analog channel was not used.

The Z axis and the X axis were used on each accelerometer due to the limited number of analog channels available. The Z axis was normal to the sample surface with +Z pointing towards the excavation equipment. The X axis ran parallel to the edge of the sample.

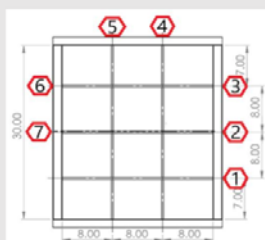


Panel Number: 3

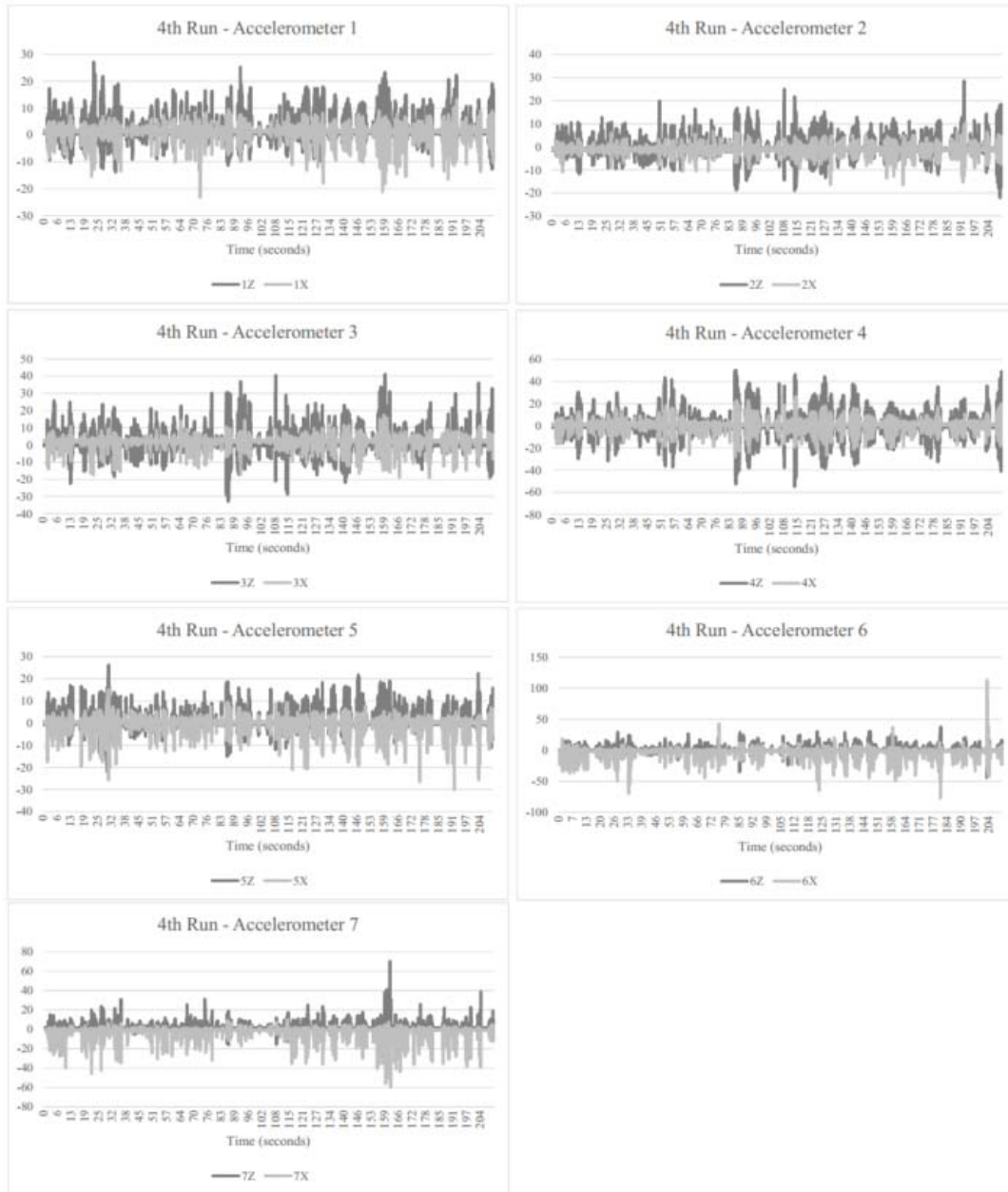
Run #: 3 of 8

Notes: Drilled upper left 1/6 section of panel face, got past wire mesh.

Run Time (sec): 210
 Run Time Segment (sec): 390 - 600
 Total Panel Run Time (sec): 1530
 Y Axis Accelerometer Units: g
 Accelerometer 1 Peak (abs value): 32.7
 Accelerometer 2 Peak (abs value): 26.7
 Accelerometer 3 Peak (abs value): 63.3
 Accelerometer 4 Peak (abs value): 52.0
 Accelerometer 5 Peak (abs value): 39.5
 Accelerometer 6 Peak (abs value): 77.3
 Accelerometer 7 Peak (abs value): 58.8



A National Instruments USB-6211 DAQ was used to read the analog signals from the accelerometers. This DAQ supported 16 analog channels. 14 of the channels were used for accelerometer data, one was used to monitor the accelerometer power supply voltage, and the remaining analog channel was not used. The Z axis and the X axis were used on each accelerometer due to the limited number of analog channels available. The Z axis was normal to the sample surface with +Z pointing towards the excavation equipment. The X axis ran parallel to the edge of the sample.

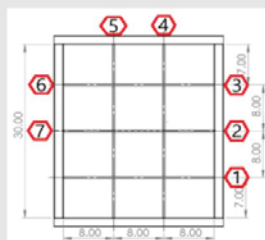


Panel Number: 3

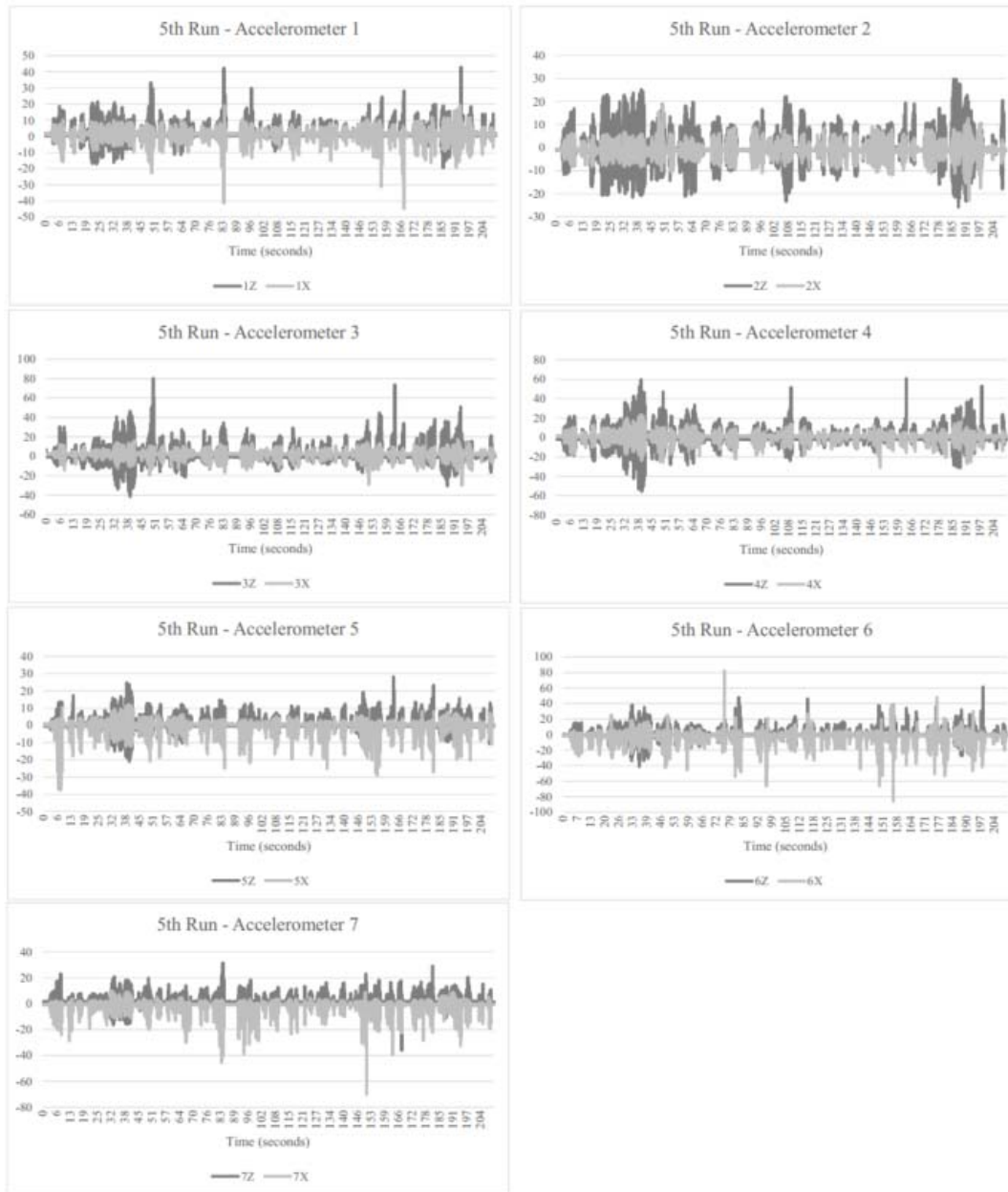
Run #: 5 of 8

Notes: Drilled middle right 1/6 section of panel face.

Run Time (sec): 210
 Run Time Segment (sec): 810 - 1020
 Total Panel Run Time (sec): 1530
 Y Axis Accelerometer Units: g
 Accelerometer 1 Peak (abs value): 44.8
 Accelerometer 2 Peak (abs value): 29.7
 Accelerometer 3 Peak (abs value): 80.3
 Accelerometer 4 Peak (abs value): 60.8
 Accelerometer 5 Peak (abs value): 37.7
 Accelerometer 6 Peak (abs value): 85.8
 Accelerometer 7 Peak (abs value): 70.1



A National Instruments USB-6211 DAQ was used to read the analog signals from the accelerometers. This DAQ supported 16 analog channels. 14 of the channels were used for accelerometer data, one was used to monitor the accelerometer power supply voltage, and the remaining analog channel was not used. The Z axis and the X axis were used on each accelerometer due to the limited number of analog channels available. The Z axis was normal to the sample surface with +Z pointing towards the excavation equipment. The X axis ran parallel to the edge of the sample.

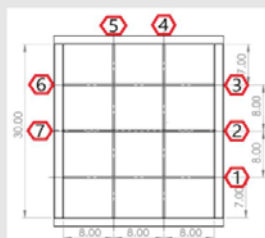


Panel Number: 3

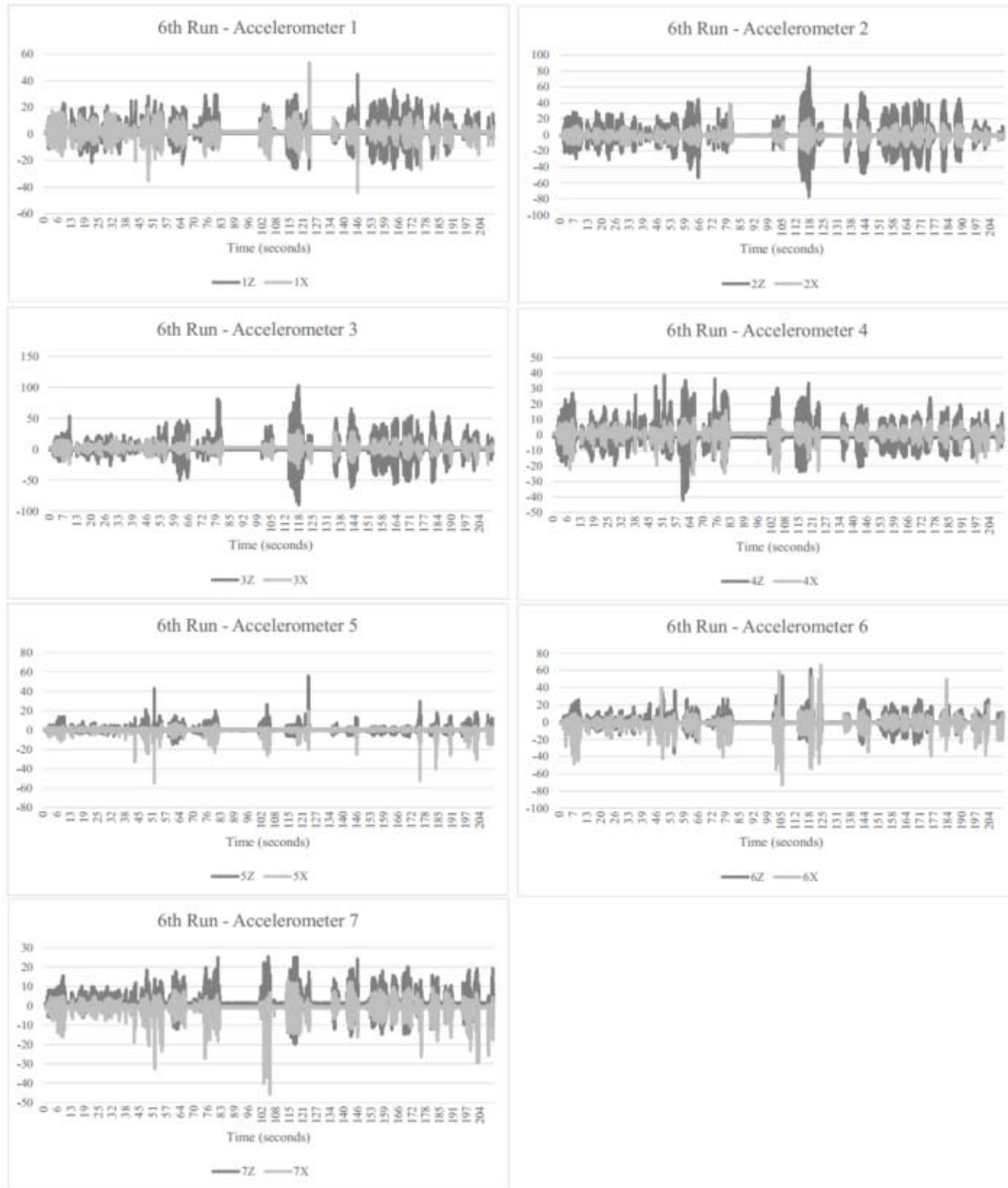
Run #: 6 of 8

Notes: Drilled bottom right and left 1/6 section of panel face. Got past wire mesh on middle right 1/6 section of panel face (delamination during testing).

Run Time (sec): 210
 Run Time Segment (sec): 1020 - 1230
 Total Panel Run Time (sec): 1530
 Y Axis Accelerometer Units: g
 Accelerometer 1 Peak (abs value): 53.7
 Accelerometer 2 Peak (abs value): 84.6
 Accelerometer 3 Peak (abs value): 103.2
 Accelerometer 4 Peak (abs value): 42.2
 Accelerometer 5 Peak (abs value): 55.8
 Accelerometer 6 Peak (abs value): 73.3
 Accelerometer 7 Peak (abs value): 45.7



A National Instruments USB-6211 DAQ was used to read the analog signals from the accelerometers. This DAQ supported 16 analog channels. 14 of the channels were used for accelerometer data, one was used to monitor the accelerometer power supply voltage, and the remaining analog channel was not used. The Z axis and the X axis were used on each accelerometer due to the limited number of analog channels available. The Z axis was normal to the sample surface with +Z pointing towards the excavation equipment. The X axis ran parallel to the edge of the sample.

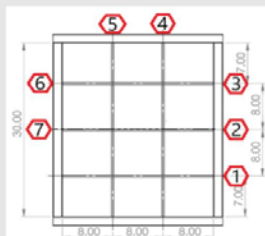


Panel Number: 3

Run #: 7 of 8

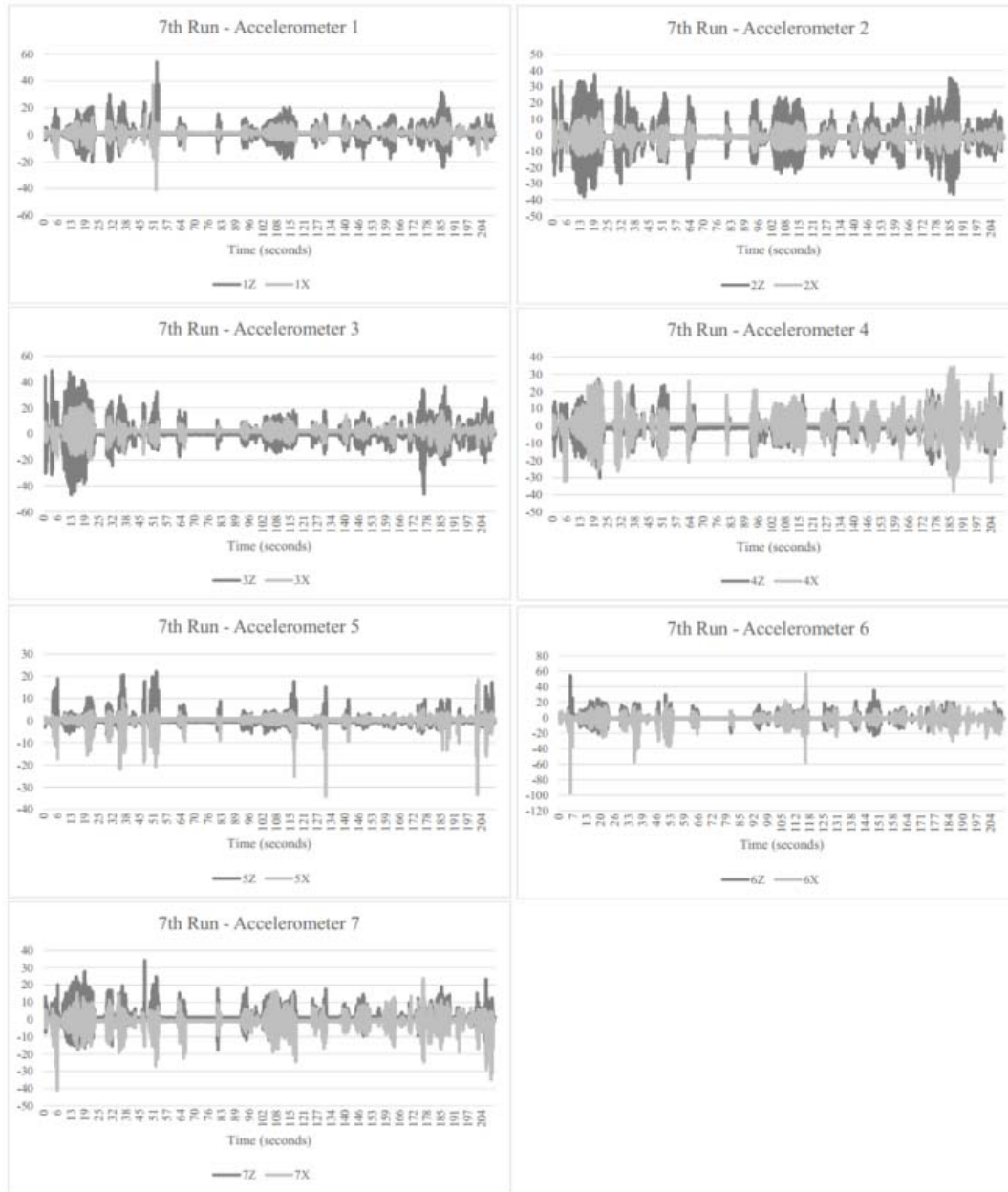
Notes: Drilled and finished bottom right and left 1/6 section of panel face.

Run Time (sec): 210
 Run Time Segment (sec): 1230 - 1440
 Total Panel Run Time (sec): 1530
 Y Axis Accelerometer Units: g
 Accelerometer 1 Peak (abs value): 54.2
 Accelerometer 2 Peak (abs value): 38.2
 Accelerometer 3 Peak (abs value): 48.8
 Accelerometer 4 Peak (abs value): 38.0
 Accelerometer 5 Peak (abs value): 34.3
 Accelerometer 6 Peak (abs value): 97.3
 Accelerometer 7 Peak (abs value): 41.2



A National Instruments USB-6211 DAQ was used to read the analog signals from the accelerometers. This DAQ supported 16 analog channels. 14 of the channels were used for accelerometer data, one was used to monitor the accelerometer power supply voltage, and the remaining analog channel was not used.

The Z axis and the X axis were used on each accelerometer due to the limited number of analog channels available. The Z axis was normal to the sample surface with +Z pointing towards the excavation equipment. The X axis ran parallel to the edge of the sample.

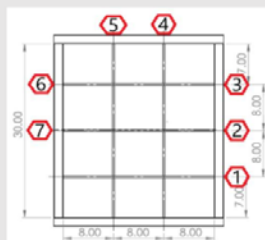


Panel Number: 3

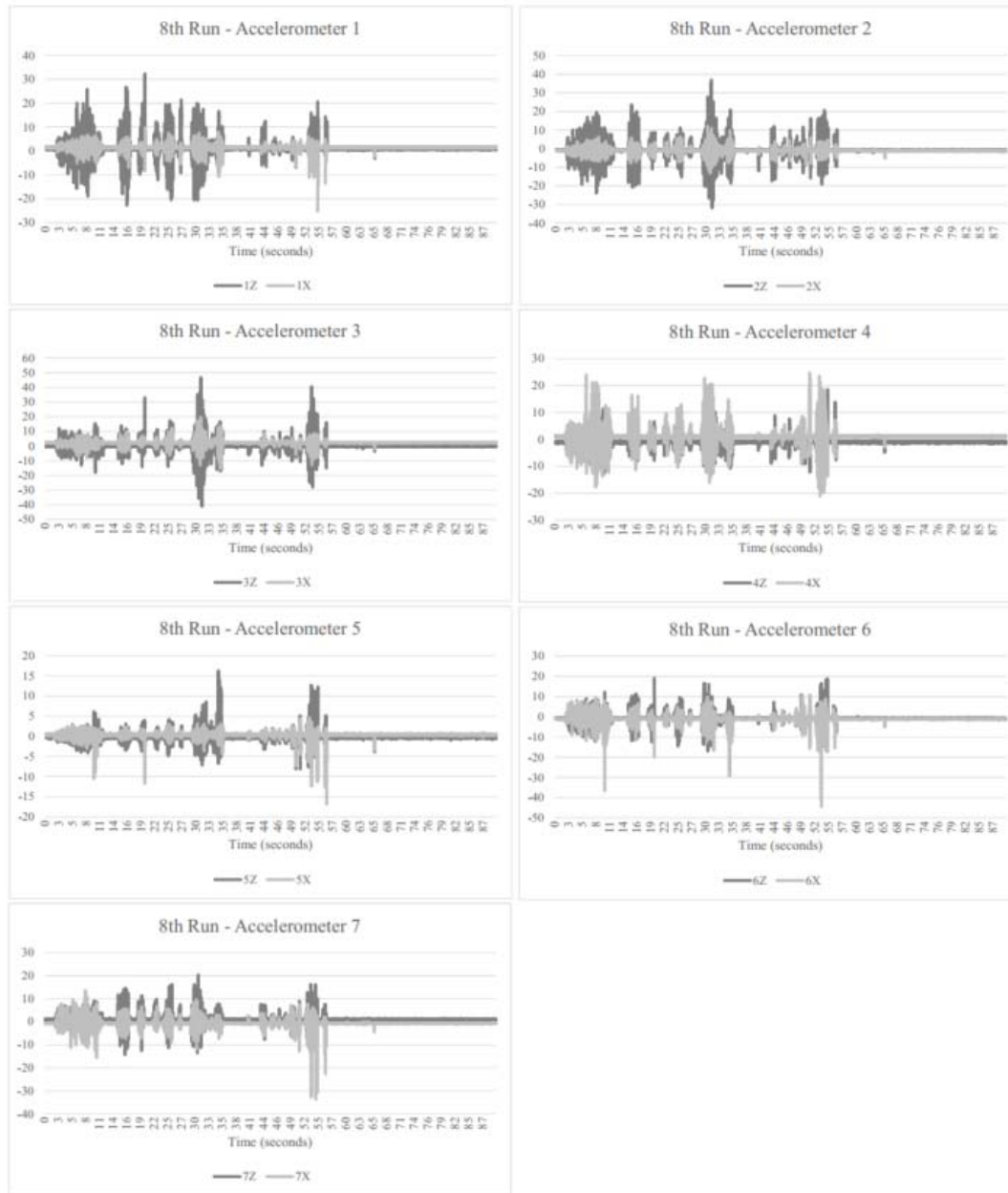
Run #: 8 of 8

Notes: Drill clean up of entire panel face.

Run Time (sec): 90
 Run Time Segment (sec): 1440 - 1530
 Total Panel Run Time (sec): 1530
 Y Axis Accelerometer Units: g
 Accelerometer 1 Peak (abs value): 32.3
 Accelerometer 2 Peak (abs value): 36.9
 Accelerometer 3 Peak (abs value): 46.6
 Accelerometer 4 Peak (abs value): 24.7
 Accelerometer 5 Peak (abs value): 16.8
 Accelerometer 6 Peak (abs value): 44.5
 Accelerometer 7 Peak (abs value): 33.7



A National Instruments USB-6211 DAQ was used to read the analog signals from the accelerometers. This DAQ supported 16 analog channels. 14 of the channels were used for accelerometer data, one was used to monitor the accelerometer power supply voltage, and the remaining analog channel was not used. The Z axis and the X axis were used on each accelerometer due to the limited number of analog channels available. The Z axis was normal to the sample surface with +Z pointing towards the excavation equipment. The X axis ran parallel to the edge of the sample.

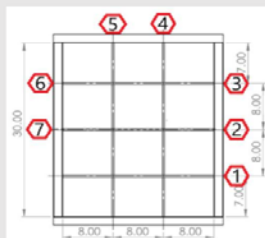


Panel Number: 4

Run #: 1 of 12

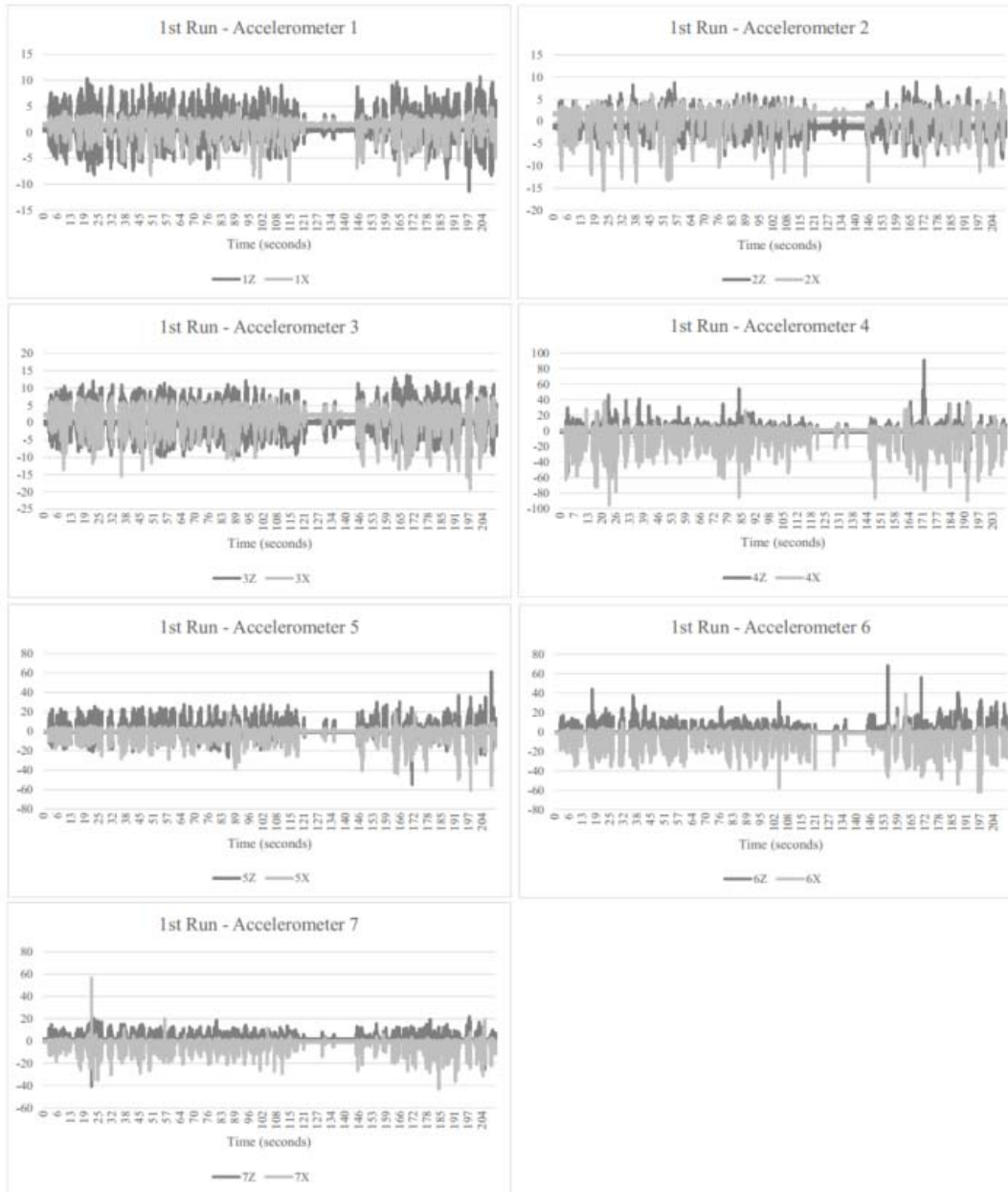
Notes: Drilled upper left 1/6 section of panel face. Not quite complete excavating section.

Run Time (sec): 210
Run Time Segment (sec): 0 - 210
Total Panel Run Time (sec): 2070
Y Axis Accelerometer Units: g
Accelerometer 1 Peak (abs value): 11.4
Accelerometer 2 Peak (abs value): 15.6
Accelerometer 3 Peak (abs value): 19.3
Accelerometer 4 Peak (abs value): 95.5
Accelerometer 5 Peak (abs value): 61.6
Accelerometer 6 Peak (abs value): 68.2
Accelerometer 7 Peak (abs value): 56.6



A National Instruments USB-6211 DAQ was used to read the analog signals from the accelerometers. This DAQ supported 16 analog channels. 14 of the channels were used for accelerometer data, one was used to monitor the accelerometer power supply voltage, and the remaining analog channel was not used.

The Z axis and the X axis were used on each accelerometer due to the limited number of analog channels available. The Z axis was normal to the sample surface with +Z pointing towards the excavation equipment. The X axis ran parallel to the edge of the sample.

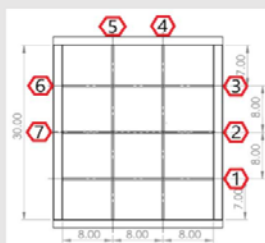


Panel Number: 4

Run #: 2 of 12

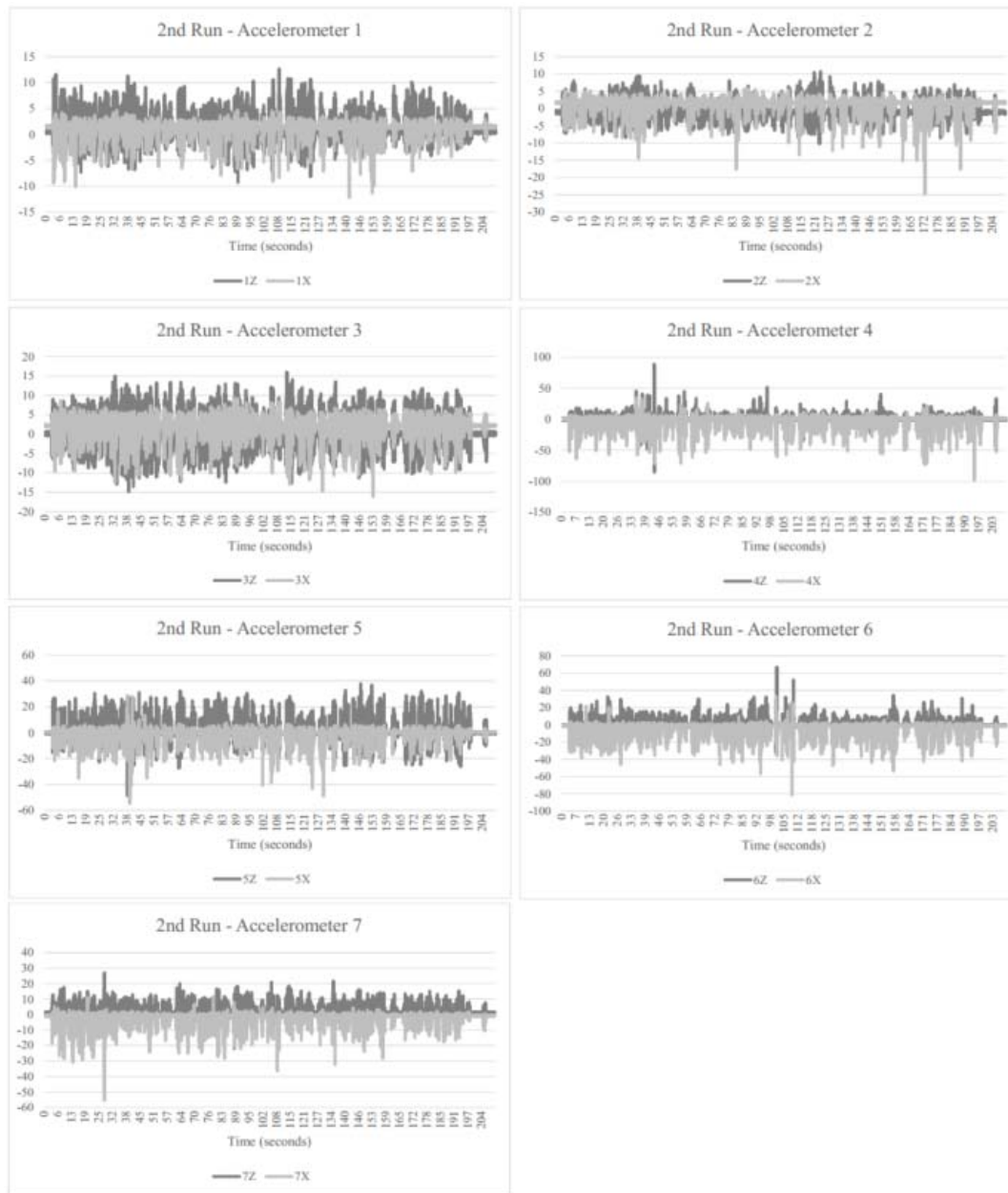
Notes: Finished upper left 1/6 section of panel face. Started middle left 1/6 section of panel face.

Run Time (sec): 210
 Run Time Segment (sec): 210 - 420
 Total Panel Run Time (sec): 2070
 Y Axis Accelerometer Units: g
 Accelerometer 1 Peak (abs value): 12.7
 Accelerometer 2 Peak (abs value): 24.8
 Accelerometer 3 Peak (abs value): 16.1
 Accelerometer 4 Peak (abs value): 98.3
 Accelerometer 5 Peak (abs value): 54.9
 Accelerometer 6 Peak (abs value): 81.4
 Accelerometer 7 Peak (abs value): 55.3



A National Instruments USB-6211 DAQ was used to read the analog signals from the accelerometers. This DAQ supported 16 analog channels. 14 of the channels were used for accelerometer data, one was used to monitor the accelerometer power supply voltage, and the remaining analog channel was not used.

The Z axis and the X axis were used on each accelerometer due to the limited number of analog channels available. The Z axis was normal to the sample surface with +Z pointing towards the excavation equipment. The X axis ran parallel to the edge of the sample.

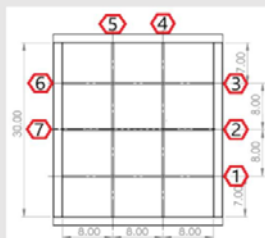


Panel Number: 4

Run #: 3 of 12

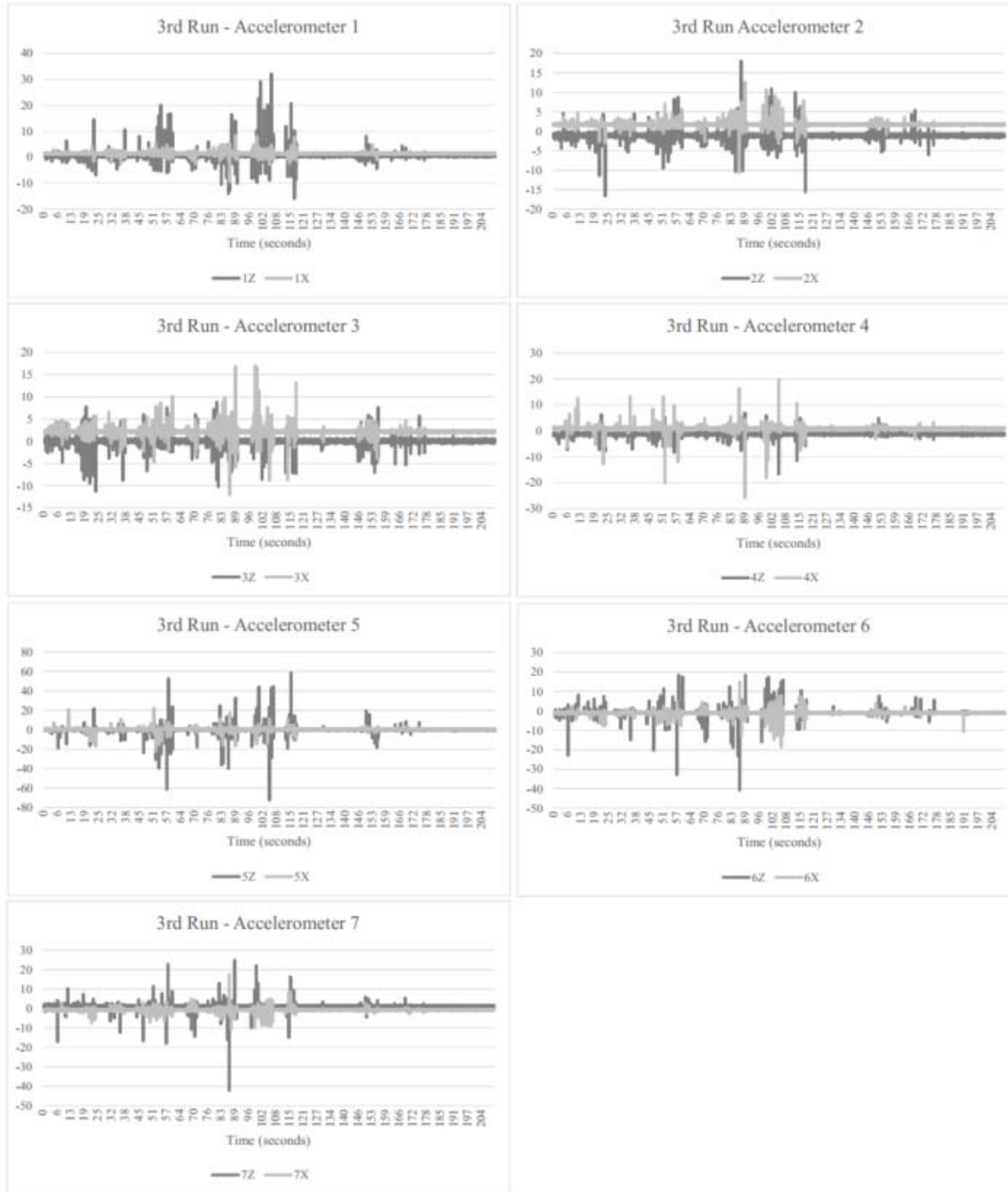
Notes: Took break after Run #2 due to tool being hot. Various hand hammering (pick file).

Run Time (sec): 210
Run Time Segment (sec): 420 - 630
Total Panel Run Time (sec): 2070
Y Axis Accelerometer Units: g
Accelerometer 1 Peak (abs value): 32.1
Accelerometer 2 Peak (abs value): 18.0
Accelerometer 3 Peak (abs value): 17.0
Accelerometer 4 Peak (abs value): 25.8
Accelerometer 5 Peak (abs value): 72.5
Accelerometer 6 Peak (abs value): 40.7
Accelerometer 7 Peak (abs value): 42.2



A National Instruments USB-6211 DAQ was used to read the analog signals from the accelerometers. This DAQ supported 16 analog channels. 14 of the channels were used for accelerometer data, one was used to monitor the accelerometer power supply voltage, and the remaining analog channel was not used.

The Z axis and the X axis were used on each accelerometer due to the limited number of analog channels available. The Z axis was normal to the sample surface with +Z pointing towards the excavation equipment. The X axis ran parallel to the edge of the sample.

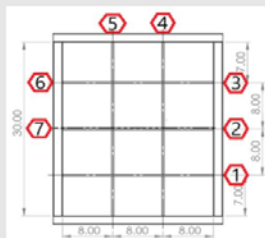


Panel Number: 4

Run #: 4 of 12

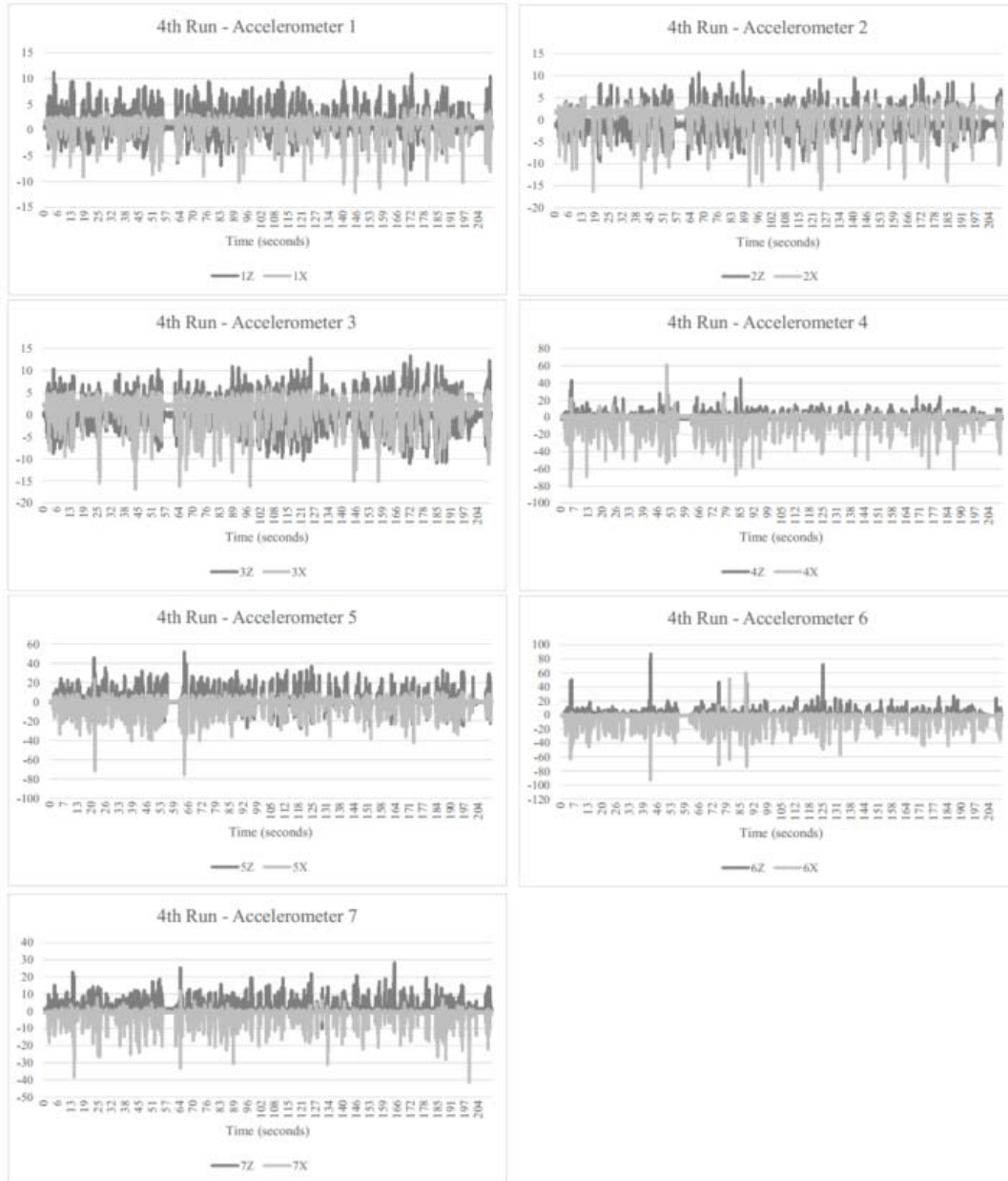
Notes: Finished upper middle 1/6 section of panel face.

Run Time (sec): 210
Run Time Segment (sec): 630 - 840
Total Panel Run Time (sec): 2070
Y Axis Accelerometer Units: g
Accelerometer 1 Peak (abs value): 12.2
Accelerometer 2 Peak (abs value): 16.3
Accelerometer 3 Peak (abs value): 16.9
Accelerometer 4 Peak (abs value): 81.4
Accelerometer 5 Peak (abs value): 75.7
Accelerometer 6 Peak (abs value): 93.1
Accelerometer 7 Peak (abs value): 41.5



A National Instruments USB-6211 DAQ was used to read the analog signals from the accelerometers. This DAQ supported 16 analog channels. 14 of the channels were used for accelerometer data, one was used to monitor the accelerometer power supply voltage, and the remaining analog channel was not used.

The Z axis and the X axis were used on each accelerometer due to the limited number of analog channels available. The Z axis was normal to the sample surface with +Z pointing towards the excavation equipment. The X axis ran parallel to the edge of the sample.

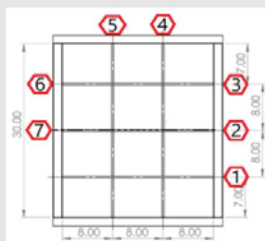


Panel Number: 4

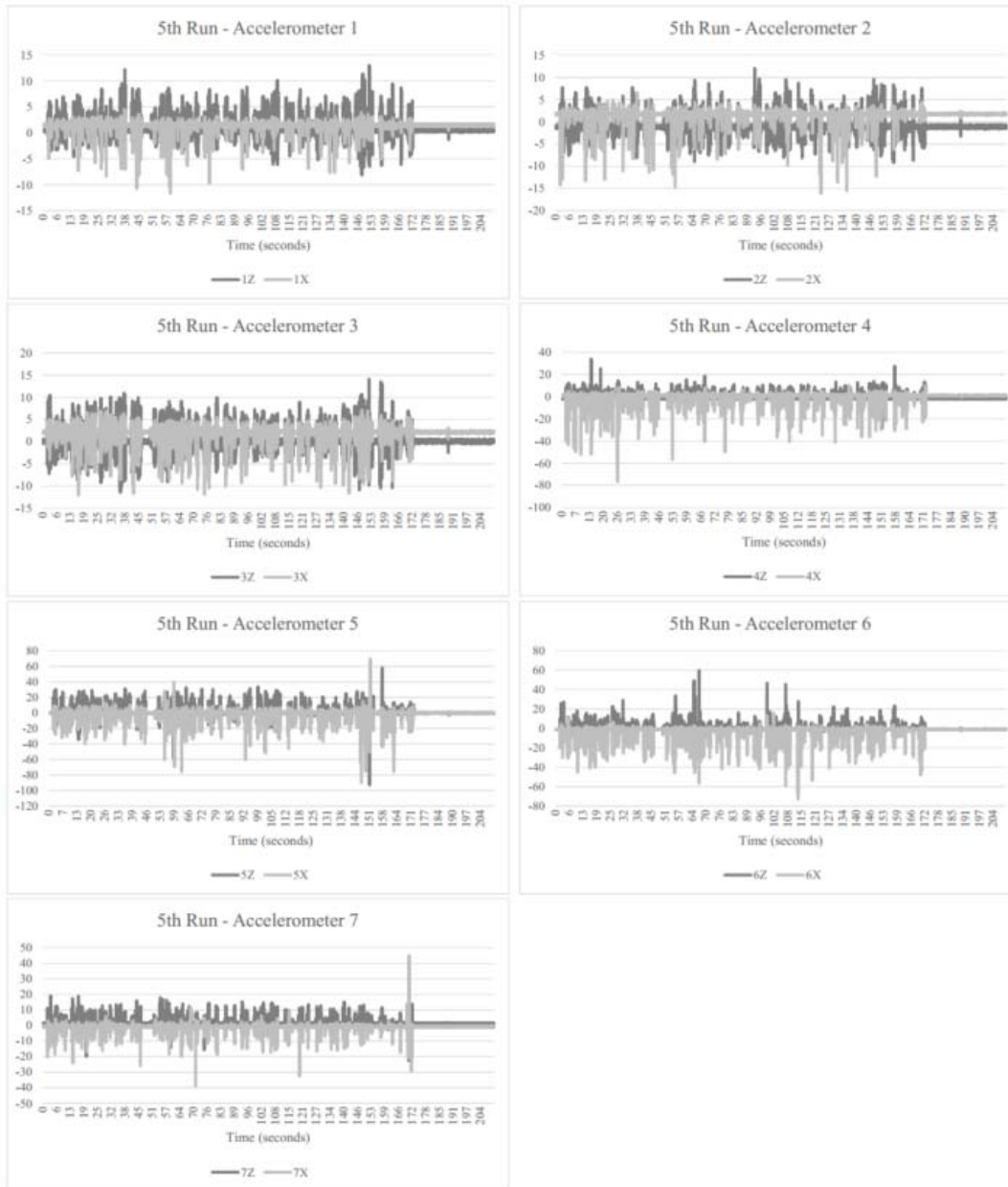
Run #: 5 of 12

Notes: Drill cleaning of previous sections.

Run Time (sec): 210
 Run Time Segment (sec): 840 - 1050
 Total Panel Run Time (sec): 2070
 Y Axis Accelerometer Units: g
 Accelerometer 1 Peak (abs value): 13.0
 Accelerometer 2 Peak (abs value): 16.1
 Accelerometer 3 Peak (abs value): 14.1
 Accelerometer 4 Peak (abs value): 76.4
 Accelerometer 5 Peak (abs value): 92.5
 Accelerometer 6 Peak (abs value): 72.9
 Accelerometer 7 Peak (abs value): 44.9



A National Instruments USB-6211 DAQ was used to read the analog signals from the accelerometers. This DAQ supported 16 analog channels. 14 of the channels were used for accelerometer data, one was used to monitor the accelerometer power supply voltage, and the remaining analog channel was not used. The Z axis and the X axis were used on each accelerometer due to the limited number of analog channels available. The Z axis was normal to the sample surface with +Z pointing towards the excavation equipment. The X axis ran parallel to the edge of the sample.

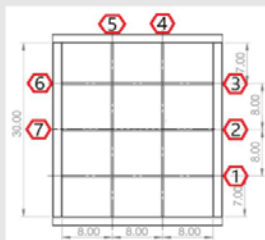


Panel Number: 4

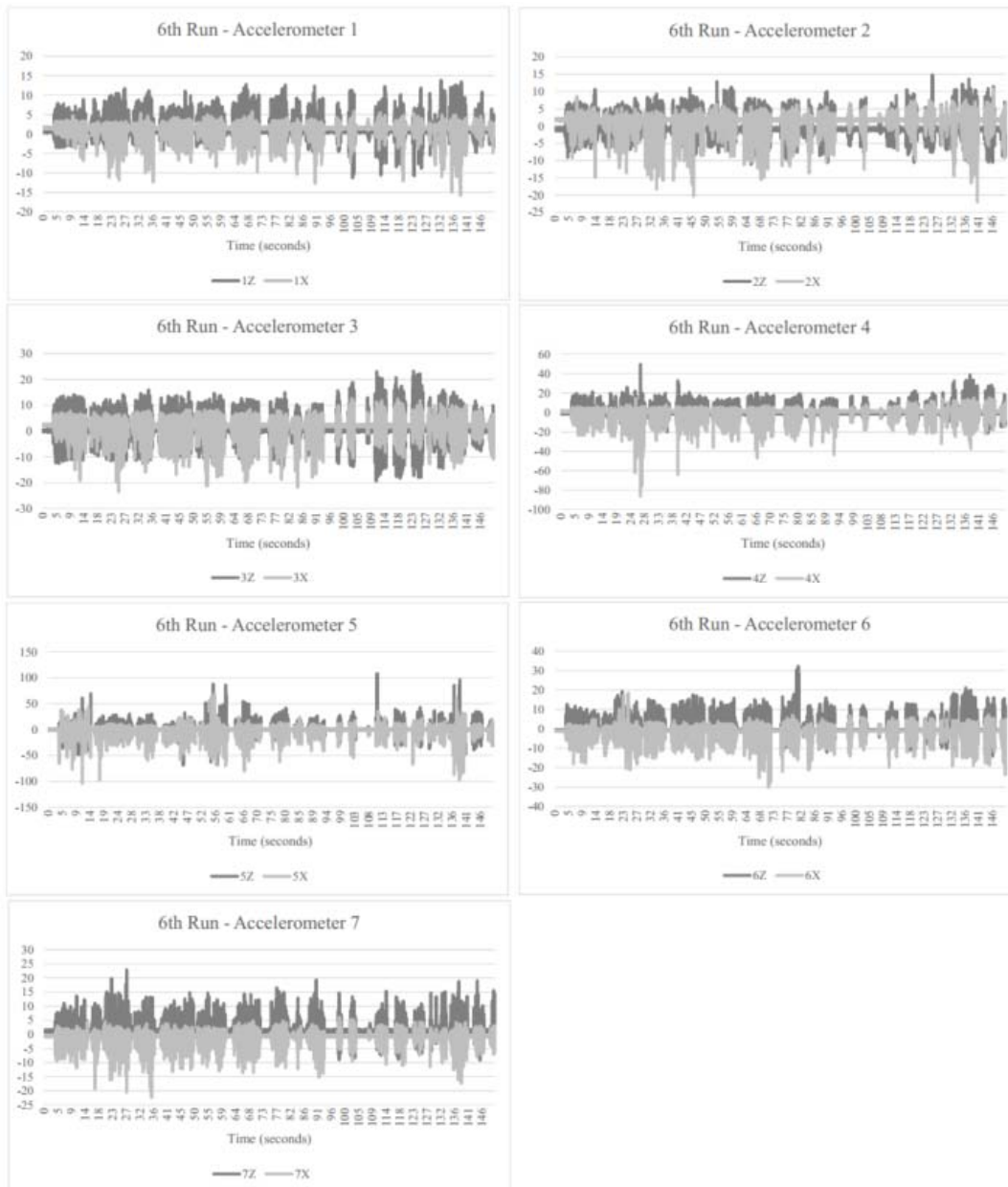
Run #: 6 of 12

Notes: Drilled upper right 1/6 section of panel face.

Run Time (sec): 150
 Run Time Segment (sec): 1050 - 1200
 Total Panel Run Time (sec): 2070
 Y Axis Accelerometer Units: g
 Accelerometer 1 Peak (abs value): 15.8
 Accelerometer 2 Peak (abs value): 22.0
 Accelerometer 3 Peak (abs value): 23.5
 Accelerometer 4 Peak (abs value): 86.2
 Accelerometer 5 Peak (abs value): 107.9
 Accelerometer 6 Peak (abs value): 32.2
 Accelerometer 7 Peak (abs value): 22.9



A National Instruments USB-6211 DAQ was used to read the analog signals from the accelerometers. This DAQ supported 16 analog channels. 14 of the channels were used for accelerometer data, one was used to monitor the accelerometer power supply voltage, and the remaining analog channel was not used. The Z axis and the X axis were used on each accelerometer due to the limited number of analog channels available. The Z axis was normal to the sample surface with +Z pointing towards the excavation equipment. The X axis ran parallel to the edge of the sample.

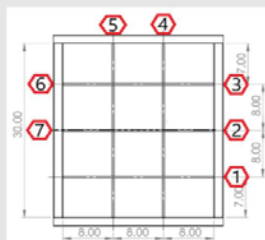


Panel Number: 4

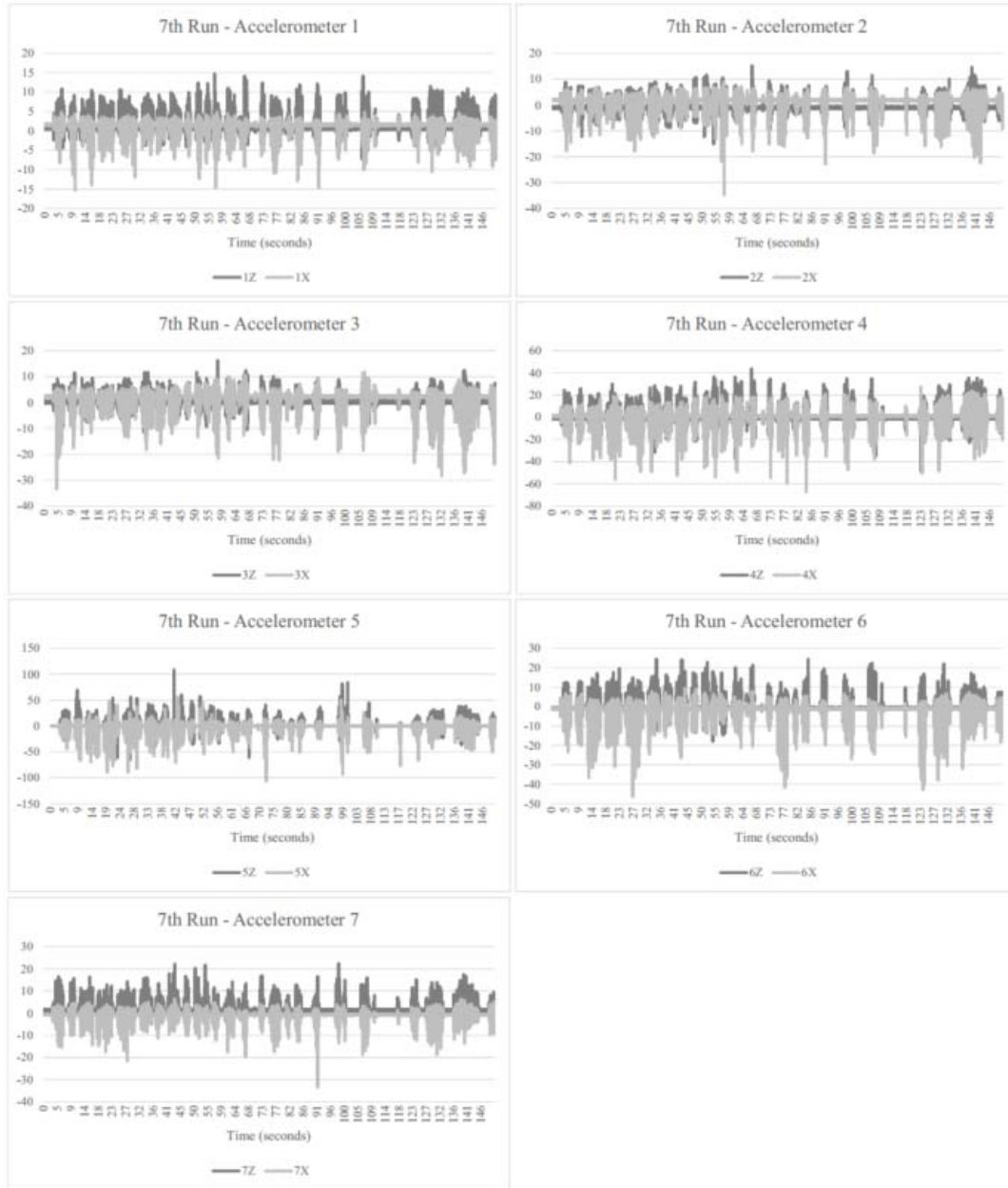
Run #: 7 of 12

Notes: Took break after Run #6 due to tool being hot. Drilled middle right 1/6 section of panel face.

Run Time (sec): 150
Run Time Segment (sec): 1200 - 1350
Total Panel Run Time (sec): 2070
Y Axis Accelerometer Units: g
Accelerometer 1 Peak (abs value): 15.3
Accelerometer 2 Peak (abs value): 34.8
Accelerometer 3 Peak (abs value): 33.5
Accelerometer 4 Peak (abs value): 67.1
Accelerometer 5 Peak (abs value): 108.4
Accelerometer 6 Peak (abs value): 46.4
Accelerometer 7 Peak (abs value): 33.4



A National Instruments USB-6211 DAQ was used to read the analog signals from the accelerometers. This DAQ supported 16 analog channels. 14 of the channels were used for accelerometer data, one was used to monitor the accelerometer power supply voltage, and the remaining analog channel was not used. The Z axis and the X axis were used on each accelerometer due to the limited number of analog channels available. The Z axis was normal to the sample surface with +Z pointing towards the excavation equipment. The X axis ran parallel to the edge of the sample.

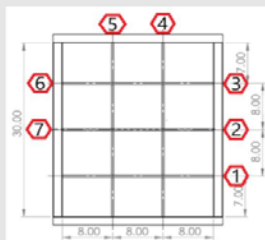


Panel Number: 4

Run #: 8 of 12

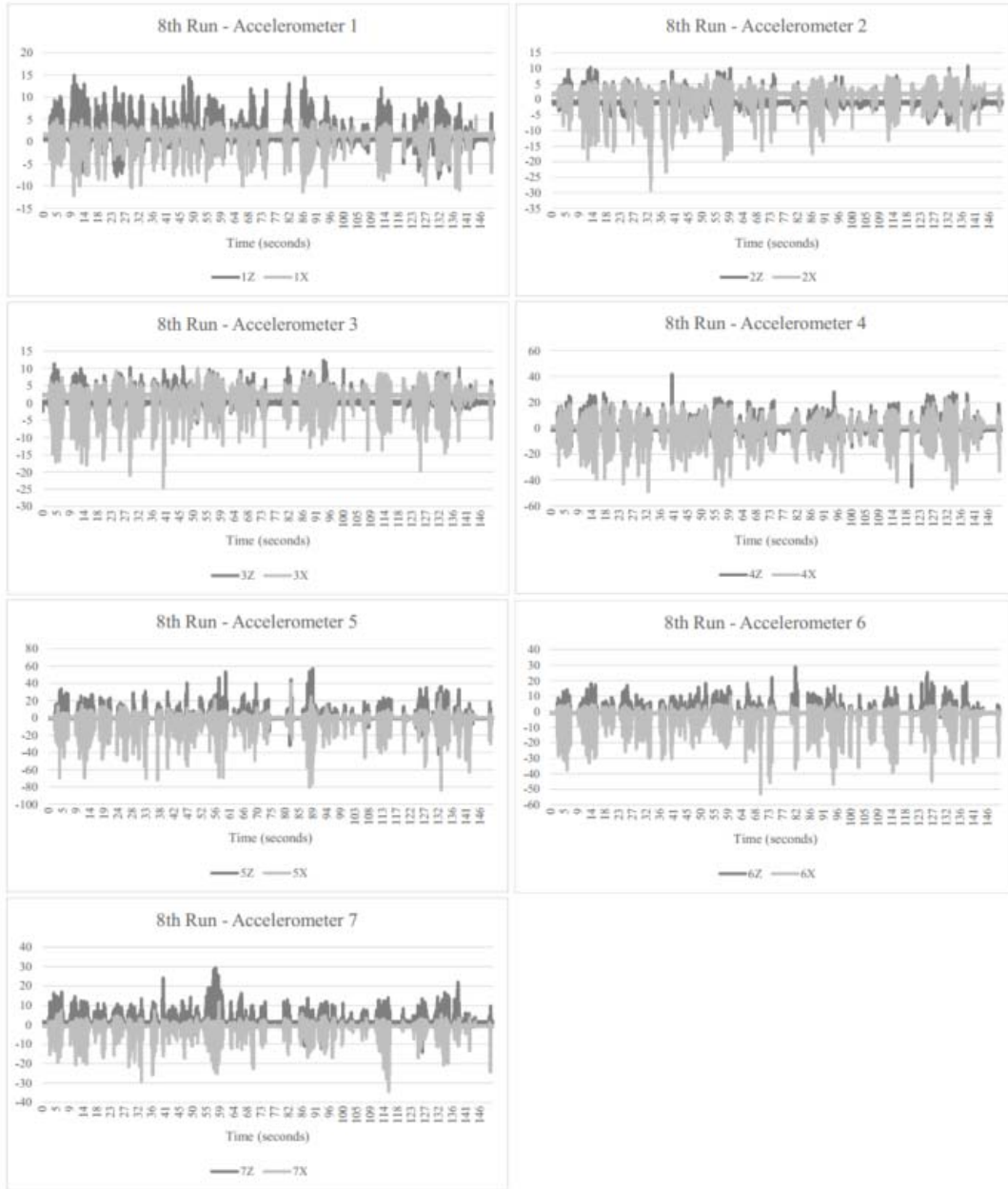
Notes: Drilled bottom right 1/6 section of panel face.

Run Time (sec): 150
Run Time Segment (sec): 1350 - 1500
Total Panel Run Time (sec): 2070
Y Axis Accelerometer Units: g
Accelerometer 1 Peak (abs value): 15.0
Accelerometer 2 Peak (abs value): 29.3
Accelerometer 3 Peak (abs value): 24.6
Accelerometer 4 Peak (abs value): 49.3
Accelerometer 5 Peak (abs value): 84.2
Accelerometer 6 Peak (abs value): 53.1
Accelerometer 7 Peak (abs value): 34.6



A National Instruments USB-6211 DAQ was used to read the analog signals from the accelerometers. This DAQ supported 16 analog channels. 14 of the channels were used for accelerometer data, one was used to monitor the accelerometer power supply voltage, and the remaining analog channel was not used.

The Z axis and the X axis were used on each accelerometer due to the limited number of analog channels available. The Z axis was normal to the sample surface with +Z pointing towards the excavation equipment. The X axis ran parallel to the edge of the sample.

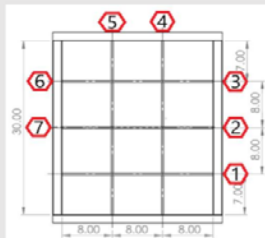


Panel Number: 4

Run #: 9 of 12

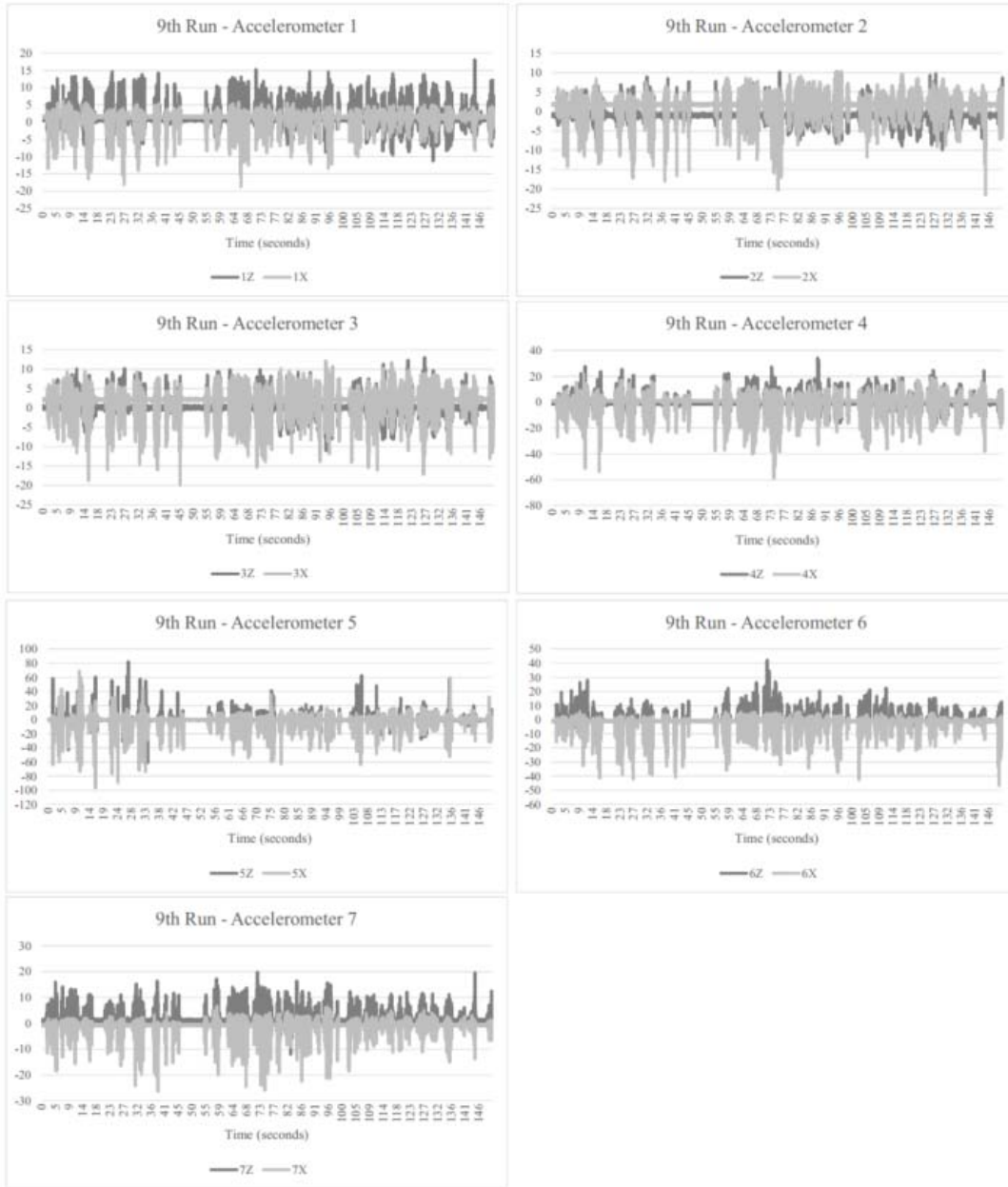
Notes: Drilled bottom right 1/6 section of panel face, bottom left 1/6 section of panel face.

Run Time (sec): 150
 Run Time Segment (sec): 1500 - 1650
 Total Panel Run Time (sec): 2070
 Y Axis Accelerometer Units: g
 Accelerometer 1 Peak (abs value): 18.7
 Accelerometer 2 Peak (abs value): 21.6
 Accelerometer 3 Peak (abs value): 19.9
 Accelerometer 4 Peak (abs value): 58.9
 Accelerometer 5 Peak (abs value): 96.8
 Accelerometer 6 Peak (abs value): 46.7
 Accelerometer 7 Peak (abs value): 26.3

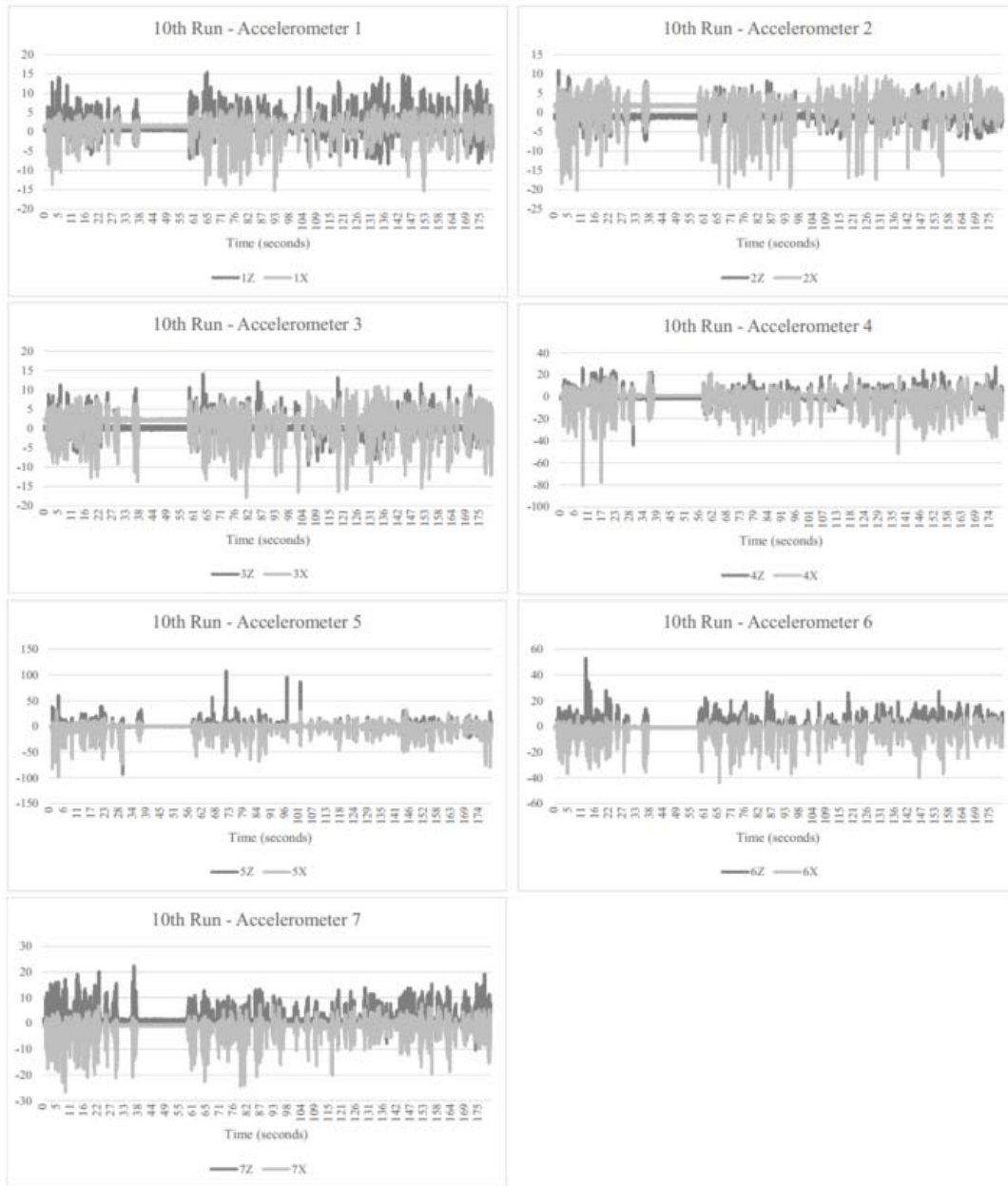


A National Instruments USB-6211 DAQ was used to read the analog signals from the accelerometers. This DAQ supported 16 analog channels. 14 of the channels were used for accelerometer data, one was used to monitor the accelerometer power supply voltage, and the remaining analog channel was not used.

The Z axis and the X axis were used on each accelerometer due to the limited number of analog channels available. The Z axis was normal to the sample surface with +Z pointing towards the excavation equipment. The X axis ran parallel to the edge of the sample.



Panel Number: 4	
Run #: 10 of 12	
Notes: Took break after Run #9 due to tool being hot. Drilled bottom right 1/6 section of panel face, bottom left 1/6 section of panel face.	
Run Time (sec): 180	
Run Time Segment (sec): 1650 - 1830	
Total Panel Run Time (sec): 2070	
Y Axis Accelerometer Units: g	
Accelerometer 1 Peak (abs value): 15.4	
Accelerometer 2 Peak (abs value): 20.2	
Accelerometer 3 Peak (abs value): 17.9	
Accelerometer 4 Peak (abs value): 80.8	<p>A National Instruments USB-6211 DAQ was used to read the analog signals from the accelerometers. This DAQ supported 16 analog channels. 14 of the channels were used for accelerometer data, one was used to monitor the accelerometer power supply voltage, and the remaining analog channel was not used.</p> <p>The Z axis and the X axis were used on each accelerometer due to the limited number of analog channels available. The Z axis was normal to the sample surface with +Z pointing towards the excavation equipment. The X axis ran parallel to the edge of the sample.</p>
Accelerometer 5 Peak (abs value): 107.9	
Accelerometer 6 Peak (abs value): 53.0	
Accelerometer 7 Peak (abs value): 26.8	

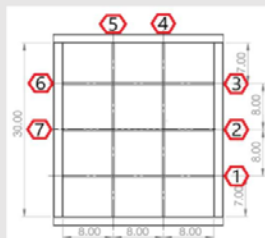


Panel Number: 4

Run #: 11 of 12

Notes: Drilled bottom right 1/6 section of panel face, bottom left 1/6 section of panel face.

Run Time (sec): 150
Run Time Segment (sec): 1830 - 1980
Total Panel Run Time (sec): 2070
Y Axis Accelerometer Units: g
Accelerometer 1 Peak (abs value): 19.5
Accelerometer 2 Peak (abs value): 25.4
Accelerometer 3 Peak (abs value): 26.8
Accelerometer 4 Peak (abs value): 81.8
Accelerometer 5 Peak (abs value): 95.1
Accelerometer 6 Peak (abs value): 56.7
Accelerometer 7 Peak (abs value): 30.5



A National Instruments USB-6211 DAQ was used to read the analog signals from the accelerometers. This DAQ supported 16 analog channels. 14 of the channels were used for accelerometer data, one was used to monitor the accelerometer power supply voltage, and the remaining analog channel was not used. The Z axis and the X axis were used on each accelerometer due to the limited number of analog channels available. The Z axis was normal to the sample surface with +Z pointing towards the excavation equipment. The X axis ran parallel to the edge of the sample.

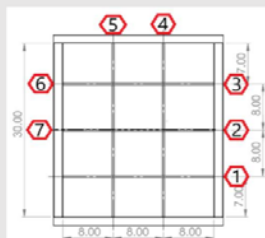


Panel Number: 4

Run #: 12 of 12

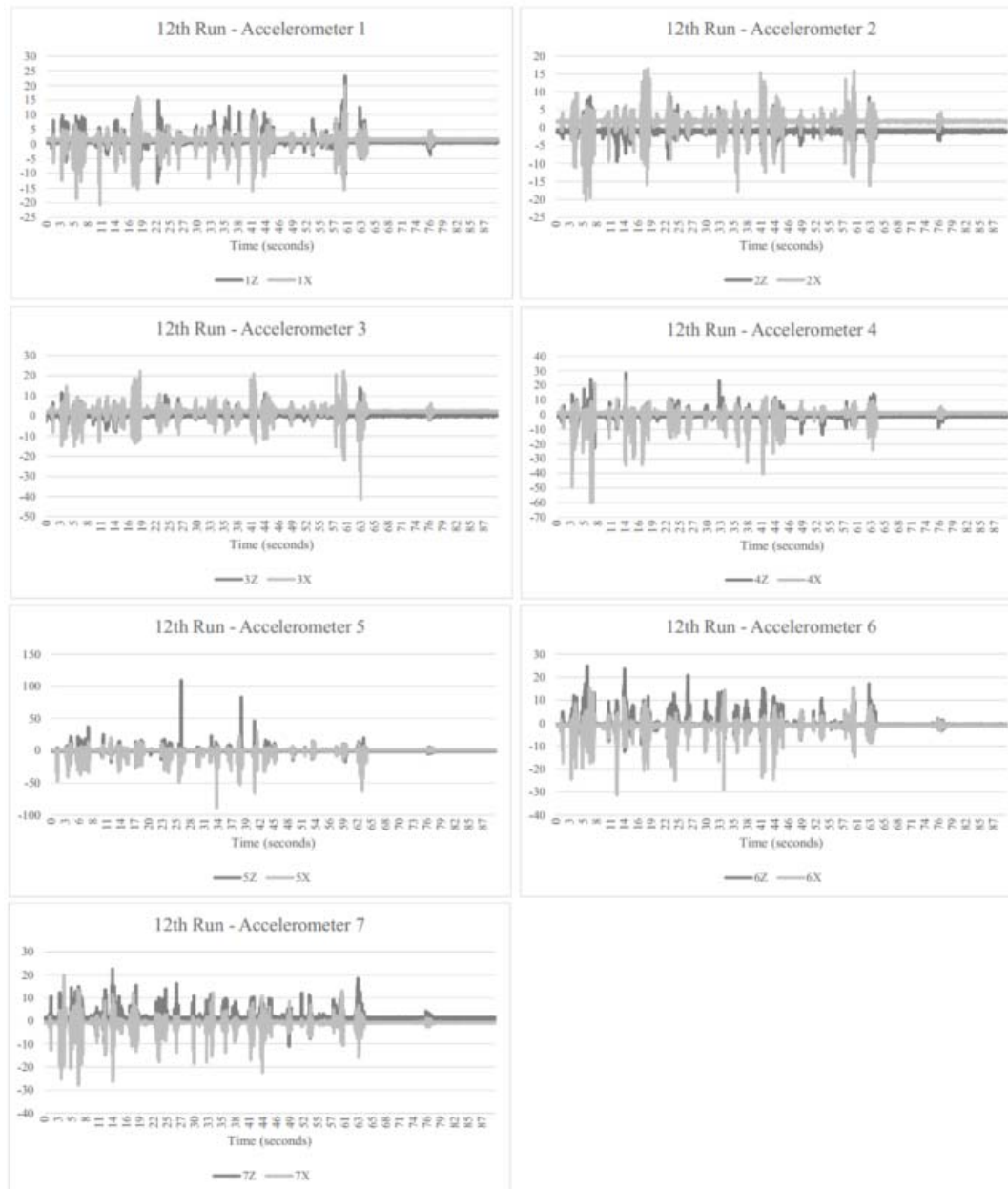
Notes: Drill clean up of entire panel face.

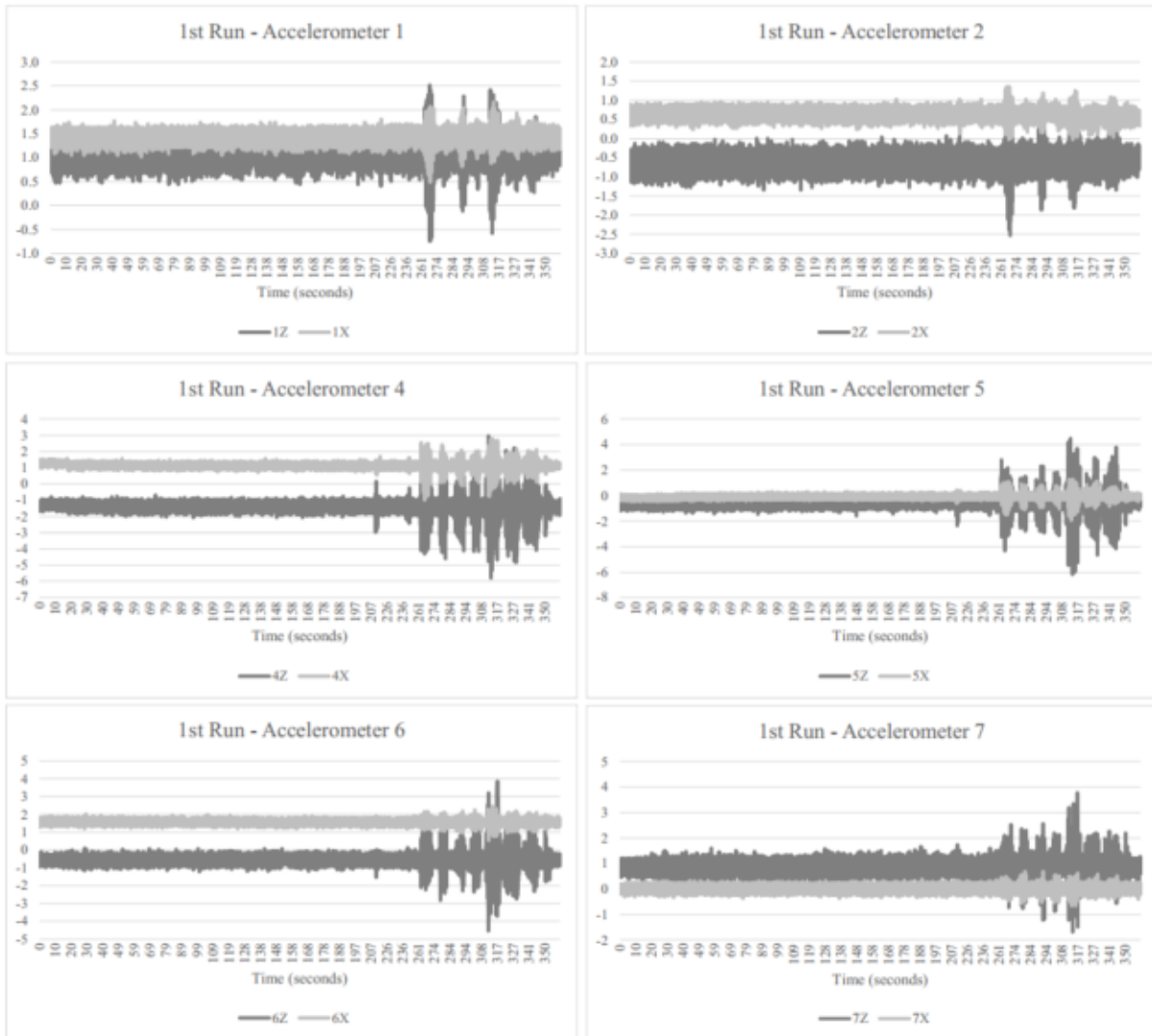
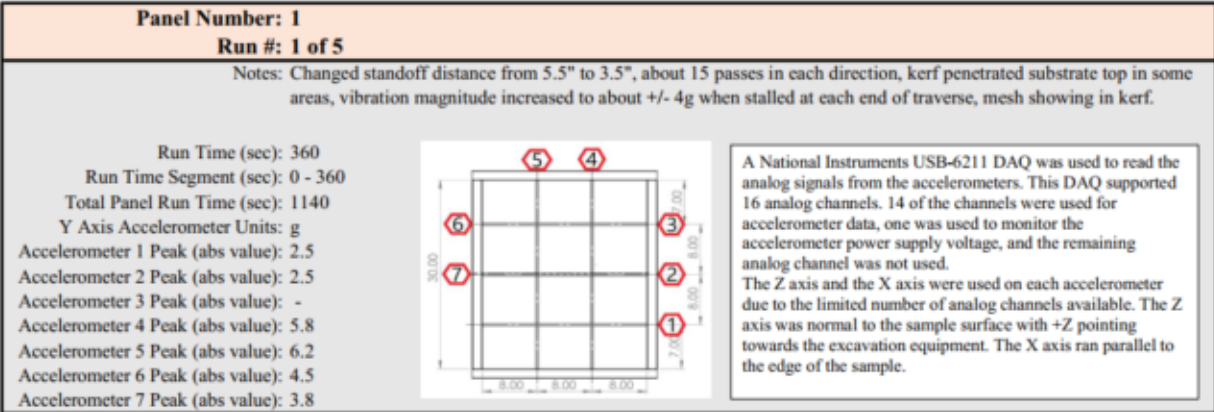
Run Time (sec): 90
 Run Time Segment (sec): 1980 - 2070
 Total Panel Run Time (sec): 2070
 Y Axis Accelerometer Units: g
 Accelerometer 1 Peak (abs value): 23.2
 Accelerometer 2 Peak (abs value): 20.4
 Accelerometer 3 Peak (abs value): 41.5
 Accelerometer 4 Peak (abs value): 60.3
 Accelerometer 5 Peak (abs value): 109.4
 Accelerometer 6 Peak (abs value): 31.3
 Accelerometer 7 Peak (abs value): 27.9

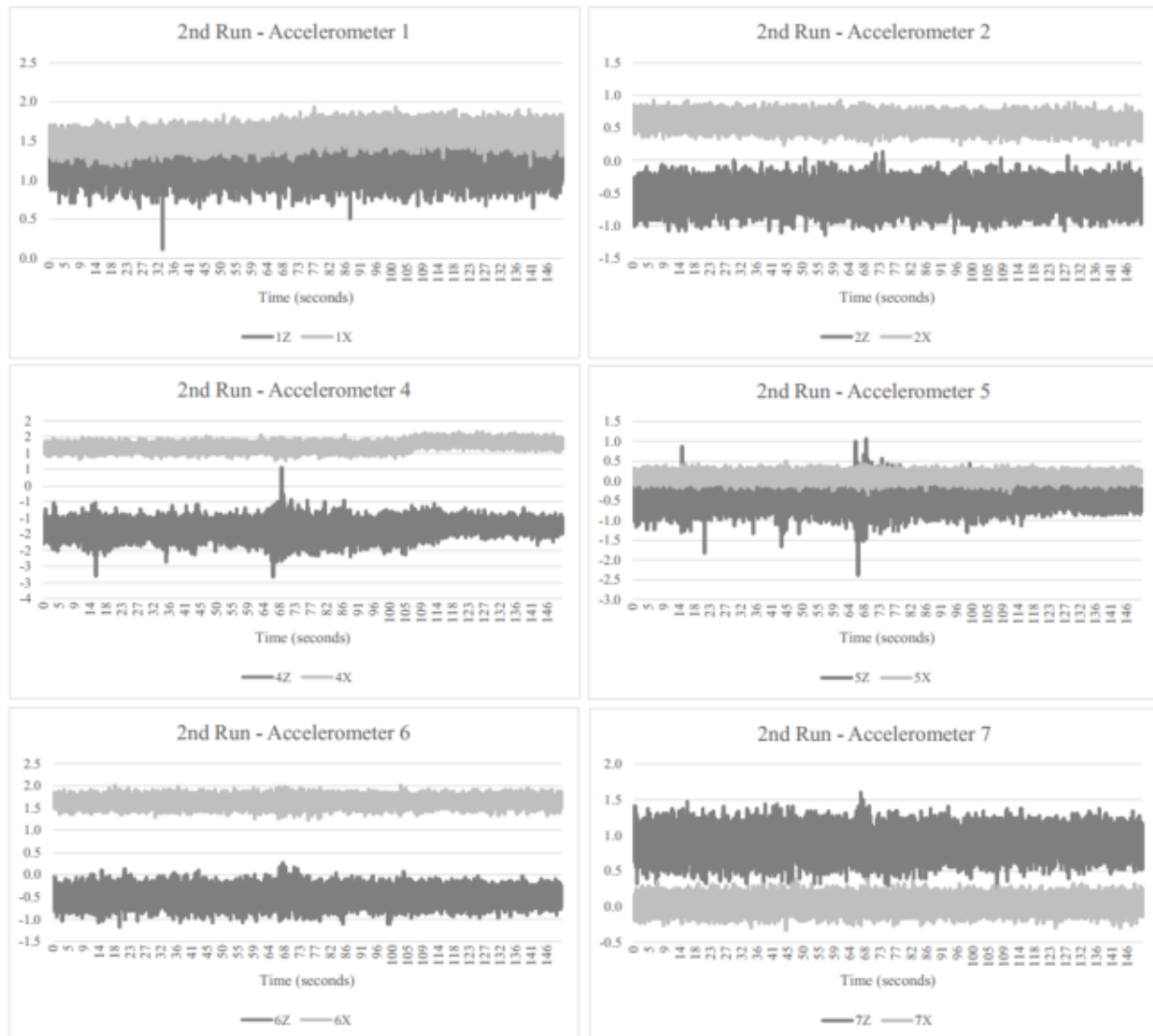
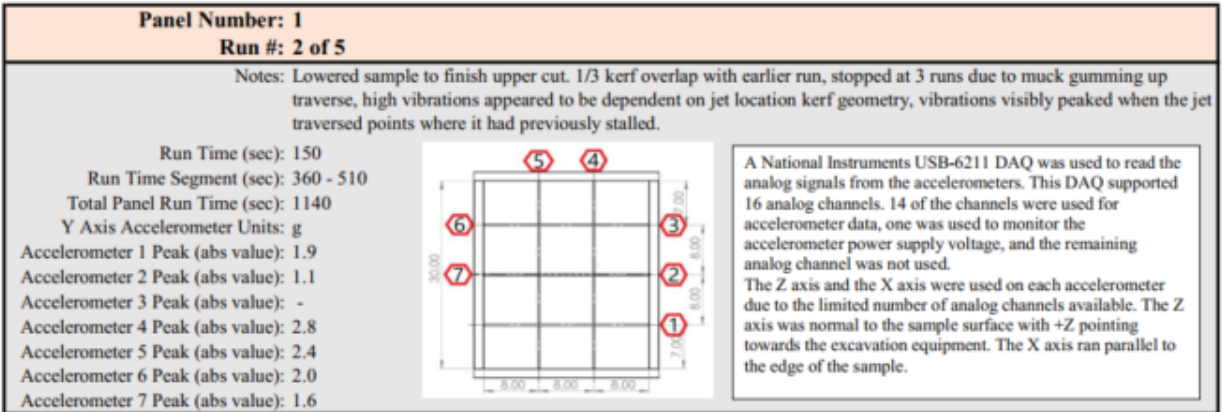


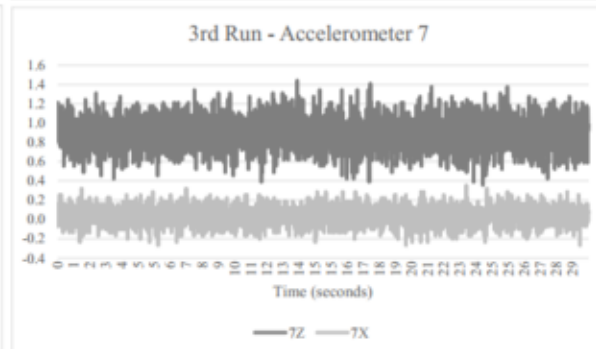
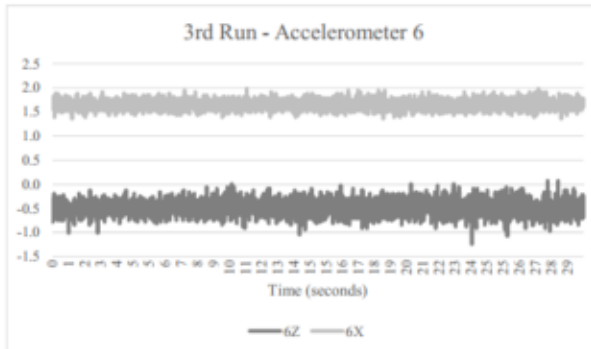
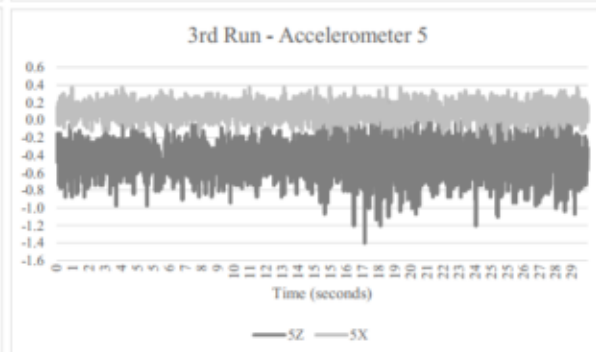
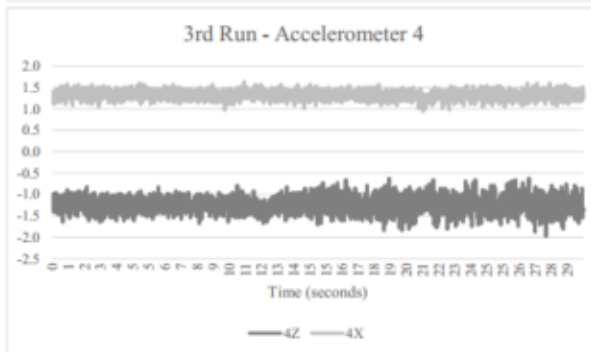
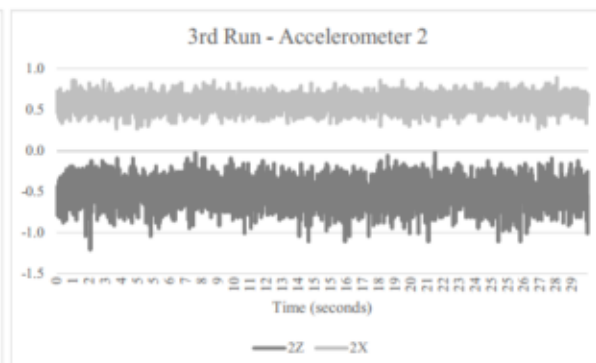
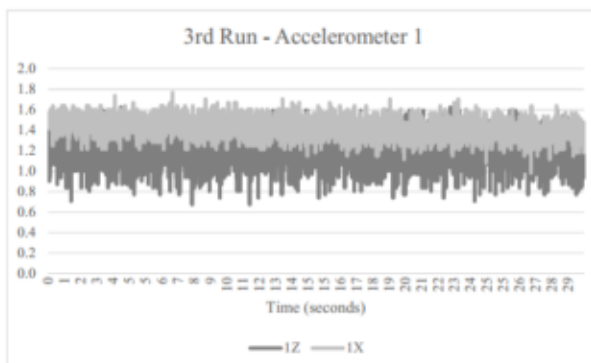
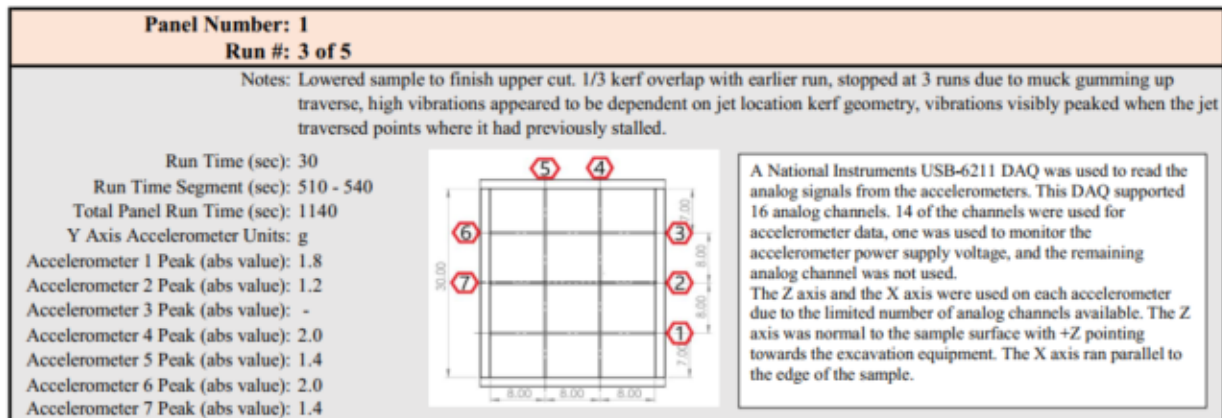
A National Instruments USB-6211 DAQ was used to read the analog signals from the accelerometers. This DAQ supported 16 analog channels. 14 of the channels were used for accelerometer data, one was used to monitor the accelerometer power supply voltage, and the remaining analog channel was not used.

The Z axis and the X axis were used on each accelerometer due to the limited number of analog channels available. The Z axis was normal to the sample surface with +Z pointing towards the excavation equipment. The X axis ran parallel to the edge of the sample.







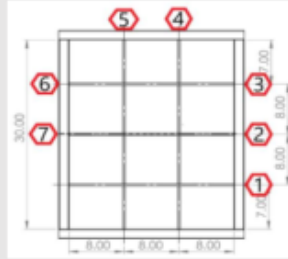


Panel Number: 1

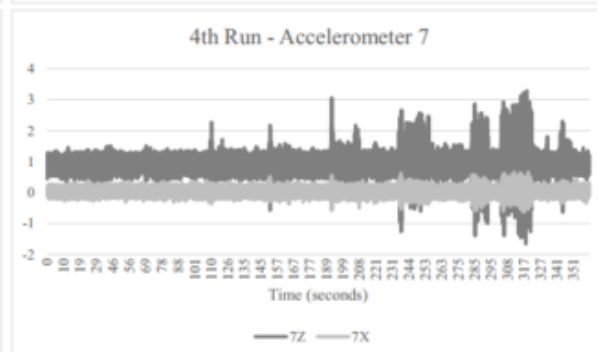
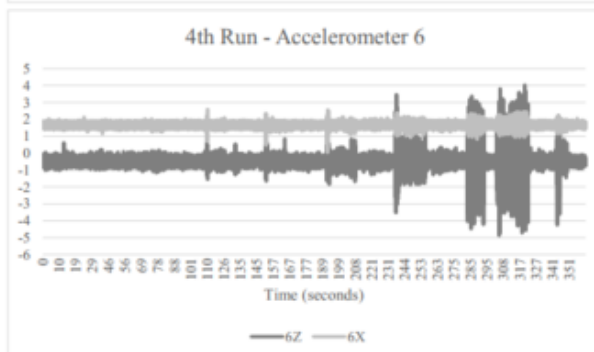
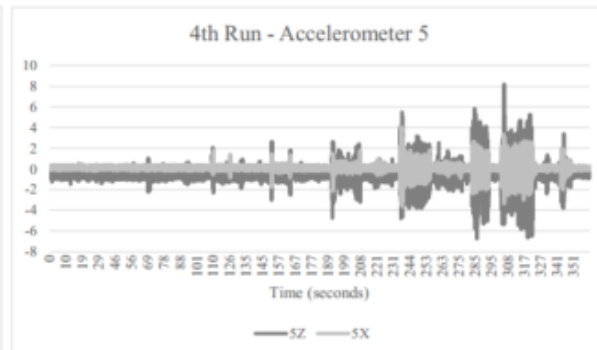
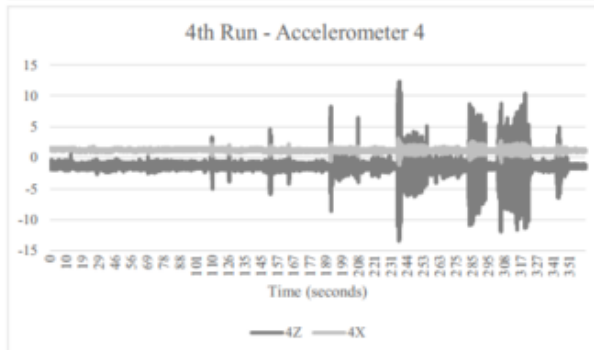
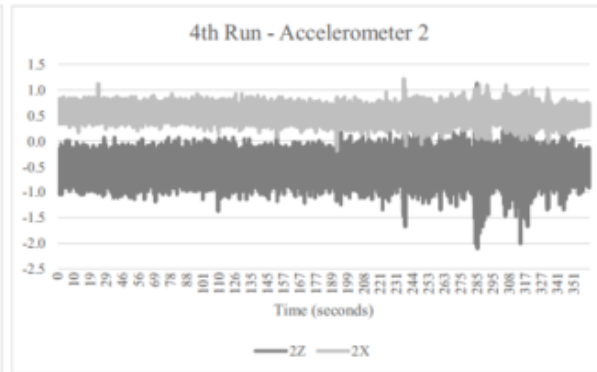
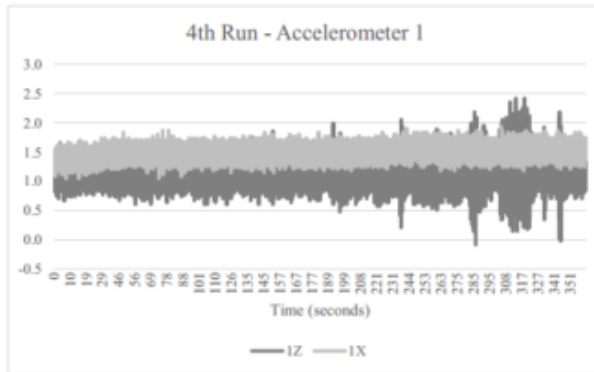
Run #: 4 of 5

Notes: Lowered sample to finish upper cut. 1/3 kerf overlap with earlier run, stopped at 3 runs due to muck gumming up traverse, high vibrations appeared to be dependent on jet location kerf geometry, vibrations visibly peaked when the jet traversed points where it had previously stalled.

Run Time (sec): 360
Run Time Segment (sec): 540 - 900
Total Panel Run Time (sec): 1140
Y Axis Accelerometer Units: g
Accelerometer 1 Peak (abs value): 2.4
Accelerometer 2 Peak (abs value): 2.1
Accelerometer 3 Peak (abs value): -
Accelerometer 4 Peak (abs value): 13.5
Accelerometer 5 Peak (abs value): 8.2
Accelerometer 6 Peak (abs value): 4.9
Accelerometer 7 Peak (abs value): 3.3



A National Instruments USB-6211 DAQ was used to read the analog signals from the accelerometers. This DAQ supported 16 analog channels. 14 of the channels were used for accelerometer data, one was used to monitor the accelerometer power supply voltage, and the remaining analog channel was not used.
The Z axis and the X axis were used on each accelerometer due to the limited number of analog channels available. The Z axis was normal to the sample surface with +Z pointing towards the excavation equipment. The X axis ran parallel to the edge of the sample.



Panel Number: 1**Run #: 5 of 5**

Notes: Killed off rib in kerf. Had high G forces in end regions where standoff distance was low, 5 passes in each direction, high vibrations occurred when stalled, likely caused by jet moving over wavy material.

Run Time (sec): 240

Run Time Segment (sec): 900 - 1140

Total Panel Run Time (sec): 1140

Y Axis Accelerometer Units: g

Accelerometer 1 Peak (abs value): 4.1

Accelerometer 2 Peak (abs value): 3.2

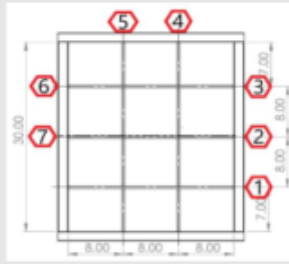
Accelerometer 3 Peak (abs value): -

Accelerometer 4 Peak (abs value): 12.3

Accelerometer 5 Peak (abs value): 19.0

Accelerometer 6 Peak (abs value): 5.5

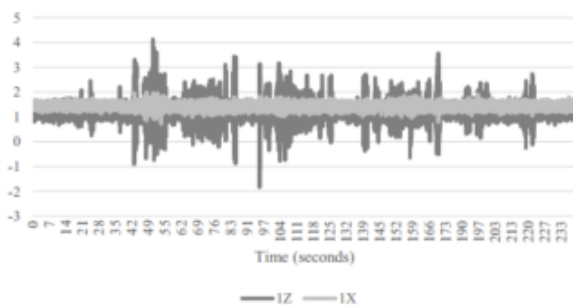
Accelerometer 7 Peak (abs value): 5.0



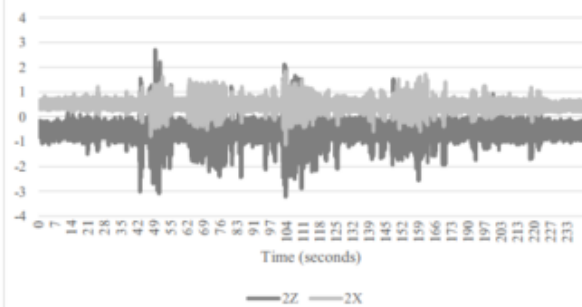
A National Instruments USB-6211 DAQ was used to read the analog signals from the accelerometers. This DAQ supported 16 analog channels. 14 of the channels were used for accelerometer data, one was used to monitor the accelerometer power supply voltage, and the remaining analog channel was not used.

The Z axis and the X axis were used on each accelerometer due to the limited number of analog channels available. The Z axis was normal to the sample surface with +Z pointing towards the excavation equipment. The X axis ran parallel to the edge of the sample.

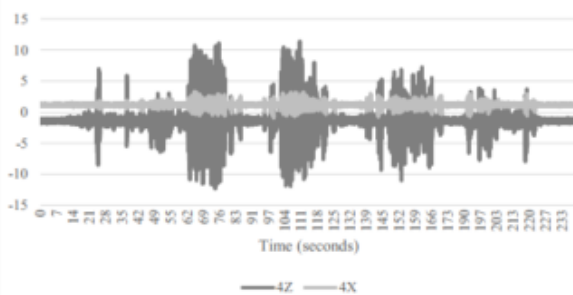
5th Run - Accelerometer 1



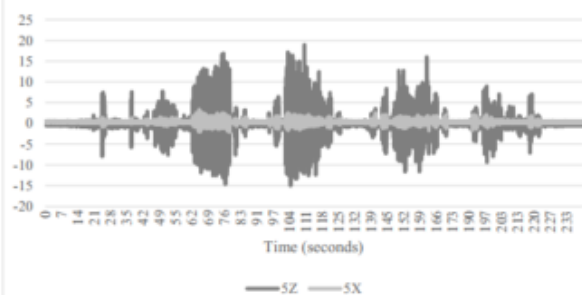
5th Run - Accelerometer 2



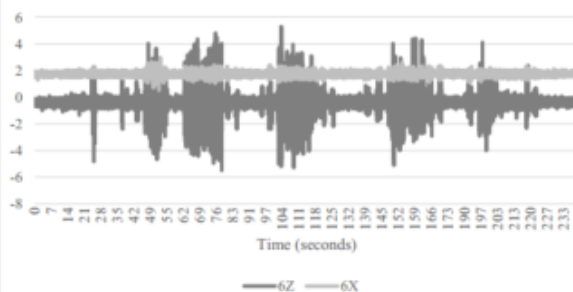
5th Run - Accelerometer 4



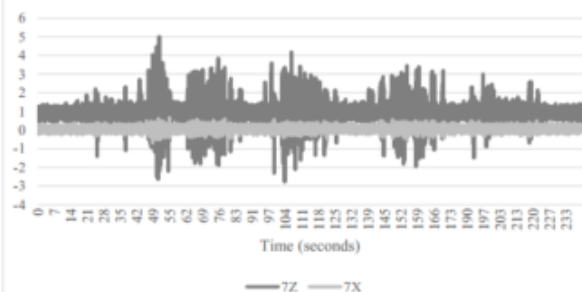
5th Run - Accelerometer 5



5th Run - Accelerometer 6



5th Run - Accelerometer 7

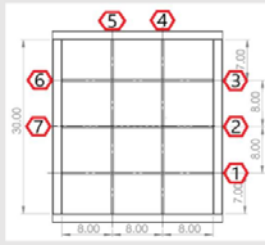


Panel Number: 7

Run #: 1 of 6

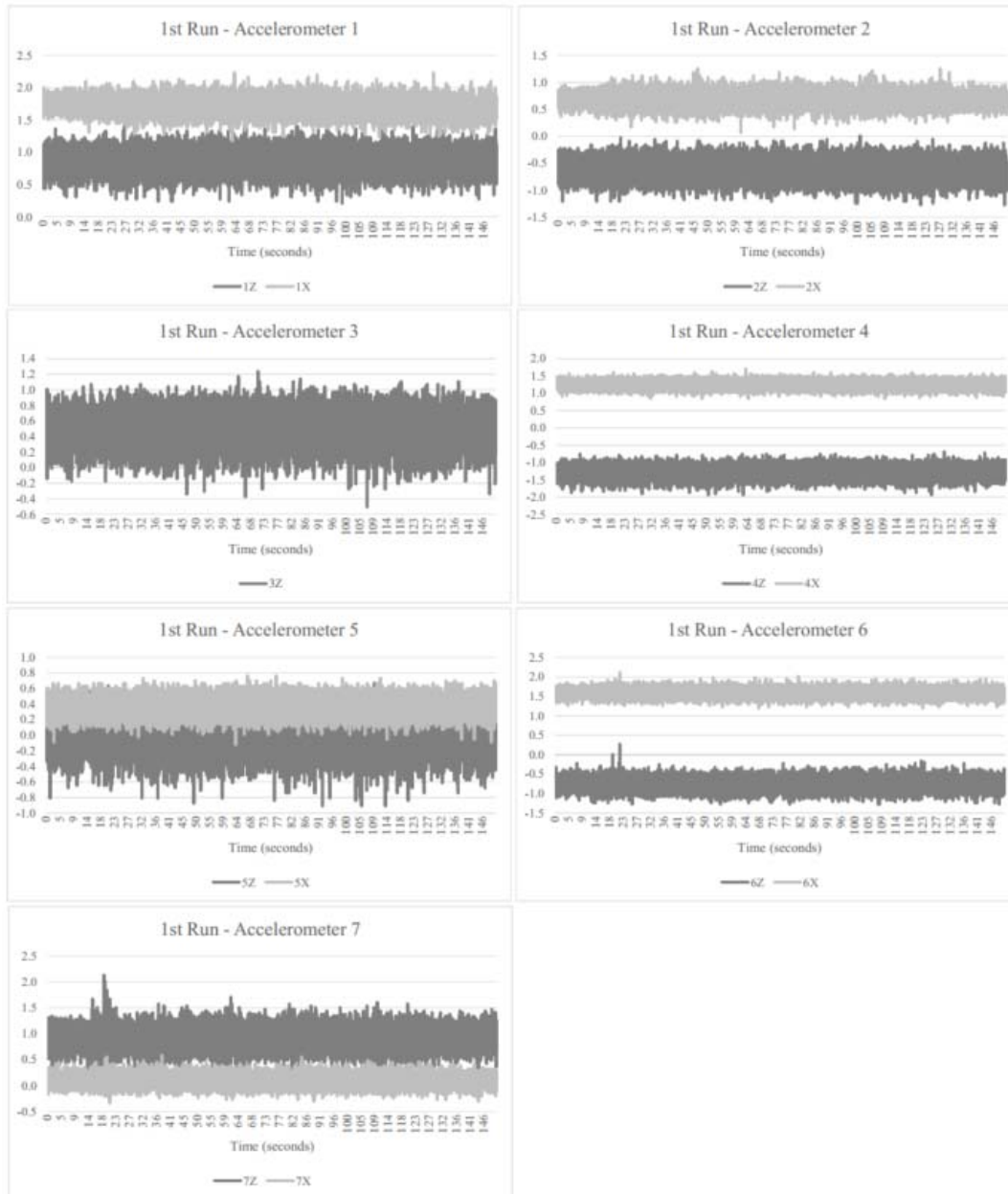
Notes: 5 passes in each direction, HP leak detected, started motion prematurely, 1.5" cut from 5 back and forth passes with 3.5" standoff.

Run Time (sec): 150
Run Time Segment (sec): 0 - 150
Total Panel Run Time (sec): 1920
Y Axis Accelerometer Units: g
Accelerometer 1 Peak (abs value): 2.2
Accelerometer 2 Peak (abs value): 1.3
Accelerometer 3 Peak (abs value): 1.2
Accelerometer 4 Peak (abs value): 1.9
Accelerometer 5 Peak (abs value): 0.9
Accelerometer 6 Peak (abs value): 2.1
Accelerometer 7 Peak (abs value): 2.1



A National Instruments USB-6211 DAQ was used to read the analog signals from the accelerometers. This DAQ supported 16 analog channels. 14 of the channels were used for accelerometer data, one was used to monitor the accelerometer power supply voltage, and the remaining analog channel was not used.

The Z axis and the X axis were used on each accelerometer due to the limited number of analog channels available. The Z axis was normal to the sample surface with +Z pointing towards the excavation equipment. The X axis ran parallel to the edge of the sample.



Panel Number: 7

Run #: 2 of 6

Notes: 15 passes in each direction, 2.75" kerf depth, as standoff increased the cutting depth did not decrease, pump feels hot to touch (decided to let it cool down before next run), 3.5" + 1.5" standoff distance due to previous cut, wire showing from previous cut.

Run Time (sec): 630

Run Time Segment (sec): 150 - 780

Total Panel Run Time (sec): 1920

Y Axis Accelerometer Units: g

Accelerometer 1 Peak (abs value): 2.1

Accelerometer 2 Peak (abs value): 2.3

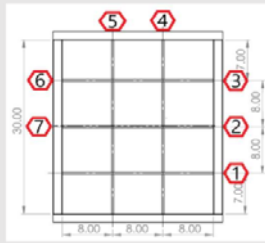
Accelerometer 3 Peak (abs value): 2.5

Accelerometer 4 Peak (abs value): 3.2

Accelerometer 5 Peak (abs value): 5.3

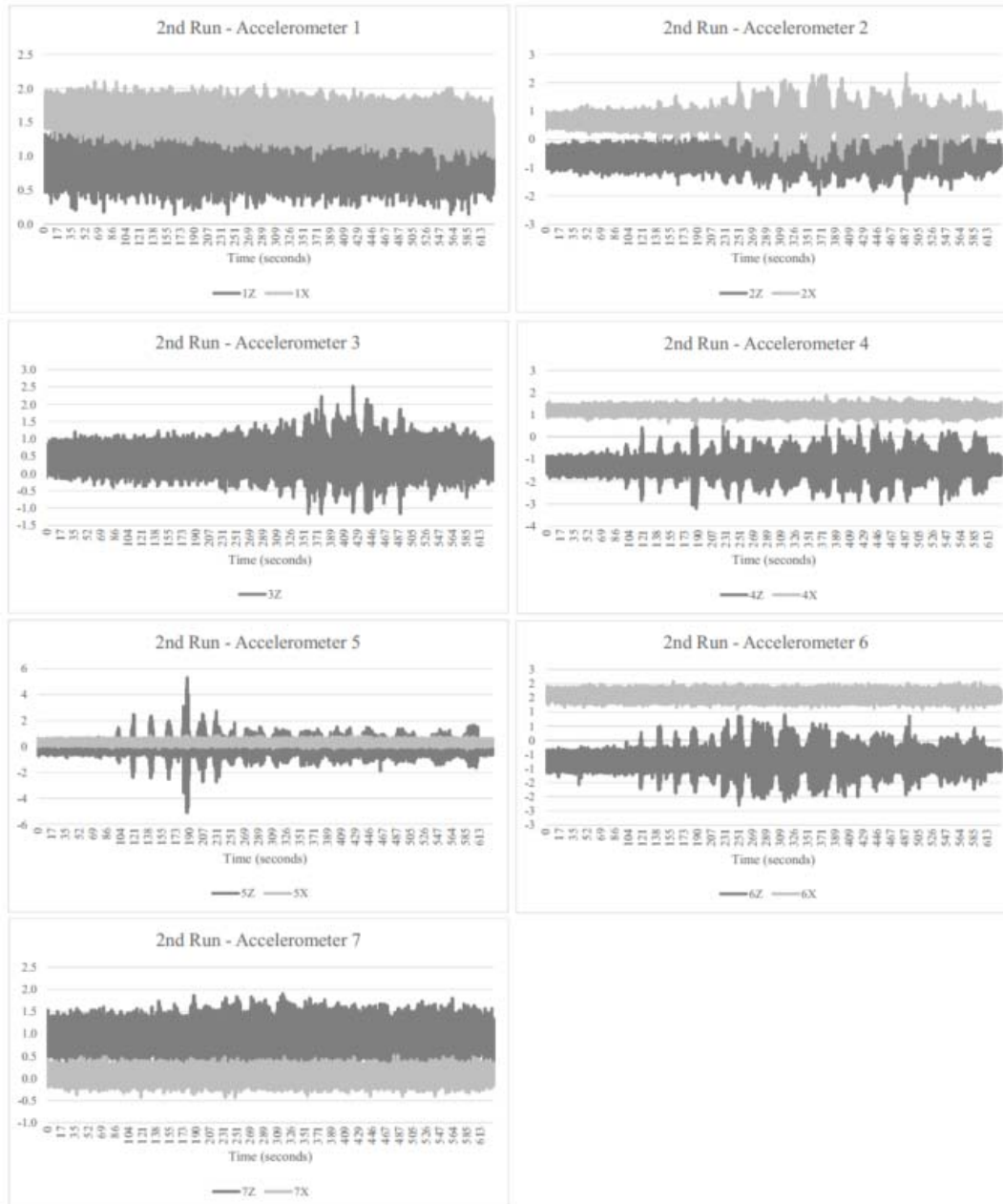
Accelerometer 6 Peak (abs value): 2.3

Accelerometer 7 Peak (abs value): 1.9



A National Instruments USB-6211 DAQ was used to read the analog signals from the accelerometers. This DAQ supported 16 analog channels. 14 of the channels were used for accelerometer data, one was used to monitor the accelerometer power supply voltage, and the remaining analog channel was not used.

The Z axis and the X axis were used on each accelerometer due to the limited number of analog channels available. The Z axis was normal to the sample surface with +Z pointing towards the excavation equipment. The X axis ran parallel to the edge of the sample.

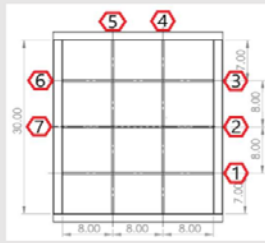


Panel Number: 7

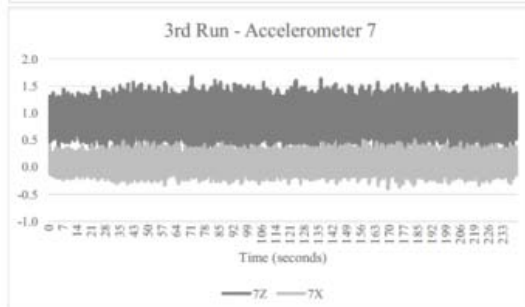
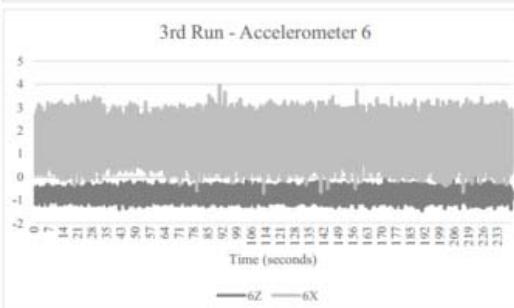
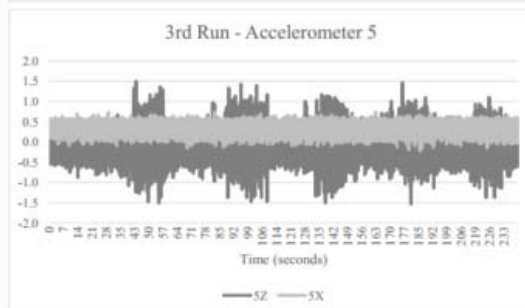
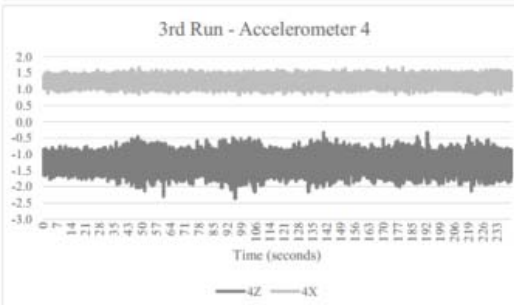
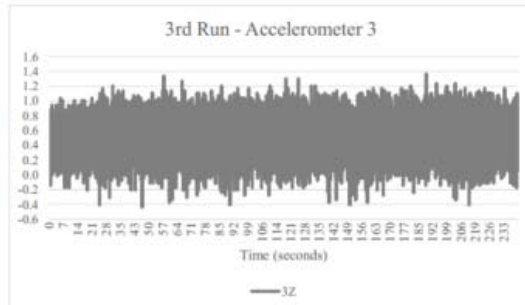
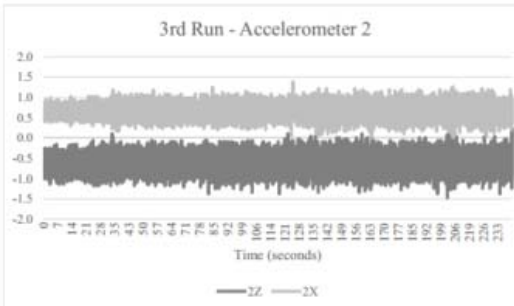
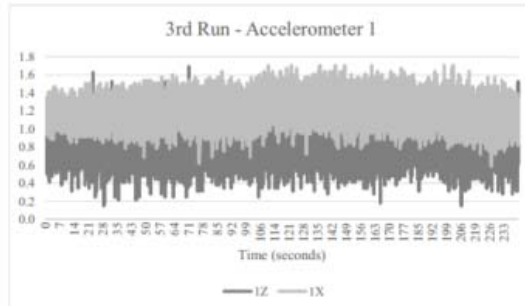
Run #: 3 of 6

Notes: 3.5" standoff. Performed runs 3, 4, 5, and 6 back to back, overall performed 25 passes in each direction, cut deep into substrate, saw light through pinhole in substrate, never had a reading above 6g.

Run Time (sec): 240
Run Time Segment (sec): 780 - 1020
Total Panel Run Time (sec): 1920
Y Axis Accelerometer Units: g
Accelerometer 1 Peak (abs value): 1.7
Accelerometer 2 Peak (abs value): 1.5
Accelerometer 3 Peak (abs value): 1.4
Accelerometer 4 Peak (abs value): 2.4
Accelerometer 5 Peak (abs value): 1.5
Accelerometer 6 Peak (abs value): 4.0
Accelerometer 7 Peak (abs value): 1.7



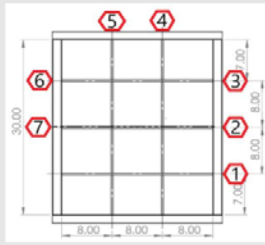
A National Instruments USB-6211 DAQ was used to read the analog signals from the accelerometers. This DAQ supported 16 analog channels. 14 of the channels were used for accelerometer data, one was used to monitor the accelerometer power supply voltage, and the remaining analog channel was not used. The Z axis and the X axis were used on each accelerometer due to the limited number of analog channels available. The Z axis was normal to the sample surface with +Z pointing towards the excavation equipment. The X axis ran parallel to the edge of the sample.



Panel Number: 7**Run #: 4 of 6**

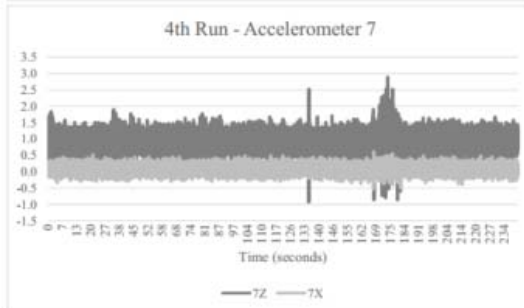
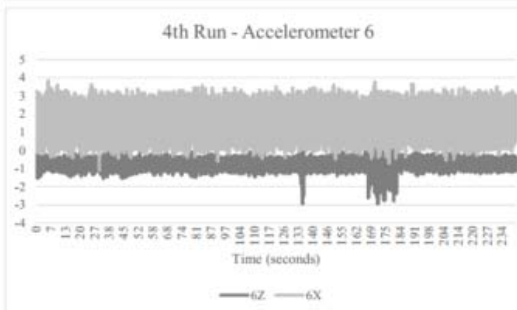
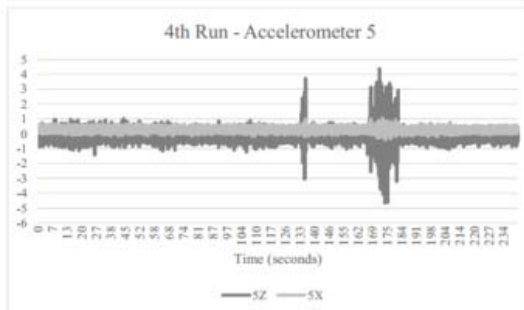
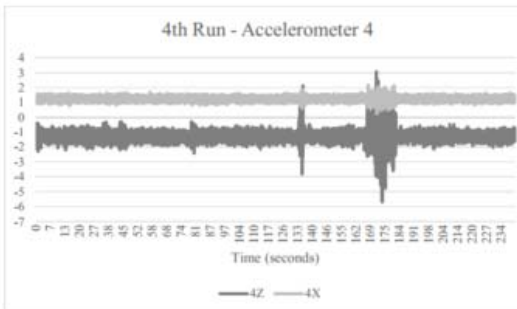
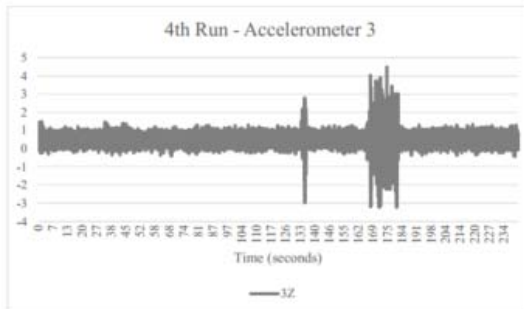
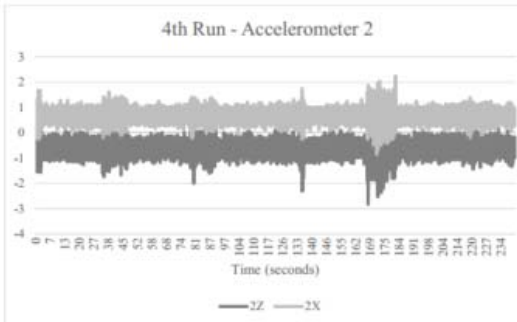
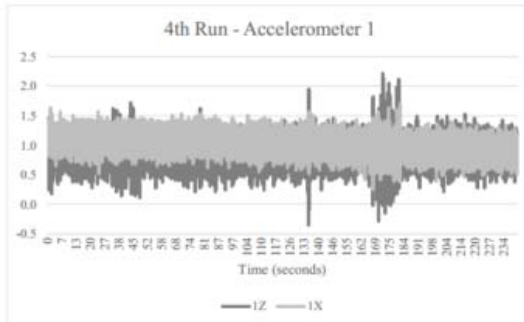
Notes: 3.5" standoff. Performed runs 3, 4, 5, and 6 back to back, overall performed 25 passes in each direction, cut deep into substrate, saw light through pinhole in substrate, never had a reading above 6g.

Run Time (sec): 240
Run Time Segment (sec): 1020 - 1260
Total Panel Run Time (sec): 1920
Y Axis Accelerometer Units: g
Accelerometer 1 Peak (abs value): 2.2
Accelerometer 2 Peak (abs value): 2.8
Accelerometer 3 Peak (abs value): 4.5
Accelerometer 4 Peak (abs value): 5.7
Accelerometer 5 Peak (abs value): 4.7
Accelerometer 6 Peak (abs value): 3.8
Accelerometer 7 Peak (abs value): 2.9



A National Instruments USB-6211 DAQ was used to read the analog signals from the accelerometers. This DAQ supported 16 analog channels. 14 of the channels were used for accelerometer data, one was used to monitor the accelerometer power supply voltage, and the remaining analog channel was not used.

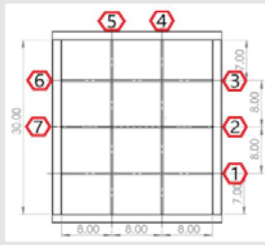
The Z axis and the X axis were used on each accelerometer due to the limited number of analog channels available. The Z axis was normal to the sample surface with +Z pointing towards the excavation equipment. The X axis ran parallel to the edge of the sample.



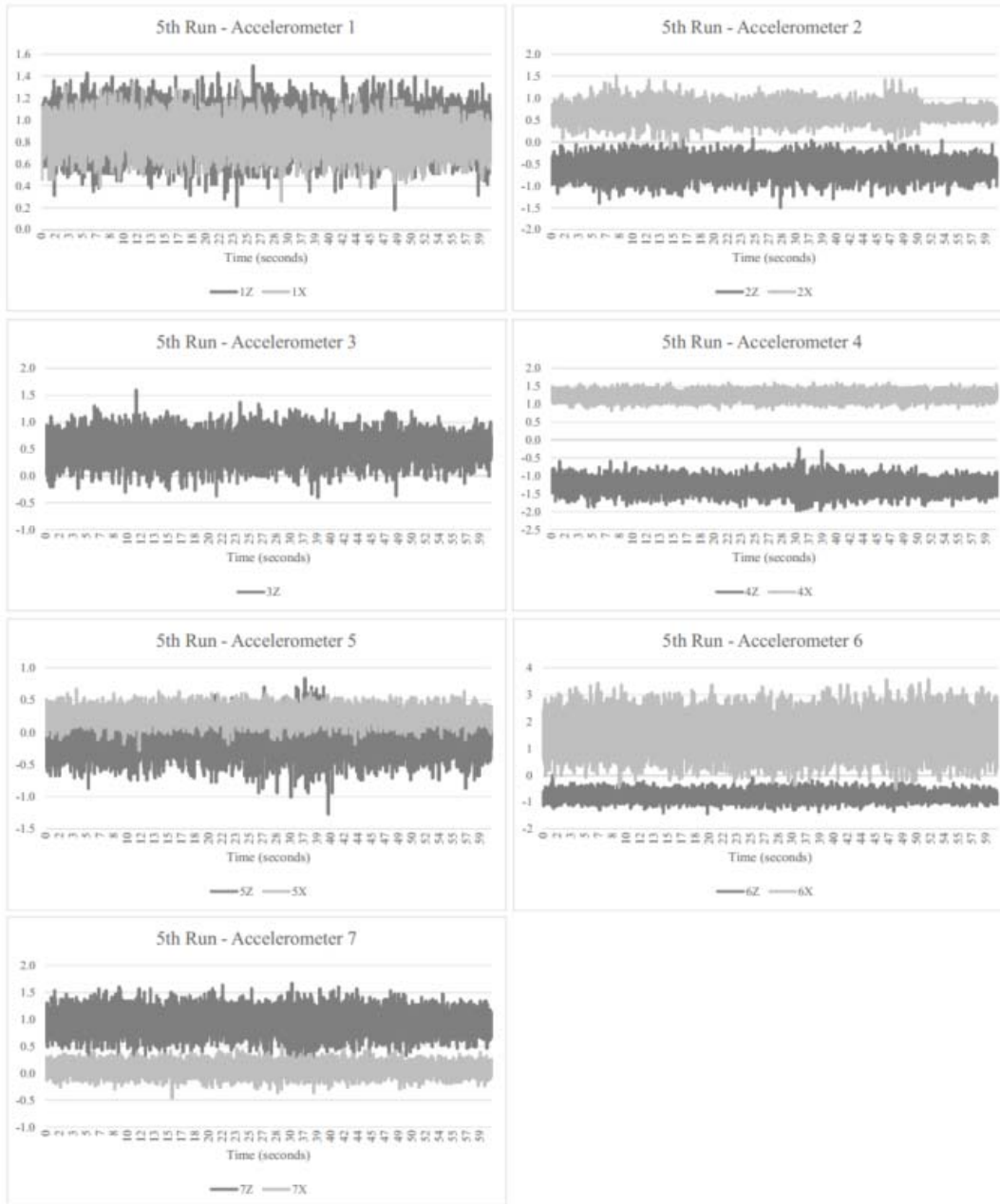
Panel Number: 7**Run #: 5 of 6**

Notes: 3.5" standoff. Performed runs 3, 4, 5, and 6 back to back, overall performed 25 passes in each direction, cut deep into substrate, saw light through pinhole in substrate, never had a reading above 6g.

Run Time (sec): 60
Run Time Segment (sec): 1260 - 1320
Total Panel Run Time (sec): 1920
Y Axis Accelerometer Units: g
Accelerometer 1 Peak (abs value): 1.5
Accelerometer 2 Peak (abs value): 1.5
Accelerometer 3 Peak (abs value): 1.6
Accelerometer 4 Peak (abs value): 2.0
Accelerometer 5 Peak (abs value): 1.3
Accelerometer 6 Peak (abs value): 3.6
Accelerometer 7 Peak (abs value): 1.7



A National Instruments USB-6211 DAQ was used to read the analog signals from the accelerometers. This DAQ supported 16 analog channels. 14 of the channels were used for accelerometer data, one was used to monitor the accelerometer power supply voltage, and the remaining analog channel was not used.
The Z axis and the X axis were used on each accelerometer due to the limited number of analog channels available. The Z axis was normal to the sample surface with +Z pointing towards the excavation equipment. The X axis ran parallel to the edge of the sample.

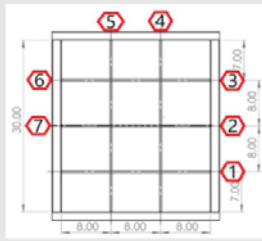


Panel Number: 7

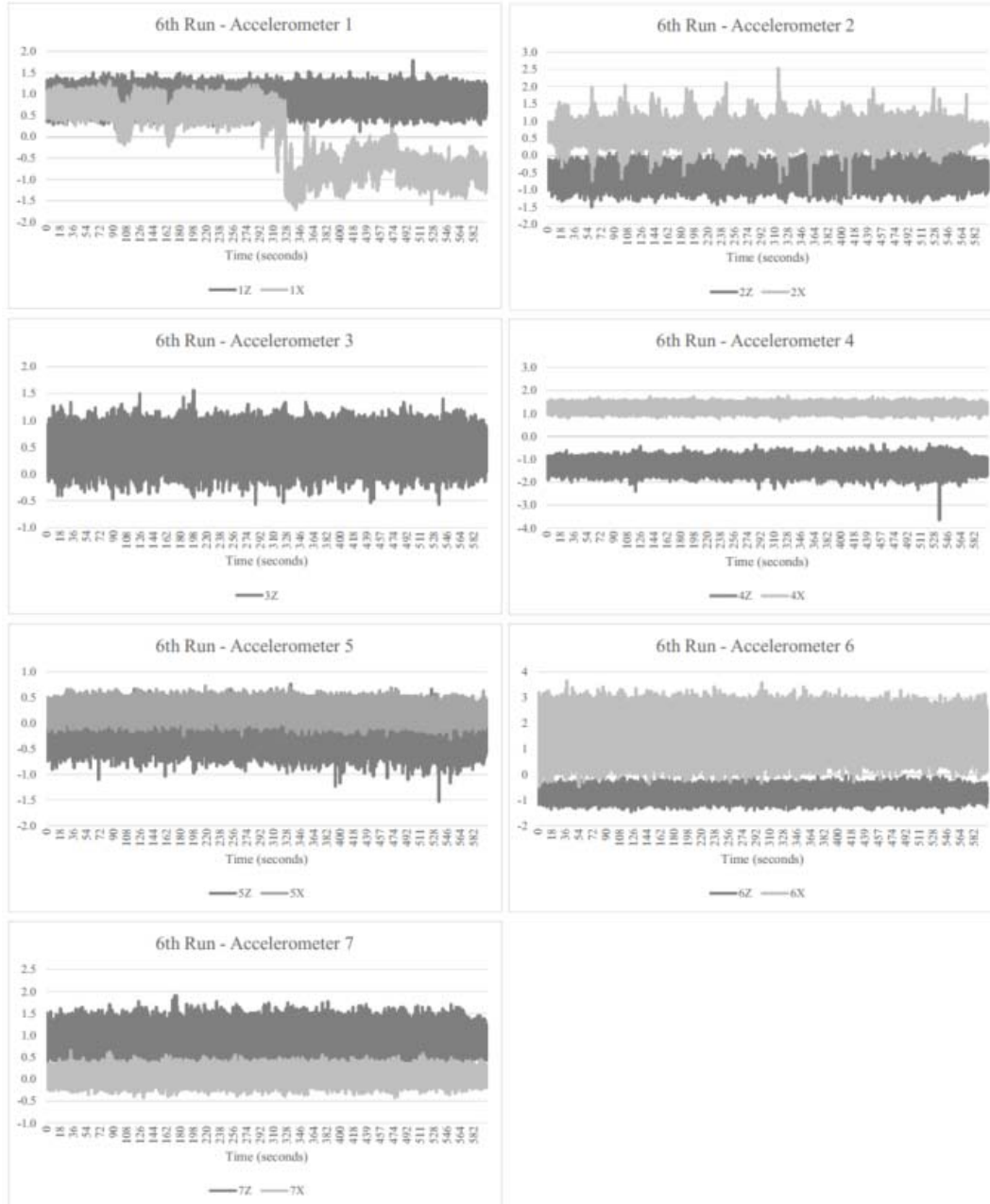
Run #: 6 of 6

Notes: 3.5" standoff. Performed runs 3, 4, 5, and 6 back to back, overall performed 25 passes in each direction, cut deep into substrate, saw light through pinhole in substrate, never had a reading above 6g.

Run Time (sec): 600
Run Time Segment (sec): 1320 - 1920
Total Panel Run Time (sec): 1920
Y Axis Accelerometer Units: g
Accelerometer 1 Peak (abs value): 1.8
Accelerometer 2 Peak (abs value): 2.5
Accelerometer 3 Peak (abs value): 1.6
Accelerometer 4 Peak (abs value): 3.7
Accelerometer 5 Peak (abs value): 1.5
Accelerometer 6 Peak (abs value): 3.7
Accelerometer 7 Peak (abs value): 1.9



A National Instruments USB-6211 DAQ was used to read the analog signals from the accelerometers. This DAQ supported 16 analog channels. 14 of the channels were used for accelerometer data, one was used to monitor the accelerometer power supply voltage, and the remaining analog channel was not used.
The Z axis and the X axis were used on each accelerometer due to the limited number of analog channels available. The Z axis was normal to the sample surface with +Z pointing towards the excavation equipment. The X axis ran parallel to the edge of the sample.



Panel Number: TEST

Run #: 1 of 2

Notes: Waterjet test runs on the developed test panel. Standoff distance of 3.5 inches.

Run Time (sec): 30

Run Time Segment (sec): 0 - 30

Total Panel Run Time (sec): 60

Y Axis Accelerometer Units: g

Accelerometer 1 Peak (abs value): 1.8

Accelerometer 2 Peak (abs value): 1.2

Accelerometer 3 Peak (abs value): -

Accelerometer 4 Peak (abs value): 1.9

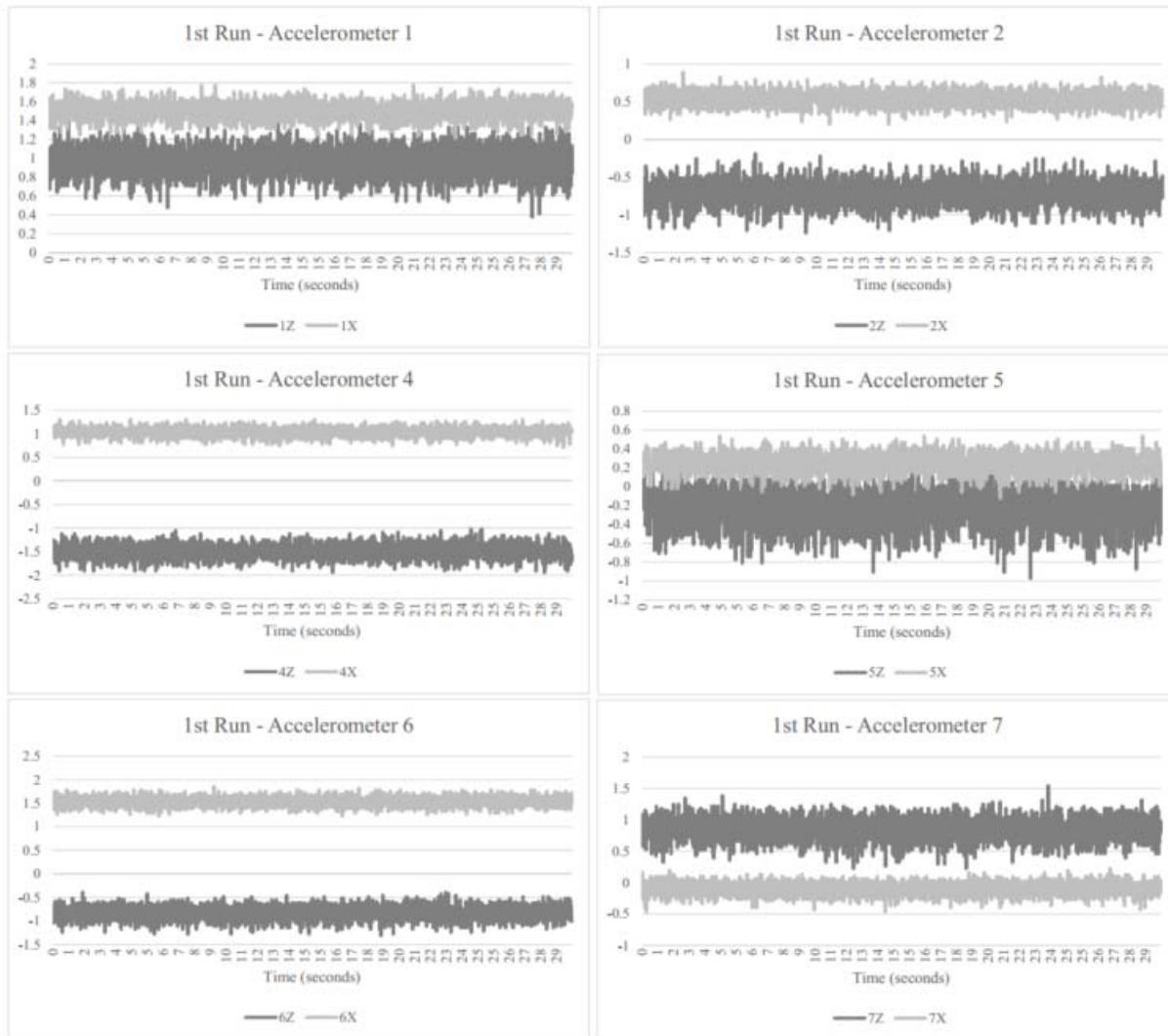
Accelerometer 5 Peak (abs value): 1.0

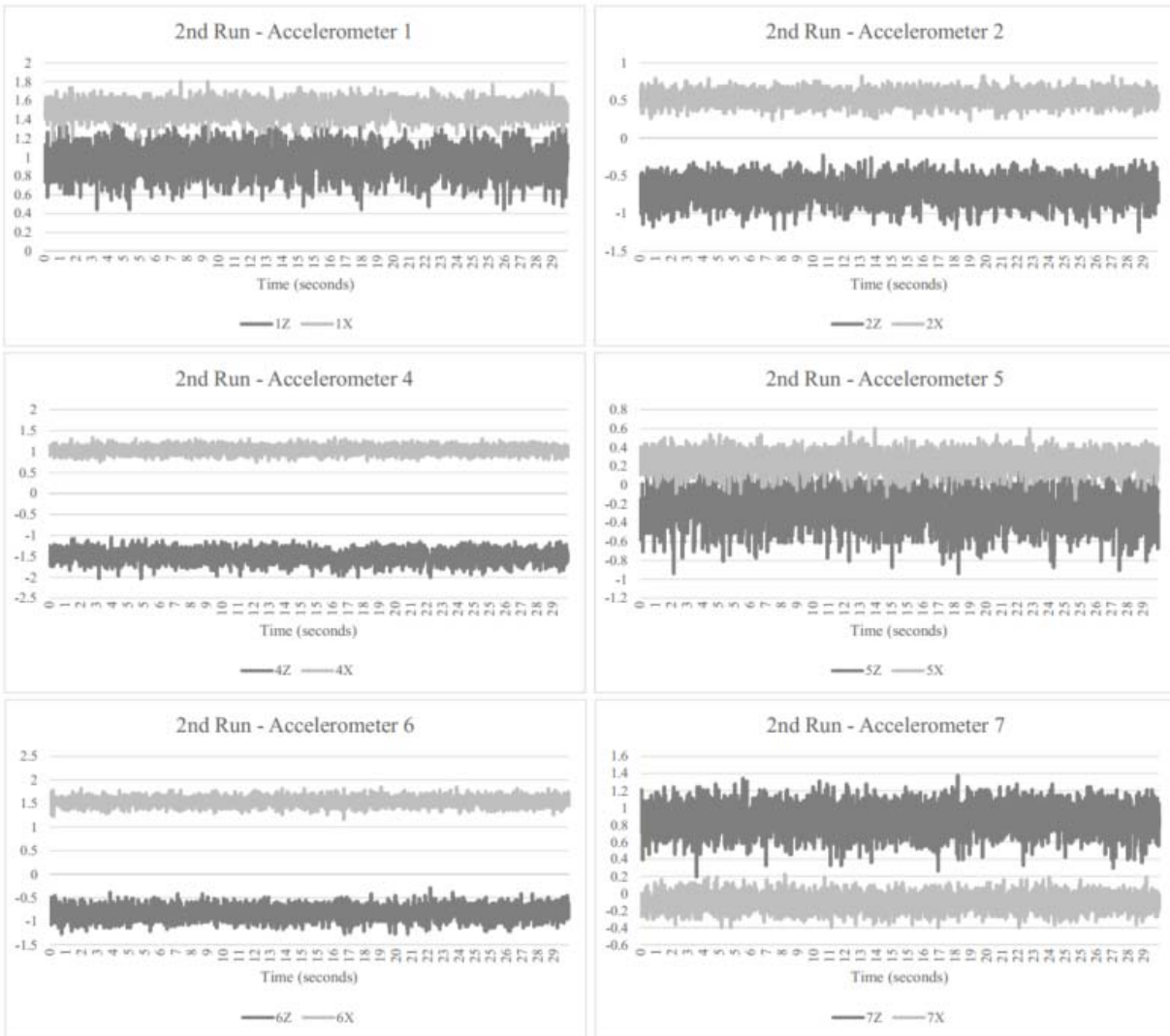
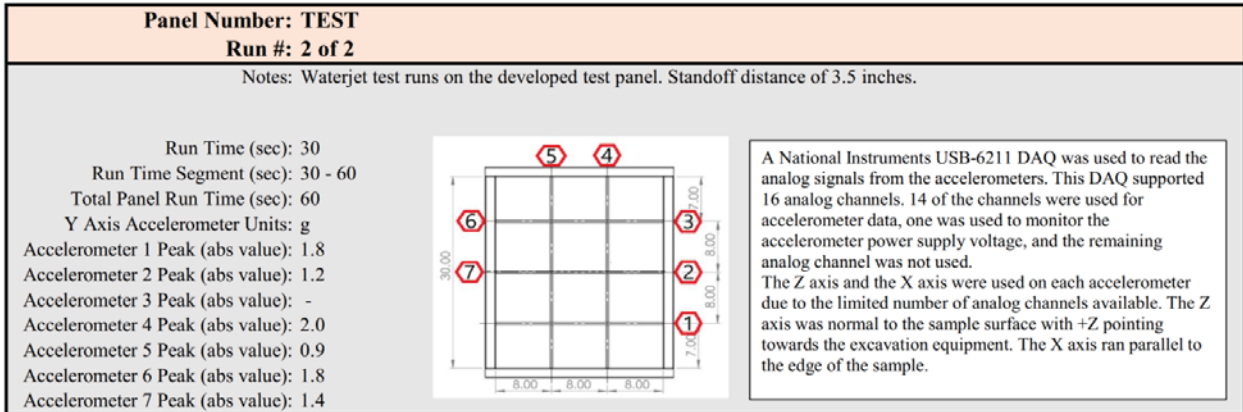
Accelerometer 6 Peak (abs value): 1.8

Accelerometer 7 Peak (abs value): 1.5

A National Instruments USB-6211 DAQ was used to read the analog signals from the accelerometers. This DAQ supported 16 analog channels. 14 of the channels were used for accelerometer data, one was used to monitor the accelerometer power supply voltage, and the remaining analog channel was not used.

The Z axis and the X axis were used on each accelerometer due to the limited number of analog channels available. The Z axis was normal to the sample surface with +Z pointing towards the excavation equipment. The X axis ran parallel to the edge of the sample.





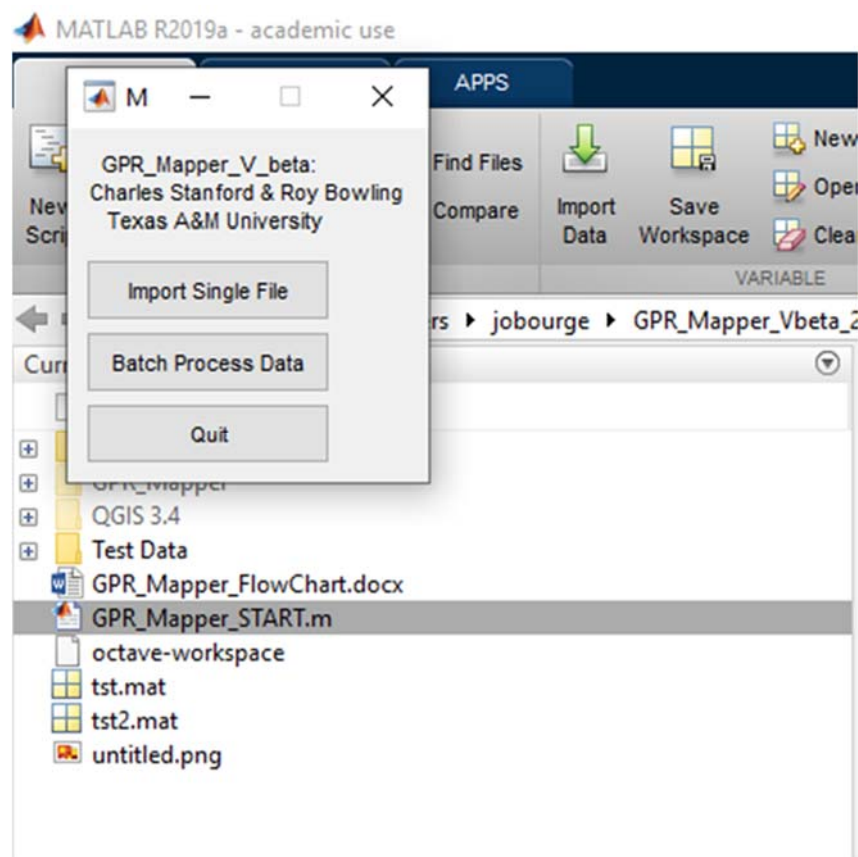
Section B-5: Ground Penetrating Radar Data

GPR Mapper Processing Sequence

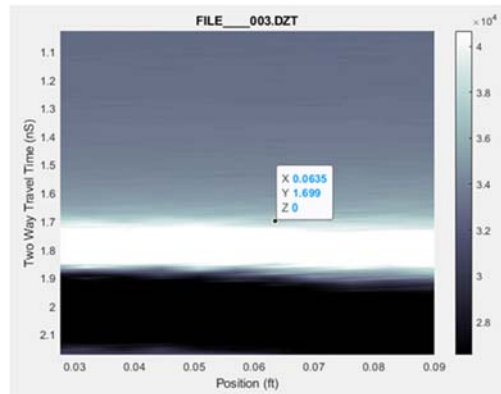
The following processing sequence was used for each scan acquired by the 2600 MHz and 1600 MHz antennas for GPR analysis. The processing steps include, in this particular order, time zero correction, deWow, Fourier filtering, time gain, and background subtraction. Each step was completed in the program GPR Mapper, a MATLAB program developed by Charles Stanford and Roy Bowling from Texas A&M University.

1. Open MATLAB.

Run GPR_Mapper_START.m

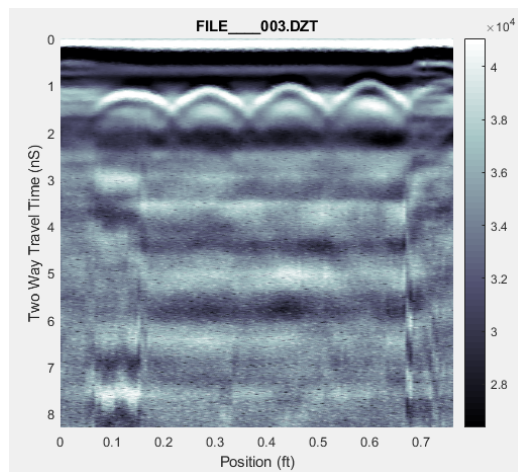


2. To perform **time zero correction**, open DZT file, view data, zoom in view to top of first reflection, use data cursor to pick point, record the Y value (ex, File__003 was 1.699). Then close plot.

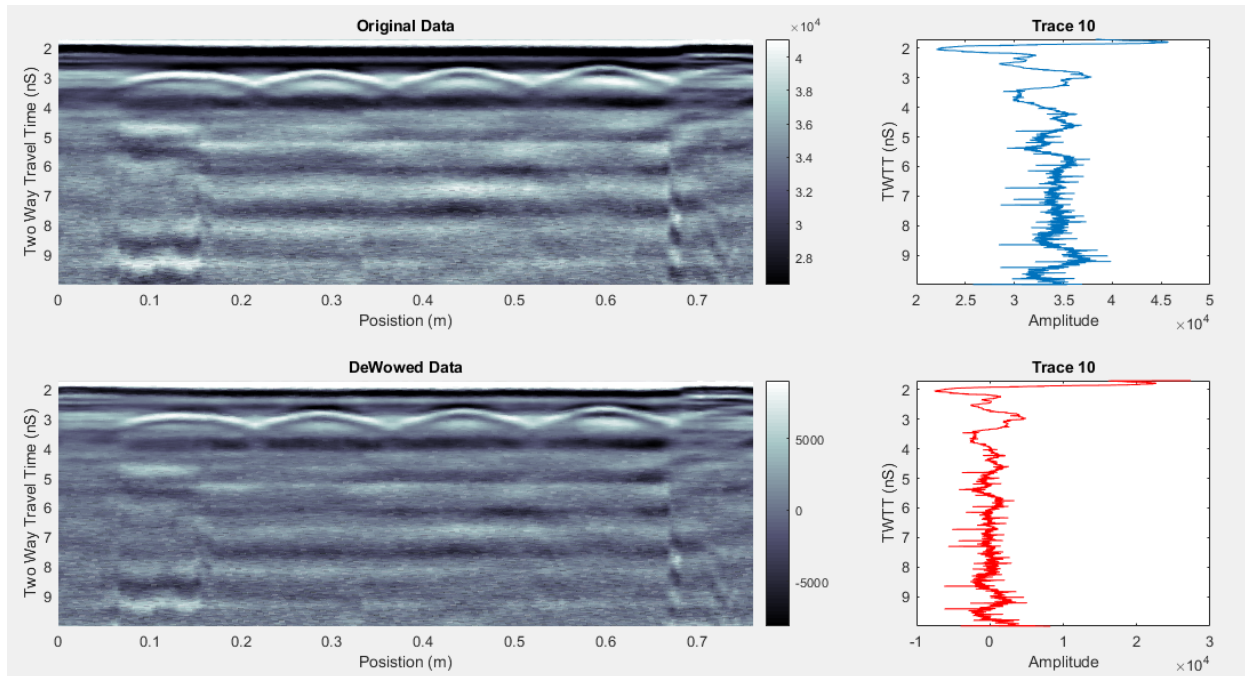


Go to edit data, crop/pad data

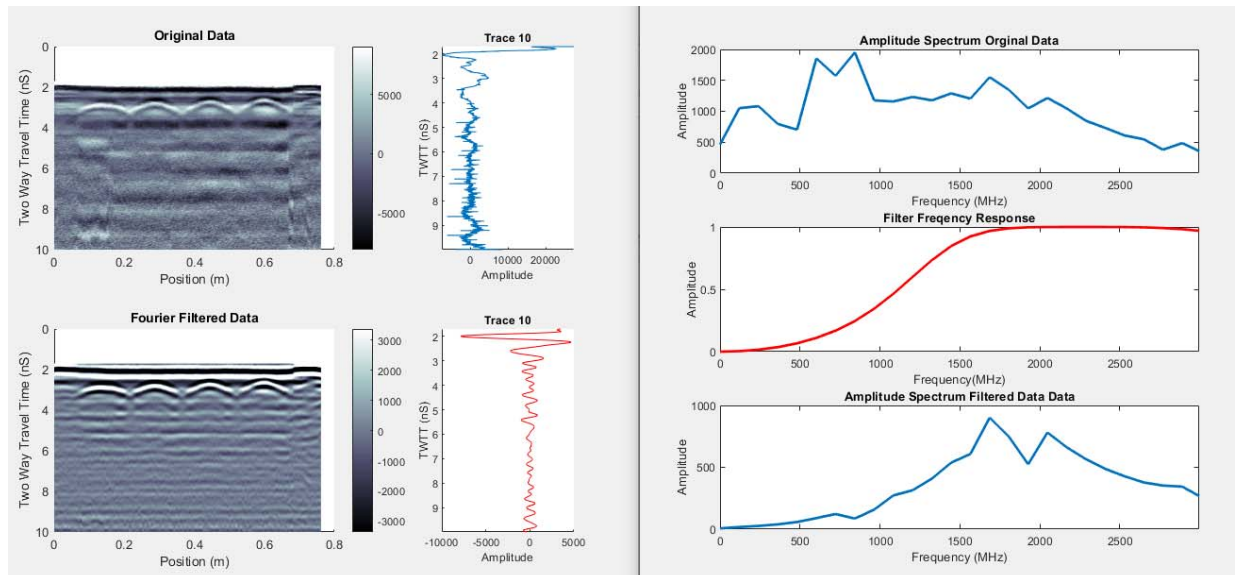
- a. Crop samples from beginning, according to two-way travel time (Y value); and
- b. Export result. Return to main menu.



3. To perform **deWow**, go to process data, Data DeWow
 - a. Select deWow parameters, use 250 as deWow value;
 - b. Update deWow plot;
 - c. Accept deWow parameters; and
 - d. Export result. Return to main menu.

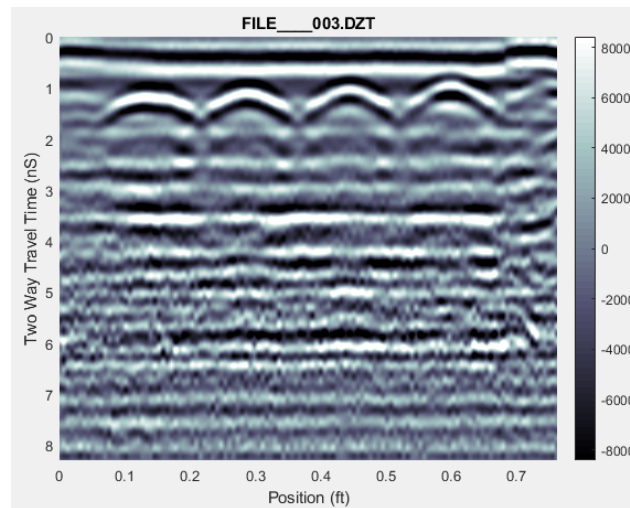


4. To perform **Fourier filtering**, go to process data, Fourier filtering
 - a. Select Fourier filter parameters, set lower limit to [Equipment MHz – (Equipment MHz/2)] and set upper limit to [Equipment MHz + (Equipment MHz/2)];
 - b. Update Fourier filter plots;
 - c. Accept Fourier filter parameters; and
 - d. Export result. Return to main menu.

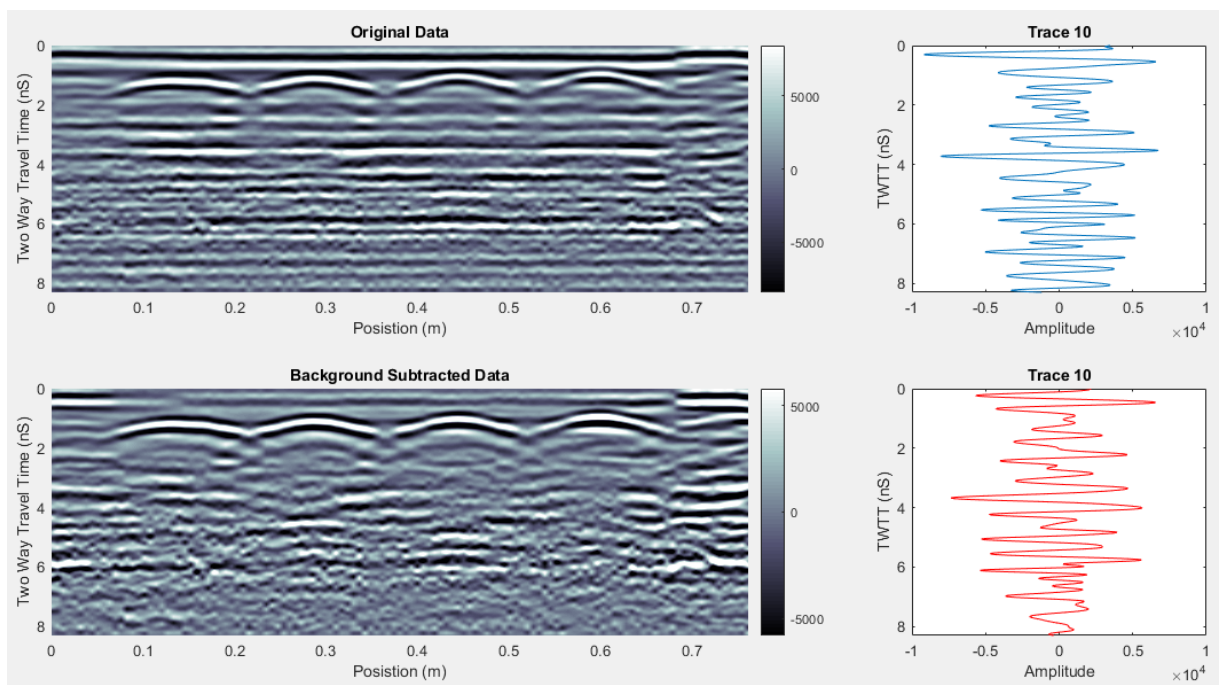


5. To perform **time gain**, go to process data, gain.
 - a. Select gain parameters, change gain type to 2;

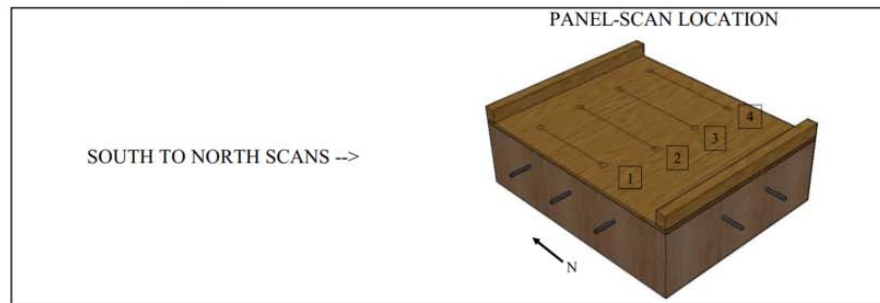
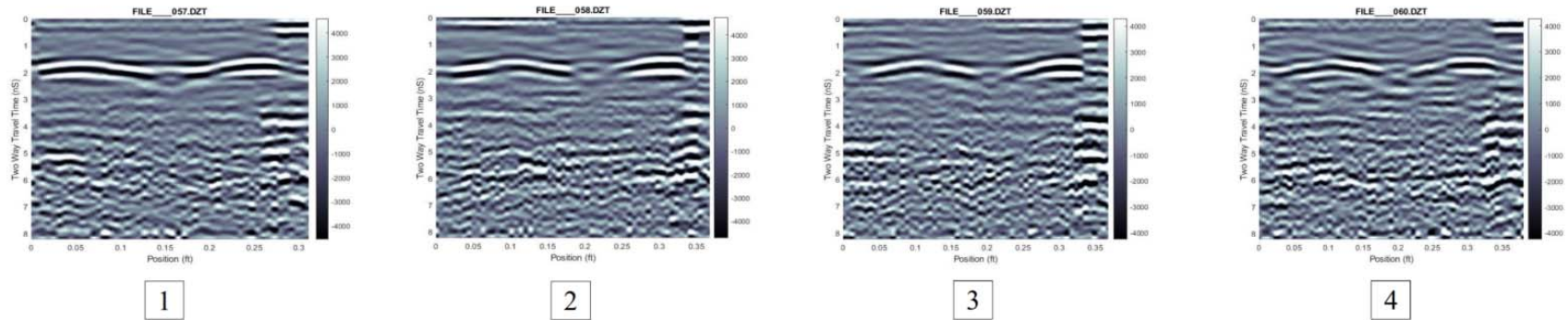
- b. Update gain plot;
 - i. Gain with respect to topographic surface? “No”
 - ii. Scaler gain = 1, Exponential gain = 1.5, Application window length = 6, End of window decay exponent = -5
 - iii. Proceed to gain full line? “Yes”
- c. Accept gain parameters; and
- d. Export result. Return to main menu.



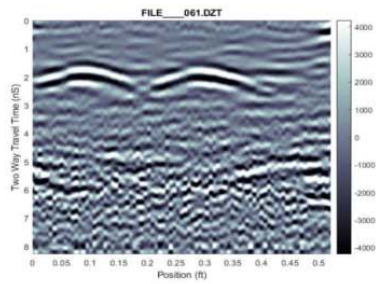
6. To perform **background subtraction**, go to process data, background subtraction
 - a. Choose the full background subtraction option; and
 - b. Export result. Processing steps have now been completed for this scan.



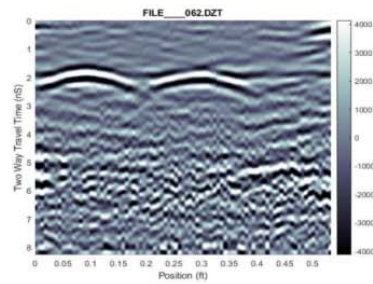
PANEL 2 - PRE EXCAVATION SCANS FROM SOUTH TO NORTH ON BOTTOM FACE USING 2600 MHZ ANTENNA



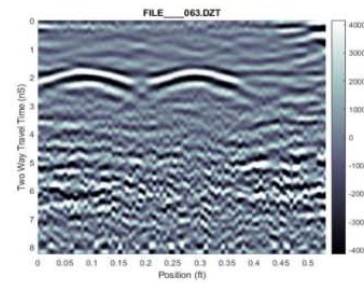
PANEL 2 - PRE EXCAVATION SCANS FROM EAST TO WEST ON BOTTOM FACE USING 2600 MHZ ANTENNA



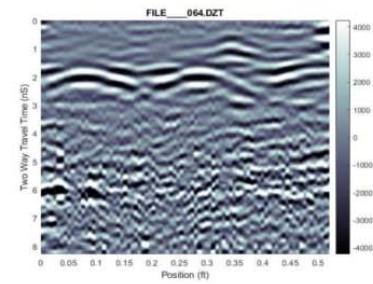
1



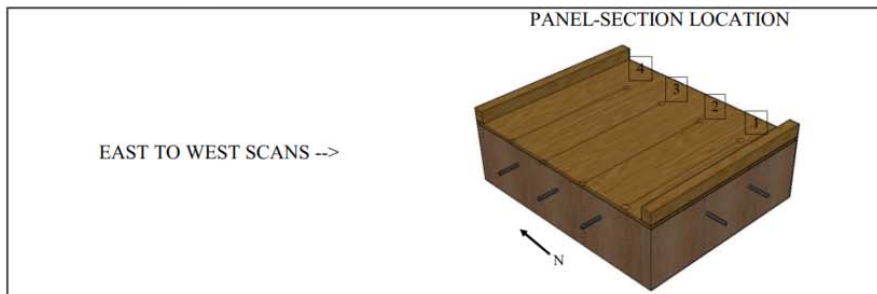
2



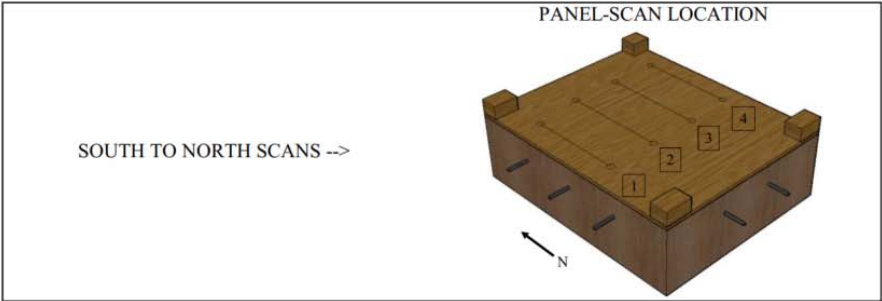
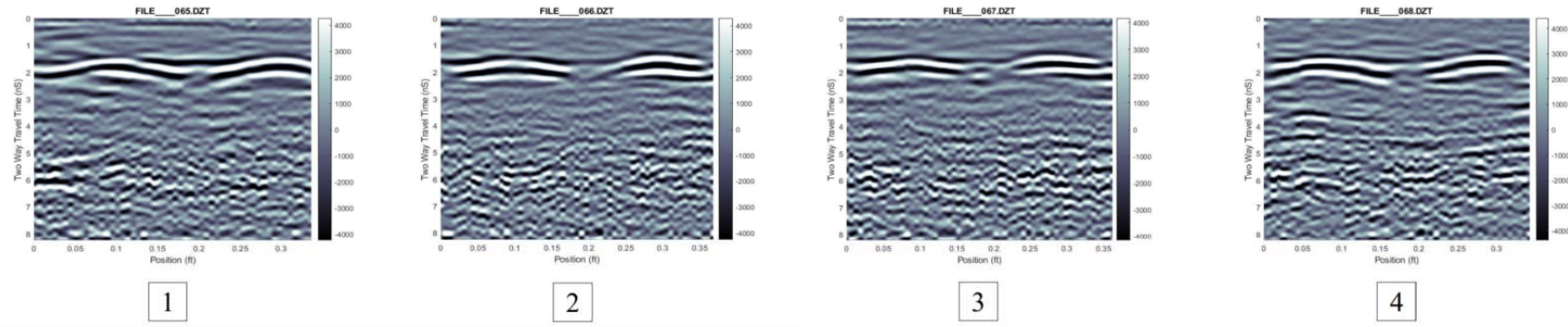
3



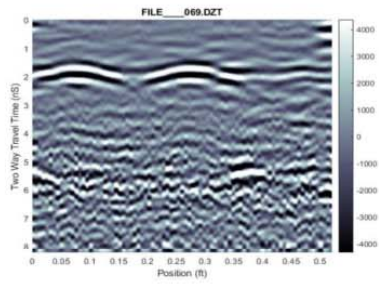
4



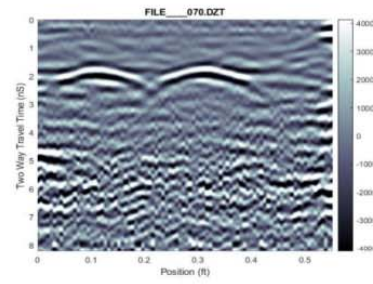
PANEL 3 - PRE EXCAVATION SCANS FROM SOUTH TO NORTH ON BOTTOM FACE USING 2600 MHZ ANTENNA



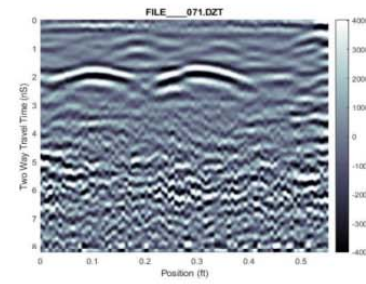
PANEL 3 - PRE EXCAVATION SCANS FROM EAST TO WEST ON BOTTOM FACE USING 2600 MHZ ANTENNA



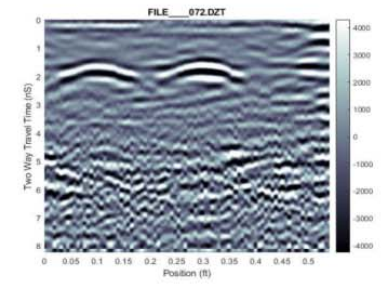
1



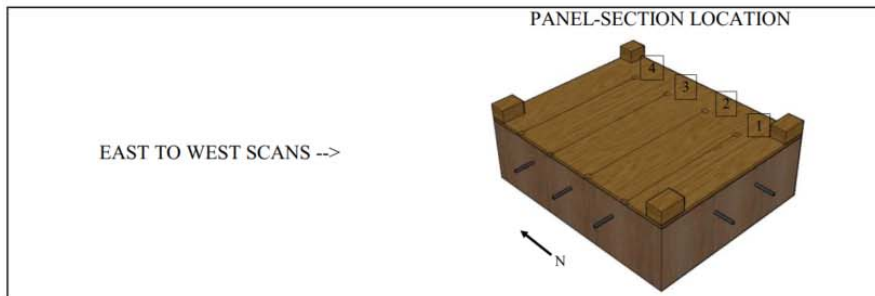
2



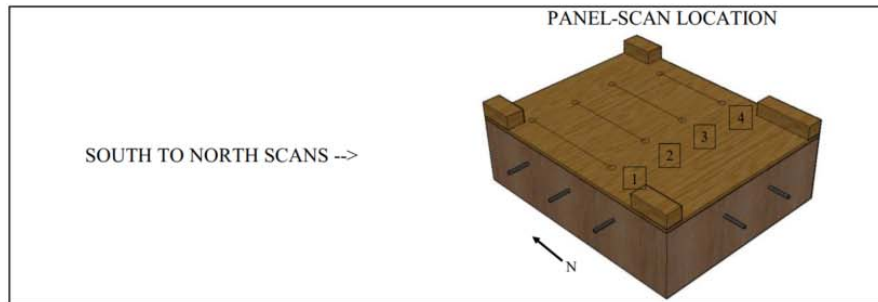
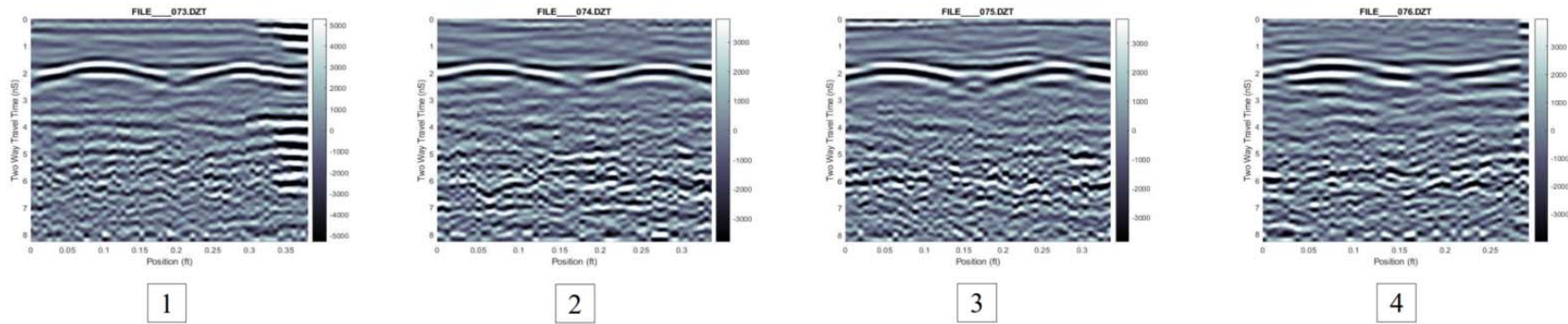
3



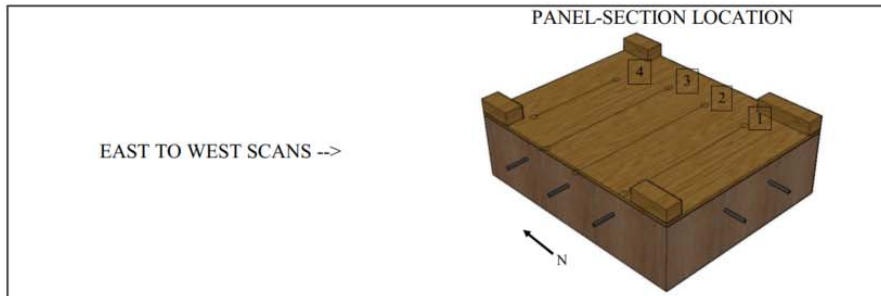
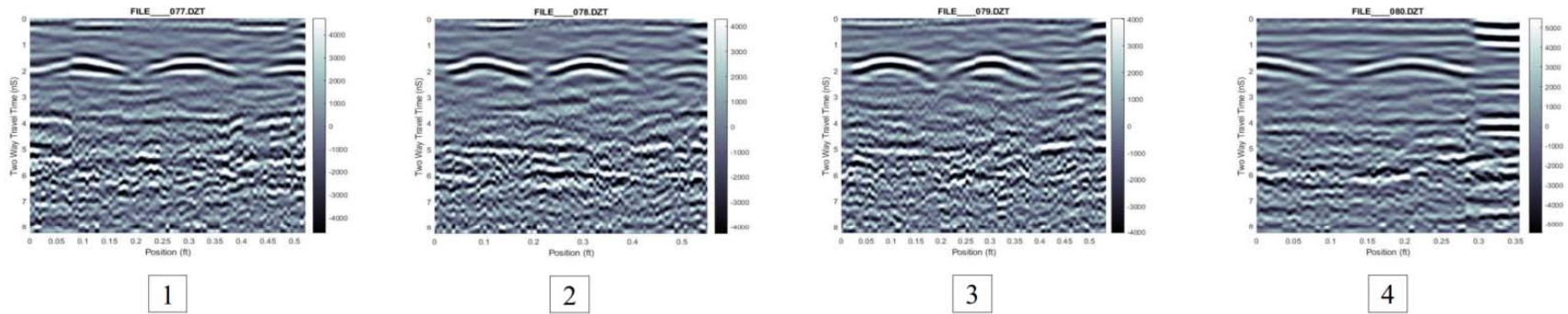
4



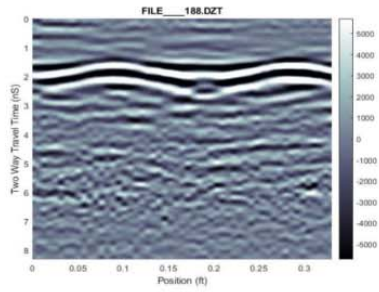
PANEL 4 - PRE EXCAVATION SCANS FROM SOUTH TO NORTH ON BOTTOM FACE USING 2600 MHZ ANTENNA



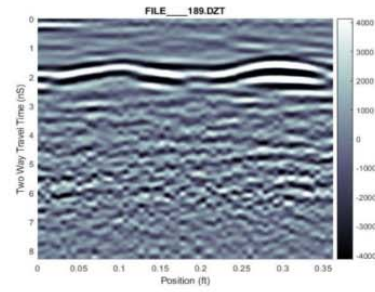
PANEL 4 - PRE EXCAVATION SCANS FROM EAST TO WEST ON BOTTOM FACE USING 2600 MHZ ANTENNA



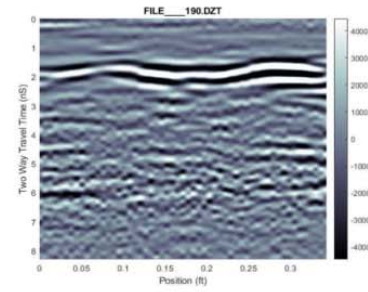
PANEL 7 - PRE EXCAVATION SCANS FROM SOUTH TO NORTH ON BOTTOM FACE USING 2600 MHZ ANTENNA



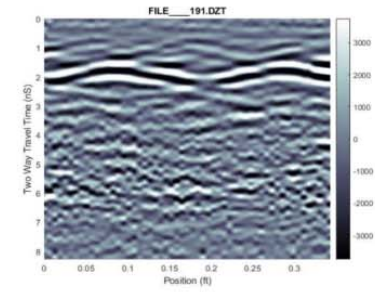
1



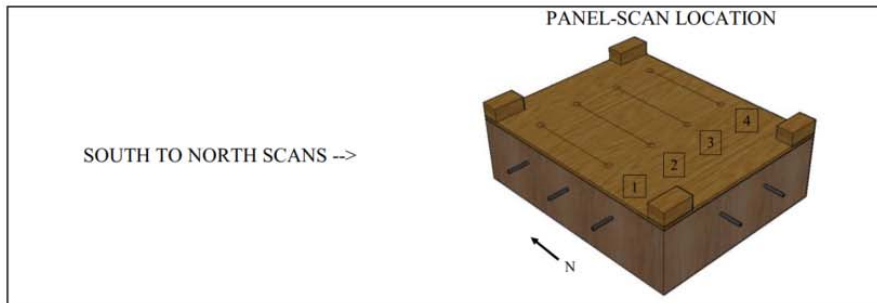
2



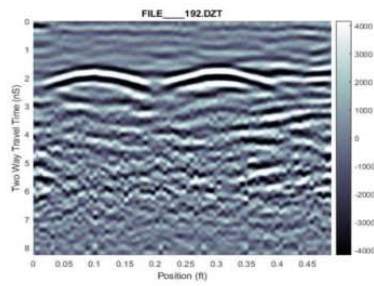
3



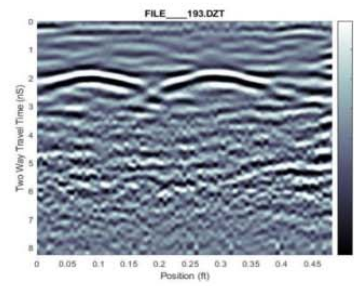
4



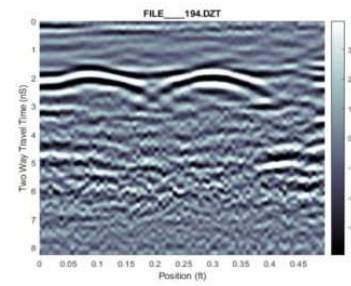
PANEL 7 - PRE EXCAVATION SCANS FROM EAST TO WEST ON BOTTOM FACE USING 2600 MHZ ANTENNA



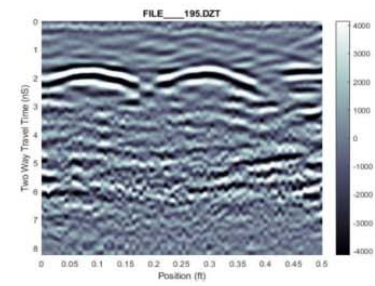
1



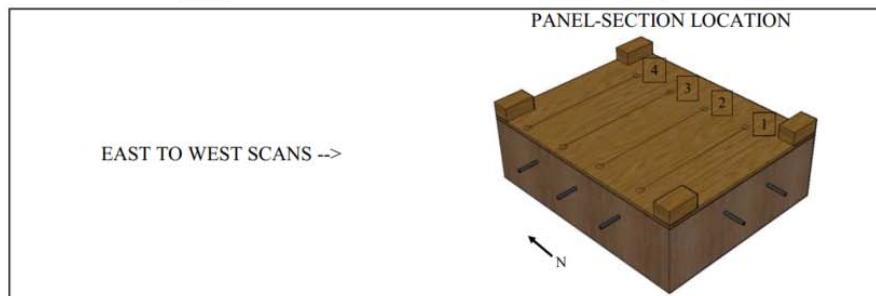
2



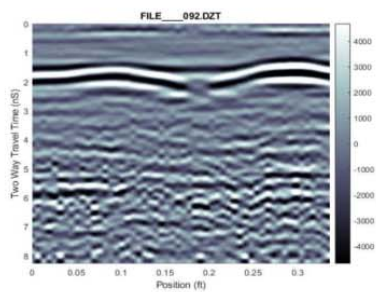
3



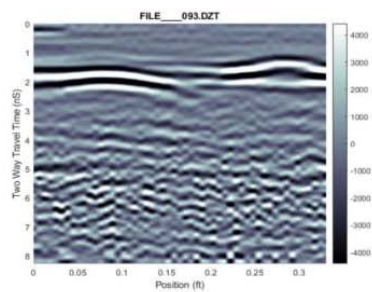
4



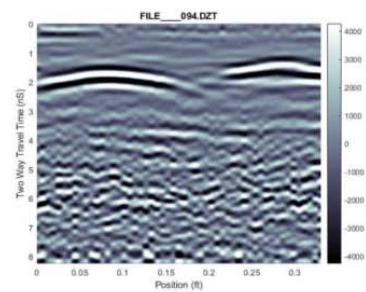
PANEL TEST - PRE EXCAVATION SCANS FROM SOUTH TO NORTH ON BOTTOM FACE USING 2600 MHZ ANTENNA



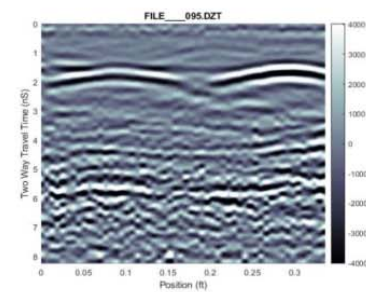
1



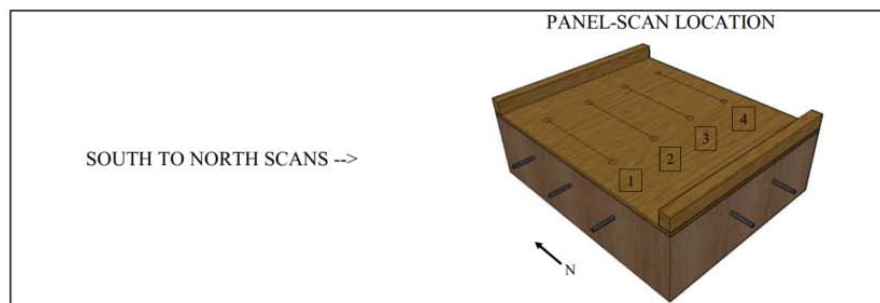
2



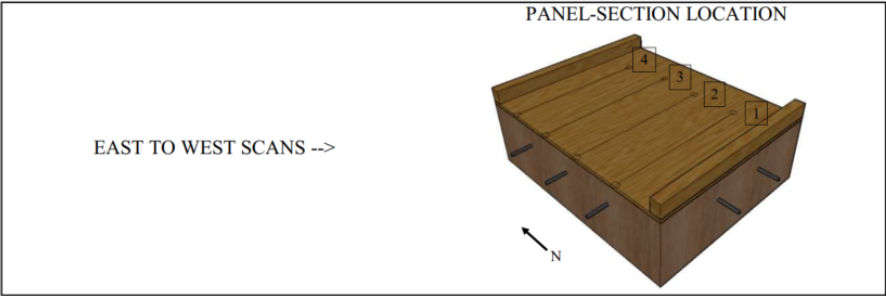
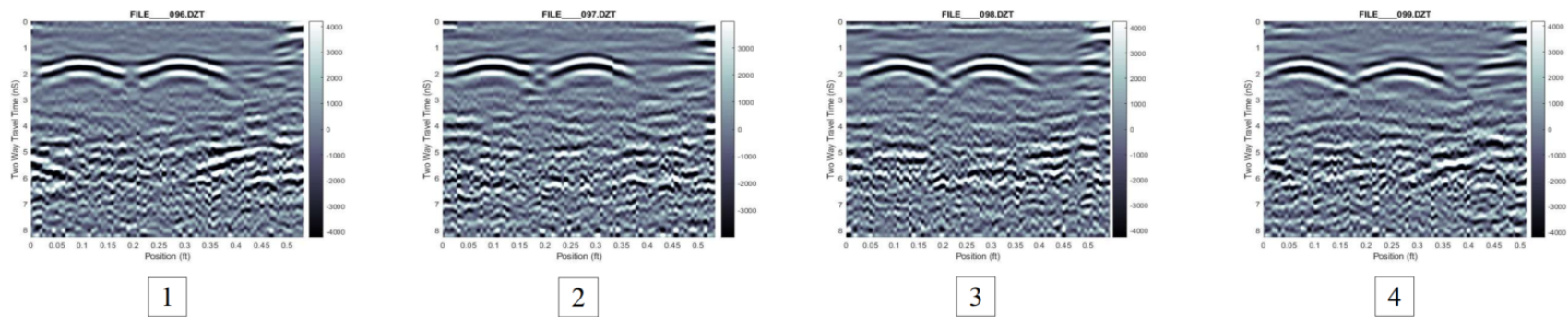
3



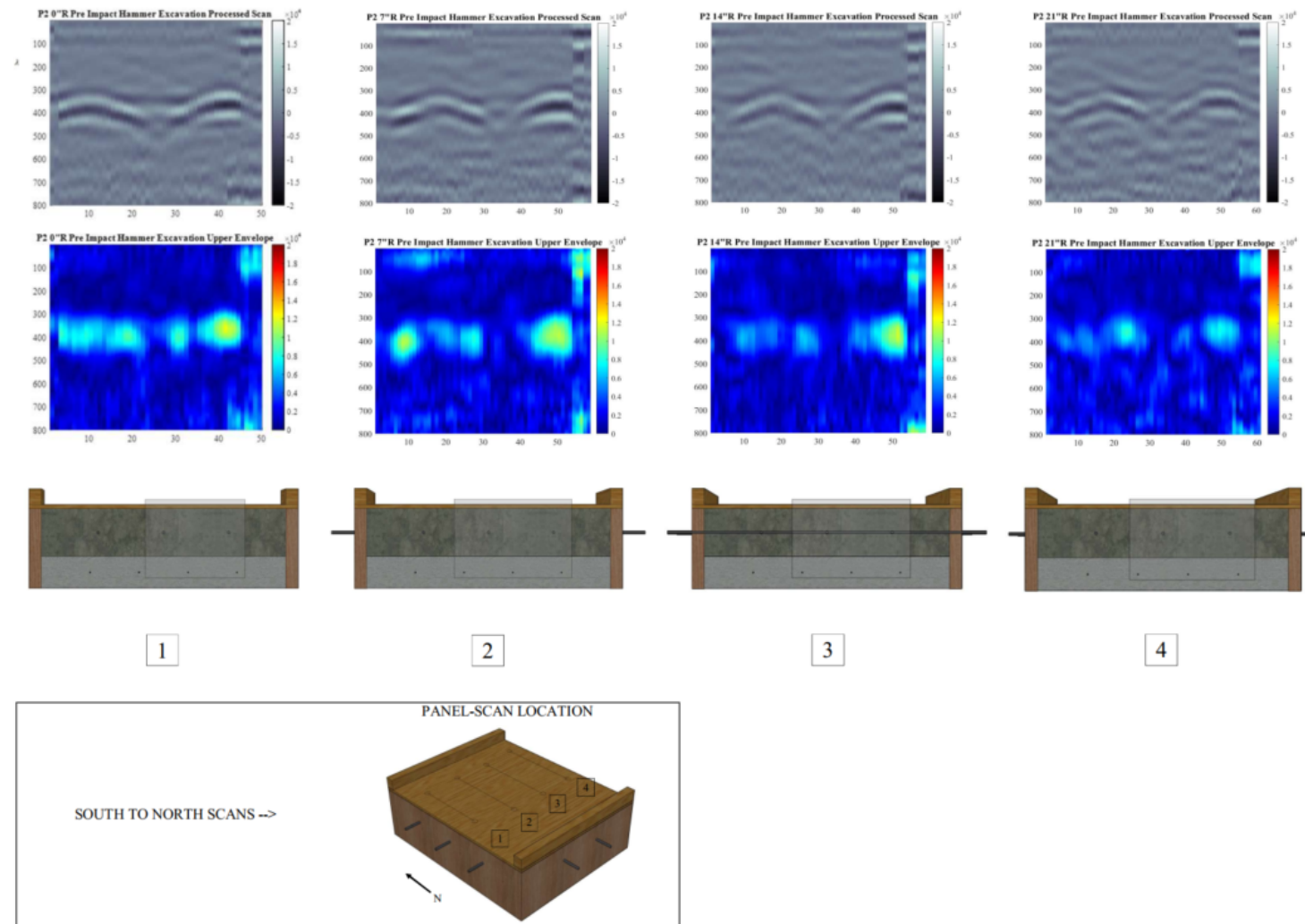
4



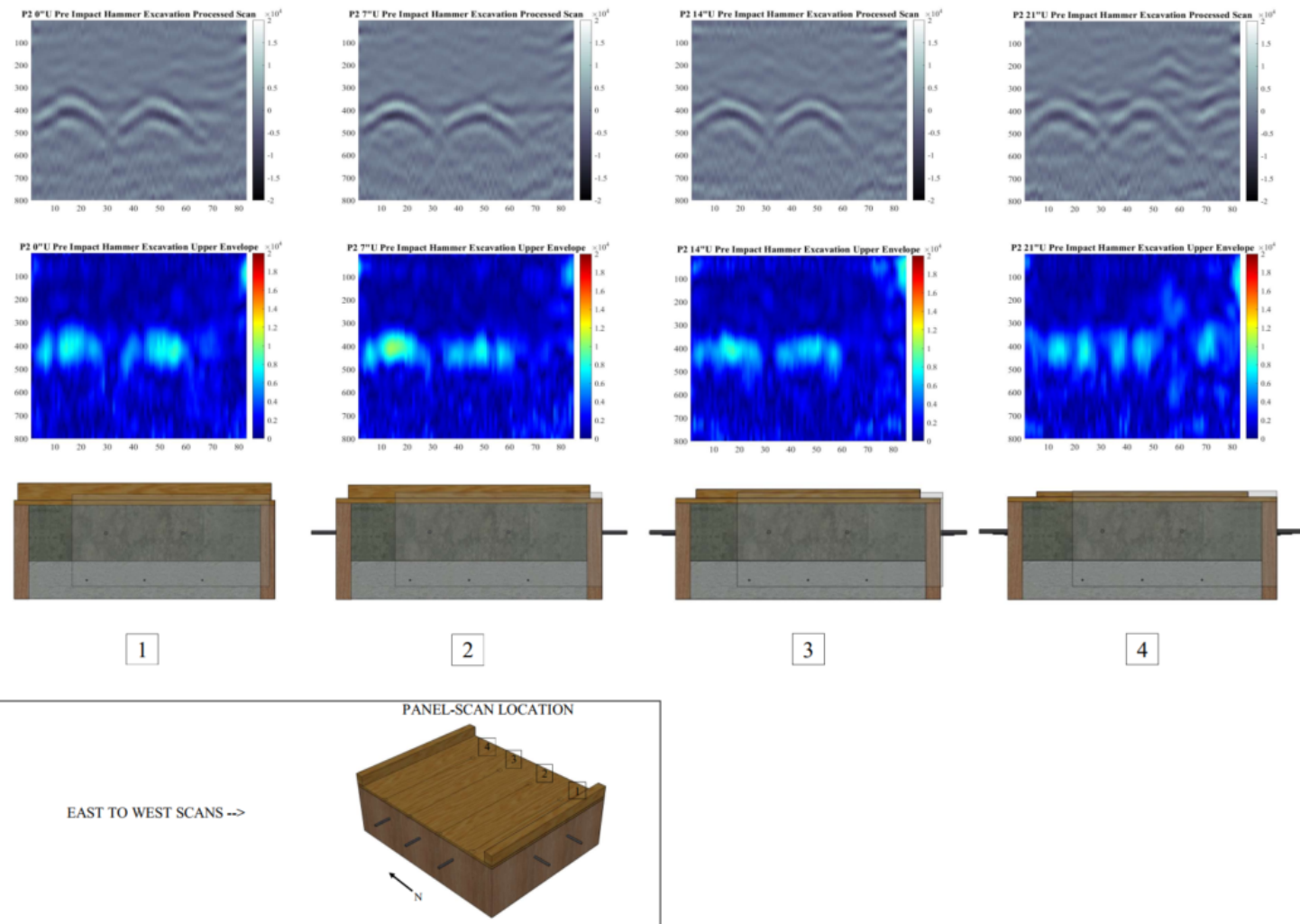
PANEL TEST - PRE EXCAVATION SCANS FROM EAST TO WEST ON BOTTOM FACE USING 2600 MHZ ANTENNA



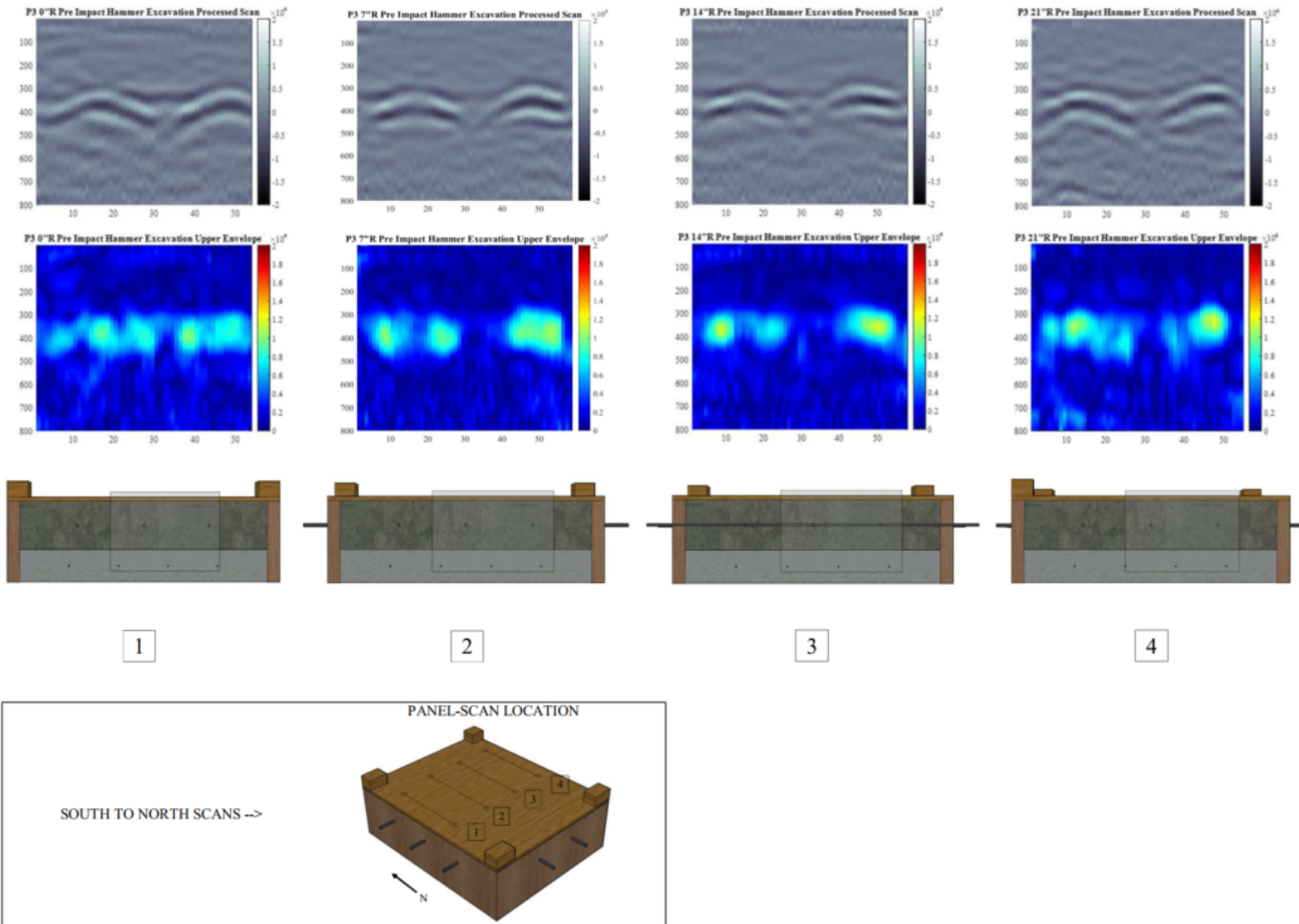
PANEL 2 - PRE IMPACT HAMMER EXCAVATION SCANS FROM SOUTH TO NORTH ON BOTTOM FACE BETWEEN PLYWOOD BOTTOM AND 1.2 NANSECONDS PAST SHOTCRETE/CONCRETE INTERFACE USING 2600 MHZ ANTENNA



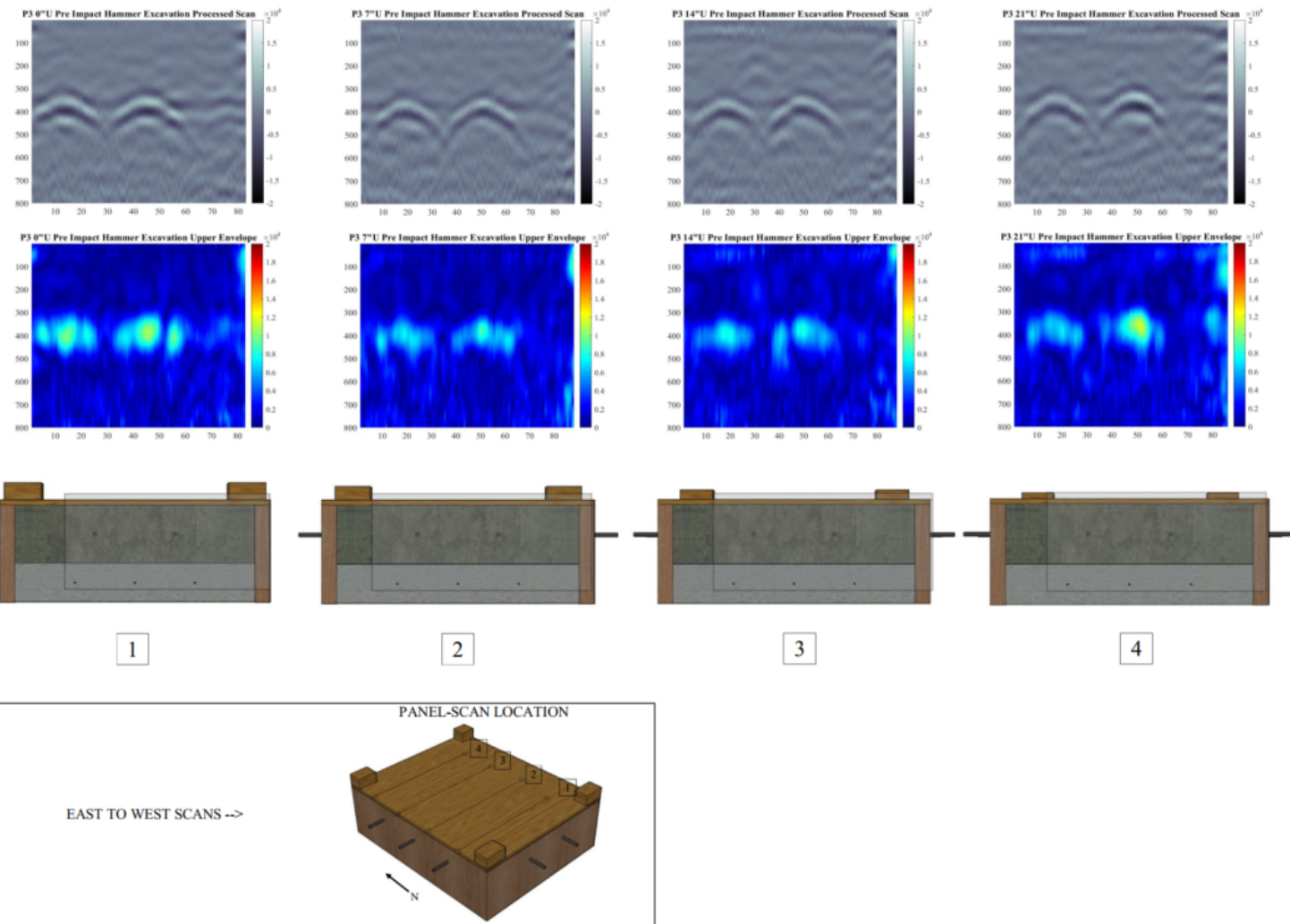
PANEL 2 - PRE IMPACT HAMMER EXCAVATION SCANS FROM EAST TO WEST ON BOTTOM FACE BETWEEN PLYWOOD BOTTOM AND 1.2 NANSECONDS PAST SHOTCRETE/CONCRETE INTERFACE USING 2600 MHZ ANTENNA



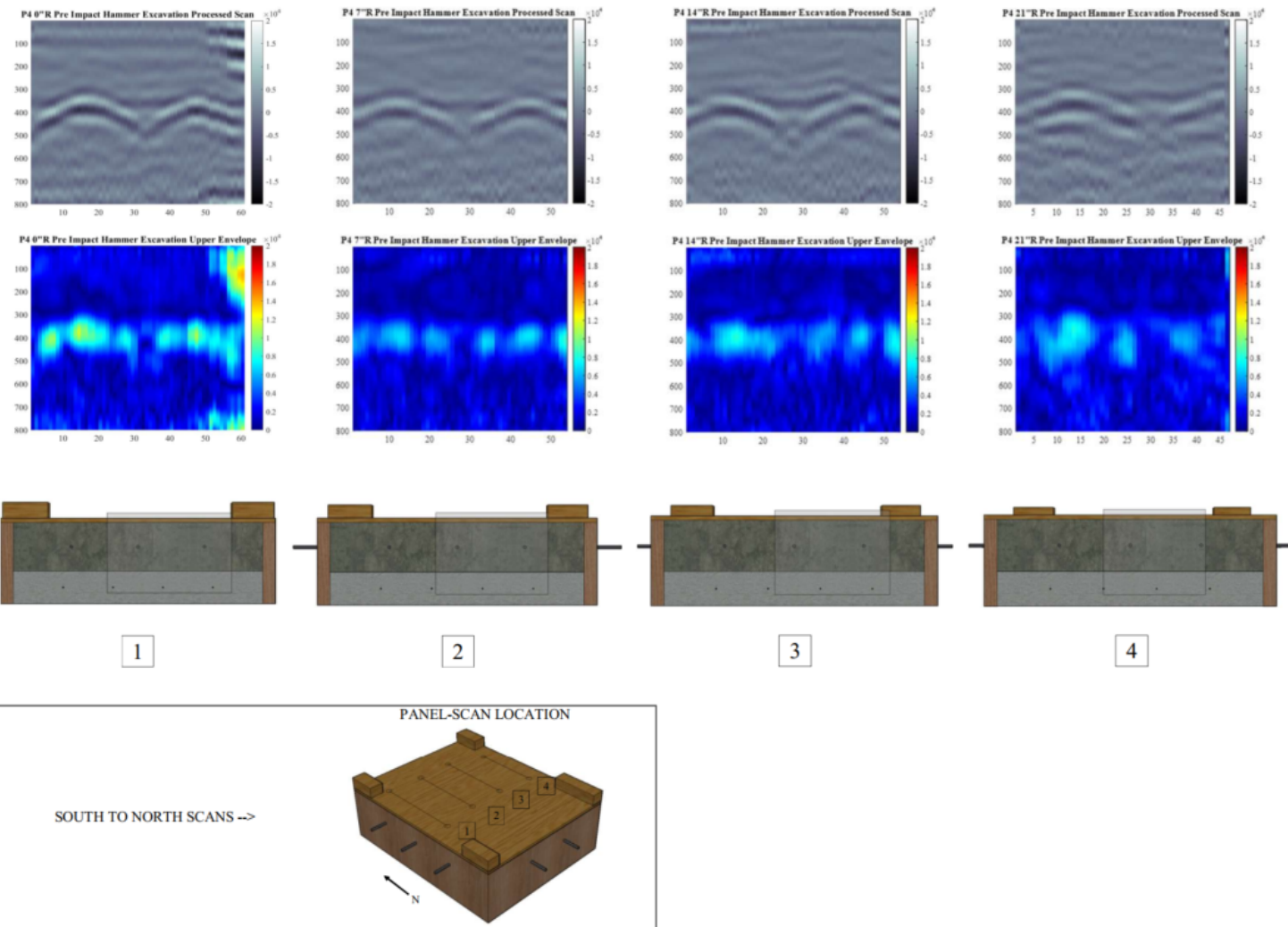
PANEL 3 - PRE IMPACT HAMMER EXCAVATION SCANS FROM SOUTH TO NORTH ON BOTTOM FACE BETWEEN PLYWOOD BOTTOM AND 1.2 NANSECONDS PAST SHOTCRETE/CONCRETE INTERFACE USING 2600 MHZ ANTENNA



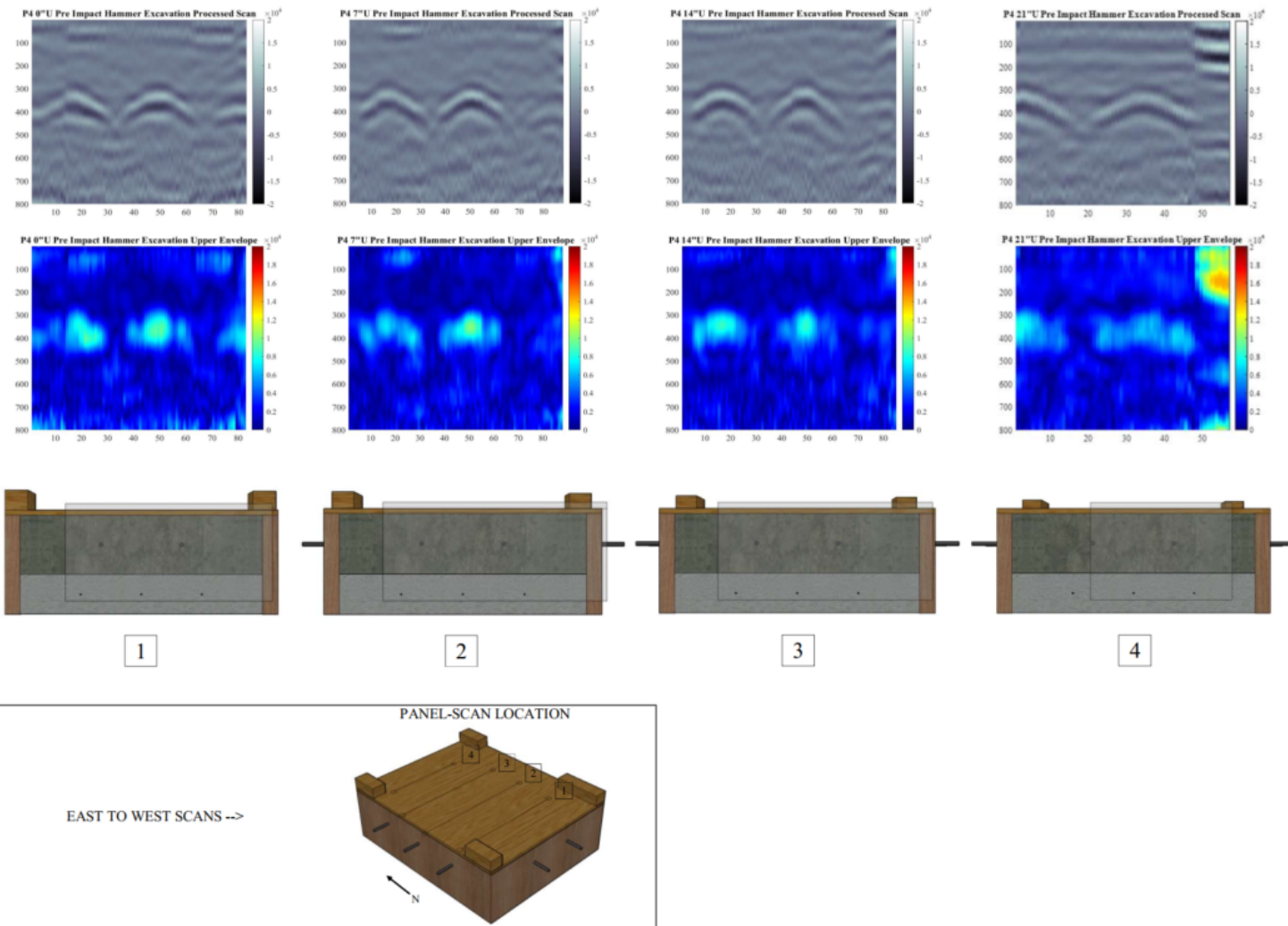
PANEL 3 - PRE IMPACT HAMMER EXCAVATION SCANS FROM EAST TO WEST ON BOTTOM FACE BETWEEN PLYWOOD BOTTOM AND 1.2 NANOSECONDS PAST SHOTCRETE/CONCRETE INTERFACE USING 2600 MHZ ANTENNA



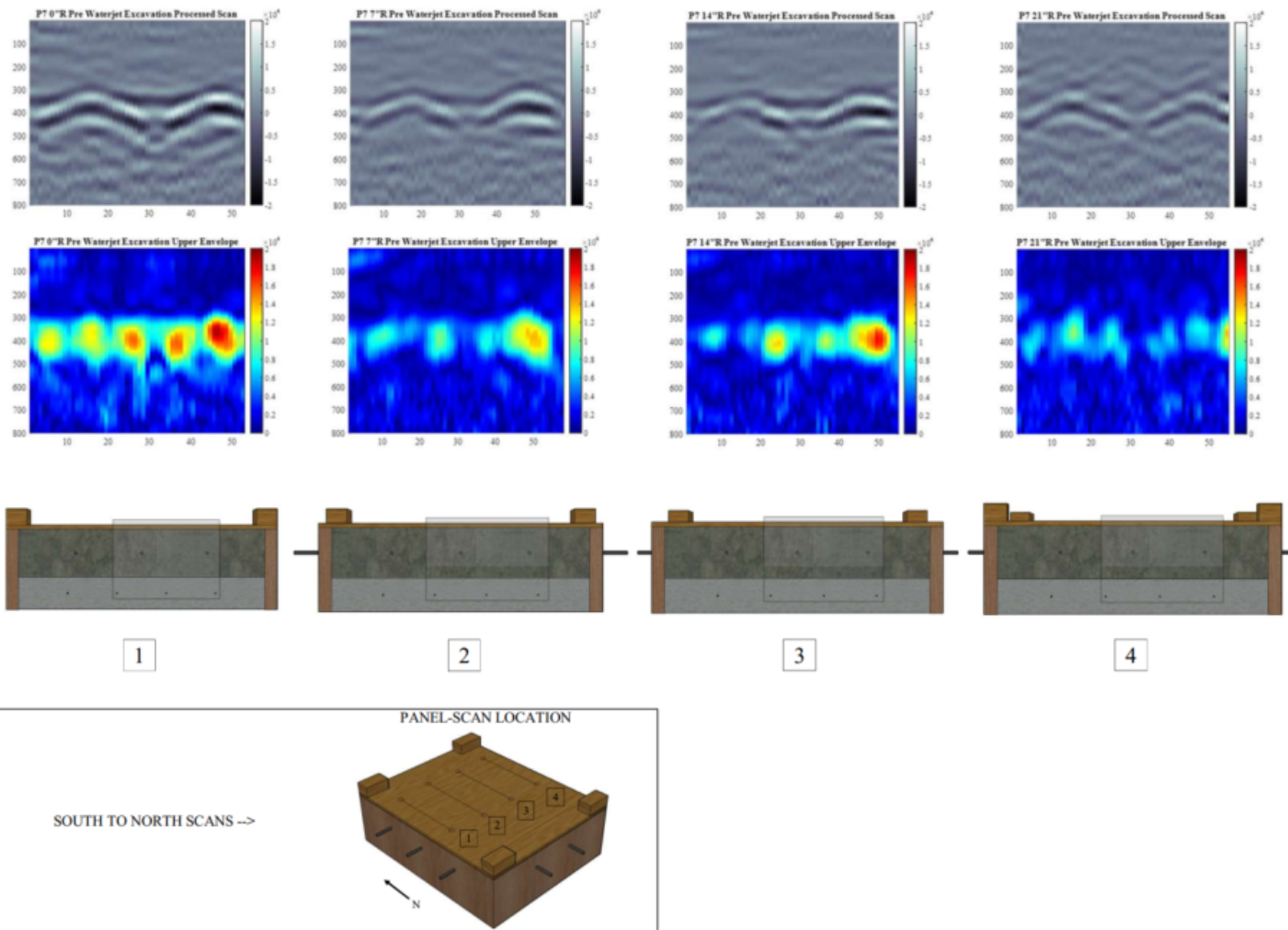
PANEL 4 - PRE IMPACT HAMMER EXCAVATION SCANS FROM SOUTH TO NORTH ON BOTTOM FACE BETWEEN PLYWOOD BOTTOM AND 1.2 NANSECONDS PAST SHOTCRETE/CONCRETE INTERFACE USING 2600 MHZ ANTENNA



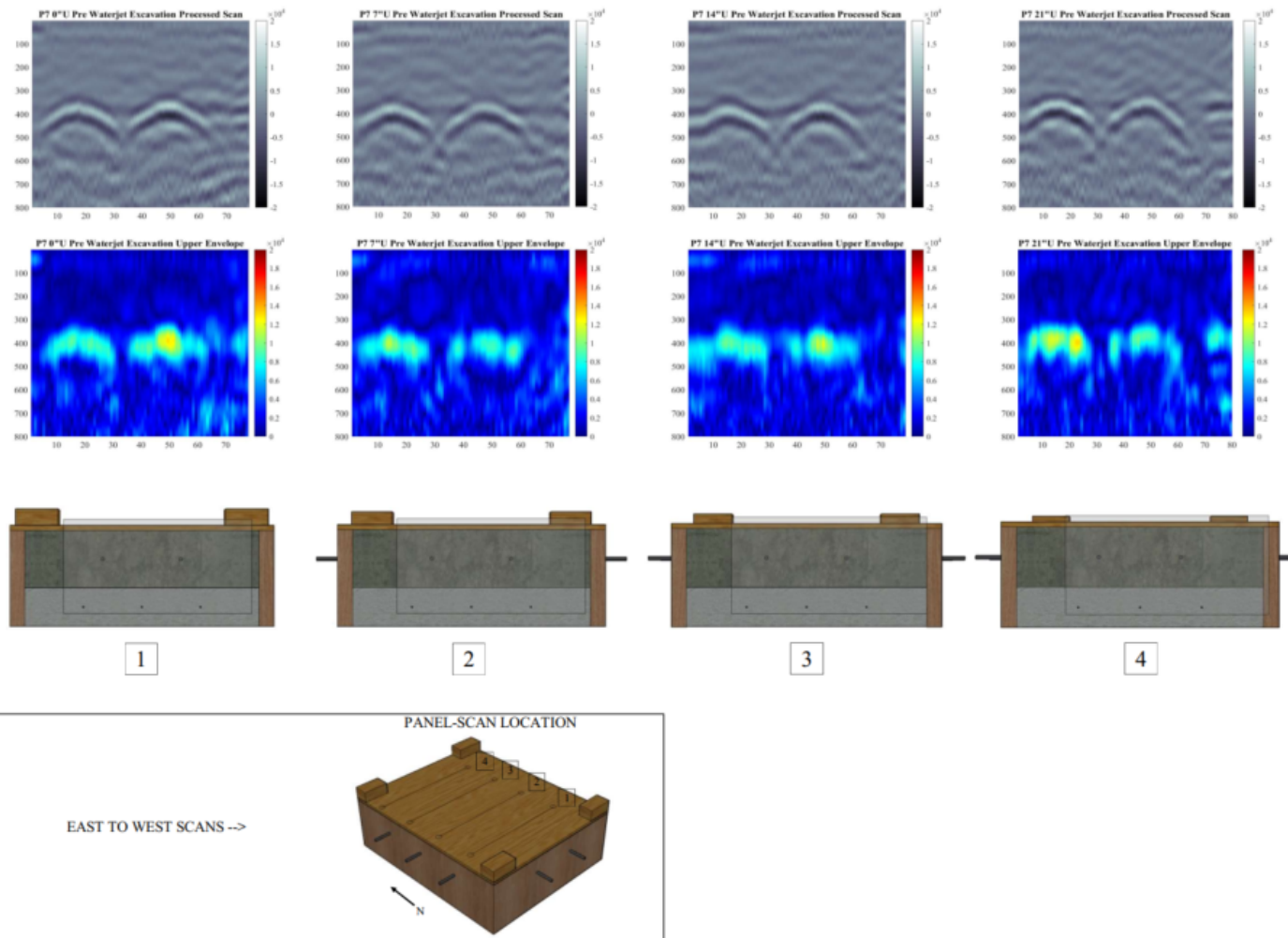
PANEL 4 - PRE IMPACT HAMMER EXCAVATION SCANS FROM EAST TO WEST ON BOTTOM FACE BETWEEN PLYWOOD BOTTOM AND 1.2 NANSECONDS PAST SHOTCRETE/CONCRETE INTERFACE USING 2600 MHZ ANTENNA



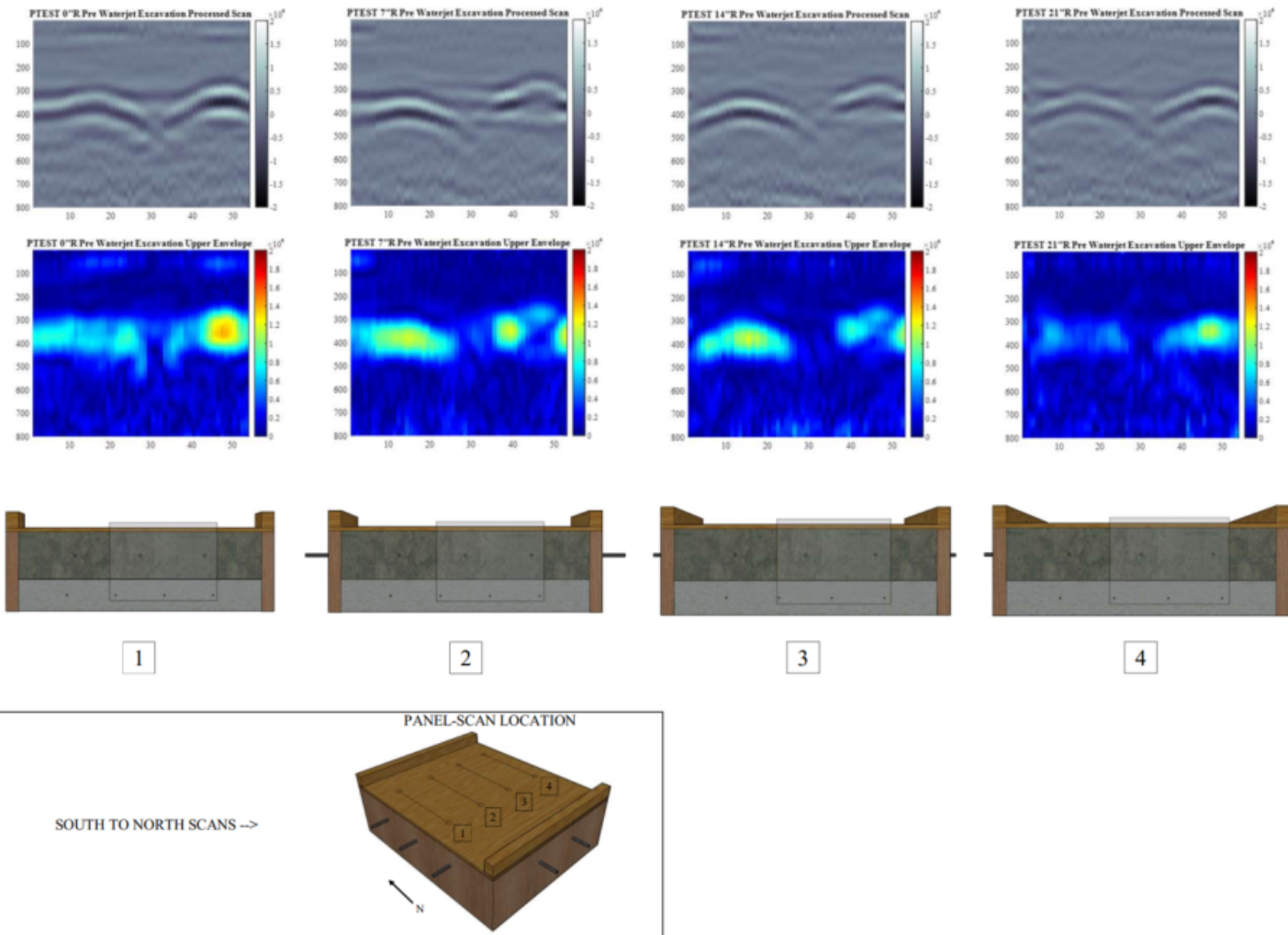
**PANEL 7 - PRE WATERJET EXCAVATION SCANS FROM SOUTH TO NORTH ON BOTTOM FACE BETWEEN PLYWOOD
BOTTOM AND 1.2 NANSECONDS PAST SHOTCRETE/CONCRETE INTERFACE USING 2600 MHZ ANTENNA**



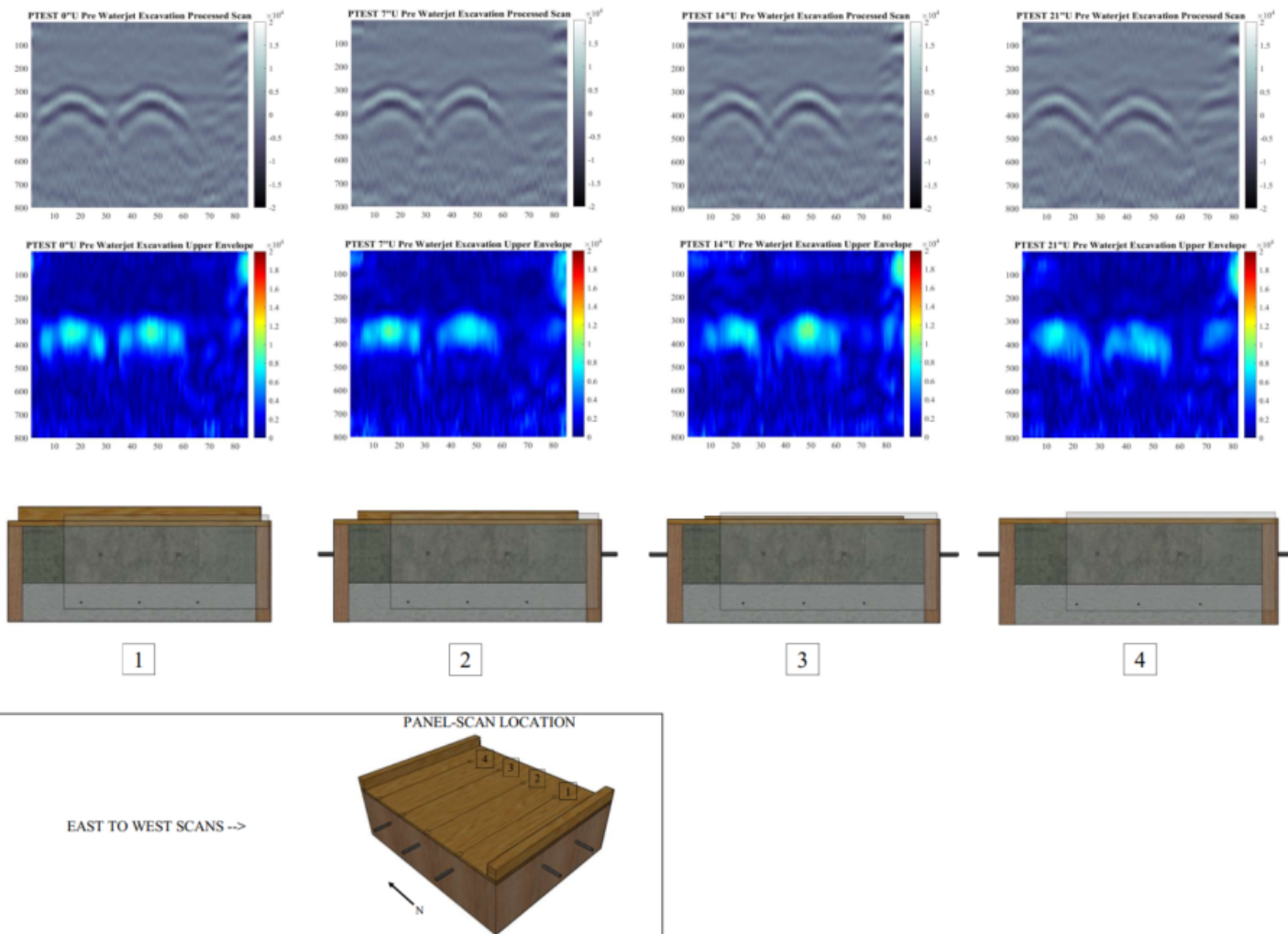
**PANEL 7 - PRE WATERJET EXCAVATION SCANS FROM EAST TO WEST ON BOTTOM FACE BETWEEN PLYWOOD
BOTTOM AND 1.2 NANOSECONDS PAST SHOTCRETE/CONCRETE INTERFACE USING 2600 MHZ ANTENNA**



PANEL TEST - PRE WATERJET EXCAVATION SCANS FROM SOUTH TO NORTH ON BOTTOM FACE BETWEEN PLYWOOD BOTTOM AND 1.2 NANSECONDS PAST SHOTCRETE/CONCRETE INTERFACE USING 2600 MHZ ANTENNA



**PANEL TEST - PRE WATERJET EXCAVATION SCANS FROM EAST TO WEST ON BOTTOM FACE BETWEEN PLYWOOD
BOTTOM AND 1.2 NANOSECONDS PAST SHOTCRETE/CONCRETE INTERFACE USING 2600 MHZ ANTENNA**



Section B-6: 1600 MHz Radargram Interpretation Notes

Panel Number	2
Excavation Method	Impact Hammer
Scan Set Direction	South to North

Scan Location #1	0”R
Is there excavation within this scan line from AutoCAD model?	No
Notes	Scan located just outside excavation profile, areas between rebar show higher amplitude in three streak lines extending from the level of the rebar to the concrete/shotcrete interface.

Scan Location #2	7”R
Is there excavation within this scan line from AutoCAD model?	Yes
Notes	Areas between rebar show higher amplitude in three streak lines extending from the level of the rebar to the concrete/shotcrete interface, and gaining even more amplitude when reaching open air.

Scan Location #3	14”R
Is there excavation within this scan line from AutoCAD model?	Yes
Notes	Areas between rebar show higher amplitude in three streak lines extending from the level of the rebar to the concrete/shotcrete interface, and gaining even more amplitude when reaching open air.

Scan Location #4	21”R
Is there excavation within this scan line from AutoCAD model?	No
Notes	Scan has much weaker signal than other three in this scan set direction. Doesn’t even have as strong signal for first two encountered rebar. Possible that aggregate is blocking signal for rebar. Still shows signs similar to 0”R between the rebar but at a weaker amplitude.

Panel Number	2
Excavation Method	Impact Hammer
Scan Set Direction	East to West

Scan Location #1	0"U
Is there excavation within this scan line from AutoCAD model?	No
Notes	Scan located just outside excavation profile, areas between rebar show higher amplitude in three streak lines, with middle streak the strongest amplitude, extending from the level of the rebar to the concrete/shotcrete interface, and gaining even more amplitude in shotcrete layer. Scan could actually be right at border of excavation profile, showing reflection similar to that of concrete/air interface.

Scan Location #2	7"U
Is there excavation within this scan line from AutoCAD model?	Yes
Notes	Areas between rebar show higher amplitude in three streak lines extending from the level of the rebar to the concrete/shotcrete interface, and gaining even more amplitude when reaching open air. Strong reflection on bottom right hand of scan outlines edge of excavation profile.

Scan Location #3	14"U
Is there excavation within this scan line from AutoCAD model?	Yes
Notes	Areas between rebar show higher amplitude in three streak lines extending from the level of the rebar to the concrete/shotcrete interface, and gaining even more amplitude when reaching open air. Strong reflection on bottom right hand of scan outlines edge of excavation profile.

Scan Location #4	21"U
Is there excavation within this scan line from AutoCAD model?	Yes
Notes	Scan has much weaker signal than other three in this scan set direction. Doesn't even have as strong signal for first two encountered rebar. Possible that aggregate is blocking signal for rebar. Shows signs similar to un-excavated profile. Still shows higher amplitude reflection between rebar extending to concrete/shotcrete interface.

Panel Number	3
Excavation Method	Impact Hammer
Scan Set Direction	South to North

Scan Location #1	0”R
Is there excavation within this scan line from AutoCAD model?	No
Notes	Scan located just outside excavation profile, areas between rebar show higher amplitude in three streak lines, with middle streak the strongest amplitude, extending from the level of the rebar to the concrete/shotcrete interface, however it seems more like connection of rebar parabola because it doesn’t extend as strong as it did in Panel 2.

Scan Location #2	7”R
Is there excavation within this scan line from AutoCAD model?	Yes
Notes	The concrete/air interface is clearer in this scan than the same for Panel 2. Streaks of higher amplitude occur between the concrete/air interface and rebar, specifically in between the rebar. Interestingly, the area between concrete/air interface and the second rebar has slightly higher amplitude throughout.

Scan Location #3	14”R
Is there excavation within this scan line from AutoCAD model?	Yes
Notes	The concrete/air interface is clearer in this scan than the same for Panel 2. Three streaks of higher amplitude occur between the concrete/air interface and rebar, specifically in between the rebar. Similar to 7”R, the area between concrete/air interface and the second rebar has slightly higher amplitude throughout.

Scan Location #4	21”R
Is there excavation within this scan line from AutoCAD model?	No
Notes	Scan has slightly weaker signal than other three in this scan set direction. Doesn’t have as strong signal for first two encountered rebar. Possible that aggregate is blocking signal for rebar. Still shows higher amplitude reflection between rebar extending to concrete/shotcrete interface.

Panel Number	3
Excavation Method	Impact Hammer
Scan Set Direction	East to West

Scan Location #1	0"U
Is there excavation within this scan line from AutoCAD model?	No
Notes	Scan located just outside excavation profile, areas between rebar show higher amplitude in three streak lines, with middle streak the strongest amplitude, extending from the level of the rebar to the concrete/shotcrete interface, however it could be a connection of rebar parabola, creating a U shape at the interface. There's also a strong reflection on bottom right corner of scan, possibly outlining the edge of the panel where the wood form is.

Scan Location #2	7"U
Is there excavation within this scan line from AutoCAD model?	Yes
Notes	Streaks of higher amplitude occur between the concrete/air interface and rebar, specifically in between the rebar. The stronger reflection between the rebar gives more of a hyperbola shape until reaching the concrete/air interface. There's also a strong reflection on bottom right corner of scan which is interesting because it should just be shotcrete.

Scan Location #3	14"U
Is there excavation within this scan line from AutoCAD model?	Yes
Notes	Streaks of higher amplitude occur between the concrete/air interface and rebar, specifically in between the rebar. Concrete/air interface shows relatively strongest amplitude compared to other Panel 3 scans.

Scan Location #4	21"U
Is there excavation within this scan line from AutoCAD model?	No
Notes	Scan has slightly weaker signal than other three in this scan set direction. Doesn't have as strong signal for first encountered rebar. Possible that aggregate is blocking signal for rebar. Still shows higher amplitude reflection between rebar extending to concrete/shotcrete interface in three streak pattern.

Panel Number	4
Excavation Method	Impact Hammer
Scan Set Direction	South to North

Scan Location #1	0”R
Is there excavation within this scan line from AutoCAD model?	No
Notes	Scan located just outside excavation profile, areas between rebar show higher amplitude in three streak lines, with middle streak the strongest amplitude, extending from the level of the rebar to the concrete/shotcrete interface.

Scan Location #2	7”R
Is there excavation within this scan line from AutoCAD model?	Yes
Notes	Streaks of higher amplitude occur between the concrete/air interface and rebar, specifically in between the rebar. There are extremely high amplitude readings at the concrete/air interface between each rebar reaching well into the concrete layer. There’s also a strong reflection on bottom right corner of scan which could be an excavation edge effect.

Scan Location #3	14”R
Is there excavation within this scan line from AutoCAD model?	Yes
Notes	Streaks of higher amplitude occur between the concrete/air interface and rebar, specifically in between the rebar. There are extremely high amplitude readings at the concrete/air interface between each rebar reaching well into the concrete layer. There’s also a strong reflection on bottom right corner of scan which could be an excavation edge effect however it’s not as strong as 7”R.

Scan Location #4	21”R
Is there excavation within this scan line from AutoCAD model?	No
Notes	Scan has much weaker signal than other three in this scan set direction. Doesn’t have as strong signal for each rebar. Possible that aggregate is blocking signal for rebar.

Panel Number	4
Excavation Method	Impact Hammer
Scan Set Direction	East to West

Scan Location #1	0"U
Is there excavation within this scan line from AutoCAD model?	Yes
Notes	Scan located right at edge of excavation profile, areas between rebar show higher amplitude in three streak lines, extending from the level of the rebar to the concrete/shotcrete interface. There is also strong reflection in bottom right corner of scan which could be located within shotcrete layer or be an edge effect of excavation profile.

Scan Location #2	7"U
Is there excavation within this scan line from AutoCAD model?	Yes
Notes	Streaks of higher amplitude occur between the concrete/air interface and rebar, specifically in between the rebar. There is a high amplitude reading at the concrete/air interface between each rebar reaching slightly into the concrete layer. There's also a strong reflection on bottom right corner of scan which could be in the shotcrete layer or an excavation edge effect.

Scan Location #3	14"U
Is there excavation within this scan line from AutoCAD model?	Yes
Notes	Streaks of higher amplitude occur between the concrete/air interface and rebar, specifically in between the rebar. There is a high amplitude reading at the concrete/air interface between each rebar reaching slightly into the concrete layer. There's also a strong reflection on bottom right corner of scan which could be in the shotcrete layer or an excavation edge effect.

Scan Location #4	21"U
Is there excavation within this scan line from AutoCAD model?	No
Notes	Scan has slightly weaker signal than other three in this scan set direction. Still shows higher amplitude reflection between rebar extending to concrete/shotcrete interface.

Panel Number	7
Excavation Method	Waterjet
Scan Set Direction	South to North

Scan Location #1	0”R
Is there excavation within this scan line from AutoCAD model?	Yes
Notes	Weaker amplitude signal throughout, there are still some signs of higher amplitude between the rebar as well as a streak to the left of the first rebar where the excavation occurred. There is also possible identification of the concrete/shotcrete interface throughout the whole scan.

Scan Location #2	7”R
Is there excavation within this scan line from AutoCAD model?	Yes
Notes	There is a rise in amplitude shown as a streak between the rebar going from the rebar level to the shotcrete/concrete interface however it is much weaker than the amplitude streaks showing up to the left of the first rebar going from the rebar level down to where the excavation occurred.

Scan Location #3	14”R
Is there excavation within this scan line from AutoCAD model?	Yes
Notes	There is a rise in amplitude shown as multiple streaks between the rebar going from the rebar level to the shotcrete/concrete interface however it is much weaker than the amplitude streak showing up to the left of the first rebar going from the rebar level down to the excavated surface.

Scan Location #4	21”R
Is there excavation within this scan line from AutoCAD model?	Yes
Notes	There is a rise in amplitude shown as multiple streaks between the rebar going from the rebar level to the shotcrete/concrete interface however it is much weaker than the amplitude streaks showing up to the left of the first rebar going from the rebar level down to the excavated surface.

Panel Number	7
Excavation Method	Waterjet
Scan Set Direction	East to West

Scan Location #1	0"U
Is there excavation within this scan line from AutoCAD model?	No
Notes	There is a vertical streak of increased amplitude that shows up between the rebar and extends to the concrete/shotcrete interface.

Scan Location #2	7"U
Is there excavation within this scan line from AutoCAD model?	Yes
Notes	There is a vertical streak of increased amplitude between the rebar and extends to the excavated surface as well as increased amplitude in groups throughout the shotcrete layer. This makes sense as this scan lines up with the waterjet excavation profile.

Scan Location #3	14"U
Is there excavation within this scan line from AutoCAD model?	No
Notes	There is a vertical streak of increased amplitude that shows up between the rebar and extends to the concrete/shotcrete interface.

Scan Location #4	21"U
Is there excavation within this scan line from AutoCAD model?	No
Notes	There is a vertical streak of increased amplitude that shows up between the rebar and extends to the concrete/shotcrete interface.

Panel Number	TEST
Excavation Method	Waterjet
Scan Set Direction	South to North

Note: Waterjet did not excavate through entirety of shotcrete layer for this particular sample.

Scan Location #1	0”R
Is there excavation within this scan line from AutoCAD model?	Yes
Notes	The amplitude of the first rebar is weak, which could be due to aggregate, and there is a vertical streak of increased amplitude between the rebar. There is also a slight increase in amplitude at the bottom right corner of the scan.

Scan Location #2	7”R
Is there excavation within this scan line from AutoCAD model?	Yes
Notes	Both rebar come in with strong amplitude for this scan and there is a noticeable increase between the rebar where the excavation occurred however it isn’t relatively strong compared to that of the impact hammer GPR scans.

Scan Location #3	14”R
Is there excavation within this scan line from AutoCAD model?	Yes
Notes	Both rebar come in with strong amplitude for this scan and there is a noticeable increase in amplitude between the rebar as well as before the first rebar where the excavation occurred.

Scan Location #4	21”R
Is there excavation within this scan line from AutoCAD model?	Yes
Notes	The amplitude of the first rebar is weak, which could be due to aggregate, and there is a vertical streak of increased amplitude between the rebar. There is also a slight increase in amplitude at the bottom left corner of the scan where the excavation occurred.

Panel Number	TEST
Excavation Method	Waterjet
Scan Set Direction	East to West

Note: Waterjet did not excavate through entirety of shotcrete layer for this particular sample.

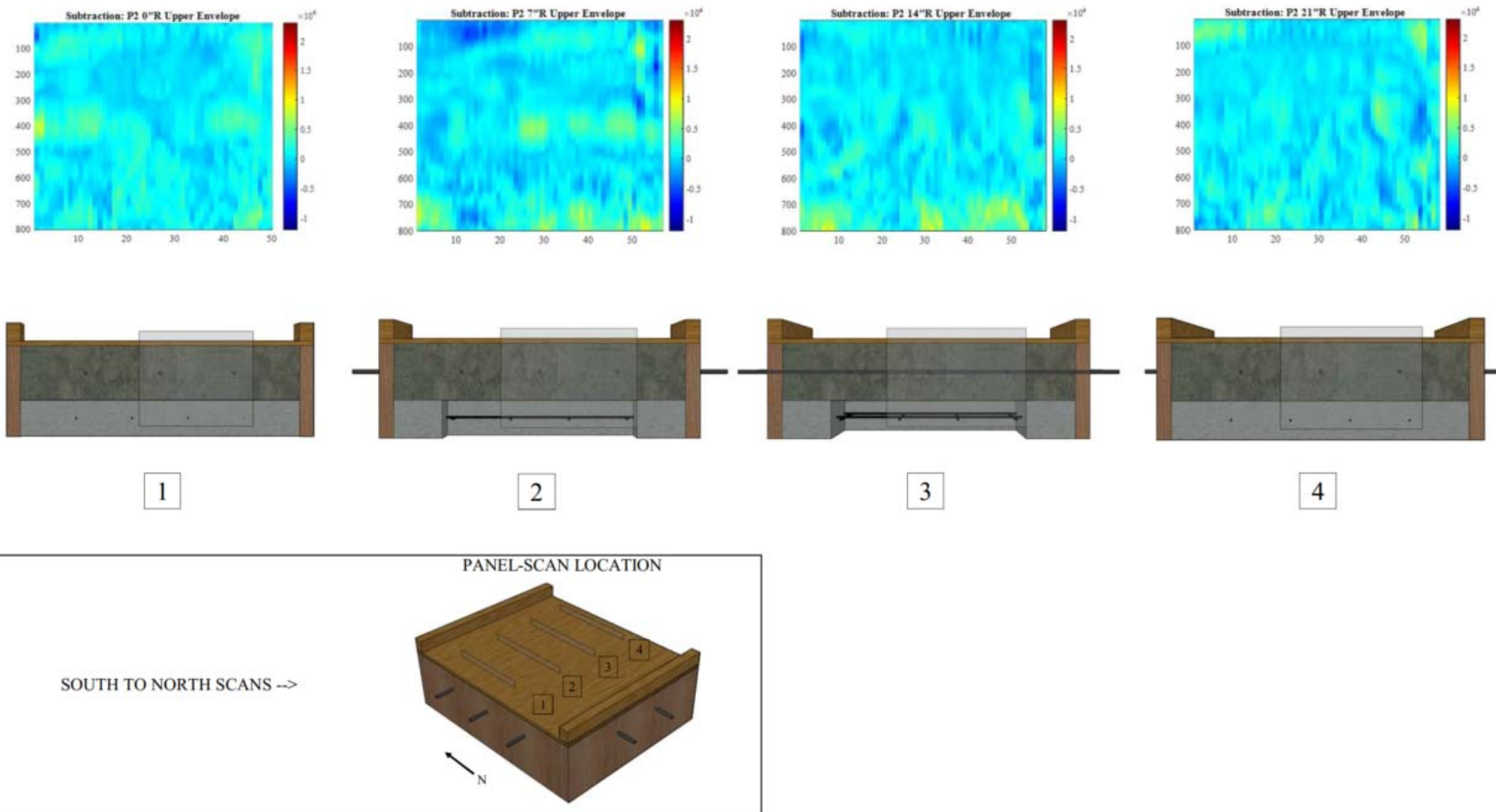
Scan Location #1	0"U
Is there excavation within this scan line from AutoCAD model?	No
Notes	There are multiple vertical streaks of increased amplitude that show up between the rebar, extending to the concrete/shotcrete interface. There is also a slight increase in amplitude at the bottom right corner of the scan, possibly due to edge effects from the wooden form.

Scan Location #2	7"U
Is there excavation within this scan line from AutoCAD model?	Yes
Notes	There are vertical streaks of increased amplitude between the rebar, extending to where the excavation occurred. There is also increased amplitude in groups throughout the excavated profile.

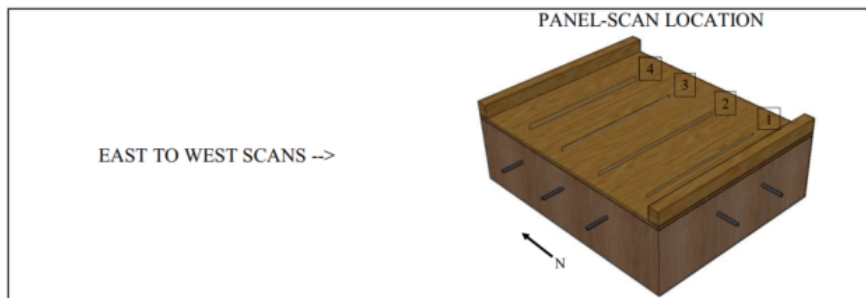
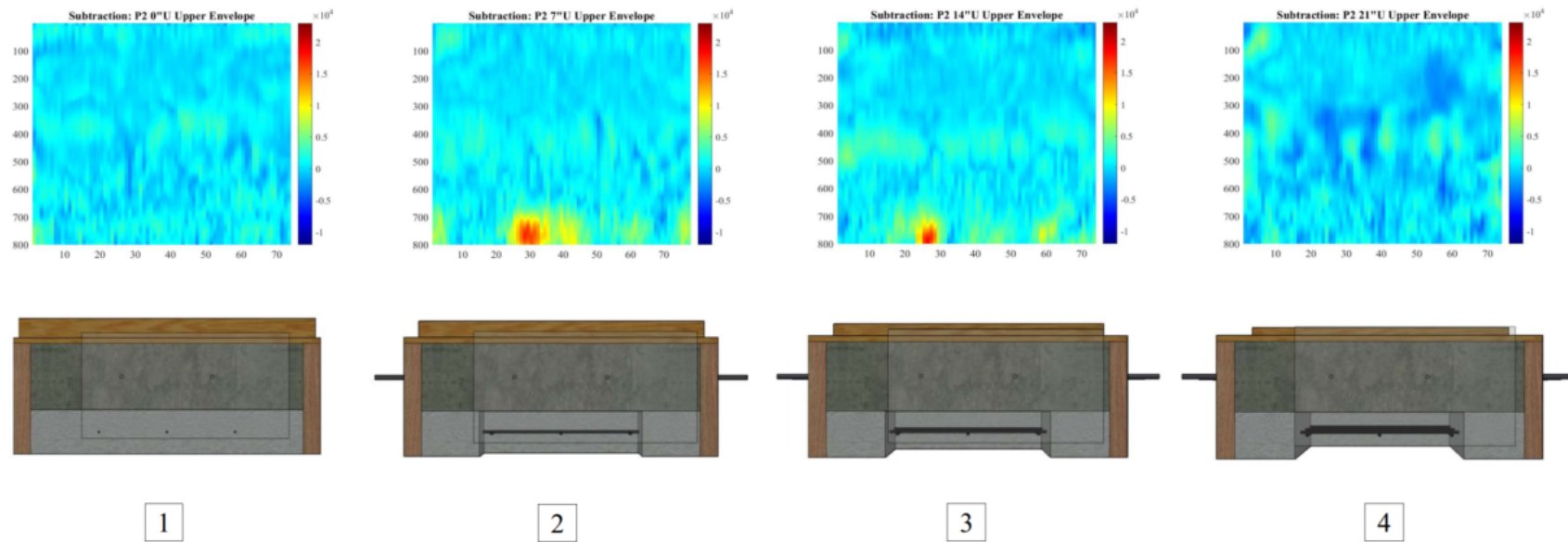
Scan Location #3	14"U
Is there excavation within this scan line from AutoCAD model?	No
Notes	There are multiple vertical streaks of increased amplitude between the rebar, extending to the concrete/shotcrete interface as well as increased amplitude in groups throughout the shotcrete layer. This scan is located parallel, and close to the edge, to the waterjet excavation profile.

Scan Location #4	21"U
Is there excavation within this scan line from AutoCAD model?	No
Notes	There are multiple vertical streaks of increased amplitude that show up between the rebar, extending to the concrete/shotcrete interface. There is also a slight increase in amplitude at the bottom right corner of the scan, possibly due to edge effects from the wooden form.

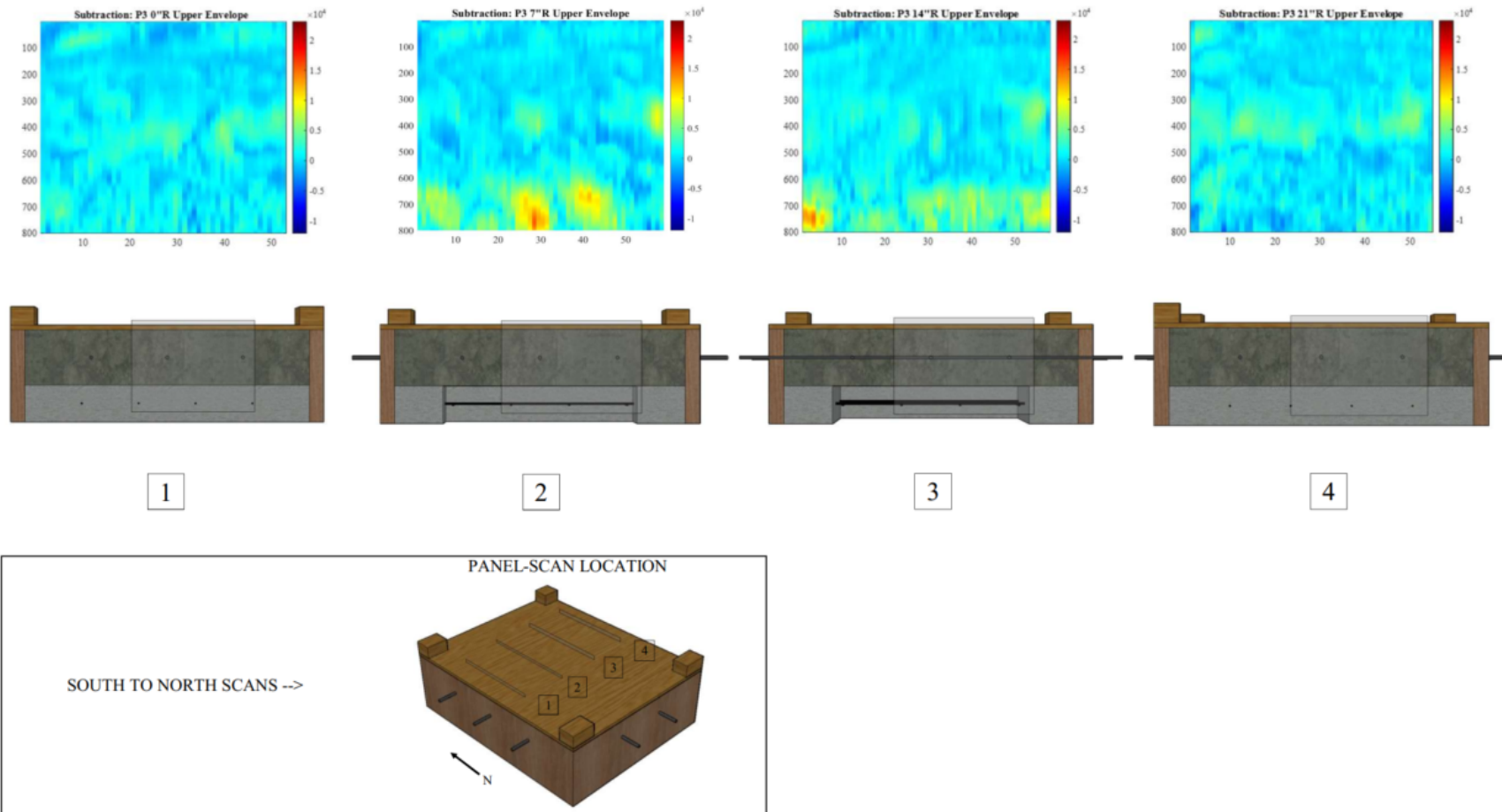
PANEL 2 - SCAN SUBTRACTION FROM SOUTH TO NORTH ON BOTTOM FACE BETWEEN PLYWOOD BOTTOM AND 1.2 NANoseconds PAST SHOTCRETE/CONCRETE INTERFACE USING 2600 MHZ ANTENNA



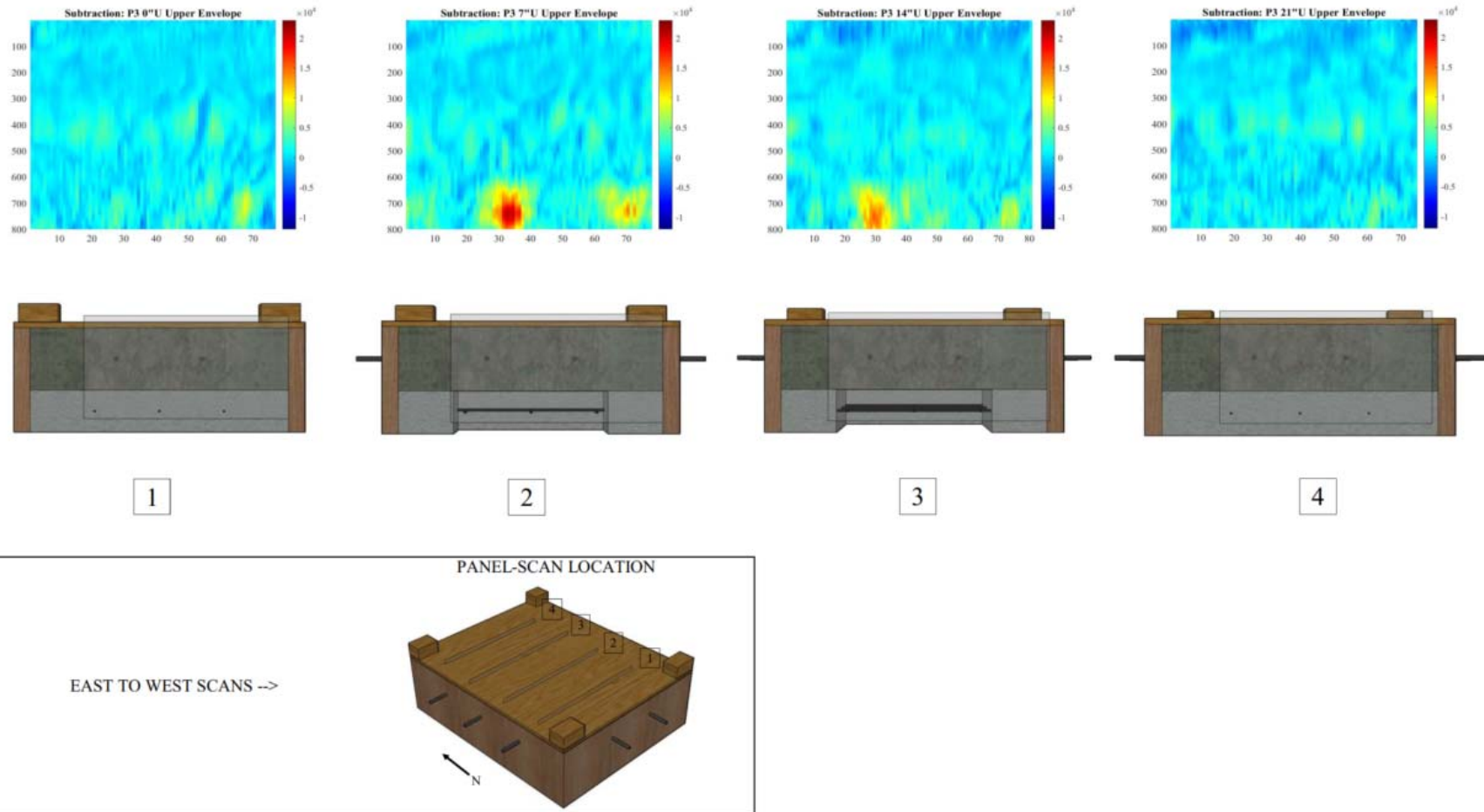
PANEL 2 - SCAN SUBTRACTION FROM EAST TO WEST ON BOTTOM FACE BETWEEN PLYWOOD BOTTOM AND 1.2 NANOSECONDS PAST SHOTCRETE/CONCRETE INTERFACE USING 2600 MHZ ANTENNA



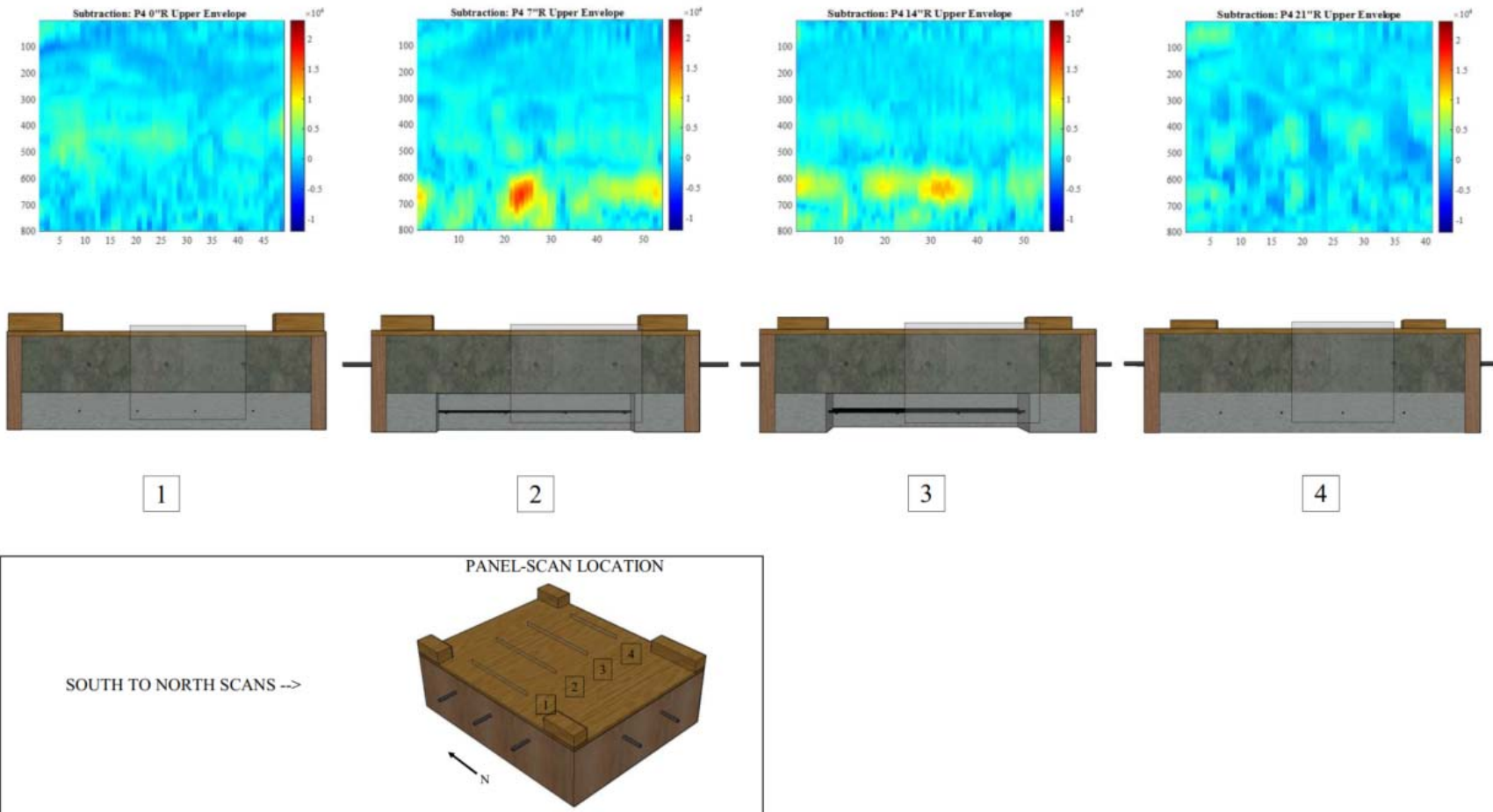
PANEL 3 - SCAN SUBTRACTION FROM SOUTH TO NORTH ON BOTTOM FACE BETWEEN PLYWOOD BOTTOM AND 1.2 NANOSECONDS PAST SHOTCRETE/CONCRETE INTERFACE USING 2600 MHZ ANTENNA



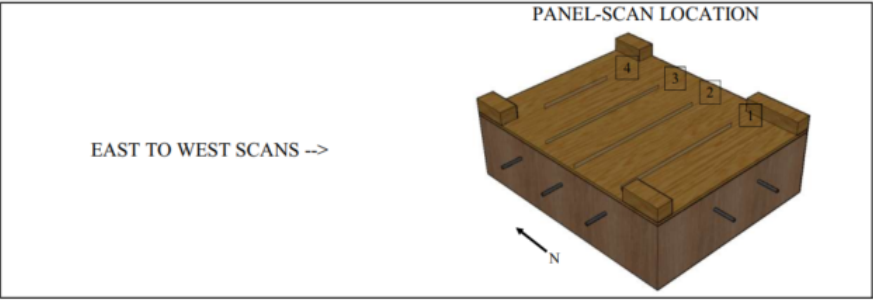
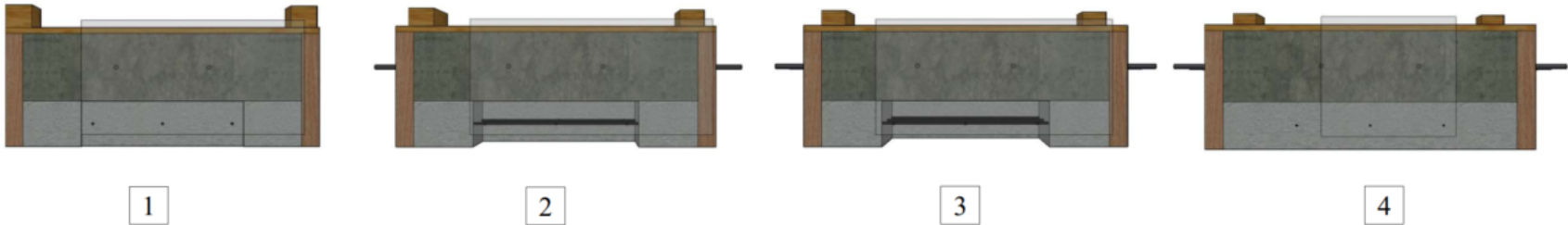
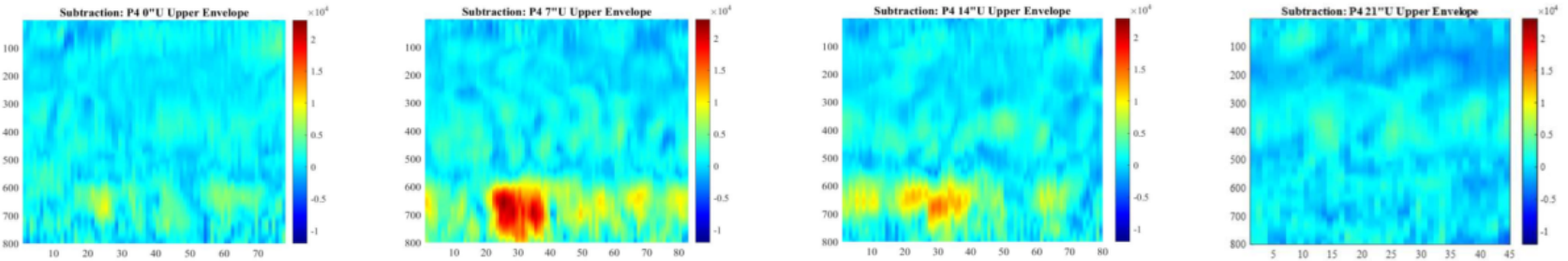
PANEL 3 - SCAN SUBTRACTION FROM EAST TO WEST ON BOTTOM FACE BETWEEN PLYWOOD BOTTOM AND 1.2 NANOSECONDS PAST SHOTCRETE/CONCRETE INTERFACE USING 2600 MHZ ANTENNA



PANEL 4 - SCAN SUBTRACTION FROM SOUTH TO NORTH ON BOTTOM FACE BETWEEN PLYWOOD BOTTOM AND 1.2 NANOSECONDS PAST SHOTCRETE/CONCRETE INTERFACE USING 2600 MHZ ANTENNA



PANEL 4 - SCAN SUBTRACTION FROM EAST TO WEST ON BOTTOM FACE BETWEEN PLYWOOD BOTTOM AND 1.2 NANOSECONDS PAST SHOTCRETE/CONCRETE INTERFACE USING 2600 MHZ ANTENNA



END OF REPORT